M.SC. Eng. Ahmed H. Hanfy

The Szewalski
Institute of Fluid-Flow Machinery, Polish Academy of Science
in Gdańsk

SURFACE ROUGHNESS EFFECT ON SHOCK WAVE BOUNDARY LAYER INTERACTION ON TRANSONIC COMPRESSOR PROFILE

Doctoral thesis submitted to the Scientific Committee of
The Szewalski Institute of Fluid Flow Machinery
Polish Academy of Sciences

Promotor:
Prof. dr. hab. inż. Paweł Flaszyński
Assistant promoter:
Dr. inż. Piotr Kaczyński

Gdańsk, *February 2026*

Abstract

The pursuit of more compact and efficient aero-engine designs demands a profound understanding of complex aerodynamic phenomena within compressor components. As engine operating speeds and overall pressure ratios increase, these components face higher aerodynamic loading, leading to performance reduction. These adverse effects, particularly the increased losses due to shock boundary layer interaction (SBLI), are especially pronounced when boundary layers remain laminar. Such conditions are typical for engines operation at high altitudes, where Reynolds number reaches low values. The interaction of shock wave with the laminar boundary layer in these conditions often results in its separation, increased blockage, and severe unsteadiness, ultimately limiting the entire engine efficiency. To mitigate this, it is highly desirable to induce a laminar-turbulent transition before the boundary layer interacts with the shockwave. This effect can be achieved, among other things, through controlled modification of the compressor blade surface. This study presents an experimental investigation into the effect of surface roughness on the interaction of shock waves with the boundary layer on the suction surface of a transonic fan profile.

The experimental work was conducted in a single passage transonic fan profile, replicating typical turbomachinery operating conditions involving a high adverse pressure gradient where SBLI-induced separation is prone to occur. Five versions of test profiles were manufactured with various texture and subjected to detailed surface evaluation. A comprehensive suite of advanced, non-intrusive techniques was employed, including high-speed schlieren imaging, oil flow visualisation, computer vision-based shock tracking, and boundary layer measurements using Laser Doppler Anemometry (LDA).

A critical finding was the relationship between favorable aerodynamic effects and flow stability. While time-averaged pressure data consistently classified the overall SBLI as laminar-type due to the stable mean shock position, the high roughness forced a highly three-dimensional, turbulent flow structure within the interaction and separation zones. This turbulent state yielded a profound, dual consequence. The aerodynamic benefit was substantial, as the enhanced turbulent mixing successfully re-energised the boundary layer, leading to superior flow recovery. This gain was confirmed by a 7.95% reduction in the overall separation area and a crucial 19.4% reduction in momentum thickness at the trailing edge region.

Conversely, this localized flow modification incurred a severe unsteadiness cost. Quantitative shock tracking analysis confirmed a significant increase in shock wave oscillations, with the high-roughness profile exhibiting an increase in oscillation amplitude of 40.58% relative to the smoothest baseline. This type of instability can be attributed to a high-frequency acoustic feedback mechanism, resulting in oscillations largely dominated by large-scale, low-frequency motion originating from the separation zone.

This investigation provides an enriched dataset and effectively improves our understanding of the operational limits of compressor blade surface roughness in the context of their aerodynamic properties. The findings are vital for developing robust design strategies aimed at optimizing performance in high-speed internal flows.

Streszczenie

Dążenie do bardziej kompaktowych i wydajnych konstrukcji silników lotniczych wymaga dogłębnego zrozumienia złożonych zjawisk aerodynamicznych w komponentach sprężarek. W miarę wzrostu prędkości obrotowej silnika oraz podwyższania stopnia sprężu jego komponenty narażone są na większe obciążenia, które mogą prowadzić do spadku jego wydajności. Tego typu niekorzystne efekty, zwłaszcza zwiększone straty wynikające z interakcji fali uderzeniowej z warstwą przyścienną (SBLI), są szczególnie wyraźne w przypadku warstwy laminarnej. Takie warunki są typowe dla pracy silnika na znacznych wysokościach, gdzie liczba Reynoldsa osiąga niskie wartości. Oddziaływanie fali uderzeniowej z laminarną warstwą przyścienną w tego typu warunkach często prowadzi do jej oderwania, skutkującego zawężeniem pola przepływu, a także niestabilnościami, czego efektem może być obniżenie sprawności całego silnika. Aby ograniczyć wyżej wymienione efekty, korzystne jest wywołanie przejścia laminarno-turbulentnego jeszcze przed oddziaływaniem warstwy z falą uderzeniową. Tego typu rezultat można uzyskać między innymi poprzez kontrolowaną modyfikację powierzchni łopatki sprężarki.

Niniejsza praca skupia się na badaniach eksperymentalnych dotyczących wpływu chropowatości powierzchni na oddziaływanie fali uderzeniowej z warstwą przyścienną na powierzchni ssącej modelu łopatki sprężarki transonicznej. Badania zostały przeprowadzone na modelu liniowej palisady sprężarkowej w tunelu transonicznym, gdzie odzwierciedlono typowe warunki pracy w stopniu sprężarkowym obejmujące ujemny gradient ciśnienia, przy którym występują sprzyjające warunki do oderwania przepływu wywołanego SBLI. W ramach kampanii pomiarowej przygotowano 5 wersji modelu profilu łopatki sprężarkowej o zróżnicowanej chropowatości oraz przeprowadzono szczegółowe pomiary optyczne powierzchni. By uchwycić złożoną fizykę przepływu w badaniach wykorzystano szereg zaawansowanych, nieinwazyjnych technik pomiarowych, takich jak wizualizacja Schlierena przy użyciu kamery szybko klatkowej, śledzenie fali uderzeniowej przy wykorzystywaniu techniki Computer Vision, a także pomiary warstwy przyściennej za pomocą Laserowej Anemometrii Dopplerowskiej (LDA).

Istotną obserwacją było określenie relacji pomiędzy korzystnymi efektami aerodynamicznymi a stabilnością przepływu. Uśrednione dane z pomiarów ciśnienia wskazywały, iż interakcja fali uderzeniowej z warstwą przyścienną jest typu laminarnego ze względu na stabilne średnie położenie fali. Jednakże w przypadku wariantu z największą chropowatością zaobserwowano powstawanie silnie trójwymiarowych turbulentnych struktur wirowych zarówno w strefie interakcji warstwy z falą uderzeniową, jak i w strefie oderwania. Turbulentny charakter warstwy miał dwojaki efekt. Korzystnym zjawiskiem było wzmocnienie procesów mieszania, co prowadziło do zwiększenia jej energii kinetycznej. Pozwoliło to na redukcję strefy oderwania o 7,95% a także ograniczenie o 19,4% grubości straty pędu w obszarze krawędzi spływowej. Jako negatywny efekt można uznać istotny wzrost oscylacji fali uderzeniowej potwierdzony w ramach ilościowej analizy polegającej na śledzeniu jej chwilowego położenia. Profil łopatki z najwyższym poziomem chropowatości powierzchni wykazał wzrost amplitudy oscylacji fali uderzeniowej o 40,58% w odniesieniu do przypadku bazowego. Tego typu niestabilność można powiązać z mechanizmem akustycznego sprzężenia zwrotnego o wysokiej częstotliwości, co skutkowało oscylacjami, w dużej mierze zdominowanymi przez wielkoskalowy ruch o niskiej częstotliwości pochodzący ze strefy oderwania.

Niniejsze badania wzbogacają wiedzę na temat operacyjnych granic stosowania chropowatości powierzchni łopatek sprężarkowych w kontekście ich właściwości aerodynamicznych. Wnioski mogą przynieść istotne wskazówki przy opracowywaniu strategii projektowych ukierunkowanych na optymalizację przepływów transonicznych przez stopnie sprężarkowe.

List of Publications

Journal Papers

1. Hanfy, A. H., Kaczynski, P., Doerffer, P., & Flaszynski, P. (2026). Enhanced line-scanning method for shock wave tracking in high-speed schlieren imaging. Aerospace Science and Technology, 168(111022), 111022. DOI: 10.1016/j.ast.2025.111022

2. Nel, P. L., Janke, C., Vasilopoulos, I., Swoboda, M., Schreyer, A.-M., Hady, A., & Flaszyński, P. (2024). Effect of Transition on Self-Sustained Shock Oscillations in Highly Loaded Transonic Rotors. AIAA Journal, 0(0):1-13. DOI: 10.2514/1.J063378

Conference papers

1. Nel, P. L., Pirozzoli, S., Swoboda, M., Grothe, P., Weiss, J. Hady, A. & Flaszyński, F. (2023). Towards Resolving Natural Shock Oscillation and Mitigation of Altitude Excitation in a Transonic Fan. In AIAA AVIATION 2023 Forum (p. 4001). DOI: 10.2514/6.2023-4001

2. Hanfy, A. H., Flaszynski, P., Doerffer, P., & Kaczynski, P. (2025). Experimental Studies of ShockWave Boundary Layer Interaction on Suction Side of Fan Representative Profile. In 16th European Conference on Turbomachinery Fluid Dynamics and Thermodynamics, ETC 2025. European Conference on Turbomachinery (ETC)

Book chapters

1. Hanfy, A.H., Flaszyński, P., Kaczyński, P., & Doerffer, P. (2025). Surface Roughness Effect on Shock Boundary Layer Interaction on Compressor Rotor Profile. In: Flaszynski, P., Babinsky, H., & Doerffer, P. (eds) Towards Effective Flow Control and Mitigation of Shock Effects in Aeronautical Applications. Notes on Numerical Fluid Mechanics and Multidisciplinary Design, vol 201. Springer, Cham. DOI: 10.1007/978-3-030-70122-1_15

Acknowledgements

The successful completion of this doctoral research was made possible through the technical and scientific contributions of several individuals and institutions. Deepest gratitude is expressed to the supervisor, Prof. Paweł Flaszyński, for the continuous scientific and personal support provided throughout the project. His extensive knowledge and guidance were generously shared at all times. Special recognition is also given to Dr. Piotr Kaczyński for his unwavering support and dedication. The fundamental principles of wind tunnel testing were imparted through his patient instruction, and every stage of the experimental setup was constructed collaboratively under his expert supervision.

The research was further enriched by the insights of Prof. Piotr Doerffer. His profound passion for research served as a constant source of inspiration, and the technical discussions held with him were found to be exceptionally valuable. Sincere thanks are also extended to the colleagues at IMP-PAN. Support was consistently provided through the sharing of knowledge, suggestions, and constructive remarks during discussions.

Significant contributions were made by the industrial partner, Rolls-Royce Deutschland (RRD). Gratitude is extended to Prof. Dr. Marius Swoboda, the RRD coordinator, for his strategic guidance and support. The complex process of surface texturing and arrangements was facilitated by Eng. Jyotis K. Sardar and Dr. Bernd Becker. Their efforts in managing the technical follow-ups are highly appreciated.

A big thank you for Michał Dobrzyński, for performing the shape and 2D roughness evaluations at the Institute of Manufacturing and Materials Technology (Gdańsk University of Technology). Technical gratitude is also directed to Prof. Matthias Voigt at the ISM of TU Dresden for his role in performing the detailed 3D texture measurements.

On a personal note, heartfelt thanks are given to friends whose support remained constant despite the distance. Most importantly, unconditional support was provided by my parents, whose sacrifices and inspiration have been fundamental to my life. Deep appreciation is also expressed to my wife and children for their patience and encouragement throughout this journey.

This project has received funding from the European Union's Horizon 2020 research and innovation programme under the Marie Skłodowska-Curie grant agreement No. 860909 - TEAMAero (Towards Effective Flow Control and Mitigation of Shock Effects in Aeronautical Applications).

Contents

List of Figures

List of Tables

Nomenclature

Latin symbols

		Units
$\mathbf{R}$	Temporal covariance matrix 2D array ($N \times N$)	
$\mathbf{s}$	Raw signal	
$\mathbf{s}_f$	The filtered or decomposed signal	
$\mathbf{V}$	Temporal eigenvector matrix 2D array ($N \times N$)	
$\mathbf{X}$	Snapshot matrix 2D array ($P \times N$)	
$\mathbf{x}$	A flattened image 1D array ($P \times 1$)	[px]
A	Area	[m^2 / px^2]
a	Speed of sound	[m/s]
A_{th}	Throat \ Opening	[m]
c	Chord length	[mm]
c_f	Skin friction coefficient ($\tau_w/0.5\rho u^2$)	
c_p	Specific heat at constant pressure	[J/kg·°K]
d_p	Particle diameter	[µm]
f	Sampling rate \ Frequancey	[Hz]
f_c	Focal length	[m]
f_w	Wavelet's centre frequency	[Hz]
$G(f_x, f_y)$	Cross spectral density function (PSD if $f_x = f_y$)	[mm^2/Hz]
H	Shape factor (δ^*/δ^{**})	
h	Enthalpy per unit mass	[J/kg]
H_t	Image height	[px]
i	Incidence angle	[deg]
k	roughness element height	[µm]
K_r	Gradient kernel	
k_s	Equivalent sand-grain roughness (6.2Ra)	[µm]
M	Mach number	
m	Line slope	
N	Total number	
n_c	Number of cycles	

n_{rs}	Number of random image samples	
n_{sl}	Number of vertical slices per image	
O_c	Camera optical centre	[px]
O_I	Camera projection centre	[px]
P	Image size (total number of pixels)	[px]
R	Universal gas constant (≈8.314)	[J/mol·K]
r	Stream-tube radius	[m]
Re_c	Chord based Reynolds number (Uc/ν)	
Re_k	Roughness Reynolds number (Uk_s/ν)	
s	Spacing between blades \ Pitch	[mm]
S_{tk}	Stokes number	
T	Fluid temperature	[°K]
t	t-distribution critical value	
U	Absolute velocity	[m/s]
u	Flow velocity in x direction \ relative velocity	[m/s]
V	Vanishing point (x, y) coordinates	[px]
W_t	Image width	[px]
$X,\ Y,\ Z$	Absolute coordinates	[mm, px]
$x,\ y,\ z$	Relative coordinates	[mm, px]
t_I	Turbulence intensity	[%]
$\mathrm{Coh}(f_x, f_y)$	Coherance function $(G(f_x, f_y)^2/(G(f_x).G(f_y)))$	
ES_x	Average streamwise effective slope (3D)	
Ra	Arithmetic average roughness (2D)	[µm]
Rk	Core roughness (2D)	[µm]
Rpk	Roughness reduced peak height (2D) [µm]	
Rq	Root mean square roughness (2D)	[µm]
Rsk	Roughness skewness (2D)	[µm]
Rvk	Roughness reduced valley height (2D)	[µm]
Rz	Maximum peak-to-valley height (2D)	[µm]
Sa	Areal average roughness (3D)	[µm]
Sk	Areal core roughness (3D)	[µm]
Spk	Areal reduced peak height roughness (3D)	[µm]
Sq	Areal root mean square roughness (3D)	[µm]
Ssk	Areal skewness roughness (3D)	[µm]
Svk	Areal reduced valley height roughness (3D)	[µm]
Sz	Areal maximum peak-to-valley height roughness (3D)	[µm]

Greek symbols

		Units
α	Angle of attack	[deg]
β	Blade angles, tangent at camber line	[deg]
β'	Flow angles, with the axis	[deg]
χ	Stagger angle	[deg]
δ	Boundary layer thickness	[mm]
δ'	Deviation angle	[deg]
δ^*	Boundary layer displacement thickness	[mm]
δ^{**}	Boundary layer momentum thickness	[mm]
δ_E	Boundary layer energy thickness	[mm]
η_{w_n}	Non-uniform weighting factor	
γ	Specific heat ratio	
κ	Von Kármán constant ($\approx$0.41)	
$\mathbf{\Lambda}$	Diagonal eigenvalue matrix 2D array $(N \times P)$	
$\mathbf{\Phi}$	Spatial eigenfunction \ POD modes matrix 2D array $(P \times P)$	
$\mathcal{F}$	Fourier transform operator	
$\mathcal{T}_\tau$	Total time duration	[s]
μ	Dynamic viscosity	[Pa/s]
ν	Kinematic viscosity (μ/ρ)	[m^2/s]
ω	Rotational speed	[deg/s, rpm]
ρ	Density	[kg/m^3]
σ	Standard deviation	
τ	Time	[s]
τ_f	Fluid time scale (δ/u)	[s]
τ_p	Particle response time $(\rho_p d_p^2/18\mu_g)$	[s]
τ_w	Wall shear stress	[Pa]
θ	Shock inclination to the horizontal	[deg]
ε	Deflection \ turning angle $(\beta_i - \beta_e)$	[deg]
ζ	Confidence level	

Superscripts

$(\ )'$	World coordinate system
$(\ )^*$	Critical state
$(\ )^+$	Dimensionalless wall parameter
$\overline{(\ )}$	Mean value

Subscripts

$(\ )_0$	Stagnation state
$(\ )_\infty$	Free stream state
$(\ )_\tau$	Shear \ Friction state
$(\ )_i$	Initial \ inlet state
$(\ )_n$	Snapshot \ partical index
$(\ )_o$	Exit \ outlet state
$(\ )_{\mathrm{a}}$	Axial state
$(\ )_{\mathrm{max}}$	Maximum value
$(\ )_{\mathrm{t}}$	Tangential state
$(\ )_{er}$	Error value
$(\ )_g$	Gas property
$(\ )_{i/o}$	Inlet-outlet ratio
$(\ )_p$	particle property
$(\ )_{shock}$	Shock state
$(\ )_w$	Weighted value

Abbreviations

APG	Adverse pressure gradient
AVDR	Axial velocity density ratio
BL	Boundary Layer
BPR	Bypass ratio
CAD	Computer-Aided Design
CFD	Computational Fluid Dynamics
CWT	Continuous wavelet transform
DFT	Discrete Fourier transform
DNS	Direct Numerical Simulation
FPG	Favourable pressure gradient
GMM	Gaussian Mixture Model
IMP-PAN	Institute of Fluid-Flow Machinery, Polish Academy of Science
ISM	Institute of Fluid Mechanics at TU Dresden
LDA	Laser Doppler Anemometer
LE	Leading-edge
LP	Lower profile
LSB	Laminar Separation Bubble
MVG	Micro-vortex generator
NumPy	Numerical Python Library

OpenCV	Open Computer Vision Library
OPR	Overall pressure ratio
PIV	Particle Image Velocimetry
POD	Proper orthogonal decomposition
PSD	Power spectral density
RANSAC	Random sample consensus
RMS	Root mean square
RRD	Rolls-Royce Deutschland
SBLI	Shock-Boundary Layer Interactions
SCB	Shock control bump
SFC	Specific fuel consumption
SNR	Signal-to-noise ratio
TEAMAero	Towards Effective Flow Control and Mitigation of Shock Effects in Aeronautical Applications EU project
TFAST	EU 7th Framework Programme project on transitional SBLIs
TS	Two-dimensional Tollmien-Schlichting transition waves
TSP	Temperature-sensitive paint
UP	Upper profile
UPSP	Unsteady pressure-sensitive paint
WEDM	Wire electrical discharge machining
WSS	Wide Sense Stationary
ZPG	Zero pressure gradient

List of Algorithms

Chapter 1

Introduction

The aviation sector's contribution to global climate change is significant, constituted by both carbon dioxide (CO_2) and non-CO_2 influences. Long-haul flights are responsible for a disproportionately large share of total emissions. These non-CO_2 effects include NO_x emissions, water vapour, and contrail formation [1]. Furthermore, non-volatile Particulate Matter (nvPM) output is projected to increase, necessitating immediate technological advancement in engine design and fuel technology [2].

The stringent targets set by Flightpath 2050, which mandate a 75% reduction in CO_2 and a 90% reduction in NO_x per passenger kilometre, necessitate a substantial focus on reducing engine size, weight, and specific fuel consumption (SFC) [3]. Increased propulsive efficiency is primarily sought through an increase in the engine Bypass Ratio (BPR). However, the resulting larger engine volumes and greater nacelle weight can negate the uninstalled SFC improvements; thus, determining an optimal BPR is essential [4]. Concurrently, thermal efficiency is enhanced by raising the Overall Pressure Ratio (OPR) of the engine core, as dictated by the thermodynamic cycle. This trend towards higher OPR is mandatory for meeting the mandated efficiency targets. These two factors are interdependent: achieving optimal overall SFC requires balancing the BPR benefit (lower jet velocity) against the OPR benefit (higher cycle efficiency), while simultaneously managing the increased weight and nacelle drag associated with larger engine size.

The implementation of higher pressure ratios directly influences the physical architecture of the engine. To achieve these ratios within demanding compact weight and size constraints, continuous efforts are concentrated on the design of highly loaded fans and compressors. One method for increasing the stage pressure ratio involves optimising the aerofoil profile shape and airflow deflection angle. However, the excessive flow turning in the blade rows is fundamentally limited by the onset of boundary layer separation [5–7].

Alternatively, the stage total pressure ratio is increased by a successive rise in the rotational speed in so called transonic compressor. This operational change leads to a considerable rise in the inflow velocity relative to the compressor blades, becoming subsonic or transonic at the hub and supersonic at the blade tip. Within this flow regime, the formation of shock waves is commonplace and constitutes the key aerodynamic challenge. The interaction of these strong shock waves with the boundary layers, the Shock Boundary Layer Interaction (SBLI), is the primary factor limiting the efficiency and operating range of modern transonic compressors. Thus, knowledge of the interaction of shock waves with boundary layers is essential for the development of more efficient aircraft and engines.

This chapter establishes the context and motivation for the research, introduces the core physical phenomena, and concludes with a guide to the structure of the remainder of the dissertation. This chapter is structured as follows:

- Section 1.1: provides the industrial and aerodynamic motivation for the study, detailing the general principles of transonic compressor design considerations, operating conditions and limitations.

- Section 1.2: introduces the fundamental fluid dynamics relevant to the SBLI. It covers boundary layer fundamentals and establishes the physics governing the interaction between shock waves and boundary layers. It then reviews established literature on flow control devices.

- Section 1.3: a review of prior research and existing knowledge is provided, covering the key roughness parameters, characteristics, and scales, generally explaining their physical effects on the boundary layer structure. In addition to the historical application of roughness in aerodynamics, its use as an active flow control device, and its specific application within transonic flow regimes.

- Section 1.4: provides the dissertation objectives and a guide to the structure of the subsequent chapters, detailing the experimental methodology, results, and conclusions of the thesis.

1.1 Transonic fans and compressors

A transonic compressor is defined as an axial flow machine in which the inlet Mach number, relative to the rotating blades, varies from subsonic values at the hub to supersonic values at the blade tips. In these stages, the flow is diffused to subsonic velocities within the rotor passages to generate a significant portion of the required stage pressure rise. Systematic research into these machines was initiated by the NACA Lewis Research Center circa 1950, leading to a rapid technological transition into first-generation turbofan engines. The primary motivation for the adoption of transonic designs is the ability to provide higher stage pressure ratios and larger airflows per unit of frontal area compared to purely subsonic configurations [8–10]. Achieving these targets allows for a reduction in the number of compression stages, which directly decreases the engine mass and size. Given that the compressor section constitutes 50-60% of an engine's length and 40-50% of its total mass, such advancements are critical for enhancing aircraft payload and economy [11, 12].

The requirement for high performance drives the design toward high axial flow Mach numbers and small hub-to-tip radius ratios. The pressure ratio available per stage rises rapidly with increasing blade tangential Mach number (M_t), as may be seen from the Euler equation for turbomachinery which states that the stagnation enthalpy rise across a rotor ($h_o - h_i$ where the subscripts i and o referes to inlet and outlet states respectively) is given by the product of the angular velocity of the rotor (ω) and the change in angular momentum per unit mass which the fluid experiences in passing through the rotor, ($U_{\mathrm{t},o}r_o - U_{\mathrm{t},i}r_i$) where U_t is the absolute tangential velocity and r is the stream-tube radius. Thus

$$h_o - h_i = \omega(U_{\mathrm{t},o}r_o - U_{\mathrm{t},i}r_i)$$

and if h is represented by c_pT_0 where c_p is the specific heat at constant pressure and T_0 is the stagnation temperature and isentropic flow is assumed so that:

$$p_o/p_i = (T_o/T_i)^{\frac{\gamma}{\gamma-1}}$$

$$\left(\frac{p_{0,o}}{p_{0,i}}\right)^{\frac{\gamma-1}{\gamma}} = 1 + \frac{(\gamma-1)M_\mathrm{t}^2}{1+\frac{\gamma-1}{2}M_\mathrm{a}^2}\left[\frac{r_o}{r_i}\frac{U_{\mathrm{t},o}}{\omega r_i} - \frac{U_{\mathrm{t},i}}{\omega r_i}\right] \tag{1.1}$$

where $M_\mathrm{t}^2 = (\omega r_i)^2/RT_i$ is the square of the tangential Mach number of the rotor blade, $\gamma \approx 1.4$ is the ratio of specific heats of air and R is the universal gas constant ≈ 8.314 J/mol·K. If for the moment is assumed that the quantity in parentheses is controlled by the geometry of a rotor and is not very sensitive to its angular velocity, the stage temperature rise increases roughly as the square of M_t with a corresponding variation of pressure ratio [8].

Historically, blade centrifugal and vibrational stresses limited tip speeds. However, the development of high-strength titanium alloys has enabled designs with tip speeds exceeding 550 m/s, corresponding to $M_\mathrm{t} = 1.7$ at the tip for an axial Mach number of $M_\mathrm{a} = 0.7$ at standard temperature.

The design of such compressors necessitates a delicate balance between aerodynamic loading and geometric constraints. Unlike subsonic designs, transonic blades must be as thin as practically possible with sharp leading edges to minimise bow shock strength and blockage.

To simplify the analysis of these flows, the blade-element method is traditionally employed as shown in Figure 1.1. In this approach, the flow is assumed to occur on independent axisymmetric

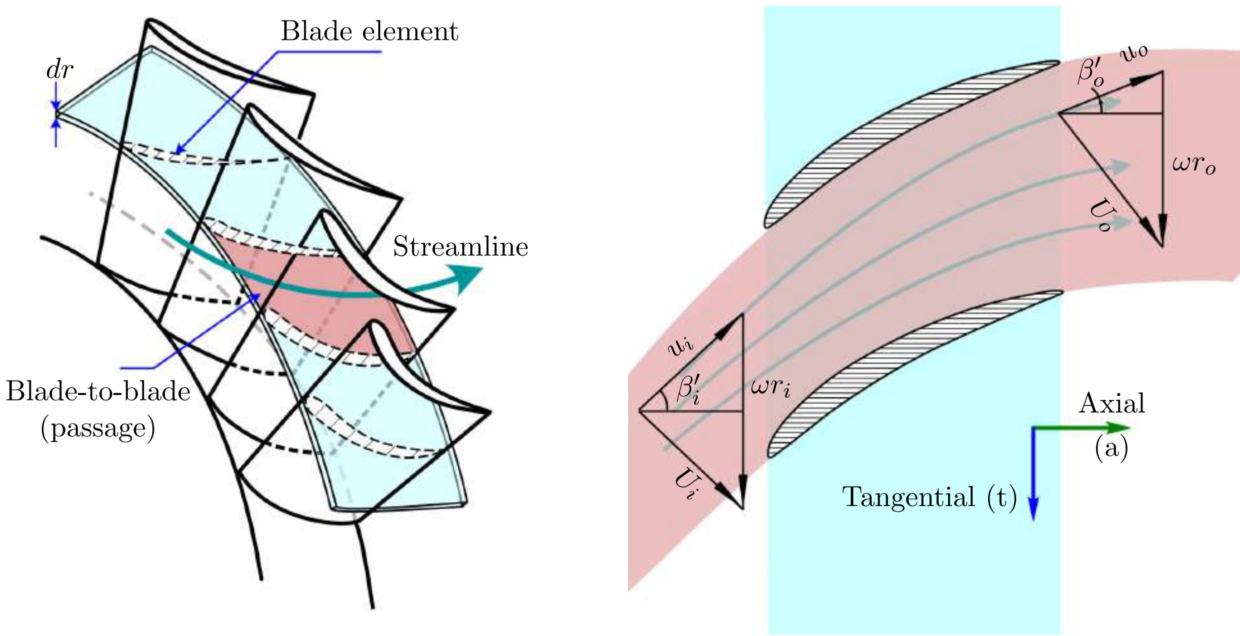

(a) Blade element concept in circumferential plane

(b) The blade-to-blade surface

Figure 1.1: Example of selected circular blade-to-blade surface

streamsurfaces, allowing the rotor to be modelled as a series of two-dimensional cascades. A cascade is defined as an infinite row of identical, equally spaced aerofoils, created by "unrolling" a cylindrical section of the blades at a constant radius. This allows for the evaluation of key parameters, especially where the flow is complex near the blade tip [9, 13].

1.1.1 Compressor operating ranges

The stable operating range of a transonic compressor is delimited by the surge and choking boundaries on a performance map. As illustrated in Figure 1.2, various aerodynamic and aeroelastic limits constrain the machine's utility across different rotational speeds. Aerodynamic stall is defined broadly as the breakdown of flow attachment on the blade surfaces. This failure occurs at both the low-flow and high-flow extremities of the operating envelope through different physical mechanisms.

Instabilities known as surge are encountered when the mass flow is reduced below a critical threshold. At these conditions, the inlet flow angle increases significantly, leading to positive incidence stall. Separation is typically initiated at the suction surface boundary layer. This failure often manifests as "rotating stall", where cells of retarded flow propagate circumferentially around the rotor [14]. As shown in Figure 1.2b, these stall cells create a local blockage that diverts the incoming flow to adjacent blades. This mechanism increases the incidence angle on neighbouring aerofoils, leading to a self-sustaining propagation of the stalled zone.

If the pressure rise across the compressor exceeds the capacity of the downstream system, a global instability called surge is triggered. Surge is characterised by large-scale, axial oscillations of the entire flow field, which may include periods of total flow reversal [15]. At high rotational speeds, the transition from stall to surge is often instantaneous, whereas at lower speeds, the machine may operate in a stable stalled condition.

At the opposite extreme of the operating range, choking is observed at high mass flow rates when the local Mach number reaches unity at the blade passage throat. In transonic designs, the effective throat area is heavily influenced by viscous blockage from the SBLI. Furthermore, operation at high mass flows induces a "negative incidence" condition. The flow is forced to turn sharply toward the pressure surface, resulting in "choke stall".

In this state, separation occurs on the pressure side of the leading edge. Unexpected choking is observed if viscous blockage significantly restricts the flow capacity, thereby preventing the "starting" of the supersonic flow system, As visualised in Figure 1.2c, the shock structure shifts

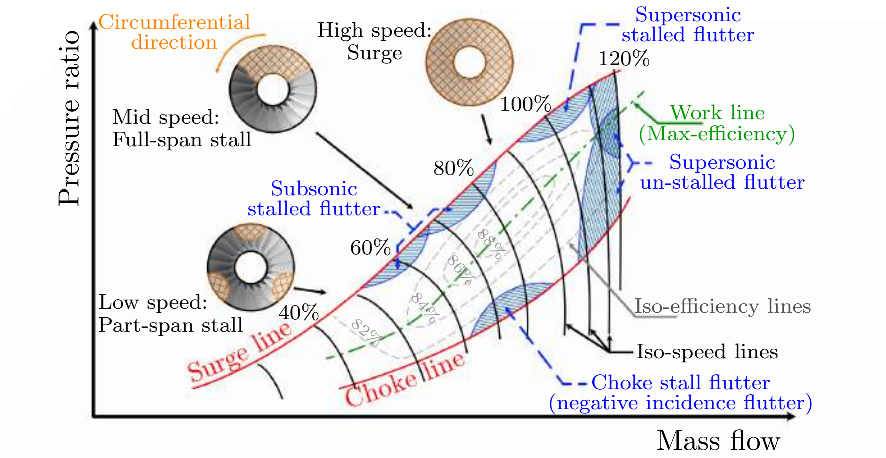

(a) Performance characteristic map for an axial compressor [17, 18]

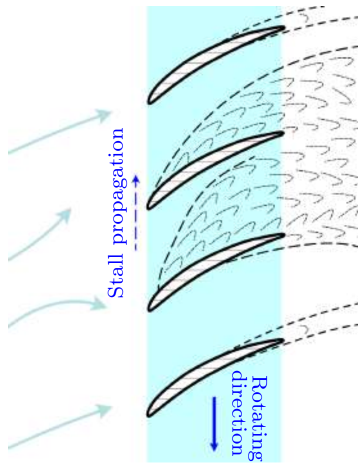

(b) Sketch of rotating stall [19]

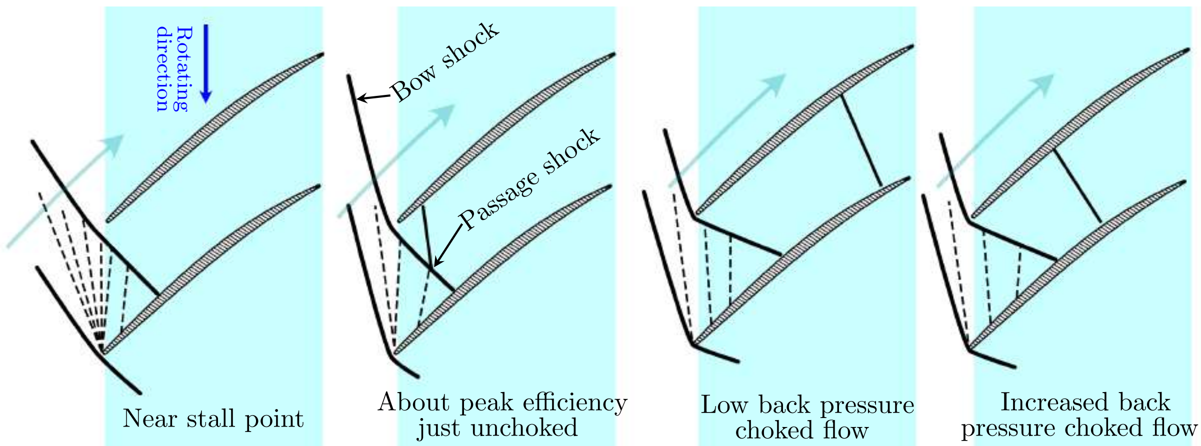

(c) Shock structures across the working range of transonic compressors [16]

Figure 1.2: Compressors operating ranges and stall conditions

significantly as back pressure is varied. The system moves from a near-leading-edge bow shock at the stall limit to a deep passage shock during choked operation [16].

Aeroelastic instabilities, specifically flutter, further restrict the safe envelope of the machine. Flutter is defined as a self-excited and self-sustained vibration of the blades, arising from the interaction between aerodynamic forces and structural dynamics. This phenomenon is particularly prevalent in transonic regimes where the movement of passage shocks provides significant energy input to the blade structure. Such vibrations often occur at specific rotational speeds and can lead to rapid high-cycle fatigue if the aerodynamic damping becomes negative [20].

At the high-flow extremity, the machine is susceptible to “choke stall flutter” (negative incidence flutter). This instability is linked to the shock-induced separation on the pressure surface during choked operation. As marked in Figure 1.2a, these aeroelastic limits often truncate the useful range of the compressor before the aerodynamic limits are reached. Such vibrations lead to rapid high-cycle fatigue, especially when aerodynamic damping becomes negative.

Persistent operation near these limits significantly curtails the structural integrity and lifespan of the compressor. Severe vibrations during surge or stall events can induce “clashing”, where contact occurs between stationary vanes and rotating blades, leading to catastrophic component failure. Furthermore, the cyclic loading imposed by stall cells and flutter promotes the development of fatigue-related cracks. These mechanisms collectively impose a rigorous constraint on the design, as aerodynamic advancements must be balanced against the necessity of ensuring mechanical durability and operational safety [14, 21].

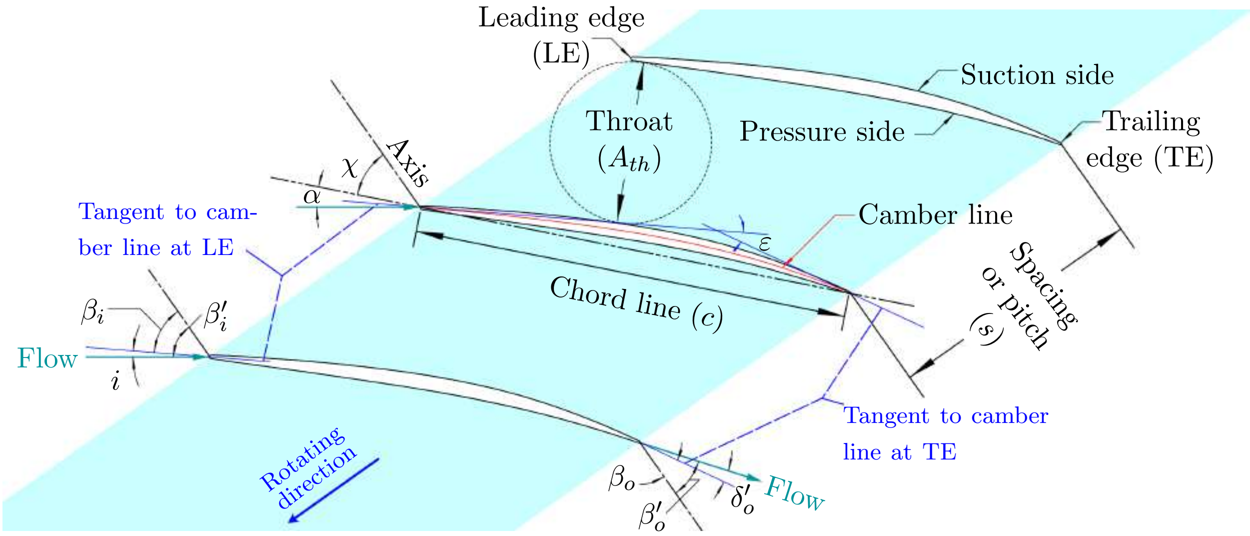

Figure 1.3: Standard cascade parameters

1.1.2 Blade-element and design considerations

To analyse the complex fluid dynamics of a transonic rotor, the flow is traditionally projected onto a two-dimensional plane to form a linear cascade. As illustrated in Figure 1.3, this abstraction represents an infinite row of identical aerofoil sections with a constant spacing or pitch (s) and a chord length (c). This configuration allows the aerodynamic performance to be isolated from the radial complexities of the actual machine, provided that axial momentum and tangential forces are correctly scaled [13, 20]. The fundamental geometric orientation is defined by the stagger angle (χ), which represents the angle of the blade chord line relative to the axial direction.

The orientation of the flow relative to the blade is defined by the inlet flow angle (β_i'). The aerodynamic incidence is expressed as the difference between the flow angle and the physical blade leading-edge angle ($i = \beta_i' - \beta_i$). In subsonic regimes, a wide range of incidence angles is accommodated without significant efficiency penalties. However, in the transonic regime, the system exhibits extreme sensitivity to these parameters due to the "Unique Incidence" principle.

This principle dictates that for a supersonic relative inlet Mach number (M_i), the inlet flow angle (β_i') is not an independent parameter but is uniquely coupled to the Mach number and the suction surface profile. This phenomenon arises from the requirement of mass flow continuity and the structure of the wave system at the leading edge. For the flow to be "started", a state where the shock system is swallowed into the passage, the mass flow entering the cascade must match the mass flow capacity of the throat (A_{th}). The throat A_{th} is defined as the minimum width between adjacent blades. To avoid choking (i.e., throat blockage), A_t must be compatible with the critical area A^*, which represents the area required for the flow to reach sonic conditions ($M = 1$). Specifically, the condition $A_{th}/A^* \geq 1$ must be satisfied.

As M_i increases, the expansion or compression waves originating from the suction surface leading edge adjust the inlet flow angle β_i'. This adjustment ensures the "captured" mass flow remains compatible with A_{th}, where A_{th}/A^* must be maintained slightly above unity to prevent the passage from choking. Consequently, a unique value of β_i' is established for every M_i to satisfy the conservation of mass and momentum across the inlet wave system. At the unique incidence, the shock system is contained within the passage, allowing for efficient pressure recovery. Deviations from this condition lead to either unstarted flow, where the shock is expelled upstream, or over-expanded flow, both of which result in severe efficiency penalties [13, 22].

The stagger angle (χ) directly influences the "starting" Mach number and the mass flow capacity of the cascade. A higher stagger angle reduces the cascade frontal area but may lead to premature choking if the physical throat area (A_{th}) is overly restricted relative to the critical area (A^*). In transonic designs, the overall work input is determined by the camber line and the resulting flow turning ($\Delta\beta' = \beta_o' - \beta_i'$), but the distribution of this camber is critical for supersonic performance, necessitating precise control over the blade's suction surface turning.

In transonic applications, the choice of aerofoil profile is a critical design consideration. Standard subsonic profiles are largely unsuitable due to excessive wave drag and shock-induced separation. Instead, specialised profiles such as the double-circular-arc (DCA) or multiple-circular-arc (MCA) are utilised. These sections are characterised by sharp leading edges and reduced thickness-to-chord ratios, which minimise the strength of the leading-edge bow shock and reduce passage blockage [9, 22–24].

Higher solidity (c/s) generally provides better flow guidance but increases skin friction losses and potential blockage in high-speed regimes. A primary measure of the aerodynamic loading and the potential for flow separation is the static pressure rise coefficient [25] or the Diffusion Factor (DF). For a compressor cascade, Lieblein et al [26] established this parameter to correlate the peak suction-surface velocity with the overall deceleration of the flow. It is defined as:

$$DF = \left(1 - \frac{u_o}{u_i}\right) + \frac{\Delta u_\mathrm{t}}{2u_i\left(\frac{c}{s}\right)} \tag{1.2}$$

where u_i and u_o are the inlet and outlet relative velocities, and Δu_t is the change in tangential velocity as discribed in Figure 1.1b. While a theoretical limit of $DF \approx 0.6$ is cited for stall, actual transonic environments the DF serves as a first-order estimate for the risk of massive boundary layer separation induced by adverse pressure gradients and shock interactions. accordingly, DF often designed for lower values to mitigate shock-induced separation. A more critical measure is the local diffusion factor ($DF_\mathrm{loc} = 1 - u_o/u_\mathrm{max}$). This accounts for the maximum deceleration from the peak surface velocity (u_max) before shock impingement.

Although the DF remains a design standard [27, 28], it frequently fails to predict stall in high-aspect-ratio compressors, where tip stall occurs regardless of DF values. Similarly, while the de Haller criterion ($u_o/u_i \leq 0.72$) is often a more effective indicator of endwall boundary layer separation [29, 30], it is subject to numerous exceptions. In many cases, compressors maintain stable operation far from the surge line despite having de Haller numbers significantly lower than the 0.72 limit [31, 32]. These two diffusion parameters are correlations that are obtained from a large amount of two-dimensional airfoil data; therefore, the prediction always fails near the end-wall regions.

1.1.3 Secondary flows and losses in transonic compressors

While linear cascades are treated as two-dimensional abstractions, the flow within actual turbomachinery is inherently three-dimensional. Secondary flow is defined as the component of the velocity vector that deviates from the primary streamsurfaces. These flows are primarily driven by transverse pressure gradients acting on low-momentum fluid within the endwall boundary layers. Fluid is transported from the pressure side to the suction side of the blade passage. This motion results in the formation of passage vortices and corner separations.

In transonic fans, these mechanisms are further complicated by the interaction with shock waves and the presence of centrifugal forces. Low-momentum fluid within the blade surface boundary layers is subjected to radial migration, often referred to as centrifugal pumping, which transports fluid towards the casing. Furthermore, the tip leakage flow (driven by the pressure differential across the rotor tip) interacts with the passage shock and the main flow. This interaction leads to a substantial reduction in stage efficiency and distorts the spanwise distribution of the flow angle.

The cumulative effect of these 3D features, alongside the growth of annulus wall boundary layers, results in streamtube contraction or expansion. This phenomenon is quantified by the Axial Velocity Density Ratio (AVDR), defined as the ratio of outlet mass flux to inlet mass flux in the axial direction:

$$\mathrm{AVDR} = \frac{\rho_o u_{a,o}}{\rho_i u_{a,i}} = \frac{\rho_o u_o \cos\beta'_o}{\rho_i u_i \cos\beta'_i} \tag{1.3}$$

where ρ is the density and u_a is the axial velocity component at the inlet (i) and outlet (o). In experimental cascade testing, the AVDR is utilised as a critical control parameter to replicate the conditions of a real compressor. While the AVDR is unity in an idealised 2D incompressible flow, real machines typically exhibit an AVDR > 1 due to the blockage effect of the boundary layers on the hub and casing. Furthermore, the meridional flow path geometry, including the slope and curvature of the annulus walls, is often designed to produce a specific AVDR. This allows for the management of aerodynamic loading and the stabilisation of the shock system by modifying the effective diffusion across the blade row [20].

Essentially, the AVDR acts as an additional degree of freedom for the designer. Higher stage pressure ratios are achieved without exceeding the diffusion capacity of the blade boundary layers. Physically, the AVDR "unloads" the blade profile by modifying the velocity distribution.

In a transonic environment, the contraction of the streamtube (high AVDR) results in a local acceleration of the core flow. This acceleration reduces the effective static pressure rise required across the row, preventing the passage shock from migrating toward the leading edge [33].

By maintaining the shock in a stable downstream position, the boundary layer is stabilised and shock-induced separation is delayed. This reduction in loading "relieves" the suction-surface boundary layer. It is thus enabled to withstand a stronger passage shock and a more severe adverse pressure gradient before detachment occurs or facilitates flow reattachment, which leads to thinner wakes and a substantial reduction in total pressure losses at the outlet.

The AVDR and the Diffusion Factor are intrinsically coupled through the continuity equation. An approximation for this change is given by:

$$\Delta DF_{\text{loc}} \approx 0.6 \text{ to } 0.9 \times (\text{AVDR} - 1.0) \tag{1.4}$$

The empirical relationship between streamtube contraction and loading implies that for a given blade geometry and inlet Mach number, an increase in AVDR from 1.0 to 1.1 reduces the experienced local diffusion by approximately 0.06 to 0.09.

However, this parameter is also limited by its effect on mass flow capacity. While streamtube contraction relieves the boundary layer, the aerodynamic throat area is effectively reduced. This may lead to an earlier onset of choking, as the local flow reaches sonic conditions at lower mass flow rates compared to a purely two-dimensional case [34].

In linear cascade testing, the AVDR is a critical control variable. A linear cascade lacks the natural streamtube contraction found in an annular cascade. Boundary layers on the tunnel sidewalls naturally grow and constrict the flow. This results in an uncontrolled increase in AVDR. To validate 2D blade profiles, designers must isolate the profile loss from these 3D effects. Sidewall suction is employed to mitigate the growth of boundary layers on the wind tunnel walls [33, 35, 36]. By regulating the suction mass flow, the desired AVDR is accurately simulated, allowing the experimental environment to replicate the specific streamtube contraction of the rotating machine.

Precise control of the AVDR is essential to simulate the streamtube contraction of a multi-stage environment. This alignment upholds the integrity of the infinite cascade assumption, ensuring that the resulting experimental data accurately captures the true stall margin and loss characteristics of the profile. Furthermore, in the transonic regime, the coupling between the AVDR and the unique incidence angle must be rigorously monitored. Because streamtube contraction modifies the effective mass flow capacity of the blade passage, a correctly matched AVDR is fundamental to the valid measurement of the shock system and the associated pressure recovery.

Losses in transonic compressors are categorised into 2D losses, which could be estimated from cascade analysis such as profile losses, and shock-related losses. The 3D effect losses include secondary losses, end-wall boundary layer losses, and tip leakage losses [37]. In the supersonic regions near the blade tip, shock wave losses represent a dominant portion of the total entropy production. It is established that shock losses can account for approximately 30% to 50% of the total stage loss in high-pressure ratio designs, depending on the inlet Mach number and blade geometry [33]. These losses originate from the irreversible total pressure drop across the bow shock and the internal passage shock system. At high supersonic speeds, the magnitude of these losses is highly sensitive to the pre-shock Mach number, which determined by the Prandtl-Meyer expansion from the leading edge, and the shock topology (such as shock wave position and strength).

The interaction between the passage shock and the suction surface boundary layer induces boundary layer thickening or separation, which increases the effective blockage and entropy generation. To mitigate these effects, modern blade profile design involves the control of suction side surface turning upstream of the shock to optimize the pre-shock Mach number and minimize the

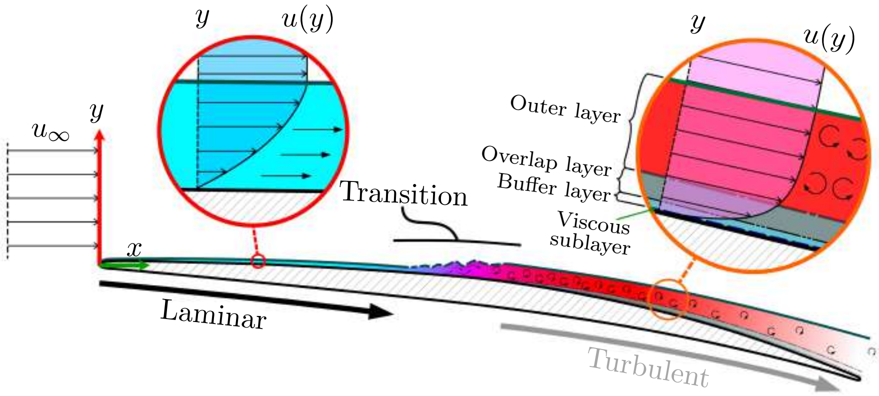

Figure 1.4: Boundary layer development

resulting stagnation pressure loss [38].

However, achieving high efficiency remains difficult due to the complex internal flow topology. As is detailed in the following sections, the investigation of SBLI is essential because this coupling dictates the effective shock strength and the resulting viscous losses [39–41]. Furthermore, SBLI is a primary source of aerodynamic unsteadiness and high-frequency flow oscillations. Rapid fluctuations of the shock can trigger blade buffet or contribute to aeroelastic instabilities such as flutter [20].

1.2 Shock boundary layer Interaction (SBLI)

In an ideal inviscid flow, a shock wave is treated as a mathematical discontinuity across which static pressure increases instantaneously. However, within a real fluid, the presence of a boundary layer modifies this behaviour. Shock boundary layer interaction is defined as the close coupling between a viscous boundary layer and an outer supersonic flow subjected to a sudden retardation.

1.2.1 Boundary layer states

In order to understand the complex physics behind SBLI, it is essential to grasp the boundary layer, its states, and its behavior with external intruders. The boundary layer concept, first proposed by Prandtl (1904), establishes that viscous effects are confined to a thin region adjacent to the solid surface [42]. Within this layer, the no-slip condition necessitates that the fluid velocity relative to the wall is zero. The transition from zero velocity at the wall to the freestream velocity (u_∞) is driven by the viscous diffusion of momentum. As the flow progresses downstream, the retarding effect of the wall is spread outward into the fluid by molecular viscosity.

The character and thickness of this region are described by the local Reynolds number (Re_x), which represents the ratio of inertial forces to viscous forces:

$$Re_x = \frac{\rho u_\infty x}{\mu} \tag{1.5}$$

where x is the length scale and μ is the dynamic viscosity. At the commencement of the blade profile ($x \approx 0$), the Reynolds number is low, signifying that viscous damping dominates the flow. Consequently, the boundary layer initiates in a laminar state, in which fluid particles move in smooth, parallel layers with minimal macroscopic mixing.

Laminar to turbulent transition

As the fluid progresses downstream, the increase in the characteristic length x results in a linear rise of the local Reynolds number. This increase reflects the growing dominance of inertial forces over the stabilising effects of viscosity. Eventually, a critical Reynolds number (Re_{crit}) is reached, marking the threshold where the flow can no longer suppress internal perturbations. In unperturbed environments with minimal flow disturbances, natural laminar-turbulent transition is observed.

This process is initiated by the exponential growth of two-dimensional Tollmien-Schlichting (TS) waves, followed by a three-dimensional instability stage. These instabilities culminate in the formation of turbulent spots that merge to create a fully turbulent boundary layer. The development of the boundary layer across laminar, transitional, and turbulent regimes is illustrated in Figure 1.4.

Alternatively, sources of high flow disturbance can accelerate the transition process through a mechanism termed bypass transition. In environments where freestream turbulence exceeds 1% [43] or significant surface roughness is present, the primary TS instability stage is circumvented. Small-scale roughness levels may amplify primary instabilities linearly, while larger irregularities distort the flow locally to trigger immediate turbulence. This bypass mechanism is particularly relevant in transonic compressors, where the flow environment is inherently chaotic and influenced by upstream blade wakes.

The resulting turbulent state is characterised by chaotic, three-dimensional eddies that significantly enhance the exchange of momentum. High-velocity fluid from the outer flow is transported towards the wall, creating a "fuller" velocity profile compared to the laminar state.

Boundary layer integral parameters

In compressible regimes, the influence of the boundary layer on the inviscid core flow is quantified using integral thicknesses that incorporate the local density (ρ). The displacement thickness (δ^*) represents the distance by which the external streamlines are shifted due to the mass flow deficit:

$$\delta^* = \int_0^\delta \left(1 - \frac{\rho u}{\rho_\infty u_\infty}\right) dy \tag{1.6}$$

Similarly, the momentum thickness (δ^{**}) is defined by the momentum flux deficit:

$$\delta^{**} = \int_0^\delta \frac{\rho u}{\rho_\infty u_\infty} \left(1 - \frac{u}{u_\infty}\right) dy \tag{1.7}$$

The ratio of these thicknesses is the shape factor ($H = \delta / \delta^{**}$). In compressible flow, H is a critical indicator of aerodynamic health [42, 44, 45]; Its value varies significantly depending on whether the flow is laminar or turbulent, and it is highly sensitive to external pressure gradients. For zero-pressure-gradient (ZPG) flows over, H remains relatively constant within its respective regime. In this case laminar BL has a shape factor of $H \approx 2.59$. While turbulent BL shape factor is ranging between $H \approx 1.3$ to 1.5. The "fuller" velocity profile of a turbulent layer results in a smaller displacement thickness relative to its momentum thickness, leading to a lower H value.

Turbulent boundary layer structure

The turbulent boundary layer possesses a complex internal structure, particularly, the inner layer which represents almost 15% of the boundary layer thickness (δ). This inner layer is defined by the dimensionless wall distance $y^+ = yu_\tau/\nu$, where u_τ is the shear velocity. According to White [46], the profile is divided into:

- Viscous or laminar sublayer ($y^+ < 5$): Where viscous shear is dominant and $u^+ = y^+$ approximately between $0 \leq y/\delta \leq 0.2\%$.
- Buffer layer ($5 < y^+ < 30$): A transition zone between viscous and turbulent dominance. Here, neither viscous nor turbulent shear exclusively governs the flow, leading to a complex velocity profile that does not conform to simple analytical expressions togather with laminar sublayer this approximately represents 2% of the boundary layer thickness.
- Log or overlap layer ($30 < y^+ < 350$): Where intense mixing occurs, described by:

  $$u^+ = \frac{1}{\kappa} \ln(y^+) + B \tag{1.8}$$

  where $\kappa \approx 0.41$ and $B \approx 5.0$ this layer corresponding roughly to the range $2\% \leq y/\delta \leq 20\%$, after which the curves either turn upward in the outer layer.

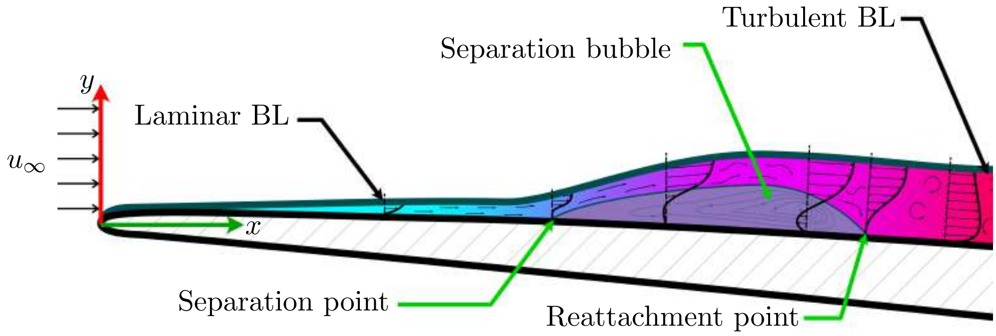

Figure 1.5: Boundary layer separation bubble

Laminar boundary layer separations

A significant portion of aerodynamic losses is attributed to skin friction, which may account for up to 50% of the total drag in subsonic transport aircraft. However, laminar skin friction is found to be as much as 90% lower than turbulent skin friction at an equivalent Reynolds number [47].

In the design of fan and compressor blades, the preservation of high aerodynamic efficiency is established as a primary objective. To minimise profile losses, the maintenance of a laminar boundary layer state is highly desirable. These conditions are naturally promoted during high-altitude operation, particularly within the fan and initial rotor stages. In these regions, the reduced air density results in a lower local Reynolds number (Re_x), which serves to effectively stabilise the laminar flow and delay the onset of transition. However, while beneficial for reducing profile losses, the laminar state presents significant challenges in transonic regimes. The resistance of the boundary layer to detachment is governed by the momentum of the fluid in the near-wall region. Laminar boundary layers are highly susceptible to separation because momentum transfer is restricted to molecular diffusion. This results in a "thin" velocity profile with low momentum near the wall. In contrast, turbulent boundary layers feature intense eddy motion. This macroscopic mixing transports high-momentum fluid from the freestream towards the surface, creating a velocity profile that can withstand much stronger pressure rises before detaching.

Flow separation is defined as the physical detachment of the boundary layer from the solid surface. This phenomenon occurs when the kinetic energy of the fluid is insufficient to overcome an adverse pressure gradient (APG), defined as $dp/dx > 0$. Physically, the velocity gradient at the wall is reduced until a stagnation point is reached. The onset of separation is mathematically identified by the condition where the wall shear stress vanishes:

$$\tau_w = \mu \left(\frac{\partial u}{\partial y} \right)_{y=0} = 0 \tag{1.9}$$

Beyond this point, flow reversal is observed and a recirculating region is formed between the surface and the mainstream flow.

Laminar Separation Bubble (LSB) occurs when a boundary layer detaches but subsequently undergoes transition within the separated shear layer, as illustrated in Figure 1.5. The formation of an LSB is driven by the competing effects of pressure gradients and flow transition. When a laminar boundary layer encounters an APG that exceeds its limited momentum, it detaches from the surface. Because the laminar layer lacks macroscopic mixing, this detachment occurs even under relatively weak pressure rises.

Once detached, the fluid forms a free shear layer that is highly unstable. In the absence of the wall's stabilising effect, infinitesimal disturbances within this shear layer are rapidly amplified, triggering a transition to turbulence. This transition is the fundamental reason for the bubble's existence; it transforms the flow from a low-energy laminar state to a high-energy turbulent state. The resulting intense eddy motion facilitates a rapid exchange of momentum from the high-speed freestream into the stagnant recirculating zone. This "re-energisation" provides the fluid with sufficient kinetic energy to overcome the remaining pressure rise, forcing the flow to reattach to the solid surface.

The region between the initial laminar separation point and the turbulent reattachment point constitutes the separation bubble. The physical significance of the LSB lies in its impact on the effective blade geometry. Although the flow reattaches, the bubble creates a local "hump" in the displacement thickness (δ^*), which alters the pressure distribution and can trigger a "short" or "long" bubble effect. If the transition process is delayed, common at low Reynolds numbers or high altitudes, the shear layer may fail to reattach before reaching the trailing edge. This results in bursting, where the bubble transforms into total separation.

A fully separated flow leads to a massive increase in pressure drag, as the lack of reattachment prevents pressure recovery at the trailing edge and creates a broad, low-pressure wake. In transonic compressors, the resulting growth in displacement thickness leads to significant aerodynamic blockage. This blockage restricts the effective area of the blade passage, ultimately causing aerodynamic stall and potentially triggering system-wide instabilities such as surge or rotating stall [20].

Effect of pressure gradients on the shape factor (H) is the primary diagnostic tool for identifying flow detachment under APG. Under an APG, a progressive distortion of the profiles is observed, particularly in the lower portion of the boundary layer. For laminar layers, separation typically occurs as H approaches 3.5, whereas turbulent layers can remain attached until H reaches values between 2.0 and 2.46.

1.2.2 Laminar and turbulent SBLI

The SBLI phenomenon was first observed experimentally on aerofoils by Ferri in 1940 [48]. Physically, a shock wave imposes an abrupt increase in static pressure upon the flow. For a normal shock, the pressure ratio p_o/p_i is governed by the Rankine-Hugoniot relation [45]:

$$\frac{p_o}{p_i} = \frac{2\gamma M_i^2 - (\gamma - 1)}{\gamma + 1} \tag{1.10}$$

where M_i represents the pre-shock Mach number, it is clear that the rise in the static pressure is proportional to the square value of the pre-shock Mach number, which also defines the strength of the shock. When this shock wave meets a solid surface, it interacts with the viscous boundary layer. This intense adverse pressure gradient distorts the boundary layer velocity profile, causing it to thicken and increasing the displacement effect on the neighbouring inviscid flow.

The fundamental mechanism of SBLI is governed by the viscous-inviscid coupling between a supersonic external flow and the wall-bounded shear layer. In the inviscid limit, a shock wave is a singularity across which the pressure jump is discrete, as illustrated in Figure 1.6c. However, the presence of a boundary layer introduces a thin subsonic region near the wall where the velocity decreases to zero at the wall to satisfy the "no-slip" condition and the local flow speed is lower than the speed of sound ($M < 1$).

In supersonic flow region ($M > 1$), the fluid is moving faster than the speed of sound (i.e., faster than pressure waves travelling), the pressure waves cannot move "upwind" against a supersonic current. While in subsonic region, pressure waves are able to travel in all directions, including upstream against the flow. Consequently, the high pressure from behind the shock "leaks" forward through the subsonic portion of the boundary layer. This allows the boundary layer to "feel" the shock before actually reaching it, a phenomenon known as upstream influence. This transmitted pressure rise imposes an intense APG on the flow over a distance of several boundary layer thicknesses (δ). The boundary layer is forced to thicken as it decelerates, and if the pressure rise is sufficiently strong, the flow will detach from the surface.

As illustrated in Figures 1.6a and 1.6b, this gradient acts as a source of momentum deficit. The fluid particles within the boundary layer, already depleted of kinetic energy due to viscous dissipation, are further decelerated. If the pressure rise is sufficiently high, the velocity gradient at the wall (τ_w) is reduced to zero, leading to flow separation. The physical response is often described by the "free interaction" theory, which suggests that the initial stages of the pressure rise are independent of the specific shock-generating mechanism and are instead determined by the local coupling between the thickening boundary layer and the external supersonic flow [50, 51].

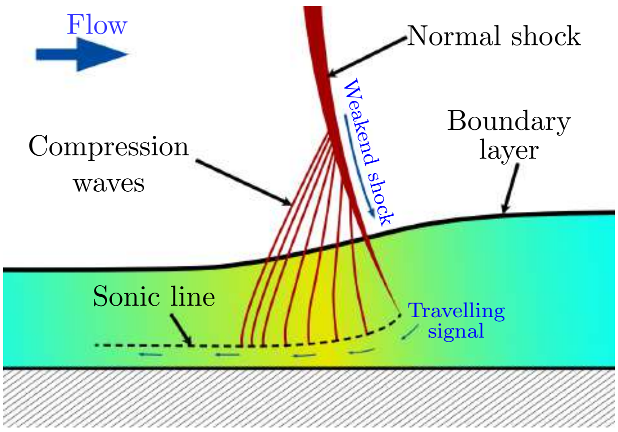

(a) Attached shock interaction

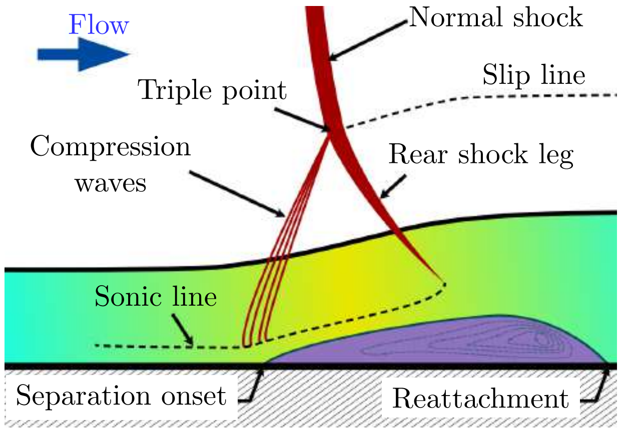

(b) Separated shock interaction

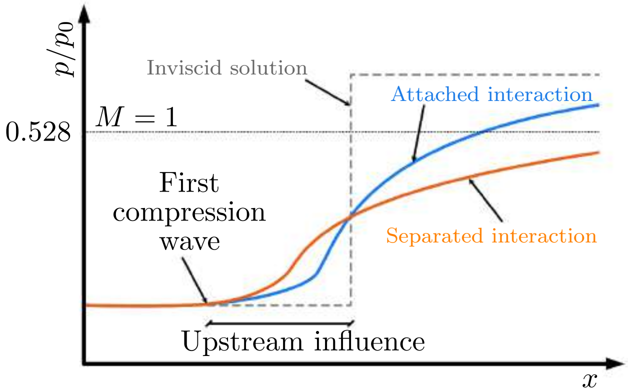

(c) Representative streamwise distribution of wall static pressure for a normal shock interaction

Figure 1.6: Schematic wave patterns for attached and separated flow fields corresponding to the normal shock interaction (Adapted from Sabnis and Babinsky [49])

At this point, a recirculating separation bubble is formed. This bubble acts as a physical obstacle to the external flow, causing the main shock to bifurcate into a "lambda" (λ) structure, consisting of a separation shock and a reattachment shock, as shown in Figure 1.6b. Therfore, the boundary layer conditions (laminar or turbulent) play an essential role in the behavior of SBLI [52].

Characteristics of laminar SBLI

Laminar boundary layers are highly susceptible to separation as disscued in Section 1.2.1 when subjected to even weak shock waves. In laminar interactions, the upstream influence is extensive, often spanning several dozen boundary layer thicknesses. The pressure rise is observed to occur gradually, as the flow separates well ahead of the primary shock location.

A distinctive feature of the laminar SBLI is the formation of a prominent "lambda" (λ) shock structure. As the flow separates, a series of compression fan waves is generated at the separation point. These waves merge to form the leading leg of the λ-shock. The main shock is weakened, and a supersonic tongue of fluid often persists between the separation and reattachment points. This structure is detrimental to aerodynamic efficiency, as it increases the entropy production and significantly alters the pressure distribution on the surface [53]. Furthermore, laminar separation bubbles are prone to "bursting", leading to massive flow detachment and stall.

In the early stages of a transonic compressor, such as the fan or the first several stages of a low-pressure compressor, the relative inlet Mach numbers at the blade tips are often supersonic ($M_i \approx 1.2$–1.6). Additionally, boundary layer may be partially laminar near the leading edge, making it vulnerable to shock-induced separation and the formation of separation bubbles. Consequently, the effective flow area of the passage is reduced. This reduction in area can lead to "choking", where the mass flow capacity of the stage is limited as discussed earlier in Section 1.1.

If the separation bubbles do not reattach, the resulting blockage can trigger a rotating stall or a system-wide surge [20, 54].

Characteristics of turbulent SBLI

In contrast to laminar flow, turbulent boundary layers exhibit a significantly higher resistance to shock-induced separation. This resilience is attributed to the presence of turbulent eddies, by which high-momentum fluid from the freestream is continuously transported towards the wall. Within a turbulent SBLI, the upstream influence is found to be highly localised. This influence typically extends only a few boundary layer thicknesses ahead of the shock.

Separation is generally suppressed unless the Mach number upstream of the shock exceeds a critical value, often cited as $M \approx 1.3$ for normal shocks [55, 56]. When separation occurs, the resulting bubble is observed to be smaller and more stable than its laminar counterpart. The pressure rise is more abrupt, and the λ-structure is considerably less pronounced or entirely absent. The interaction strength is predominantly governed by the freestream Mach number, M_∞. For $M_\infty < 1.3$, the boundary layer typically remains attached, although a rapid increase in the shape factor, H, is experienced. Beyond this limit, significant viscous losses are produced and the profile drag of the aerodynamic body is increased [57].

The flow environment is characterised by high Reynolds numbers and significant freestream turbulence in the later stages of the compressor. At that point the air has been significantly compressed, leading to higher temperatures and densities. While the Mach numbers are generally lower (subsonic or transonic), laminar flow is rarely maintained in these high-energy environments, the boundary layers are thicker and fully turbulent. The interaction in later stages is also influenced by the accumulation of "secondary flows" and "corner vortices", which in role decreases the AVDR resulting in a tendency to promote stronger three-dimensional separation zones when BL interact with the shock leading to higher overall losses especialy at the junction of the blade and the casing [33, 54].

Unsteadiness in SBLI

The unsteadiness associated with normal SBLI is a fundamental phenomenon in high-speed aerodynamics. It is characterised by periodic oscillations of the shock system, even under nominally steady upstream conditions. These fluctuations are broadly categorised into high-frequency and low-frequency components. High-frequency unsteadiness is generally attributed to the convective scales of the turbulent boundary layer. Conversely, the low-frequency motion occurs at scales significantly lower than the characteristic frequency of the incoming flow [55, 58].

The mechanism of low-frequency unsteadiness is frequently explained by the "breathing" of the separation bubble formed at the shock foot. For a normal shock, a λ-shock (lambda) structure is typically produced as the boundary layer separates. The recirculating zone under this structure undergoes periodic expansion and contraction, which modulates the position of the shock system [59]. It is observed that while the leading separation shock may remain relatively fixed, the rear leg and the main normal shock undergo significant streamwise excursions. These oscillations are also influenced by the downstream pressure field. In parallel-walled or diverging ducts, the shock motion is strongly coupled to variations in back pressure [60, 61].

In the context of transonic compressors, the interaction is confined within the blade passages. The unsteadiness is of critical importance due to its impact on aerodynamic stability and mechanical integrity. At the design point, the compressor is optimised to maintain a stable shock position with minimal boundary layer separation. The suction side Mach number is usually limited to approximately 1.25 to prevent massive separation and ensure high efficiency especially at late compressor stages, where turbulent boundary layer is pronounced [54].

At this design condition, the shock is often positioned such that the pressure rise is managed by the blade geometry, and the oscillation amplitude is minimised to roughly 10% of the blade chord [62]. At the design point, the frequency of the shock oscillations is influenced by the internal passage dynamics and the blade-to-blade spacing (s).

Significant attention has been directed towards laminar SBLI in recent years [63, 64]. This interest is driven by the requirement for higher efficiency high altitudes especially with fan and first compressor stages, as discribed earlier. Particular concern is associated with laminar SBLIs because they typically exhibit significantly higher levels of unsteadiness compared to turbulent interactions. Large-scale shock oscillations are characteristic of laminar SBLI unsteadiness. These oscillations are frequently found to be more severe than those encountered in fully turbulent flows. The increased severity of unsteadiness in laminar shock-wave boundary-layer interactions is driven by a lack of near-wall momentum. As a large separation bubbles are formed even under the influence of weak shocks.

The interaction dynamics are exacerbated by the coupling between the separation bubble and the external inviscid flow. An effective fluidic ramp is created by the presence of a large separation zone. The displacement thickness of the boundary layer is significantly increased by this phenomenon. Shock positions are determined by this altered effective geometry of the aerofoil surface. Large displacements of the shock wave are forced by any fluctuation in the bubble volume. Large-scale oscillations are produced by the periodic accumulation and shedding of fluid mass within the bubble [65]. Heightened sensitivity is also linked to the unstable nature of the laminar-to-turbulent transition location within the separated shear layer. A stationary location is not maintained by the spatial position of this transition point. Shifting of the transition point is heavily influenced by the unsteady pressure field and the instantaneous shock movement. A high-gain feedback loop is established between the shock motion and the shifting transition point [66]. Such mechanisms are largely absent in fully turbulent flows.

Maintaining the shock at the design point is essential to avoid the onset of transonic buffet, where large-scale oscillations can lead to aeroelastic instabilities and high-cycle fatigue [67]. The management of these unsteady loads is a primary challenge in the design of highly loaded transonic compressor stages. As the compressor moves away from the design point toward stall, the unsteadiness increases. The shock foot may then fluctuate within a range of up to 23% of the chord [68]. Such large-scale oscillations can lead to aeroelastic instabilities and high-cycle fatigue in the rotor blades.

Flow control devices

To mitigate the detrimental effects of SBLI, various flow control strategies are categorised as either passive or active. Passive control is often preferred for its simplicity and lack of external energy requirements. Early transition from laminar to turbulent flow is forced to improve the boundary layer's resistance to separation. Common methods include the use of boundary layer tripping steps (Figure 1.7a) and roughness patches (Figure 1.7b) positioned upstream of the shock [69–72]. Although detrimental effects on flat plate performance and shock unsteadiness have been reported [73, 74], these devices often yield positive results in compressor applications. Turbulent states are forced to increase shear forces and momentum exchange, which significantly reduces the separation region.

Although a turbulent boundary layer is more resilient to separation, this robustness comes at the cost of increased skin-friction drag. As a result, overall aerodynamic efficiency may be reduced in cases where the shock is too weak to induce separation and laminar flow could otherwise be maintained under off-design conditions. Furthermore, as reported in the EU FP7 TFAST project [40], tripping devices that are improperly sized relative to the local boundary-layer thickness may themselves become a source of additional drag or induce small-scale separation bubbles. Therefore, the use of such passive control devices should be carefully evaluated with respect to the operating conditions and the local shock strength.

Advanced passive techniques include micro-vortex generators (MVGs) (Figure 1.7c) and shock control bumps (SCBs) [55, 75–78]. MVGs generate counter-rotating streamwise vortices to entrain high-momentum fluid from the free stream into the near-wall region. This re-energisation of the flow effectively suppresses shock-induced separation.

A permanent drag penalty is introduced by MVGs because the vanes must protrude into the flow. This "device drag" persists even at off-design conditions where shock-induced separation is not present. Furthermore, the re-energising effect may dissipate if the shock is located too far

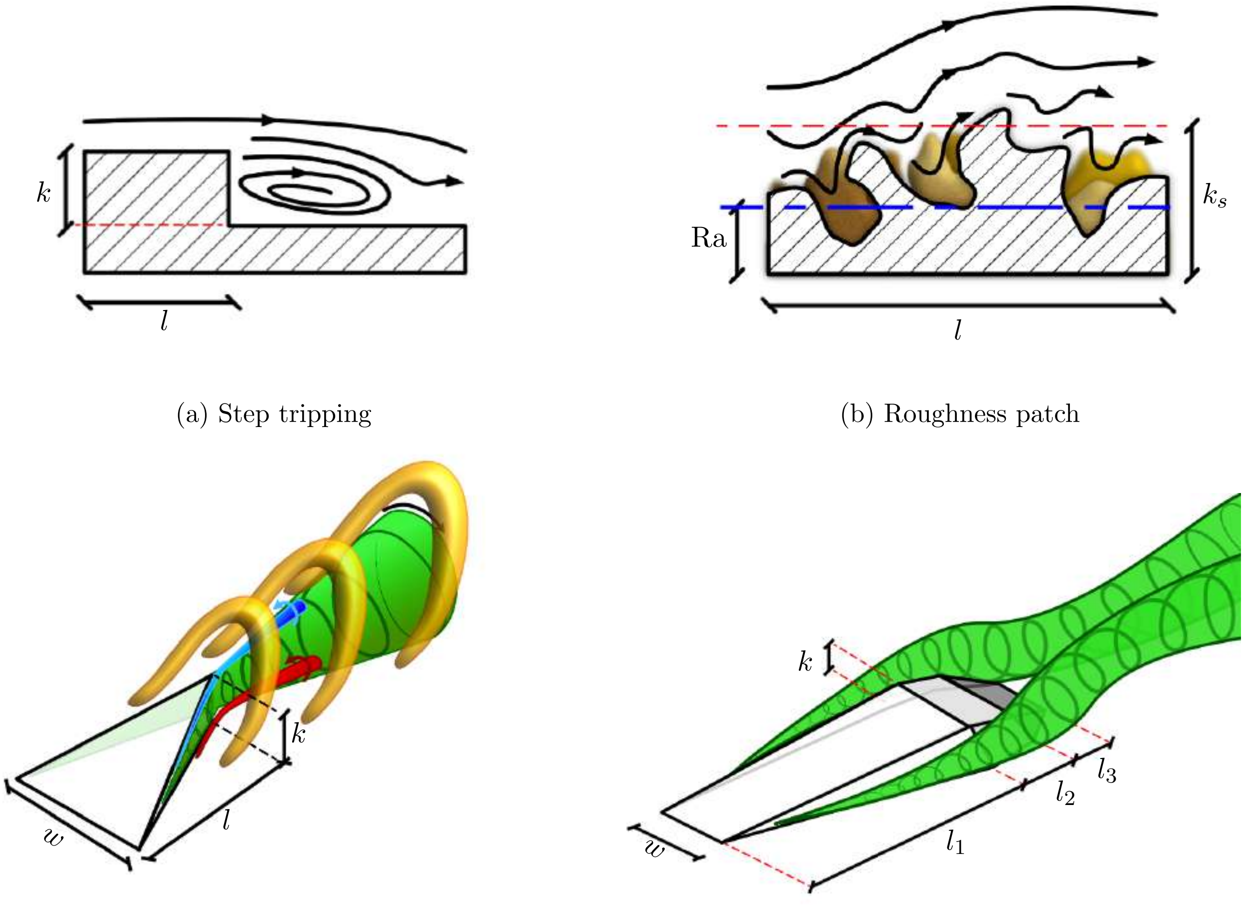

(a) Step tripping

(b) Roughness patch

(c) MVGs

(d) Bump

Figure 1.7: Examples of boundary layer control devices

downstream of the decaying vortices. Conversely, SCBs utilise three-dimensional surface contouring to smear the passage shock foot [78]. The flow is pre-decelerated by weak compression waves produced by the curved windward geometry. This reduces the total pressure rise of the primary shock and leads to a more stable flow field in transonic rotor blades.

Sensitivity to the design point limits the implementation of shock control bumps. Specific shock Mach numbers and locations are required for optimal contouring. If the operating condition changes, the shock may move away from the SCB, causing the bump to act as a topographical obstacle. Earlier separation or additional compression waves may be triggered, thereby increasing total pressure loss. Furthermore, the manufacturing and structural integrity of thin compressor blades are complicated by the three-dimensional nature of these bumps. Consequently, the application of SCBs requires precise alignment with the expected shock position across the operating range.

Active control methods, such as suction or tangential blowing, offer high performance at the cost of increased weight and mechanical complexity. Low-energy fluid is removed from the wall to prevent massive stall, particularly in corner regions. A passive-active hybrid approach has been proposed where air is removed via suction from one stage and redirected for blowing on a preceding stage [79]. A self-sustaining control loop is created to maintain high stage loadings without external power. However, these coupled systems are sensitive to pressure balancing and involve complex internal manifolding. Maintenance difficulty and production costs are significantly increased by these internal architectures.

Figure 1.8: An example of a roughness patch utilized in the operational jet engines

1.3 State of Art

The aerodynamic performance and surface integrity of compressor components are fundamentally influenced by manufacturing techniques and subsequent operational environments. High-strength titanium alloys are typically utilised for transonic fan blades to accommodate extreme centrifugal and vibrational loads. These materials enable the maintenance of thin profiles necessary for efficient transonic operation (see Section 1.1). Within this regime, the chordwise location of boundary layer transition is identified as a critical factor governing the topology and stability of SBLI (see Section 1.2).

Superior surface finishes may lead to preserve laminar flow and delay transition. Such high-quality surfaces also serve to mitigate the accumulation of foreign deposits and limit the impact of particle-induced erosion. Degradation of the leading-edge geometry and profile shape is often avoided through these stringent surface requirements. However, the attainment of high-precision finishes in hardened titanium alloys necessitates complex machining processes and significantly increases production costs.

Various flow control devices, including strategically placed roughness patches, are utilised to trigger transition, as discussed in Section 1.2. Through the introduction of a specific roughness patch in a specific location and width for a specific flow conditions, the boundary layer is transitioned to a turbulent state upstream of the shock wave. Large laminar separation bubbles are effectively suppressed by this mechanism. Resistance to shock-induced separation is increased due to the enhanced momentum exchange within the boundary layer. Furthermore, significant reductions in shock-front unsteadiness and aeroacoustic engine noise are achieved.

The practical viability of this approach is evidenced by its implementation in several operational jet engines, as shown in Figure 1.8. The dimensions and scales of these patches are arbitrarily defined to satisfy specific aerodynamic design criteria. However, the integration of these features necessitates additional manufacturing operations that differ from standard blade profiling. These processes are considered sophisticated and contribute to increased production costs. The selection of roughness parameters is therefore governed by a balance between aerodynamic gain and manufacturing complexity.

1.3.1 Roughness fundamentals and parameters

Surface roughness refers to the small-scale irregularities and deviations present on a solid surface. These imperfections can arise from various sources, including manufacturing processes, material properties, and operational wear. The topology is often categorised into three main components: roughness, waviness, and form. Roughness encompasses the fine-scale irregularities resulting from manufacturing processes, while waviness refers to larger-scale undulations caused by factors such as machine vibrations or tool deflections. Form represents the overall shape or geometry of the surface, which may include intentional design features.

Roughness is traditionally quantified through two-dimensional (2D) profile parameters and measured through contact or non-contact profilometry techniques such as stylus profilometers, laser

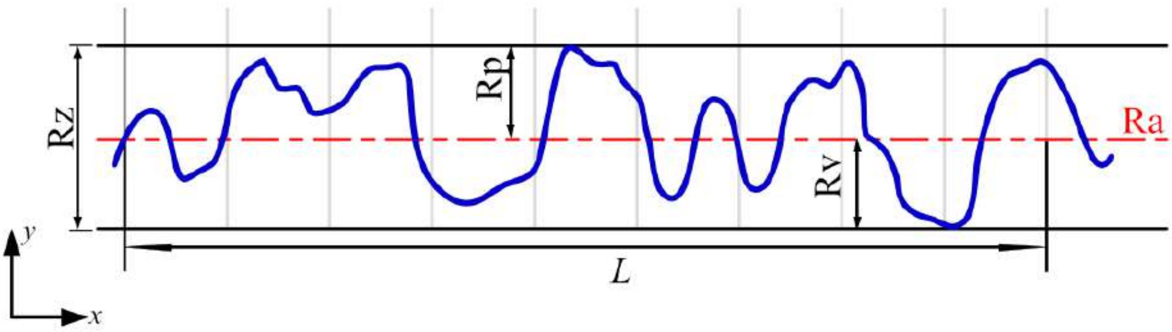

Figure 1.9: Two-dimensional (2D) profile parameters

scanning confocal microscopy, white light interferometry, or atomic force microscopy.The locations and orientation of the profile are critical, as they influence the measured roughness values. Parameters are typically derived from a single line scan across the surface, capturing the vertical deviations (y) from a mean line over a specified evaluation length (L) [80].

As illustrated in Figure 1.9, the arithmetic mean deviation (Ra) and the root-mean-square deviation (Rq) are the most widely utilised 2D metrics. Ra is defined as the average of the absolute values of the profile height deviations from the mean line. Rq is calculated as the square root of the mean of the squared vertical deviations, as shown in the following equation:

$$\mathrm{Ra} = \frac{1}{L}\int_0^L |y(x)|dx, \tag{1.11}$$

$$\mathrm{Rq} = \sqrt{\frac{1}{L}\int_0^L y^2(x)dx} \tag{1.12}$$

The characterisation of surface roughness in two dimensions is further refined through the use of peak and valley height parameters. The maximum profile peak height (Rp) is defined as the distance between the mean line and the highest point of the profile within a sampling length. Conversely, the maximum profile valley depth (Rv) is measured as the distance between the mean line and the deepest point. The total height of the profile (Rz) is defined as the sum of Rp and Rv:

$$\mathrm{Rz} = \mathrm{Rp} + |\mathrm{Rv}| \tag{1.13}$$

In many engineering standards, Rz is also referred to as the average peak-to-valley height when calculated over several sampling lengths. These parameters are often supplemented by higher-order statistical moments, such as skewness (Rsk), to describe the symmetry and "peakedness" of the profile.

On the other hand, three-dimensional (3D) or areal parameters provide a more comprehensive characterisation of surface texture. Because real-world surfaces exhibit complex, nonuniform roughness patterns, 3D measurements capture the spatial distribution of surface features over an area rather than a single line. A single line trace cannot distinguish between distinct morphological features, such as isolated peaks and continuous ridges, if they share an identical cross-sectional profile. Areal parameters capture the full spatial distribution and connectivity of these features. Additionally, Areal measurements are obtained from a defined sampling area rather than a single sampling length. This approach provides a significantly higher density of data points, which increases the statistical reliability of the results. The sensitivity of the measurement to the exact position of the trace is reduced, as local defects or inhomogeneities are contextualised within the wider surface area. The measurements are typically obtained using advanced techniques such as laser scanning confocal microscopy, white light interferometry, or atomic force microscopy.

The areal arithmetic mean height (Sa) and root-mean-square height (Sq) represent the 3D equivalents of Ra and Rq. The maximum peak height of the evaluated surface is denoted as Sp, while the maximum pit depth is denoted as Sv. The maximum height of the scale-limited surface

Sz is defined as the sum of the largest peak height and the largest pit depth within the defined area.

In 3D characterisation, the skewness (Ssk) is evaluated over an area rather than a single line. Skewness is utilised to differentiate between surfaces dominated by peaks (Ssk > 0) or valleys (Ssk < 0). The core roughness is defined through the material ratio curve, also known as the Abbott-Firestone curve. This curve represents the cumulative height distribution of the surface topography [81]. In the ISO 25178-2 standard, the core roughness depth is denoted as Sk. This parameter characterises the height of the "core" region of the surface, excluding the most prominent peaks and deepest valleys. It is complemented by the reduced peak height (Spk), which represents the average height of the peaks above the core, and the reduced valley depth (Svk), which represents the average depth of the valleys below the core [82]. The characterisation of surface topography through core roughness parameters provides a more statistically robust representation of flow-surface interactions compared to extreme value metrics. Parameters such as Sz, Sp, and Sv are determined solely by the single highest or lowest points within a sampling area and are highly susceptible to measurement noise and isolated topographic outliers. In the context of aerodynamic applications, such outliers do not necessarily reflect the global aerodynamic influence of the surface; a single abnormal peak does not influence the boundary-layer displacement thickness as significantly as the collective distribution of the surface core.

1.3.2 Roughness in aerodynamic applications

Surface roughness is widely investigated in aerodynamics because it significantly alters fluid dynamics and heat transfer [83–89]. It was first pioneered by researchers such as Hagen (1854) and Darcy (1857), who identified that roughness significantly affects pressure drop by increasing drag force and blockage. The primary aerodynamic penalty associated with roughness is the substantial elevation of skin friction and pressure drag. These effects are produced through the induction of velocity profile perturbations and enhanced turbulent mixing within the boundary layer. Conversely, roughness is strategically utilised in specific convective applications to enhance heat transfer and promote transition. In engineering practice, these phenomena are encountered on gas turbine aerofoils, aircraft wings, and within internal flow passages.

Roughness-induced transition

Boundary layer transition from a laminar to a turbulent state is strongly influenced by surface topography. The onset and rate of transition are quantified by the specific geometric characteristics of the roughness elements. In the transitional regime, surface disturbances create elevated shear layers and alternating high- and low-speed streaks near the wall. These streaks are susceptible to secondary instabilities, which facilitate the breakdown of laminar flow. Transition mechanisms are frequently triggered by roughness at Reynolds numbers significantly lower than those predicted by linear stability theory [87]. Transient growth is identified as a critical factor in this bypass mechanism, where disturbances grow due to the "lift-up" effect. Furthermore, hairpin vortices are observed behind roughness protuberances. These vortices act as primary structures that facilitate the breakdown into localized three-dimensional turbulence [88].

The critical roughness height required to trigger transition is dependent on the local boundary layer thickness and roughness Reynolds number.

$$Re_k = \frac{k_s u_\infty}{\nu} \tag{1.14}$$

Alternatively, the non-dimensional roughness height in wall units is expressed as:

$$k_s^+ = \frac{k_s u_\tau}{\nu} \tag{1.15}$$

Smaller roughness elements are sufficient to induce transition in thinner boundary layers at higher Reynolds numbers. The shape, distribution, and orientation of roughness elements also play significant roles in determining their effectiveness in promoting transition [90].

Critical boundary layer roughness is defined as the maximum height a surface element can reach before the transition from a laminar to a turbulent state is significantly accelerated. Through various bypass mechanisms, surface irregularities trigger transition far upstream of the natural transition point predicted by linear stability theory. This shift occurs abruptly once the roughness Reynolds number exceeds a critical threshold. For isolated roughness elements, Redford et al. [84] identified a critical roughness Reynolds number of approximately $Re_k^* \approx 600$. However, investigations into distributed roughness indicate that this critical value is strongly dependent on element morphology. Sharp-edged geometries, such as triangular profiles, are found to be more effective transition triggers than spherical elements of equivalent height. These triangular structures initiate transition movement at significantly lower Reynolds numbers, typically ranging between 800 and 1000, compared to approximately 1500 for rounded elements [91].

In the context of turbomachinery, for distributed roughness elements, Schlichting (1961) observed that the position of the transition point remains stationary provided Re_k remains below 120. This limit is remarkably robust and is largely independent of the prevailing local pressure gradient. Data from Bammert and Milsch (1972) suggest that in certain compressor cascades, even when roughness levels are several times this threshold, the transition point may not be shifted significantly forward [37]. This indicates a degree of stability in the laminar boundary layer of specific aerofoil profiles that resists bypass transition despite surface degradation.

Roughness effects in turbulent boundary layers

In a fully turbulent boundary layer, the flow is categorised into three regimes: hydraulically smooth ($k^+ < 5$), transitionally rough ($5 < k^+ < 70$), and fully rough. In the fully rough regime ($k^+ > 70$) , the viscous sublayer is completely destroyed by the roughness elements. Consequently, the skin friction coefficient (c_f) becomes independent of the Reynolds number and depends solely on the relative roughness height [92]. Roughness alters the near-wall momentum and heat transport. The mean velocity profile is shifted downwards in the logarithmic layer. This shift is defined as the roughness function [46]:

$$\Delta u^+ = \frac{1}{\kappa} \ln\left(1 + 0.3 k_s^+\right) \tag{1.16}$$

where κ is the von Kármán constant (approximately 0.41).

The admissible roughness Reynolds number is traditionally constrained to $Re_k \leq 100$ in gas turbine applications [93, 94]. This value represents a fundamental physical threshold where roughness elements remain submerged within the viscous sublayer. Within this hydraulically smooth regime, the surface irregularities do not contribute to additional momentum exchange or pressure drag. Once this limit is exceeded, the elements penetrate the buffer layer, and aerodynamic losses begin to increase rapidly due to the destruction of the viscous sublayer. For axial-flow compressors, this threshold is critical because surface degradation leads to a thickened boundary layer and increased viscous dissipation. This degradation directly penalises the stage efficiency and can lead to a premature reduction in the stable operating range of the engine.

Equivalent sand-grain roughness

A distinction is made between isolated roughness elements, distributed roughness, and natural random roughness based on their spatial regularity and spectral composition. Isolated elements are frequently utilised in fundamental research to simplify the transition problem and isolate specific instability mechanisms [84, 95, 96]. However, this approach inherently neglects the complex interactions between multiple scales, such as element pitch and packing density. Distributed roughness typically comprises ordered arrays of uniform geometries, including cubes, hemispheres, or bars. In these configurations, the instability wavelengths and the subsequent breakdown to turbulence are strictly governed by the periodic spacing between elements [88, 90, 97].

In contrast, natural random roughness resulting from operational factors such as corrosion, erosion, or biofouling is stochastic in nature. Unlike manufactured arrays, these surfaces possess a multi-scale topographical character that cannot be adequately described by a single height parameter. The characterisation of such surfaces instead necessitates the use of statistical moments and power spectral density functions to capture the random distribution of peaks and valleys. In transonic compressor environments, the interaction of these stochastic features with the boundary layer leads to a non-uniform distribution of wall shear stress and heat transfer.

The equivalent sand-grain roughness (k_s) is utilised to globalise diverse surface topographies into a singular aerodynamic metric. This approach allows the complex, multi-scale nature of real-world roughness to be collapsed into a one-dimensional length scale. Geometric parameters, such as Ra, Rz, and Ssk, are translated into k_s to facilitate the use of standard boundary-layer equations. This globalisation is essential for engineering applications where the detailed resolution of every surface peak is computationally prohibitive [83]. The concept of equivalent sand-grain roughness (k_s) was established by Johann Nikuradse in 1933. Systematic experiments were conducted using pipes coated with closely packed, uniform sand grains of specific diameters. These experiments provided a baseline where the geometric height of the grains was directly linked to the measured pressure drop and friction factor. k_s is therefore defined as the height of monodisperse sand grains that would produce the same profile as the actual surface [98].

The correlation, proposed by Koch and Smith (1976) [37]:

$$k_s = C_s \mathrm{Ra} \tag{1.17}$$

is frequently adopted, with $C_s = 6.2$ being a common empirical constant [93, 99–101]. In the present research such coefficient is adopted to maintain simplicity and ensure compatibility with established turbomachinery datasets. Nevertheless, a significant degree of variability exists in the literature, with reported values ranging from 2 to 9 depending on the specific manufacturing process and surface morphology [94, 102–104]. This correlation is widely utilised in compressor design as it provides a straightforward, linear translation from standard industrial metrics to aerodynamic parameters. Through this empirical relationship, the equivalent sand-grain roughness is estimated directly from the arithmetic mean roughness (Ra).

Despite its widespread application, it is recognised that this linear model may over-predict k_s for surfaces characterised by highly skewed or dense distributions. The correlation is most accurate for stochastic, isotropic roughness patterns that closely resemble the uniform sand grains used in Nikuradse's original experiments. For surfaces featuring highly anisotropic or structured roughness, such as those resulting from specific milling or coating processes, the linear assumption may fail to capture the directional sensitivity of the flow. In these instances, alternative correlations or direct experimental measurements of k_s are necessary to ensure the accurate prediction of boundary layer development and skin friction coefficients [86, 105]. Consequently, while the $C_s = 6.2$ constant provides a robust baseline, the influence of surface skewness (Ssk), root-mean-square (Sq), peak-to-valley height (Sz), and streamwise effective slope (ES_x) must be acknowledged when evaluating the aerodynamic performance of non-uniform technical surfaces [106–109].

1.3.3 Roughness application in transonic regimes

Compressibility introduces additional complexity to the interactions between surface topography and the boundary layer. In high-speed flows, isolated roughness elements generate detached shear layers and streamwise vorticity. Fundamental research at Mach 3 and Mach 6 indicates that while the magnitude of streamwise vorticity is relatively insensitive to the Mach number, transition is generally delayed by wall cooling and higher Mach numbers [84]. The role of roughness height remains paramount; elements that protrude significantly into the boundary layer can generate shocks and acoustic disturbances that further accelerate the transition process.

The effect of surface roughness on unseparated turbulent SBLI was investigated by Babinsky and Inger [110] at Mach 2.5 on a flat plate. Roughness scales were varied with Rz/δ ranging from 2.5×10^{-4} to 7.5×10^{-3}, resulting in Re_k values between 24.8 and 967. It was found that roughness elements increased the skin friction coefficient and altered the shock topology, leading to a more stable interaction. In the numerical Direct Numerical Simulation (DNS) study by Quadros et al. [97], the influence of distributed roughness on a flat plate was examined at $M = 1.7$. With a significant roughness height of $k/\delta = 0.5$ and $Re_k \approx 3100$, the interaction length was found to be larger for transitional cases than for fully turbulent cases. This transitional SBLI is characterised by a wider spreading of the wall pressure rise and a notably slower recovery of the boundary layer downstream of the shock. Furthermore, experimental work by Giepman et al. [73] at Mach 1.7 utilised distributed roughness patches (Rz/δ = 0.5, $Re_k \approx 3500$) to trigger transition 30δ downstream of the patch. While the separation bubble was suppressed, the boundary layer thickness and shock instability were increased. These flat-plate studies serve as critical benchmarks for comparing the fundamental mechanisms of SBLI control with the more complex flow physics observed on compressor aerofoils.

In contrast to the fundamental flat-plate configurations, research on highly loaded compressor profiles has demonstrated the potential for loss reduction through the application of distributed surface structures. Boese [111] investigated the impact of V-groove riblets across the entire suction side of a compressor cascade at $Re_i = 4.5 \times 10^5$ and $M_i = 0.67$. Even in the absence of shock waves, the total pressure loss coefficient was reduced by up to 5%. This benefit was achieved by the riblets' ability to modify the near-wall turbulent structures and reduce the turbulent skin friction. Lietmeyer et al. [112] further explored these effects at lower Reynolds numbers ($Re_i = 1.5 \times 10^5$, $M_i = 0.5$) using riblet scales of Rz/$\delta \approx 0.02$. Their findings indicated a maximum profile loss reduction of 7.2% when the riblets were applied to both the suction and pressure sides. In these subsonic regimes, the riblets functioned primarily by suppressing laminar separation bubbles, effectively triggering an earlier but controlled transition that prevented massive flow detachment. However, the efficacy of these structured surfaces is highly dependent on their chordwise placement and the local Mach number. Lietmeyer et al. observed that placing riblets near the leading edge actually caused a significant increase in losses. This penalty was attributed to the premature triggering of transition in a region that would otherwise remain laminar and low-friction, thereby increasing the integrated skin friction along the blade. Furthermore, these studies were conducted at $M_i \leq 0.67$, where the flow remains entirely subsonic or only weakly transonic. In such environments, the primary loss mechanisms are viscous dissipation and separation, rather than shock-induced phenomena. Additionally, The application of such structured roughness or riblets to operational compressor blades introduces significant practical challenges. The manufacturing of precise V-grooves or micro-structured arrays necessitates sophisticated production processes, such as laser-surface texturing or high-precision forging, which substantially increment the unit cost.

Leipold et al. [113] investigated random roughness on a transonic compressor profile ($k/\delta \approx$0.3) within a Reynolds number range of 3×10^5 to 10^6 at $M_i = 0.67$. While the laminar boundary layer remained largely insensitive to roughness, transition and separation characteristics were significantly altered. At $Re \approx 6 \times 10^5$, the laminar separation bubble was completely suppressed, resulting in a reduced displacement thickness compared to smooth blades. However, this mitigation was frequently offset by increased viscous dissipation within the turbulent boundary layer. At elevated Reynolds numbers, this increased dissipation potentially leads to premature turbulent separation. Aerodynamic sensitivity was found to be most acute at positive incidence angles, where surface textures triggered unfavorable boundary layer growth and a net increase in total pressure losses. These findings emphasize that even without shock-wave interactions, stochastic roughness at Rz/$\delta \approx 0.3$ often exceeds the admissible limits, causing parasitic drag that outweighs separation control benefits.

In the presence of strong shock waves, the interaction between the shock and the boundary layer becomes a dominant source of loss and instability. Research by Klinner et al. [72] on a transonic compressor profile at $M_i = 1.21$ and $Re_c = 1.48 \times 10^6$ utilised a random roughness patch (ANSI grit 180) at $0.16x/c$. The study demonstrated that triggering transition upstream of the shock foot significantly reduces the shock-induced separation bubble. A frequency ratio of 0.23 was achieved compared to the laminar baseline, indicating a substantial damping of the low-frequency shock oscillation. Similarly, Szwaba et al. [71] investigated various roughness scales (ANSI grit 240-400) at $M_i = 1.22$. Their results confirmed that wake losses and shock unsteadiness are minimised when a turbulent interaction is induced. It was observed that positioning the roughness closer to the shock foot limits viscous dissipation, while placement further upstream at $0.11x/c$ provides more effective suppression of flow unsteadiness.

Despite these potential gains in stability and separation control, a recurring limitation in the literature is the use of roughness scales that significantly exceed the admissible Re_k threshold. Klinner et al. utilised a roughness Reynolds number of $Re_k \approx 1750$, while Szwaba et al. reported values ranging from 694 to 1407. These scales are nearly an order of magnitude higher than the admissible limit of 120 established by Schlichting [37]. Such large scales are often selected for experimental convenience to ensure transition, yet they lack a rigorous aerodynamic justification. The use of these "overtripped" configurations risks high degradation of aerodynamic performance, particularly in off-design conditions where the boundary layer is naturally thicker. In such scenarios, the excessive roughness can lead to a thickened turbulent boundary layer and increased viscous dissipation that may negate the benefits of separation suppression.

Furthermore, the implementation of these features in an industrial environment introduces significant manufacturing and economic challenges. The production of specific roughness patches or structured surface textures necessitates additional manufacturing operations, such as precision laser etching, chemical milling, or advanced forging, which differ from standard blade profiling. These sophisticated processes significantly increase the unit cost and production time of compressor blades. Moreover, maintaining the integrity of these precise roughness scales in the erosive and corrosive environment of an operational gas turbine is difficult. The lack of studies justifying the economic viability or the performance impact across the entire engine operating map represents a critical research gap. Consequently, while the aerodynamic ability to control SBLI via roughness is proven, the selection of parameters remains a trade-off between structural stability, production cost, and thermodynamic efficiency.

1.4 Dissertation objectives and outline

This research is founded upon the following hypothesis:

"The surface roughness of a transonic compressor blade, determined by the final surface finishing process, affects shock wave oscillations and reduces shock-induced flow separation."

The primary objectives of this dissertation are to investigate the critical interplay between surface roughness and SBLI. An overview of the current understanding of these phenomena is provided to contextualise the research within the field of turbomachinery. Insights are sought through aerodynamic experimental studies conducted at the IMP-PAN transonic wind tunnel. The clarification of key aerodynamic characteristics and the enrichment of the existing SBLI dataset for internal flows are intended.

A central aim is to address the research gap regarding the physical justification of roughness scales. Much of the existing literature utilises roughness heights that significantly exceed the admissible Re_k threshold, often leading to excessive "overtripping" and increased viscous dissipation. This research evaluates roughness parameters that balance the suppression of the shock-induced separation bubble with the preservation of overall stage efficiency. Crucially, the roughness configurations investigated are designed to be compatible with standard machining processes. This approach ensures that the aerodynamic benefits are achieved without the necessity for additional production stages or increased manufacturing costs, which often hinder the practical implementation of flow control devices.

Furthermore, the implications of these modifications are considered across the operating map, including off-design conditions where excessive roughness may deteriorate component efficiency. By establishing a link between aerodynamic gain, dynamic stability, and the economic reality of standard manufacturing requirements, a more robust framework for the strategic application of roughness in transonic compressors is developed. This work aims to demonstrate that transition control can be integrated into the existing production cycle of transonic components, offering a cost-effective method for enhancing the performance and stability of modern axial-flow compressors.

With these objectives, the test section geometry employed in this study was designed to reproduce the passage flow and shock structures characteristic of modern aircraft transonic compressor components. The fan profile geometry and surface texture specifications were provided by Rolls-Royce within the framework of the collaborative EU research project TEAMAero, funded under the Marie Skłodowska-Curie programme. Additional support was provided through contributions from external academic institutions, enabling access to specialised manufacturing and measurement capabilities. The initial profile geometry and two-dimensional surface roughness characterisation were performed at the Institute of Manufacturing and Materials Technology (Gdańsk University of Technology), guaranteeing dimensional fidelity and surface quality. Subsequently, three-dimensional surface optical measurements were carried out at the Institute of Fluid Mechanics (ISM) at TU Dresden, utilising their advanced non-contact measurement systems. Aerodynamic testing and data analysis were conducted at IMP-PAN by the author. Throughout the study, close technical collaboration with Rolls-Royce and supporting academic partners ensured that the experimental design, data interpretation, and resulting conclusions remained aligned with industrial standards and practical application requirements.

In this dissertation, general introductions to transonic compressors and the associated design challenges are provided in Chapter 1. Modern requirements for high aerodynamic loading and the SBLI problems encountered during low Reynolds number operation are discussed.

Chapter 2 presents the governing physics and the experimental methodologies employed in this study. The configuration of the single-passage test section in the IMP-PAN transonic wind tunnel is described. Techniques used to capture shock structure and unsteady motion are introduced. Methods for observing surface flow topology and for performing boundary layer measurements are also detailed. Procedures for data acquisition and uncertainty quantification are outlined.

The geometry of the transonic fan profile is detailed in Chapter 3. The evaluation of the manufactured surfaces is presented to verify the fidelity of the test profiles. The shape definition and the application of controlled surface roughness are specified.

Chapter 4 provides the analysis methods developed for this study. Proper orthogonal decomposition (POD) and computer vision-based shock tracking are employed to capture and analyse flow unsteadiness in high-speed schlieren imaging. Additionally, image transformation technique is implemented to improve the accuracy of oil-flow visualisations for the high-fidelity detection of separation features. Moreover, statistical approach for the analysis near-wall flow is described.

The sensitivity of the test section to minor changes is presented in Chapter 5. Variations in the inflow angle, stagger angle, and blade-to-blade distance are examined to establish the robustness of the experimental facility. The positioning of the profiles relative to the test section walls is also evaluated to mitigate unintended facility effects and to ensure similar flow conditions. The influence of the AVDR on the flow field is specifically addressed. These sensitivity analyses ensure that the baseline flow structures are accurately established prior to the implementation of surface roughness.

Chapter 6 investigates the influence of different roughness parameters on the SBLI topology. Changes in the extent of shock-induced separation and the resulting aerodynamic effects are analysed. The impact of surface roughness on shock-induced unsteadiness is quantified.

Finally, the main conclusions in Chapter 7 drawn from the study are compiled in Conclusions chapter. The dual consequences of using surface roughness, involving aerodynamic benefits and shock unsteadiness costs, are discussed. Recommendations for the integration of controlled roughness in future compressor designs are proposed.

Chapter 2

Experimental Setup

This chapter details the experimental apparatus and measurement systems used to investigate textured fan profiles under transonic conditions. Our experiments primarily focused on flow measurements, which we conducted at the transonic wind tunnel facility of the Institute of Fluid-Flow Machinery (IMP-PAN) in Gdańsk, Poland. This facility is specifically designed for steady, high-speed aerodynamic measurements. This facility is specifically designed to enable steady, discontinuous, high-speed aerodynamic measurements, and the test section was tailored to investigate passage flows over a representative fan profile.

The test section geometry replicates the passage flow and shock structures characteristic of modern aircraft transonic compressor components.

This chapter is organized as follows:

- Section 2.1 provides an overview of the IMP-PAN wind tunnel facility, including its operational parameters and flow conditioning systems.
- Section 2.2 describes the test section geometry, details its mounting, and highlights the resulting flow structure and manipulation.
- Section 2.3 outlines the measurement techniques and instrumentation employed for flow diagnostics.

2.1 Wind tunnel operation

The experimental investigations were conducted utilizing the IMP-PAN transonic wind tunnel, a blow-down tunnel characterized by a discontinuous operating mode. A comprehensive schematic illustrating the primary components of this facility is presented in Figure 2.1.

The operational sequence begins with ambient air being drawn into the tunnel system. This intake air first passes through (1) the air dryer, a robust steel tank containing two tons of silica gel granulate. The granulate functions to effectively remove moisture, thereby ensuring a consistent and controlled dryness of the gas stream, irrespective of ambient atmospheric conditions. Regeneration of the silica gel is performed after specific number of running cycles by heating the entire mass, a process that releases the absorbed water in the form of steam.

Following the drying stage, the air travels through a connecting pipeline (internal diameter: 437 mm) that incorporates a (2) honeycomb straightener. This critical component, with a thickness of 100 mm, is integrated within welded steel pipe sections. Its fundamental purpose is to homogenize and calm the flow velocity field, ensuring optimal conditions upstream of the test section [114].

Further downstream in the pipeline, the flow encounters a series of (3) essential pipeline devices designed for particle injection and evaluating total conditions. For advanced flow diagnostics, (3a) an oil seeding fog probe is integrated, connected to a (3b) Flow Tracker 700 CE. This system is responsible for generating the fine seeding particles necessary for Laser Doppler Anemometry (LDA) and Particle Image Velocimetry (PIV) measurements. The Flow Tracker is supplied with a continuous and stable high-pressure supply from a dedicated (4) high-pressure compressor, ensuring consistent particle generation throughout the measurement duration. Additionally, (3c) Prandtl

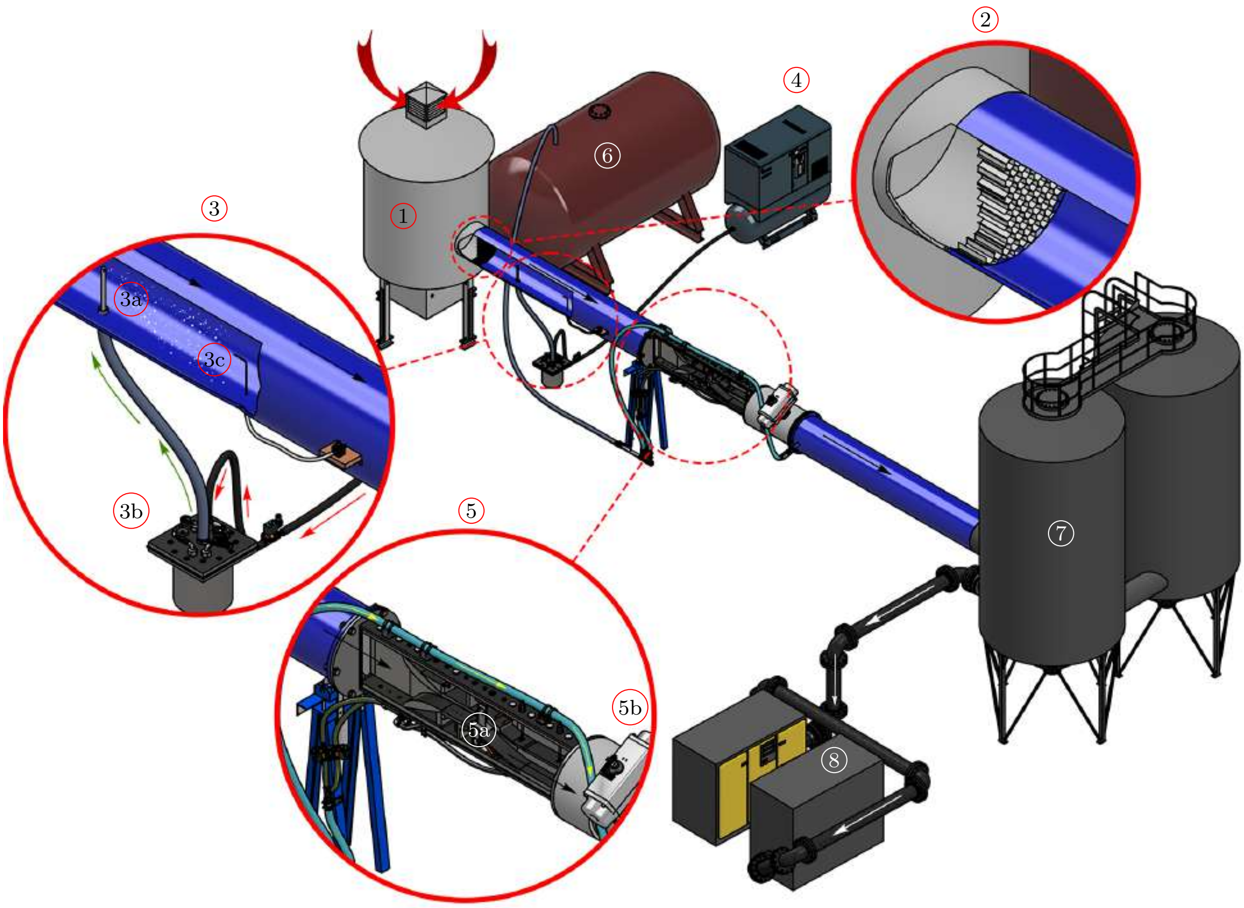

Figure 2.1: The schematic diagram of IMP-PAN transonic blowdown wind-tunnel

probe, which measures the total pressure, and K-type thermocouple to measure total temperature, equipped with appropriate transducers, provide precise measurements of the flow parameters entering the core research area.

Subsequently, the conditioned air enters (5) the research area, which is situated within the laboratory. This element of the tunnel is replaceable and measures 1800 mm in length, featuring an internal rectangular cross-section of 100×350 mm. The research area houses (5a) the test section and is equipped with provisions for the installation of additional measuring instruments. Its hinged side walls, which incorporate glass windows, facilitate convenient internal access for adjustments between measurements and provide essential optical access for non-intrusive diagnostic techniques. To further refine the flow and mitigate the influence of secondary flows, a separate (6) vacuum tank can be employed to enable a dedicated suction system. This suction system operates independently of the primary wind tunnel flow, allowing for precise control of boundary layer effects. The initiation and cessation of the main flow are managed by (5b) an electrically controlled ball valve, which is actuated by a pneumatic drive and exhibits an opening time of approximately 2 seconds.

Upon exiting the measurement area, the air is directed through the aforementioned (5b) valve to a series of (7) steel vacuum tanks, which collectively possess a substantial total capacity of 120 m^3. Once this valve is closed, the evacuation of air from these tanks (6 and 7) is performed by (8) two coupled KAESER vacuum pumps (models BSV100 and CSV150). These pumps, with respective power ratings of 20 kW and 30 kW, are capable of achieving absolute pressures as low as 10 mbar. Upon reaching this minimum pressure, they automatically transition into a pressure-maintaining mode. During active measurement phases, both pumps operate in parallel until a vacuum pressure of 0.1 bar is attained. Below this threshold, pumps are automatically disconnected from the vacuum system and enters an idle mode. Following the completion of a measurement "blow", the pumps revert to drive mode, efficiently preparing the tunnel for subsequent experimental runs.

This facility, with a test section, has a nozzle throat cross-section of 100 mm^2, is capable of sustaining a stable critical flow for durations of 15 to 20 seconds, with a typical recovery time of approximately 15 minutes between successive runs. This operational cycle ensures the consistent and repeatable experimental conditions essential for high-fidelity transonic investigations.

2.2 Test section model

The single-passage test section, central to this investigation, was designed at IMP-PAN as part of the EU project TFAST [40]. This design, detailed in Appendix A, was based on data from compressor cascade and CFD simulations, with the nozzle walls representing the flow streamlines derived from the cascade CFD. This setup aims to precisely replicate shock-induced separation effects on the suction side of the fan profile, allowing the exploration of SBLI from various perspectives, including the impact of surface roughness, the potential of passive flow control devices, and Reynolds number variations. As shown in Figure 2.2a, the single-passage test section incorporates two fan profiles; their specific details will be further elaborated in Section 3.1. For this configuration, the inflow Mach number (M_i) is set at 1.22 (measured at the end of the straight path of the nozzle, specifically 113.95 mm upstream of the lower profile, which corresponds to 1.14 x/c upstream of the lower profile). Additionally, repeated LDA measurements have consistently shown the inlet turbulence intensity to be in the range of 2.4-2.7%.

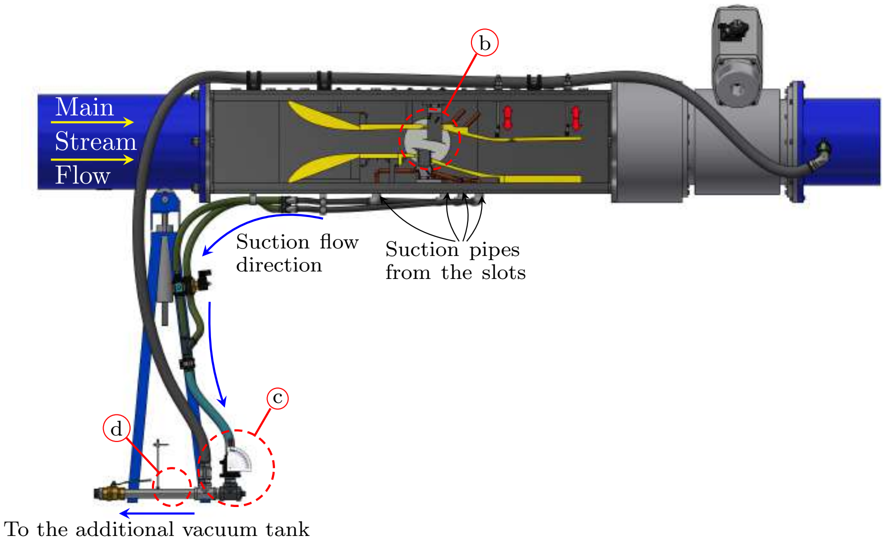

(a) Test section setup and suction piping system

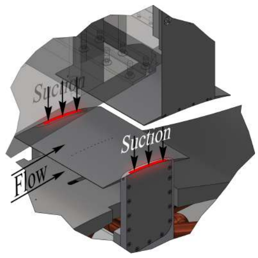

(b) Suction slots

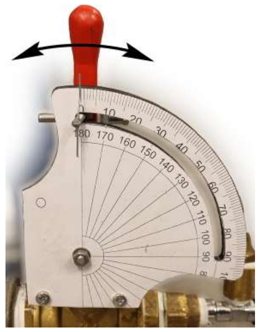

(c) Flow control valve

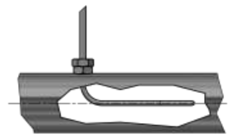

(d) Pitot tube

Figure 2.2: Test section and suction control systems

To prevent flow blockage within the test section, the design integrates a perforated plate on the upper wall and a slot on the lower wall. These are directly connected to the main vacuum tanks (7), where the pressure is maintained at approximately 10% of the ambient pressure. The primary role of this suction on the upper and lower walls is to reduce the boundary layer thickness, eliminate potential blockage, and ensure a consistent mass flow through the upper and lower passages. This, in turn, directly impacts the mass flow in the middle passage.

Furthermore, two suction slots are located on the lower sides of the profile, as depicted in Figure 2.2b. These slots connect to an additional vacuum tank (6). The flow through these slots is controlled by two distinct valve systems: the first uses ON/OFF solenoid valves, while the

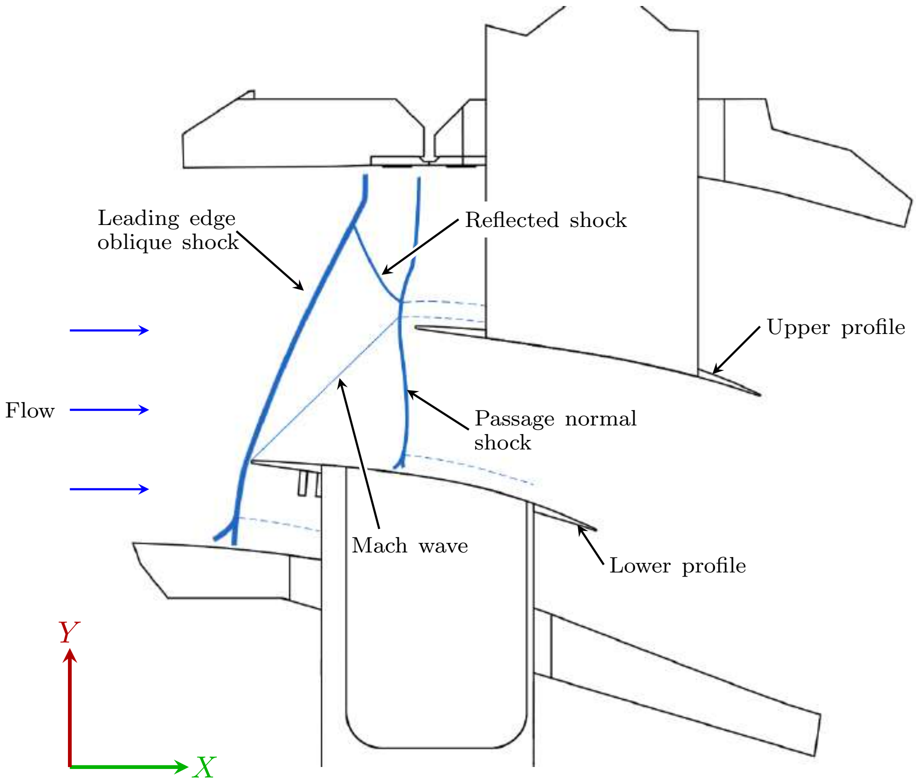

Figure 2.3: Single passage transonic fan profile and shock structure

second employs a ball flow control valve, illustrated in Figure 2.2c. This ball valve enables precise regulation of the suction mass flow. The primary function of these side wall suction slots is to regulate the mass flow within the middle passage, reduce secondary flows along the side walls, and mitigate corner vortices. This ultimately ensures the profiles achieve their designed axial velocity density ratios (AVDR) and, consequently, the desired shock structure.

Direct flow measurements upstream of the suction points proved challenging due to the intricate piping system and the small dimensions of these slots. To address this, a pitot tube (shown in Figure 2.2d) was positioned just before the main valve of vacuum tank (6). This pitot tube provides a crucial measurement of the downstream total pressure of the suction, complementing static pressure measurements taken within the pipes. Together, these provide an indirect yet reliable indication of the mass flow rate within the pipes and slots.

The resulting shock structure within the test section are illustrated in Figure 2.3. Within this configuration, the lower profile initiates the formation of a (detached/oblique) shock wave, referred to as the leading-edge shock. This shock wave subsequently interacts with the upper wall of the test section, leading to its reflection (reflected shock). Concurrently, an expansion wave originates at the leading edge of the lower profile, giving rise to a distinct Mach line. Simultaneously, the upper profile generates a normal shock, termed the passage shock, which represents a primary focus of this test section model.

The leading-edge shock's upper segment and its corresponding reflected shock demonstrate an unsteady nature, primarily due to their interaction with the boundary layer developing on the test section's upper wall. In contrast, the Mach wave largely maintains a steady state. However, the passage shock, being the central subject of the study, exhibits significant unsteadiness stemming from its pronounced interaction with the boundary layer on the lower profile.

To ensure the accurate replication of the desired flow conditions, precise control over the back pressure is paramount, given that total flow conditions are inherently linked to ambient atmospheric parameters. This essential control mechanism, vital for achieving the target inflow Mach number and the desired shock structure, is effectively accomplished by adjusting the nozzle outlet area. This adjustment is facilitated through the manipulation of the outlet's upper wall, which is precisely governed by a screw mechanism.

2.3 Flow measurements techniques and methods

Understanding the intricate relationship between surface topography and aerodynamic performance requires a thorough analysis of the resulting flow field. To this end, multiple measurement techniques were systematically employed to provide a comprehensive and different perspective of the flow. Each method was selected to address specific aspects of the flow structure, from quantifying mean velocity and turbulence levels to characterizing its dynamic and unsteady behavior. This section details the methodologies used to acquire the rich data set necessary to evaluate the aerodynamic impact of each textured profile.

2.3.1 Pressure measurements and Mach number estimation

To characterize the flow conditions and locate the shock wave, a pressure measurement system was employed. The inflow Mach number distribution upstream of the profiles was determined using five static pressure taps positioned on the bottom wall just behind the nozzle throat. The location of these taps is well represented in Appendix A. A Pitot tube, fixed far upstream of the test section, provided a direct measurement of the inflow total pressure (p_{01}), as indicated in Figure 2.1. With these values, the isentropic Mach number (M) was calculated using the following relationship for an ideal gas:

$$M = \sqrt{\frac{2}{\gamma - 1}\left[\left(\frac{p_0}{p}\right)^{\frac{\gamma-1}{\gamma}} - 1\right]} \tag{2.1}$$

Where γ=1.4 is air specific heat ratio. Static pressure along the lower profile's suction side was measured using twelve pressure taps, starting at 0.15 x/c and extending to cover 46% of the chord length. These taps were located at the mid-span, beneath the shock interaction region, as illustrated in Figure 2.4. Additionally, four pressure taps were connected to suction tubes (p_{suc}) to ensure an even flow distribution on both sides of the suction slots for symmetrical flow. Moreover, additional pitot tube was positioned just before the main valve of the vaccum tank (p_{02}) provides a measurement of the downstream total pressure of the suction as mentioned in the previous section.

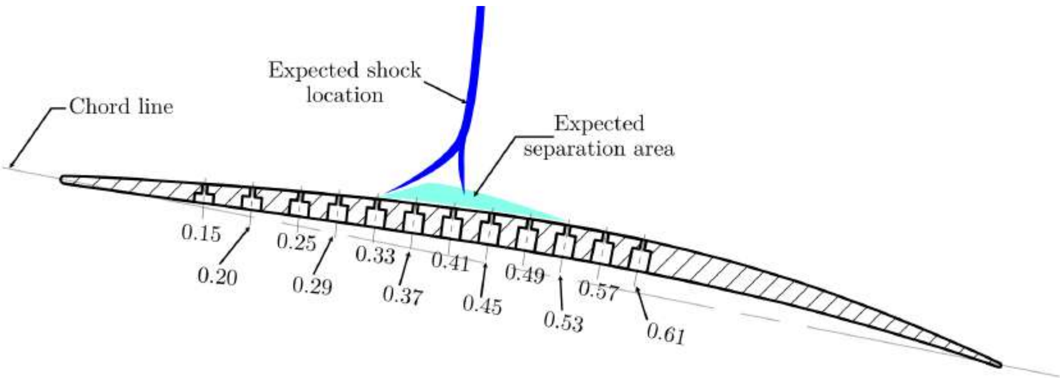

Figure 2.4: A side section of the lower profile showing the pressure tap locations along the suction side where x/c is the chordwise location normalized by the profile chord length.

All pressure taps were connected to a Pressure System 9010 transducer set. This system consists of two transducers, each with 16 channels, that both use the ambient pressure as their reference and have an accuracy between ±0.05-0.08% of their respective ranges [115].

- 10 psi transducer with a range of 10 psi (68.95 kPa), was intended for the nozzle pressure measurements, where the pressures are relatively high. Its accuracy translates to an error margin of ±0.005-0.008 psi (±34.47-55.16 Pa)
- 15 psi transducer, with a wider range of 15 psi (103.42 kPa), was used for the low pressures on the profile's suction side and suction slots, especially when reducing the Reynolds number

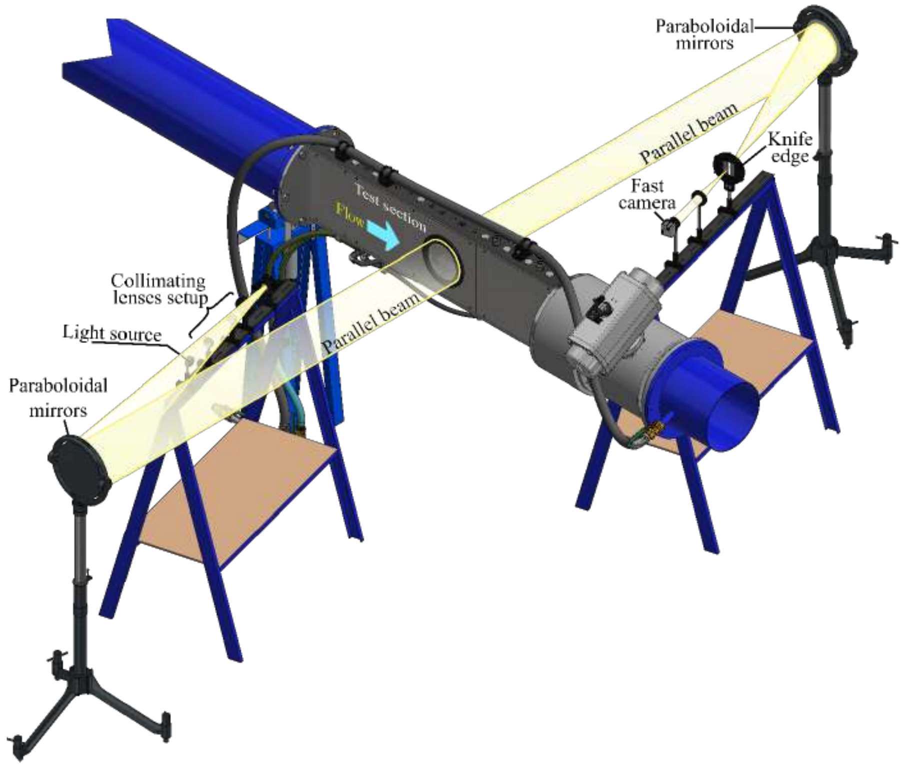

(a) Schlieren z-type layout

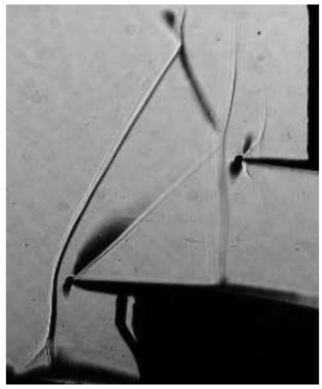

(b) Horizontal knife setup

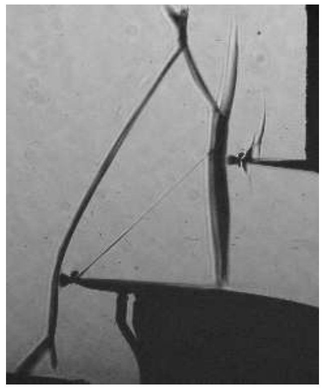

(c) Vertical knife setup

Figure 2.5: Schlieren imaging configurations

by decreasing the inflow total pressure. This results in a proportionally larger absolute error, with an accuracy of ±0.0075-0.012 psi (±51.71-82.74 Pa).

While the 10 psi transducer technically provides finer absolute accuracy, the error values for both transducers are considered well within an acceptable range for this study. The Mach number distribution uncertainty analysis is based on the standard deviation of repeated measurements.

2.3.2 Schlieren and high-speed schlieren

Z-Configuration schlieren system was used to capture the flow structure as shown in Figure 2.5a, providing both instantaneous and time-resolved images. A Canon EOS M50 was used for static snapshots, while a Fastec Imaging HiSpec 2G mono high-speed camera was used for unsteady analysis. The system utilized a continuous-mode xenon lamp as the light source, and a pair of two-and-a-half-meter focal length paraboloidal mirrors were used to generate a parallel light beam. The key parameters of the schlieren setup are summarized in the Table 2.1.

The schlieren imaging technique provides a detailed visualization of the flow field, with the captured image's content directly dependent on the orientation of the knife edge. A horizontal knife edge, as shown in Figure 2.5b, effectively highlights vertical density gradients, making features like boundary layer separation and expansion waves clearly visible, while rendering the passage shock less distinct. In contrast, a vertical knife edge, as used in Figure 2.5c, is ideal for detecting horizontal density gradients, thereby making normal and near-normal shock waves easily discernible for detection and tracking.

The sensitivity of the schlieren system, and thus the clarity of the resulting image, is dependent on the magnitude of the density gradient. This gradient is affected by the total pressure (p_0) of the flow, which can be adjusted to control the Reynolds number. When p_0 is reduced, the pressure difference across shocks decreases, leading to a diminished density gradient and reduced ray deviation. This presents a challenge in the schlieren setup, requiring a trade-off between

Table 2.1: Z-configuration schlieren system parameters

Component	**Parameter**
Light Source	35 W Xenon Lamp (Hamamatsu L2193)
Light Source Temp.	6000 K
Pinhole Size	0.01 mm
Paraboloidal Mirrors:	
Focal Length (f_c)	2.5 m
Diameter	220 mm
Cameras:	
Snapshots Camera	Canon EOS M50 (6000×4000 px)
High-speed Camera	Fastec HiSpec 2G (Max. 112 kfps at 128×2 px)

the quality and sharpness of the shock visualization and the capture of smaller-scale flow details. Additionally, the rapid movement of the shock relative to the camera's exposure time can cause blur, further reducing sharpness.

Therefore, meticulous control of these parameters is crucial for capturing high-quality schlieren images. These images are essential for accurately identifying the shock structure, which in turn allows for detailed shock tracking and unsteadiness investigation, as further described in Section 4.2.

2.3.3 Oil flow visualization

To visualize the flow structure on the suction side of the lower profile, a titanium dioxide oil paint solution with a concentration of 10-35% was used. In most experiments, the oil was brushed onto the surface to cover the separation area up to the trailing edge. This approach was specifically chosen to preserve the roughness effects on the upstream flow, allowing for an accurate analysis of the boundary layer behavior. The development of the oil flow patterns was captured using a single camera view, as shown in Figure 2.6. The side wind tunnel windows provided clear insight into the test section, enabling precise image acquisition.

Figure 2.6: Oil visualization setup

The recorded images were then post-processed using matrix transformation and scaling techniques to enhance their measurability, as further described in Section 4.3.

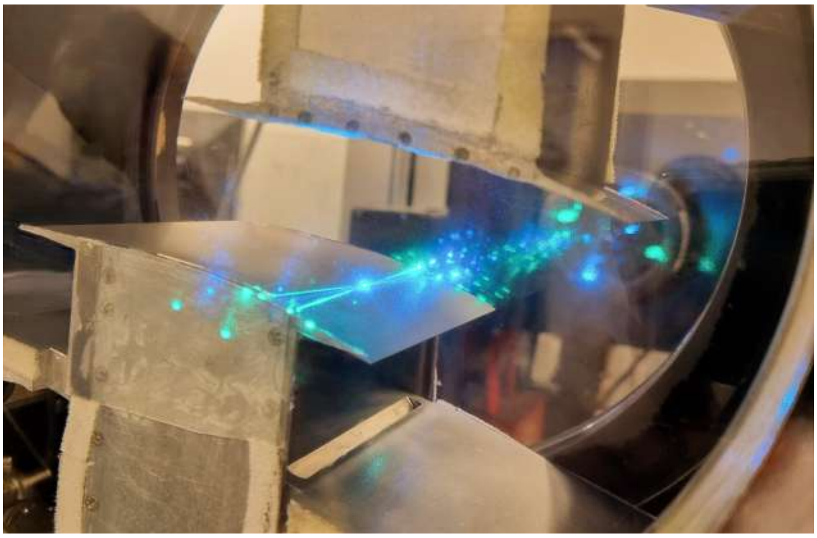

Figure 2.7: LDA setup at the surface of the profile for boundary layer measurements

2.3.4 Laser Doppler Anemometer and traverse

LDA was employed to measure both the inflow conditions and the boundary layer on the lower profile. For the boundary layer measurements, a single-component setup was operated to enable accurate near-wall measurements as shown in Figure 2.7.

The system uses a Coherent Innova 70C 5 W Argon-Ion laser as the light source, which is coupled with a FiberFlow system from Dantec Dynamics to split the laser beam and employ the back-scatter configuration. All technical parameters of the LDA system are summarized in Table 2.2.

Table 2.2: Laser Doppler Anemometry system parameters

Parameter	Unit	Value
Laser power used	W	1.5-2.5
Focal Length (f_c)	mm	500
Measuring volume		
- Diameter (dx)	µm	G: 80.11,
	µm	B: 75.98
- Length (dz)	mm	G: 1.08,
	mm	B: 1.03
Seeding		
- Partical generator	-	Flow Tracker 700 CE
- Seeding material	-	Di-Ethyl-Hexyl-Sebacic
		(ρ: 910-914 kg/m^3, μ: 22-24 mPa.s)
- Max particle size	µm	2

LDA measurement traverses

To quantify the inflow conditions, both probe components were used for the vertical traverses indicated in Figure 2.8 as traverse-a and traverse-b. These traverses were positioned 20 mm upstream of the lower profile, with the probe components aligned with the horizontal and vertical axes.

- This vertical traverse measured the upstream velocity ahead of the shock system to quantify the turbulence level and inflow Mach number.
- Positioned equidistant from both the upper and lower profiles' leading edges, this traverse was used to measure the velocity upstream of the shock waves and the velocity developing downstream, along with the inflow angle.

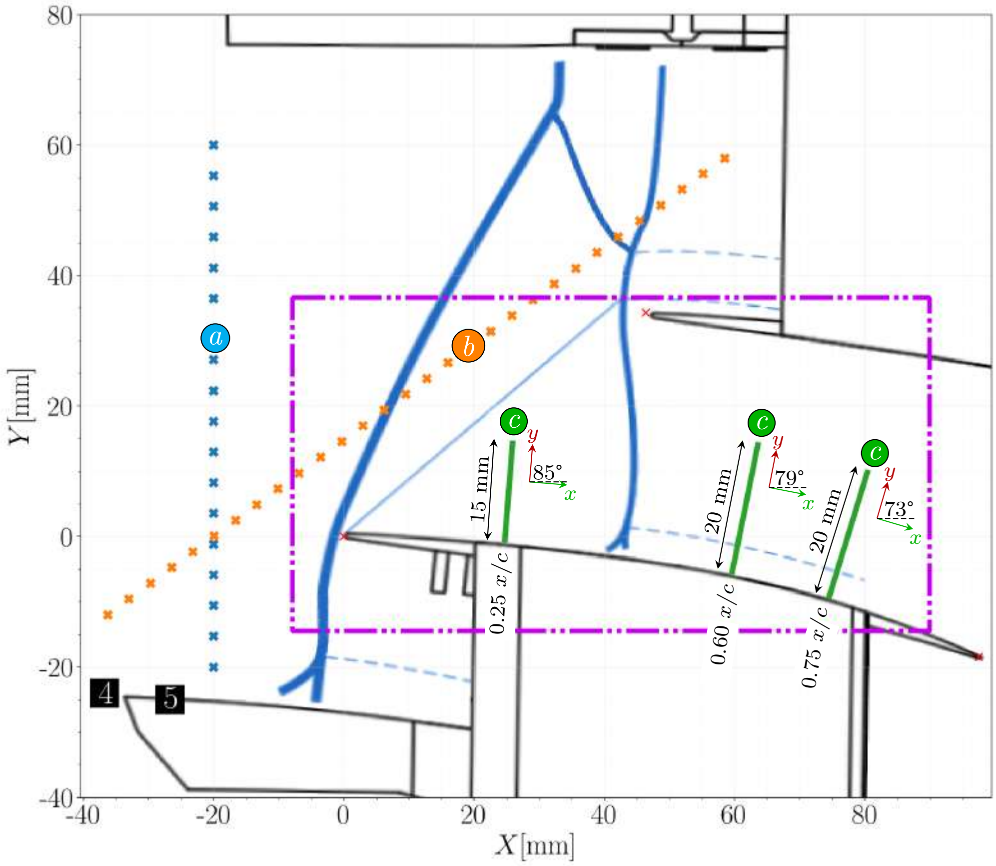

Figure 2.8: Window sight and LDA travers

Due to the curvature of a fan profile, especially downstream of the shock, defining the boundary layer measurement positions posed a considerable challenge. To address this, a dedicated Python script was developed, which uses the profile's CAD model information to facilitate the precise determination of measurement locations for the LDA system [116].

Based on the leading and trailing edge coordinates, which are acquired using the laser traverse system, the script establishes the profile's chord line within the experimental coordinate system. Subsequently, for each desired measurement location (defined by its chord-wise position x/c), the script calculates the coordinates of the desired surface point and the position of the laser's measuring volume.

This is achieved by retrieving crucial information directly from the profile's pre-defined CAD model. This includes the distance between the chord line and the profile surface and the angle of the local surface normal relative to the chord line. By combining these two sources of data, the automated process ensures that all boundary layer measurements are taken at the correct physical locations on the profile, regardless of its curvature.

For each profile, boundary layer measurements were carried out on the lower profile at three distinct chord-wise locations, as shown in traverse-c in the figure:

- 0.25 x/c representing the boundary layer upstream of the shock. The measurement traverse was positioned from 0.15 mm to 15 mm above the surface.
- 0.6 x/c representing the start of the reattachment zone downstream of the shock. The measurement was elevated from 0.2 mm to 20 mm above the surface.
- 0.75 x/c representing the well-developed flow far downstream of the shock. The measurement was also elevated from 0.2 mm to 20 mm above the surface.

Additionally, the probe system was rotated according to the angle of the normal line to the surface, as indicated in the figure, to ensure accurate near-wall measurements.

Measurements accuracy

Seeding particles were injected far upstream of the test section, as indicated in Section 2.1, to ensure that seeding was fully developed with the flow. However, the particle size distribution introduced significant challenges for LDA accuracy, particularly near the shock wave. The suitability of seeding particles for tracing the flow is quantified by the Stokes number (S_{tk}):

$$S_{tk} = \frac{\tau_p}{\tau_k} \tag{2.2}$$

where $\tau_p = \rho_p d_p^2/18\mu_g$ is the particle response time and $\tau_k = \delta/u_\infty$ is the characteristic time scale of the flow. The Stokes number is a dimensionless parameter, which compares the particle response time to the characteristic time scale of the flow. A high S_{tk} indicates strong particle inertia and poor tracing capability, whereas a low S_{tk} implies that particles closely follow the fluid streamlines. For tracing accuracy errors to be below 1%, the Stokes number should ideally be less than 0.1.

Regarding the upstream measurements, the profile chord length is considered as the characteristic length scale. The average free-stream velocity (u_∞) is 375 m/s based on previous experimental campaigns in TFAST [63]. The estimated particle response time (τ_p) of 14.27 µs, results in $S_{tk} \approx 0.05 < 0.1$. This reflects the high precision of the measurements at this location and confirms the reliability of using them to quantify the inflow turbulence level, as the particles capture most of the turbulence scales.

Based on CFD modeling of the test section by Piotrowicz et al. [117], considering the boundary layer thickness as a local length scale at 0.242 x/c (upstream of the shock) is approximately 0.25 mm. With a u_∞ of 398 m/s, the calculated Stokes number is very high, $S_{tk} \approx 22.72 \gg 1$. Such conditions imply that particles diverge strongly from the fluid streamlines due to their dominant inertia, especially across the abrupt deceleration at the shock. This results in significant measurement bias, with particle velocities underestimating the true flow speed. Furthermore, this slip effect leads to oil particle accumulation on the profile surface, making upstream near-wall measurements exceptionally difficult and unreliable.

Conversely, downstream of the shock, where the shock-boundary layer interaction is expected to induce turbulence, the Stokes number at 0.60 x/c and 0.75 x/c reduces to $S_{tk} \approx 1.2$ and 0.64, respectively. While this suggests that particles follow most turbulent structures, the value is still above the ideal threshold of 0.1 required for high-fidelity measurements. Therefore, a notable velocity slip persists, and due to the polydisperse nature of the seeding droplets, artificial velocity fluctuations may arise. This is a recognized source of error in LDA when polydisperse seeding is used, as larger particles respond more slowly than smaller ones, producing an apparent turbulence intensity that can be mistakenly attributed to the flow rather than to particle lag.

In addition to particle inertia, several optical and statistical issues further limited LDA accuracy near the profile wall. Reflections from the surface reduced the signal-to-noise ratio (SNR), and the low particle concentration in this region decreased the burst count, which lowered statistical confidence. The backscatter configuration posed further difficulty, as only a small fraction of light is scattered backward by the particles [118]. These factors collectively introduced higher uncertainty in the measured mean velocity and increased scatter in the velocity distributions. The finite size of the measurement volume relative to the steep velocity gradients near the wall also introduced additional bias, a phenomenon known as velocity-gradient broadening.

Uncertainty quantification

To mitigate the aforementioned challenges, near-wall measurements were conducted at a minimum distance of 0.15-0.2 mm from the surface, where optical reflections and velocity-gradient effects were more manageable. An augmented amount of seeding was specifically injected for these measurements, and each location was sampled repeatedly to reduce statistical uncertainty and achieve a more statistically representative dataset. As shown in Figure 2.9a, the near-wall data required multiple trials to enhance the statistical evaluation of the mean flow speed. In contrast, Figure 2.9b demonstrates that freestream measurements (benefiting from higher seeding density and minimal gradients) produced narrow velocity distributions and higher fidelity.

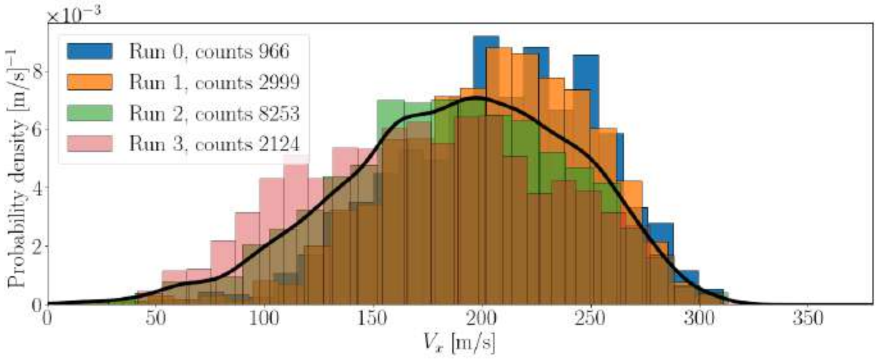

(a) The point close to the surface (0.2 mm from the surface)

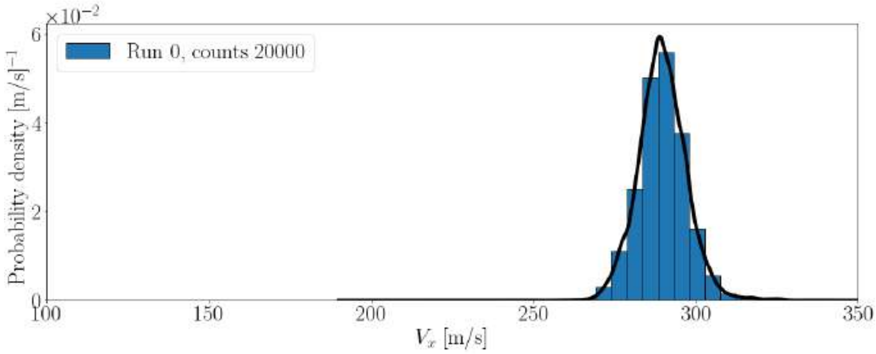

(b) free stream (20 mm from the surface)

Figure 2.9: Velocity range of detected seeding elements at 0.75 x/c

A key consideration for high-speed LDA is velocity bias, where a simple arithmetic average of recorded velocity samples favors higher velocities. [119]. To address this, a non-uniform weighting factor η_{w_i} is applied, using the transit time of each particle to provide a bias-free statistical average [120]. This method is defined as:

$$\eta_{w_n} = \frac{t_n}{\sum_{j=0}^{N-1} t_j} \tag{2.3}$$

Here t_n is the transit time or residence time of the n^{th} seeding particle passing through the LDA measuring volume, and N is the total number of counted seeds.

Accordingly, the mean velocity ($\overline{u}$) and the Root Mean Square velocity (u_{rms}) for each component are calculated as:

$$\overline{u} = \sum_{n=0}^{N-1} \eta_{w_n} u_n \tag{2.4}$$

$$u_{rms} = \sum_{n=0}^{N-1} \eta_{w_n} (u_n - \overline{u})^2 \tag{2.5}$$

For a measurement point to be considered valid, the total number of counted seeds had to be above 500, with a data rate exceeding 1000 particles per second. (The data rate was calculated based on the total number of counts (N) from all repeated measurements at a specific location divided by the total duration of them). This rigorous qualification process ensured a high level of confidence in the presented results.

The unbiased sample variance for weighted data ($\overline{u^2}$) is calculated to provide a more accurate estimate of the population variance for finite sample sizes. This value is essential for calculating the confidence intervals. The formula is:

$$\overline{u^2} = \frac{N}{N-1} \left(\sum_{n=0}^{N-1} \eta_{w_n} u_n^2 - 2\overline{u} \sum_{n=0}^{N-1} \eta_{w_n} u_n + \overline{u}^2 \sum_{n=0}^{N-1} \eta_{w_n} \right) \tag{2.6}$$

The confidence interval of the sample mean (ζ) is dependent on the measurement location. The uncertainty of the mean velocity data is estimated at a 95% confidence level using the formula by Benedict and Gould [121]:

$$\zeta_{\overline{u}} = t_{N-1;0.025}\sqrt{\frac{\overline{u^2}}{N}} \tag{2.7}$$

Here $t_{N-1;0.025} \approx 1.96$ for $N > 100$. The confidence interval for the RMS velocity is also calculated as:

$$\zeta_{u_{rms}} = t_{N-1;0.025}\sqrt{\frac{\overline{u^2}}{2N}} \tag{2.8}$$

Chapter 3

Characterization of the fan profile

The fan profile shape and surface textures were provided by Rolls-Royce as part of a collaborative EU TEAMAero research project. This work combines multi-institutional expertise and advanced facilities to ensure the accuracy and consistency of the profile surface texture evaluation. The initial profile shape and two-dimensional surface roughness characterization were meticulously performed at the Institute of Manufacturing and Materials Technology (Gdańsk University of Technology), guaranteeing dimensional fidelity and surface quality. To provide even more detailed topological data, three-dimensional surface optical measurements were subsequently carried out at the Institute of Fluid Mechanics (ISM) at TU Dresden, utilizing their advanced non-contact measurement systems.

- Section 3.1 focuses on the documentation of the profile geometries used in this study.
- Section 3.2 presents the evaluation of the manufactured profile shapes against the nominal CAD model.
- Section 3.3 details the initial surface roughness evaluation of the unmachined profiles.
- Section 3.4 discusses the surface roughness evaluation after the application of the intended surface textures.
- Section 3.5 provides a comprehensive analysis of the three-dimensional surface roughness measurements.

3.1 Profiles modeling

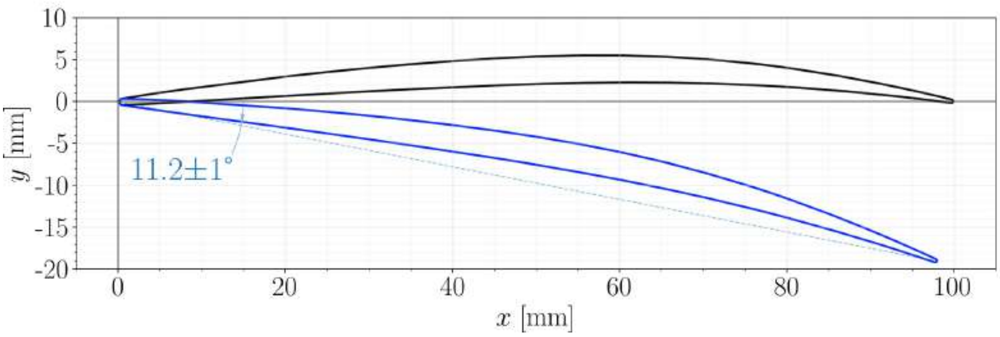

Figure 3.1: Compressor profile

The design and optimization of the profiles used in this study originated from compressor cascade geometry data provided by Rolls-Royce Deutschland (RRD). This data was supplied during the EU FP7 TFAST predecessor project. The shape of the profile is illustrated in Figure 3.1, and its corresponding geometric parameters are detailed in Table 3.1. To facilitate a focused investigation into SBLI on the suction side of the lower profile, where the shock interaction is localized, five

Table 3.1: Parameters of the TFAST cascade

Parameter	Unit	Value
Real Chord length (c)	mm	100
Stagger Angle (χ)	deg	44.39
Pitch to Chord Ratio (s/c)	-	0.6
Thickness to Chord Ratio	-	0.033
Blade Inlet Angle (β_i)	deg	50.91
Blade Exit Angle (β_o)	deg	33.22
Deflection Angle (ε)	deg	14.86
Leading Edge radius	mm	0.38
Trailing Edge radius	mm	0.21
AVDR	-	1.203

replicas of the lower profile were manufactured. Titanium alloy was chosen as the material to ensure that these replicas would respond similarly to an actual fan blade during subsequent machining processes. These processes include planned alterations to the surface texture and roughness on some of the profiles.

3.2 Pre-surface texturing shape evaluation

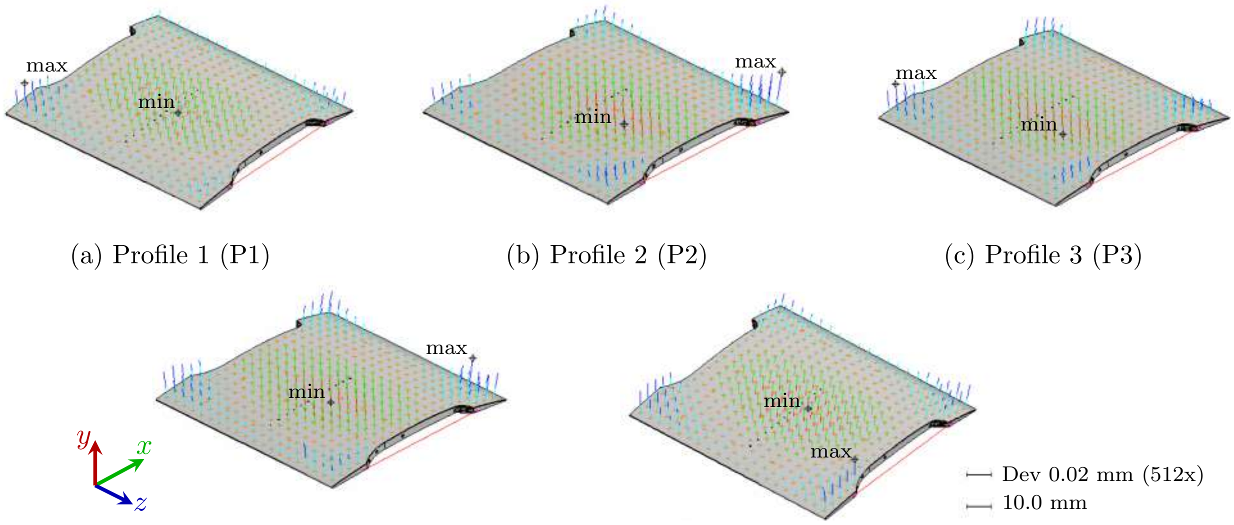

(a) Profile 1 (P1)

(b) Profile 2 (P2)

(c) Profile 3 (P3)

(d) Profile 4 (P4)

(e) Profile 5 (P5)

Figure 3.2: Profiles shape verification

The profile replicas were manufactured using wire electrical discharge machining (WEDM), a precision technique that ensured high geometric fidelity. This process achieved an average shape error of ±0.022 mm (±22 µm) from the nominal CAD model. The shape evaluation was performed using a Nikon Altera 7.5.5, which has a maximum possible error of 2.8 µm.

A closer look at the shape deviation, illustrated in Figure 3.2, reveals a clear trend. The profile's shape deviates negatively from the intended middle path, with an average deviation of -16.6 µm. Conversely, a positive deviation is observed at the corners, averaging 27 µm. The maximum and minimum deviations for each manufactured profile are summarized in Table 3.2.

Table 3.2: Shape maximum and minimum deviation from CAD model

	P1	P2	P3	P4	P5
Min (mm)	-0.0151	-0.0172	-0.0174	-0.0163	-0.0170
Max (mm)	0.0227	0.0319	0.0257	0.0288	0.0262

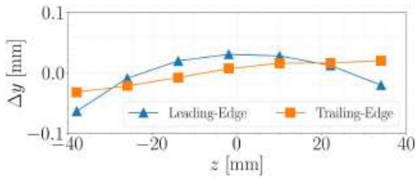

(a) P2

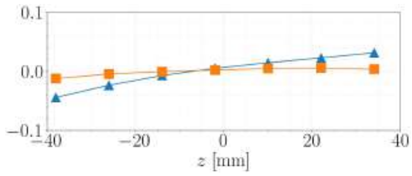

(b) P3

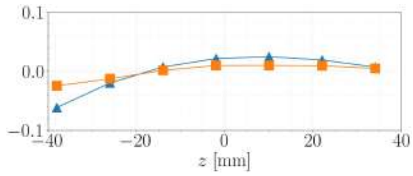

(c) P5

Figure 3.3: Leading and trailing edge shape and alignment

In addition to the overall shape evaluation, the straightness of the leading and trailing edges and the profiles' symmetry along the flow axis were also assessed under similar inflow and outflow conditions for all profiles. A magnified view of the leading and trailing edges is presented in Figure 3.3, providing a closer look at these critical areas, where the mid-span of the leading-edge is the origin of the coordinates.

The analysis revealed several minor imperfections. A small curvature was observed on the leading edges of profiles P2 and P5. Furthermore, profile P3 showed a slight tilting of its leading edge, measured at an angle of 0.001°. In the trailing edge analysis, profiles P3 and P5 were found to be nearly straight. Profile P2's trailing edge, while mostly straight, exhibited a tiny tilt with an angle of 0.0008°.

Despite these minor deviations, the overall shape variation is considered negligible. The leading and trailing edges of all profiles can be considered effectively straight, confirming the high quality of the manufacturing process and the suitability of the profiles for the intended experimental work.

3.3 Evaluation of surface roughness due to manufacturing

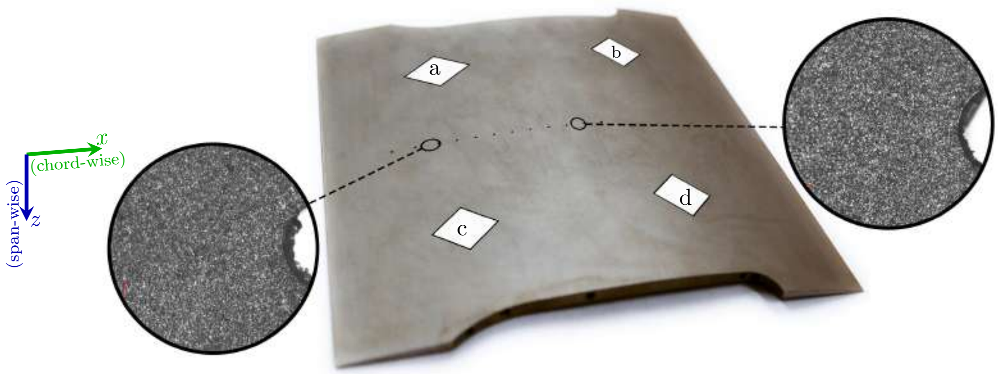

Figure 3.4: Roughness evaluation location

Before the final texture was applied, the profiles underwent a thorough evaluation using 2D Stylus diamond equipment (Mitutoyo SV-C3200). Roughness measurements were systematically performed at four distinct locations, indicated by the letters a, b, c, d in Figure 3.4. At each of these locations, measurements were taken in both the chord-wise direction (x) and the span-wise direction (z). The parameters used for these measurements are summarized in Table 3.3.

The average values for the main roughness features of all profiles are presented in Table 3.4, with a detailed dataset for each profile available in Appendix B. The profiles' surface characteristics are a direct result of WEDM process, specifically utilizing multiple trim cuts and low-energy settings. This approach is consistent with established literature, which shows that such a strategy can reduce the arithmetic average roughness (Ra) of titanium alloy to sub-micron levels, effectively refining the surface morphology by removing the initial rougher layers [122–124].

All profiles exhibit a fine and similar Ra, falling within a narrow range of 0.53 µm to 0.65 µm ($k_s \approx 3.35 - 3.93$µm). This consistency underscores the uniform application of the WEDM process. However, a detailed analysis of the core roughness parameters, particularly the Reduced Peak Height (Rpk) and Reduced Valley Depth (Rvk), reveals a surface topology dominated by protruding

Table 3.3: Roughness evaluation parameters

Parameter	Unit	Value
Measuring Length	mm	4.80
Measuring Step	mm	0.0005
Measuring Speed	mm/s	0.60
Measuring force	mN	0.75
Stylus Tip Angle	deg	60
Stylus Tip Radius	µm	2.00
Data processing software	-	Formtracepak v6.0

peaks. This is evident from the fact that Rpk values are consistently and significantly higher than Rvk values across all profiles, a characteristic also reflected by the positive skewness (Rsk) values.

Profile P3 was found to have the smoothest surface. It exhibits the lowest Ra values, ranging from 0.52 µm to 0.57 µm, and shows the least variation in its maximum peak-to-valley height (Rz), which consistently falls between 3.59 µm to 4.22 µm. The core of its roughness (Rk) is also low and uniform, and its reduced peak and valley heights (Rpk, Rvk) are minimal, indicating a smooth, consistent surface profile. Detailed values for this profile are available in Table B.3.

In contrast to Profile P3, Profile P5 appears to be the roughest. Its Ra values range from 0.58 µm to 0.69 µm, and it exhibits significant variations in its Rz, which spans from 3.89 µm to 5.57 µm. Notably, Profile P1 also presents high peak-to-valley values, with an average Rz of 4.82 µm in the chord-wise direction, comparable to the 4.91 µm observed in P5's span-wise measurements. The maximum Rz for P1 (5.31 µm) is also similar to that of P5 (5.57 µm).

These particularly high Rz values for both P1 and P5 are concentrated near the trailing edge (location 'b'). The impact of this roughness on the flow depends critically on the local boundary layer thickness. In this trailing-edge region, CFD simulations report a boundary layer thickness (δ) of approximately 5.8 mm [69]. Consequently, the roughness-to-boundary layer thickness ratio (Rz/δ) is less than 1e-3 and $k_s^+ \approx 1.81$, which is well below the thickness of the viscous sublayer. In this region, the boundary layer is already developed and thickened due to shock interaction, suggesting that these small roughness variations are unlikely to impact the overall flow characteristics.

However, in locations closer to the leading edge (locations 'a' and 'c'), the boundary layer is considerably thinner, with a reported CFD thickness of approximately 0.25 mm [117]. This results in a roughness-to-boundary layer thickness ratio (Rz/δ) of approximately 0.02 and roughness Reynolds number ($Re_k \approx 48 - 56$), which for a laminar BL considered still within a limit far from trigger transition. The higher Rpk values for P1 and P5, compared to P3, indicate that their roughness topology is characterized by sharper, more pronounced peaks.

The detailed roughness values for Profile P1 and Profile P5 are provided in Table B.1 and Table B.5, respectively.

Table 3.4: Pre-texturing profiles' average roughness values

	dirction	P1	P2	P3	P4	P5
Ra [µm]	Chord-wise	0.5987	0.6258	0.5283	0.5636	0.6214
	Span-wise	0.5705	0.6318	0.5541	0.6020	0.6484
	Overall average	0.5846	0.6318	0.5412	0.5828	0.6349
Rz [µm]	Chord-wise	4.8221	4.4871	3.9530	4.1583	4.4108
	Span-wise	4.0846	4.5048	3.8971	4.2598	4.9108

3.4 Textured profiles evaluation

Profiles P3 and P5 were selected as the unmachined baseline profiles, representing the smoothest and roughest surfaces produced by the WEDM process. The remaining profiles (P1, P2, and P4) were designated for surface texturing. Specifically, P1 and P2 were intended to be refined using a robot-polishing, while P4 was roughened using a manual-hand drill.

These textures were applied to the entire suction side of the profiles, with the exception of the leading and trailing edge tips. This was done for two primary reasons: firstly, the structural integrity of these slender regions was preserved by avoiding machining in thin-walled sections susceptible to damage. Secondly, the risk of 'overtripping' via premature boundary layer transition was mitigated. As indicated by Suder et al. [125] and Hergt et al. [126], transition triggered too far upstream increases viscous losses without yielding a commensurate aerodynamic benefit. The resulting machined profiles are shown in Figure 3.5, where the magnified surface texture in the bubbles was captured using a Nikon ECLIPSE Ti-S microscope with 5x magnification.

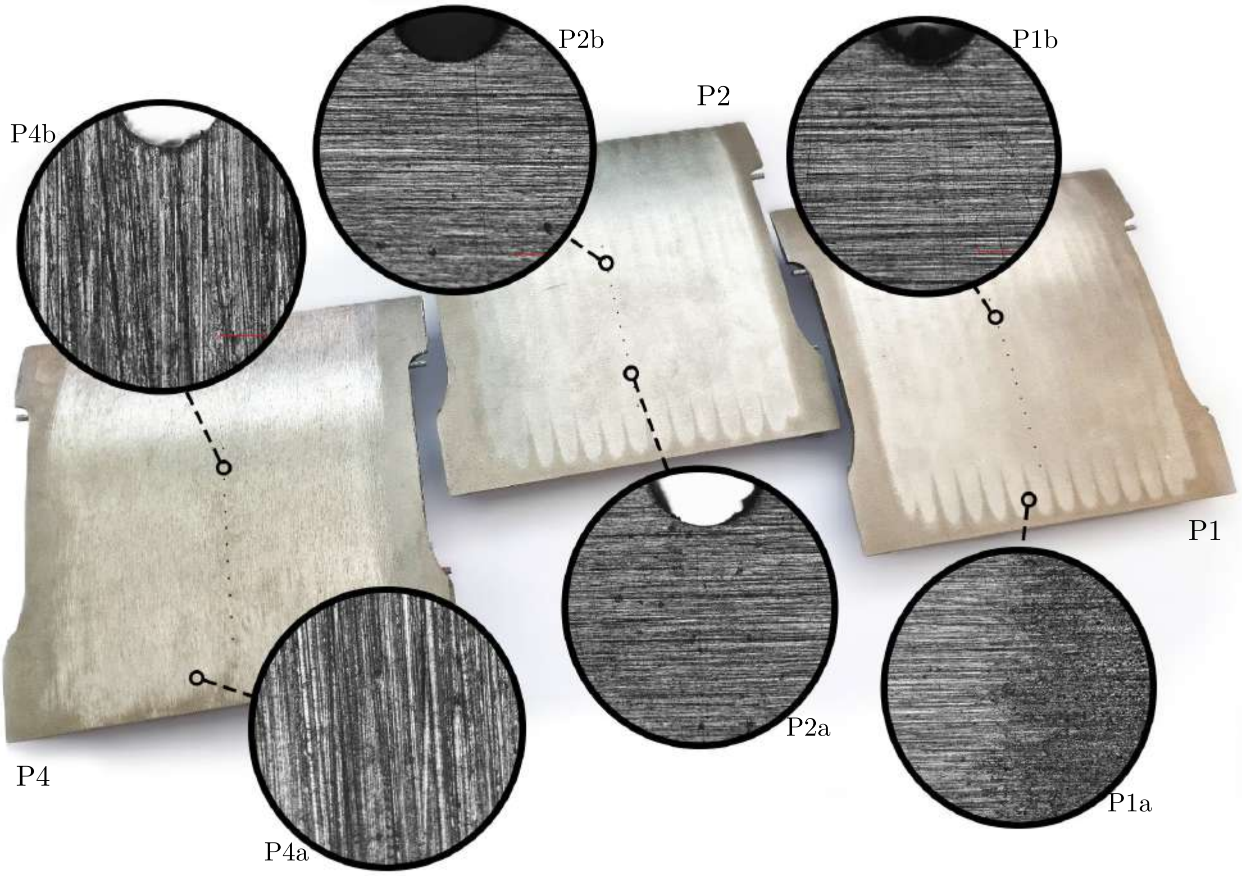

Figure 3.5: Machined profiles

Although surface textures were intended at the micrometre scale, larger-scale alterations to the overall profile geometry were unavoidably introduced during the machining process. As summarized in Table 3.5, the textured profiles exhibited an average shape deviation of approximately ±0.094 mm (±94 µm) from the nominal CAD model and ±0.072 mm (±72 µm) from the manufactured profile. These macro-scale geometric alterations were considered to have a limited influence on the local flow field and aerodynamic performance. This assessment was based on the small magnitude of the deviations relative to the total chord length and their distributed nature across the profile surface. The maximum and minimum deviations for each manufactured profile are summarized in Table 3.5.

Table 3.5: Shape maximum and minimum deviation from CAD model

	P1	P2	P4
Min (mm)	-0.098	-0.087	-0.113
Max (mm)	0.099	0.089	0.080

Table 3.6 presents the average values for 2D roughness measurements of the machined profiles, which were analysed using the same parameters outlined in Table 3.3. For a more detailed dataset, refer to Appendix B. The post-texturing measurements differentiate the three machined profile

surface topologies:

Table 3.6: Post-texturing profiles' average roughness values

	dirction	P1	P2	P4
Ra [µm]	Chord-wise	0.2526	0.3020	0.6773
	Span-wise	0.0822	0.1044	2.3007
	Overall average	0.1674	0.2032	1.4890
Rz [µm]	Chord-wise	2.1386	2.4584	4.1204
	Span-wise	0.5653	0.6564	17.2357

- **P1 and P2 (Robot-polishing):**

  The generated surface clearly shows a distinct pattern of wide, parallel finishing passes running in the flow (chord-wise) direction, with each containing fine scratches that are perpendicular to the flow (span-wise direction). As shown in Figure 3.5,The surface appears less pronounced with a more uniform, satin-like finish towards the center of the plate, while the edges show more distinct striation marks.

  This surface topography is reflected in the roughness measurements, which show a significant reduction in roughness values compared to the unmachined baselines.

  - Profile P1 appear to has the lowest Ra values, measuring on average 0.25 µm in the chord-wise direction and an even finer 0.08 µm in the span-wise direction, resulting in average k_s of 1.04 µm. The magnified bubble labeled P1a shows the transition between the machining marks and the original texture near the leading edge, while P1b illustrates the span-wise uniform scartches finish at the mid-chord (between 0.5 and 0.6 x/c).
  - Profile P2 marginally rougher than P1. P2's average Ra values are 0.30 µm in the chord-wise direction and 0.10 µm in the span-wise direction, leading to an average k_s of 1.26 µm. The surface texture's uniformity is consistent across the profile, as shown by the similarity between the magnified bubbles at 0.25 x/c (P2a) and 0.6 x/c (P2b).

  This consistent anisotropy confirms that the finest surface texture is aligned perpendicular to the main flow in both profiles.

  Furthermore, their low maximum peak-to-valley heights (Rz) indicate a smooth and uniform surface. For both P1 and P2, the roughness-to-boundary layer thickness ratio (Rz/δ) is approximately 5.1e-3, 6.2e-3, respectively, near the leading edge. The roughness Reynolds number (Re_k) for these profiles is estimated to be around 15 and 18, which is well within the viscous sublayer for laminar boundary layer. This suggests that the refined surfaces of P1 and P2 are unlikely to significantly disrupt the boundary layer or induce premature transition. Moreover, for developed turbulent boundary layers near the trailing edge, these values remain comfortably much lower than the original profiles (Rz/δ $\approx$ 3e-4 with $k_s^+ < 1$), indicating a minimal impact on the flow (i.e., hydraulically smooth). The minimal values for Rpk and Rvk suggest a refined surface with fewer extreme peaks and valleys. The negative skewness (Rsk) values for these profiles indicate a plateau-honed-like surface, with the height distribution shifted below the mean line and a predominance of valleys.

- **P4 (Manual-hand drill):**

  This profile, intentionally roughened, exhibits a steep increase in roughness. Even with efforts to avoid texturing the leading edge, some scratches are visible close to it, and unlike the uniform textures on P1 and P2, these scratches are not even in size. As shown in P4a close to the leading edge.

  The roughness measurements confirm that P4 has a highly anisotropic surface texture dominated by deep, directional grooves that run predominantly in the main flow direction (chord-wise). The average Ra is significantly higher than all other profiles, particularly in the span-wise direction, where it reaches an average of 2.3 µm. This is mirrored by the maximum peak-to-valley height (Rz) which soars to over 17 µm in the span-wise direction.

The roughness parameters for P4 highlight a different type of surface topology, one defined by its high degree of non-uniformity due to the manual texturing process. A considerable variation in both Ra and Rz across the profile.

- The left side of the profile (locations 'a' and 'b') exhibits significantly higher roughness compared to the right side locations 'c' and 'd'. For instance, the chord-wise Ra at location 'a' is 0.95 µm, while at location 'c' it is only 0.41 µm. This disparity is even more pronounced in the span-wise direction, where the Ra at 'a' is 2.91 µm, compared to 1.77 µm at 'c'. The overall average k_s for P4 is approximately 9.23 µm, indicating a very rough surface.
- The non-uniformity is further confirmed by the Rz. At location 'a', the span-wise Rz is a staggering 20.37 µm, whereas the lowest span-wise Rz is 13.454 µm at location 'c'.

When comparing the roughness to the boundary layer thickness, these variations become even more critical for the aerodynamic analysis. Considring the captured high roughness in the span-wise direction the roughness at location 'a' results in a (Rz/δ) ratio of 0.081. In contrast, the lower roughness at location 'c' the same span-wise yields a ratio of 0.054. The average values of span-wise and chord-wise roughness resulting in Rz/δ of 0.051 at location'a' and 0.033 at location 'c'. The roughness Reynolds number (Re_k) close to the leading edge is approximately 132, indicating that could significantly disrupt the boundary layer and potentially trigger early transition (as exceeding the critical value of 120).

The values close to TE are still very small (Rz/$\delta \approx$ 1.88e-3 and $k_s^+ \approx 4.53$) almost on the margins of the transitionally rough regime and unlikely to impact the developed turbulent boundary layer.

The roughness parameters highlight a surface dominated by deep, open valleys, as confirmed by the highly negative skewness values in the span-wise direction (down to -0.830), and the very high Reduced Valley Depth (Rvk) values (reaching up to 5.677 µm). In contrast, the high Reduced Peak Height (Rpk) values in the chord-wise direction (up to 1.786 µm) suggest a surface with sharp, protruding peaks that can locally disrupt the flow.

This pronounced roughness and its directional dependency are key features of this profiles, as they provide a clear contrast to the smooth, refined profiles and will be critical for evaluating the influence of surface texture on the flow field.

3.5 3D surface texture characterization

While the two-dimensional roughness measurements (2D) provided valuable insights into the profiles' surface texture, a more comprehensive three-dimensional (3D) analysis was performed to better understand the complex flow behavior observed during the wind tunnel experiments. The 3D surface measurements were carried out at the Institute of Fluid Mechanics (ISM) at TU Dresden, utilizing a non-contact optical measurement system.

An Alicona optical microscope with a 20x magnification, vertical resolution of 0.27 µm and lateral resolution 2.93 µm, the measurements for the five profiles were carried out at for main locations contains four sub-locations each 1.0233×1.0233 mm.

The 3D analysis focused on key areal roughness parameters, including the (Sa), and the maximum peak-to-valley height (Sz), etc. These parameters are the 3D equivalents of the 2D roughness parameters presented earlier.

Profiles P1, P2, P3, and P5 were found to exhibit low surface roughness values within a remarkably narrow numerical range. The 3D arithmetic mean heights (Sa) were recorded between 0.36 µm for P2 and 0.42 µm for P5, representing a marginal variation of 0.07 µm. Conversely, the 2D arithmetic mean roughness (Ra) exhibited a significantly broader distribution, with values ranging from 0.17 µm for P1 to 0.54 µm for P3. This difference of 0.37 µm highlights the inherent

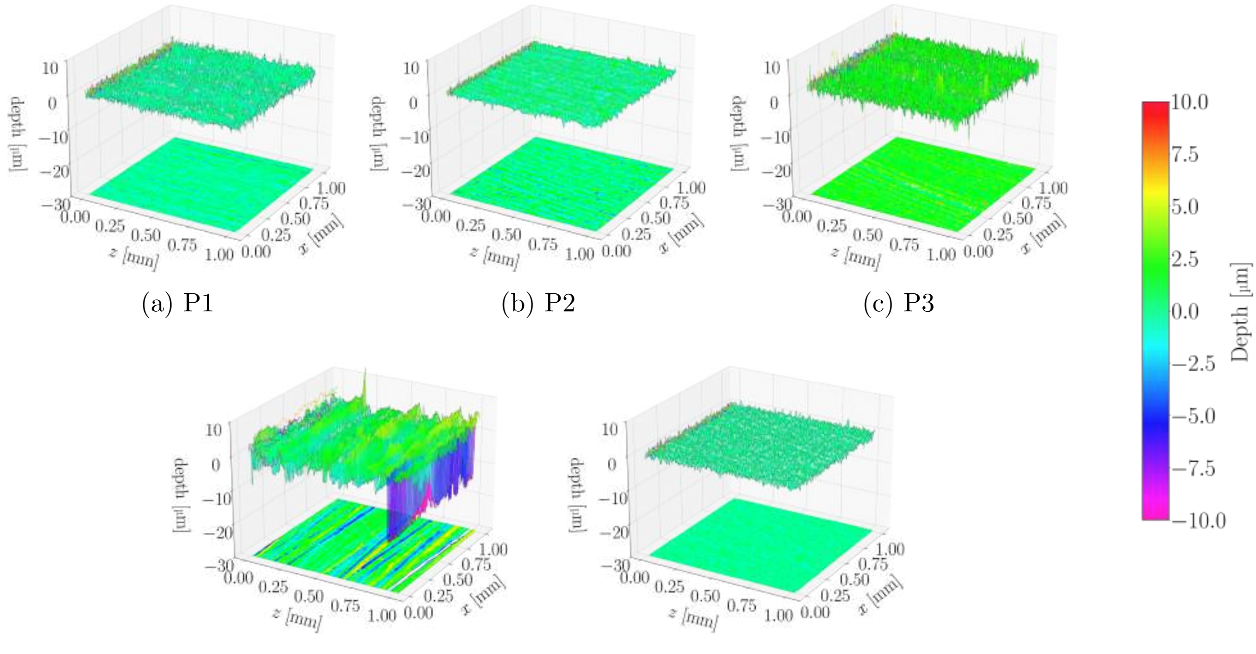

(a) P1 (b) P2 (c) P3

(d) P4 (e) P5

Figure 3.6: 3D surface texture measurements of all profiles at location ‘a’

limitations of 2D roughness quantification in representing global surface topography. The sensitivity of 2D roughness to specific measurement locations is demonstrated, even when random and repeated sampling and multiple data points are utilised.

A significant deviation from the baseline is identified in the coarse regime of Profile P4. A highly rugged surface morphology is exhibited by this profile, distinguishing it from the more uniform textures of the other test cases. The overall average Sa is recorded as 1.77 µm, which represents an approximate fourfold increase in surface height compared to the alternative profiles. Despite the numerical differences between the Ra and Sa parameters, the relative ranking of the profiles remains consistent. Profile P4 is identified as the roughest, followed by a cluster consisting of P2, P1, P3, and P5, all of which are characterised as smooth with values below 0.45 µm.

Near the trailing edge, where the boundary layer is significantly thickened, the flow is observed to be less sensitive to surface textures. This is evidenced by the low S_z/δ ratios, which range between 1e-3 for P2 and 5e-3 for P4, suggesting the roughness remains largely within the hydraulically smooth regime. Conversely, the leading edge regions are characterised by much thinner boundary layers, rendering them more susceptible to roughness variations.

In these sensitive leading edge regions, the distinction between 2D and 3D measurements becomes critical for the accurate prediction of transition. The 3D areal measurements provide a more comprehensive account of the peak distributions that are likely to protrude through the thin viscous sublayer and trigger bypass transition. Therefore, the increased sensitivity at the leading edge necessitates the more robust 3D characterisation provided in this study. The average roughness values for all profiles at the leading edge locations ‘a’ and ‘c’ are summarised in Table 3.7. Also, Figures 3.6 and 3.7 illustrate the 3D surface texture measurements for all profiles at locations ‘a’ and ‘c’, respectively. The complete dataset for each profile is available in Appendix B.

Considering the Sz values at the leading edge, Profiles P1, P2, P3, and P5 exhibit remarkably similar characteristics. Their average Sz values range narrowly from 7.04 µm for P2 to 10.20 µm for P1, resulting in Sa/δ ratios of approximately 0.028 to 0.044. Regardless the applied surface texture, these profiles maintain a consistent surface with the 3D measurements, and confirming the similarity indicated by Sa results.

The distinguishing feature of this study is the marked disparity between P4 and the remaining group. Roughness peak-to-valley height (Sz) analysis of P4 noted a critical variation in the Sz of the surface on P4 between the left and right leading edges, similar to the 2D roughness results.

Location ‘a’ (Left LE) exhibited an average Sz of 31.01 µm. However, Location ‘c’ (Right LE)

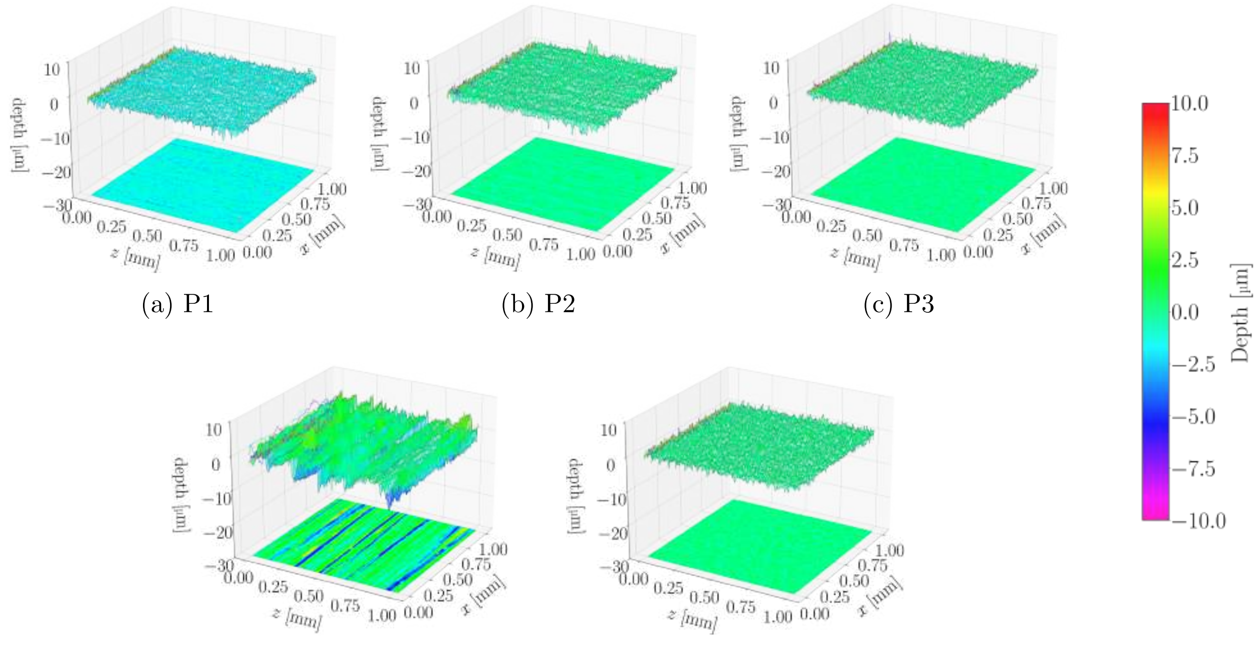

(a) P1 (b) P2 (c) P3

(d) P4 (e) P5

Figure 3.7: 3D surface texture measurements of all profiles at location ‘c’

Table 3.7: 3D profiles’ average roughness values at LE (locations ‘a’ and ‘c’)

	Unit	P1	P2	P3	P4	P5
Sa	[µm]	0.3687	0.3528	0.3709	1.9409	0.4129
Sq	[µm]	0.4817	0.4536	0.4716	2.6200	0.5376
Sz	[µm]	10.200	7.0365	7.6651	25.378	10.997
Ssk		0.3716	0.0678	0.0668	-0.5586	1.3238
Sk	[µm]	1.1625	1.1221	1.2007	5.6704	1.3166
Spk	[µm]	0.4665	0.4751	0.4716	2.4655	0.5745
Svk	[µm]	0.5565	0.4909	0.4799	3.7175	0.5439

exhibited an average Sz of 19.75 µm. This discrepancy indicates a non-uniform application of the manual polishing force or abrasive contact time between the opposing sides of the aerofoil.

To contextulise these roughness values within aerodynamic boundary layer physics, Sz/δ values for P4 at location ‘a’ ≈ 0.124, while at location ‘c’ ≈ 0.079. Ideally, for a surface to be considered hydraulically smooth, roughness elements should remain well submerged within the viscous sub-layer. A ratio of Sz/$\delta \approx 0.124$ near the leading edge (Location ‘a’) is significant. In high-speed flows and roughness elements of this size relative to the boundary layer thickness, potentially causing premature transition from laminar to turbulent flow or increasing skin friction drag.

Chapter 4

Development of measurement methods

The rapid progression in CFD and numerical methods has facilitated highly detailed predictions of complex transonic flows. However, this advancement has underscored the necessity for equivalent improvements in experimental measurements to validate these simulations with comparable accuracy. To achieve this, techniques that can provide a comprehensive, instantaneous, and non-intrusive depiction of whole-field flow properties, such as Mach numbers and shear forces, are essential.

Optical flow-visualization techniques and laser-based methods, such as LDA, are ideal for this purpose. They can be used to ascertain flow features both on and around blades and are typically categorized by the type of information provided: surface flow (e.g., oil flow), surface properties (e.g., pressure-sensitive paint), and off-surface features (e.g., schlieren and shadowgraph) [127]. While LDA provides highly accurate quantitative data at a single point.

This chapter focuses on the enhancement of the post-processing of two key flow visualization methods: schlieren and oil flow visualization. Recent advancements in computer vision and signal processing are leveraged to significantly elevate image analysis capabilities beyond the limitations of traditional techniques. This allows for the direct observation of aerodynamic parameters without intruding on the flow, thereby providing a better understanding of the studied phenomena. The insights gained from this analysis, especially regarding boundary layer features and their fluid mechanics properties, are further improved by using an optimization function to reduce the uncertainties discussed in previous sections.

This chapter is structured as follows:

- Section 4.1: A Proper Orthogonal Decomposition (POD) analysis of high-speed schlieren images is presented to gain a deeper understanding of how the altered shock structure affects flow dynamics and to identify potential sources of shock unsteadiness.

- Section 4.2: An enhanced algorithm for the line-scanning technique is introduced to process noisy and poor-quality schlieren images. These improvements are designed to boost shock localization accuracy and to precisely determine shock oscillation frequencies using wavelet analysis to study the frequency-time dependency.

- Section 4.3: A novel method is proposed to correct the perspective and flatten the image of a curved suction side for a constant-chord aerofoil. This technique utilises a single camera view to analyse oil flow visualisation while preserving the perspective distortion inherent in the original captured image for accurate spatial mapping.

- Section 4.4: An overview of the estimation of boundary layer features from the processed data is provided.

4.1 High-speed schlieren POD analysis

POD is a highly effective tool for model reduction and the extraction of coherent structures from large datasets, originally proposed by Lumley [128] for identify and extract coherent turbulent flow structures.

POD has been successfully applied to time-resolved schlieren images in high-speed aerodynamics. This application facilitates the decomposition of complex density fluctuation fields into a basis of orthogonal spatial eigenfunctions (modes) and corresponding time-dependent coefficients, allowing direct correlation with underlying flow physics. Typically, large-scale coherent structures give rise to extensive regions of spatially correlated density fluctuations, which are effectively captured by the most energetic POD modes.

In a study by Berry [129], snapshot POD was applied to schlieren images to examine a multi-stream single expansion ramp nozzle. This analysis aimed to extract spatial eigenfunctions and time-dependent coefficients associated with flow structures. Similarly, GUO [130] utilized schlieren POD to quantify small-scale pulsations and large-scale fluctuations in the context of SBLI. Their investigation focused on SBLI physical properties in a compression corner subjected to an oblique shock wave at a Mach number of 2.0.

Building upon this framework, the objective is to facilitate further investigations into how altered shock structures affect flow dynamics and to isolate the eigenmodes responsible for distinct spectral peaks observed in shock-tracking data.

A critical challenge in this context is the massive size of the input data, often comprising tens of thousands of high-resolution schlieren snapshots. This scale necessitates a highly memory-efficient implementation of the POD algorithm.

The primary theoretical principle employed is the Snapshot POD method. Given a sequence of N instantaneous schlieren snapshots, each discretized into $P = H_t \times W_t$ pixels, Each snapshot $\mathbf{x}_n$ (a flattened image) is a column vector of size $P \times 1$. The mean image $\overline{\mathbf{x}}$ is the average of all snapshots:

$$\overline{\mathbf{x}} = \frac{1}{N} \sum_{i=n}^{N} \mathbf{x}_n \tag{4.1}$$

The data matrix $\mathbf{X}$ is $P \times N$:

$$\mathbf{X} = [\mathbf{x}_1, \mathbf{x}_2, \ldots, \mathbf{x}_N] \tag{4.2}$$

The fluctuating data matrix $\mathbf{X}_f$ is constructed by subtracting the mean from each snapshot:

$$\mathbf{X}_f = [\mathbf{x}_1 - \overline{\mathbf{x}}, \mathbf{x}_2 - \overline{\mathbf{x}}, \ldots, \mathbf{x}_N - \overline{\mathbf{x}}] \tag{4.3}$$

When $N \ll P$ (many more pixels than snapshots, which is typical for high-resolution imaging data), the Snapshot POD method is computationally advantageous. It focuses on the temporal covariance matrix $\mathbf{R}$:

$$\mathbf{R} = \mathbf{X}_f^T \left(\frac{\partial \rho}{\partial x}, \tau \right) \mathbf{X}_f \left(\frac{\partial \rho}{\partial x}, \tau \right) \tag{4.4}$$

where $\frac{\partial \rho}{\partial x}$ represents the density gradient and τ represents time. For a typical high-speed schlieren dataset with $N = 10,000$ snapshots of size $H_t = 963$ and $W_t = 1088$ pixels, the flactuating data matrix $\mathbf{X}_f$ would be of size $1,047,744 \times 20,000 \approx 10^9$ element (requires $\approx$ 80 GB of memory for double "8-bytes" or 160 GB for decimal "16-bytes") makes loading such a matrix into memory is impractical. However, the temporal covariance matrix $\mathbf{R}$ is only of size $N \times N$ (e.g., $20,000 \times 20,000 = 4 \times 10^8$ elements, requiring approximately 3.2 GB for double precision), which is much more manageable.

In order to compute $\mathbf{R}$ optimaly without loading the entire $\mathbf{X}_f$ into memory, the acquisition of data is performed in discrete segments to manage computational memory effectively. A mean image is subtracted from each snapshot to obtain the fluctuating component. These snapshots are subsequently organised into temporary data blocks, $\mathbf{A}$ and $\mathbf{B}$. Each block is structured with b snapshots as rows and P pixels as columns. The resulting matrix shape is defined as $b \times P$. Every row is constituted by a flattened and mean-subtracted image.

The local temporal covariance is determined through a specific matrix operation. Block $\mathbf{A}$ is multiplied by the transpose of block $\mathbf{B}$. This relationship is expressed as $\mathbf{R}_{\text{block}} = \mathbf{A} \cdot \mathbf{B}^T$. The operation involves a $(b \times P)$ matrix and a $(P \times b)$ matrix. A result of size $(b \times b)$ is produced. Each entry represents the dot product between two individual images. The integrity of the temporal covariance matrix $\mathbf{R}$ is maintained through this block-wise accumulation. In this manner, the complete temporal covariance matrix is constructed without the need to load the entire dataset into memory at once. For instance, with $N = 10,000$ snapshots and a block size of $b = 500$, the process would require 20 iterations to fully assemble $\mathbf{R}$ and would only need to store two blocks of size $500 \times 1,047,744$ in memory, which is approximately 4 GB for double precision.

The eigenvalues are obtained from the equation:

$$\mathbf{RV} = \mathbf{V\Lambda} \tag{4.5}$$

Where $\mathbf{V}$ contains the eigenvectors, $\mathbf{v}_{(n)}$, which are the temporal coefficients (or temporal modes) $N \times N$:

$$\mathbf{V} = [\mathbf{v}_1(\tau_n), \mathbf{v}_2(\tau_n), ..., \mathbf{v}_N(\tau_n)] \tag{4.6}$$

The diagonal matrix $\mathbf{\Lambda}$ contains the eigenvalues, λ_n. signifies the nth eigenvalue, corresponding to the energy contained within the nth eigenmode, and N denotes the index of schlieren snapshots at time τ.

The spatial POD modes, $\mathbf{\Phi}$ with a single spacial mode of ϕ_n, are then expressed as linear combinations of the fluctuating snapshots:

$$\phi_n = \frac{1}{\sqrt{\lambda_n}} \sum_{j=1}^{N} (\mathbf{x}(\tau_j) - \overline{\mathbf{x}}) \mathbf{v}_n(\tau_j) \tag{4.7}$$

Where ϕ_n is a column vector of size $P \times 1$, representing the nth spatial mode. As massive datasets are involved, the computation of spatial modes is also performed for only selected modes of interest, rather than all N modes. Mostly the first few 200 modes contain the majority of the flow energy (above 95% of the energy) and are of primary interest.

4.2 High-speed schlieren shock wave detection and tracking

Accurate prediction and control of shock-wave unsteadiness are critical for optimising aerodynamic performance and operational reliability. Shock unsteadiness usually monitored using Kulite pressure transducers due to their compact size and broad bandwidth [131, 132]. However, their application requires multiple sensors, increasing setup complexity and expense. Alternatives, such as unsteady pressure-sensitive paint (UPSP) and piezo foils [57, 133], offer two-dimensional pressure data. These methods are limited by intricate calibration requirements, low frequency response, and the potential for physical intrusion on thin turbomachinery profiles, thereby disturbing the boundary layer.

Recent advancements in computer vision, coupled with high-speed schlieren imaging, offer a distinct advantage over pressure sensors. This optical approach provides direct, non-intrusive observation of shock locations with high temporal and pixel-level spatial resolution. For shock tracking, computationally efficient methods such as the line-scanning technique are widely employed, particularly for normal shocks. Tracking is typically achieved by identifying the minimum light intensity (Darkest-spot) or the maximum absolute light intensity gradient (Max-Grad) within a pixel slice [62, 134–138].

However, these basic line-scanning methods are susceptible to failure in complex, noisy environments. They ignore the shock's history and struggle to distinguish the true shock from flow artefacts, such as the λ-foot structure created by side-wall interactions. Furthermore, they can misidentify thick shock fronts, leading to artificial high-frequency peaks in the tracked signal.

A robust enhancement to the line-scanning technique is developed. This method is effective even for noisy and poor-quality schlieren images, allowing for a more precise assessment of detection accuracy. The approach enables the detailed determination of shock oscillation frequencies and the characterization of complex shock unsteadiness [139].

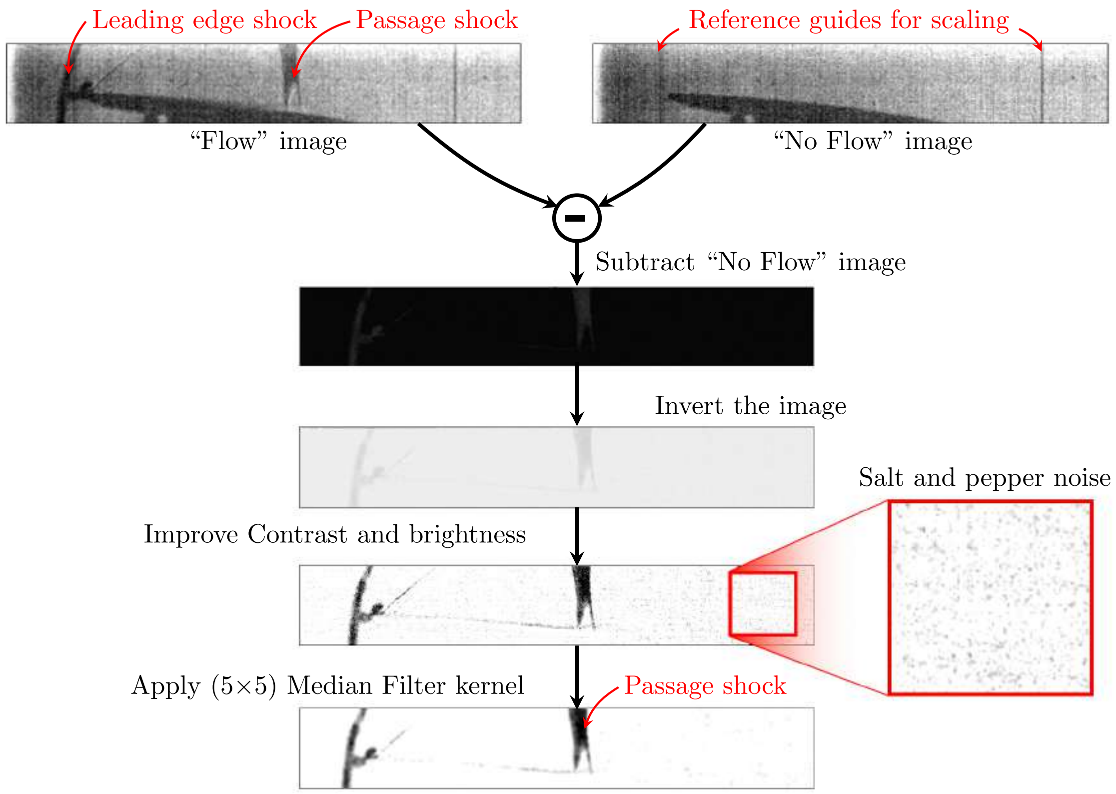

Figure 4.1: Pre-cleaning and binarization for captured image at high shutter speed (15 kHz)

The analysis of unsteady shock motion is conducted using a dedicated Python script. This script leverages the OpenCV image processing library [140]. The primary function is to identify, track, and analyse a single shock wave with high accuracy. The method is divided into three main operational phases:

- Generating the slice list.
- Detecting and tracking the shock.
- Filtering the resulting signal.

4.2.1 Image processing

Generating the slice list

The initial phase involves rigorous pre-cleaning. This process aligns and subtracts the background image (No-Flow) from the flow images. High-speed images often contain salt-and-pepper noise due to high gain. This noise is effectively mitigated using a 2D median filter before further processing is conducted as shown in Figure 4.1.

Accurate shock tracking relies on the creation of a slice list. This list converts a time-series of 2D images into a 1D signal for computational efficiency. When a background image is unavailable, an average image is generated from the flow set. To maintain contrast, the shock region in this average image is masked and reconstructed using image inpainting [141]. Then the subtraction process is done.

The dynamic behaviour of shocks is challenging while handling large datasets of high-speed schlieren images. Relying on a single pixel row for shock tracking can fail when low contrast occurs. This is particularly true when shock velocity exceeds the camera's shutter speed or when density gradients are weak. While vertical averaging of additional pixel rows can enhance contrast, it is not always a viable solution.

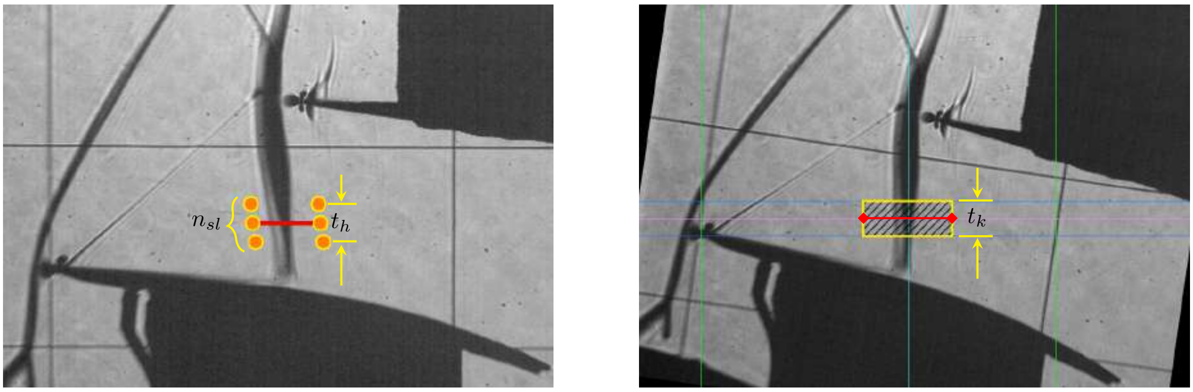

(a) Shock angle tracking parameters (b) Rotated image with estimated shock angle

Figure 4.2: Pre-rotation and slice list parameters

Here proper image alignment is essential, especially for non-normal shocks. A statistical approach is used to estimate the shock inclination angle, by selecting a set of random samples (n_{rs}) of schlieren images. The shock is tracked across multiple vertical slices (n_{sl}, where $n_{sl} > 5$) using the Integral method discribed in Section 4.2.1. The Random Sample Consensus (RANSAC) algorithm [142].

After fitting the line, its accuracy is evaluated for each image using linear regression relations to estimate point scatter, identify outliers, and determine the confidence (ζ_j) of the estimated line at each slice j [143, 144]. The confidence interval is calculated as:

$$\zeta_j = t_{n_{sl}-2;\alpha/2}\sigma_{X^*} \tag{4.8}$$

where

$$\sigma_{X_j^*} = \sigma_{er}\sqrt{\frac{1}{n_{sl}} + \frac{\left(Y_j^* - \overline{Y}\right)^2}{\sum\left(Y_j - \overline{Y}\right)^2}} \tag{4.9}$$

and $t_{n_{sl}-2;\alpha/2}$ is the critical value from the t-distribution for a confidence level $(1-\alpha)$, Y_j represents the individual slice y-locations, and Y_j^* is the y-location on the fitted line. Since Y is the dependent variable, each slice location Y_j coincides with its corresponding fitted value Y_j^*. $\overline{Y}$ is the mean y-location of the slices, and σ_{er} is the standard error.

From the entire set of images, the average shock angle can be estimated using either an arithmetic average ($\overline{m}$) or the average is a weighted by the standard deviation of the slopes ($\overline{m_w}$). For each image, the slope's standard deviation ($\{\sigma_m\}_n$) is calculated as:

$$\{\sigma_m\}_n = \frac{\sigma_e}{\sqrt{\sum\left(Y_j - \overline{Y}\right)^2}} \tag{4.10}$$

When the shock perfectly aligns with the fitted line, $\{\sigma_m\}_n$ may equal zero. In this case, the weighted average slope is calculated using a hybrid approach:

$$\begin{aligned} \overline{m_1} &= \frac{\sum_n^{N-r} \frac{m_n}{\{\sigma_m\}_n^2}}{\sum_n^{N-r} \frac{1}{\{\sigma_m\}_n^2}} \forall\ \{\sigma_m\}_n > 0, \\ \overline{m_2} &= \sum_n^r m_n \forall\ \{\sigma_m\}_n = 0 \end{aligned} \tag{4.11}$$

where r is the number of images when $\{\sigma_m\}_n = 0$. Finally, the overall weighted average slope is calculated as:

$$\overline{m_w} = \frac{\left((N-r)\,\overline{m_1} + r\overline{m_2}\right)}{N} \tag{4.12}$$

This robustly estimates the mean shock slope (m_w), ensuring the shock front is perpendicular to the slice, which improves vertical averaging.

By estimating average shock angle each image is rotated and then cropped to the slice thickness (t_k) for vertical averaging as indicated in Figure 4.2. For each image the pixel rows are averaged into a single-row slice. The single slice is then appended to the previous slice until a list of processed image slices is completed.

This approach ensures that the total memory consumption remains proportional to the size of the slice list, not the entire image dataset. Furthermore, the algorithm is implemented using well-optimised libraries like OpenCV and NumPy, which are capable of leveraging parallel processing. This design makes the method suitable for large datasets by ensuring high computational efficiency. The slice list generation algorithm is summarized in Algorithm 1.

Integral shock tracking algorithm

The core method is the Integral Shock Tracking Algorithm. It determines the shock location (X) by identifying local minima (valleys) in the light intensity of each pixel slice as shown in Figure 4.3. The valley with the largest area ($A_{\max}$) is identified as the true shock location. The algorithm distinguishes between two conditions. Condition 1 (merged phase) is solved by finding the midpoint of the largest valley after adjusting by the root mean square (RMS) intensity of the valley.

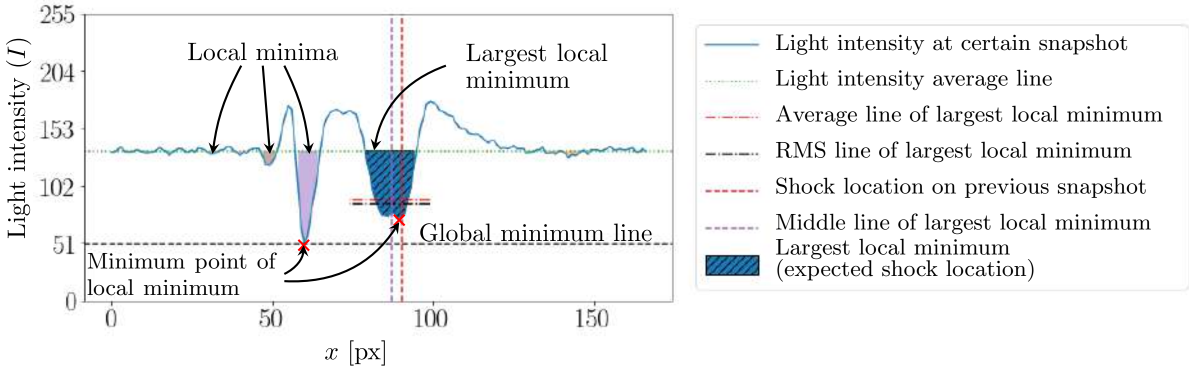

Figure 4.3: Snapshot slice features and shock detection

Condition 2 (transitional phase shown in Figure 4.4) involves multiple sub-valleys. In this instance, the sub-valley closest to the shock's historical location is selected. The uncertainty ratio (η) is calculated to quantify detection confidence. Results are deemed acceptable only when η remains below 15%. The slice list generation algorithm is summarized in Algorithm 2.

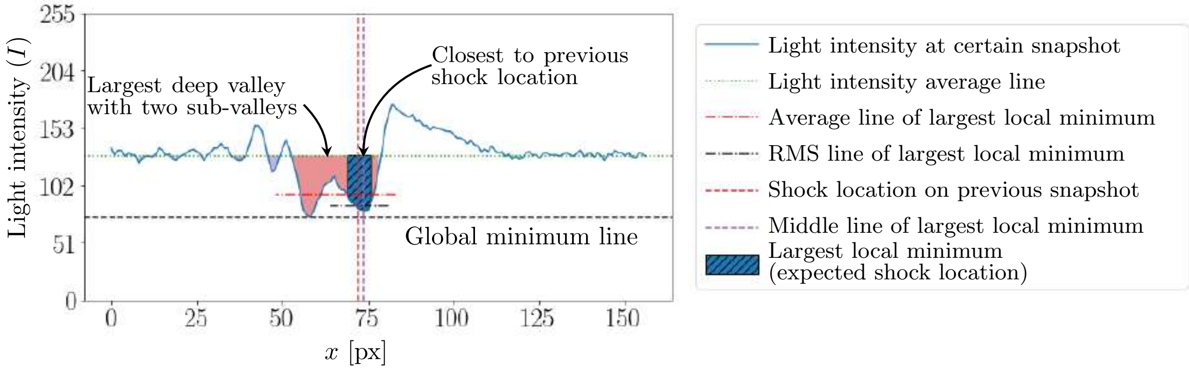

Figure 4.4: Multi sub-valleys under the largest, with uncertainty

The uncertainty in determining the shock location within this algorithm stems from potential inaccuracies in pinpointing the shock wave's position. It is essential to note that an uncertain shock location does not necessarily imply the identified location is incorrect.

The algorithm is designed to track a single shock wave. A primary source of inaccuracy is the presence of other shock waves with similar properties, which can cause the algorithm to become confused. Based on this, the main contributors to these inaccuracies include valleys of nearly equal size (e.g. $A_{\max -1}/A_{\max} \geq 0.6$), variations in sub-valley selection compared to the largest one, the presence of nearly identical sub-valleys as in Figure 4.4, and the initial pixel slice containing sub-valleys without a recorded shock location history and in this case the sub-valley with the largest area is chosen. In such instances, the algorithm may yield uncertain detections of the shock wave.

The algorithm complexity compared to other exiting method is discriped in the following Table 4.1 where x is the slice width, K_r is the gradient kernel whish is usualy 3×3 matrix.

Table 4.1: Algorithms performance

Method	Computational complexity
Max-Grad	$O(K_r.x.N)$
Darkest-spot	$O(x.N)$
Integral	$O(x^2.N)$

Finally, the generated shock position signal is refined to ensure reliability two filters can be employed. A Median filter is first applied to smooth the signal and preserve sharp transitions. A subsequent Wiener filter is employed to minimise the mean square error, further enhancing accuracy.

4.2.2 Sensitivity analysis

To test and optimise the algorithm's operational parameters, a data captured at five different sampling rates, ranging from 2 kHz to 15 kHz are used. The analysis focused on tracking the highly unsteady passage shock. This shock is significantly influenced by boundary-layer interaction. All subsequent analysis used a consistent tracking accuracy of 0.13 mm/px.

Schlieren imaging of the test setup is shown in Figure 4.5. The image capture duration consistently set at $\mathcal{T}_\tau = 5$ s, producing $N = 10,000$ to $50,000$ images. For the highest sampling rate of 15 kHz, the duration is slightly reduced to $\mathcal{T}_\tau = 4.5$ s, generating $N = 67,500$ images. A detailed summary of the captured images is provided in the Table 4.2.

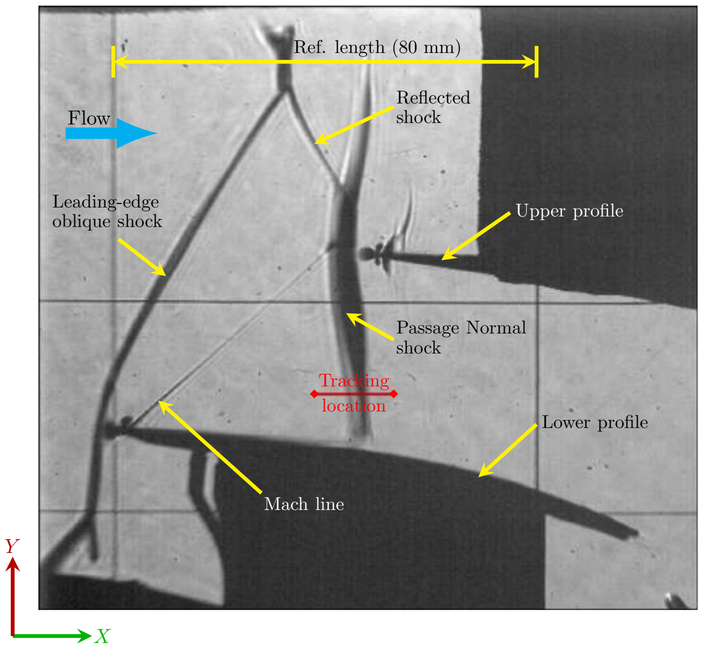

Figure 4.5: Test case 1 shock configuration, and captured domain at a frame rate of 2 kHz

Image cleaning proved essential for improving accuracy. Pre-cleaning significantly reduced the variance in estimated shock angles, leading to a narrower normal distribution (Figure 4.6). The tracking height (t_h) was identified as a critical parameter. Increasing t_h consistently reduced angle variance and improved accuracy. This occurs because a larger sample area helps mitigate local defects. The number of slices (n_{sl}) directly links to t_h. The arithmetic average remained largely

Table 4.2: Captured images' features

Sampling rate [kHz]	Exposure time [µs]	Resolution [px]	N [sample image]
2	495	960×880	10,000
3	328	960×592	15,000
6	161	960×296	30,000
10	95	832×204	50,000
15	61	832×136	67,500

unaffected by n_{sl} except at very low slice counts where this reduced data compromised the RANSAC algorithm's ability to identify the angle. Conversely n_{sl} significantly affected the weighted average angle (Figure 4.7). Stability improved markedly when n_{sl} was maintained at a ratio of above 60% of the tracking height.

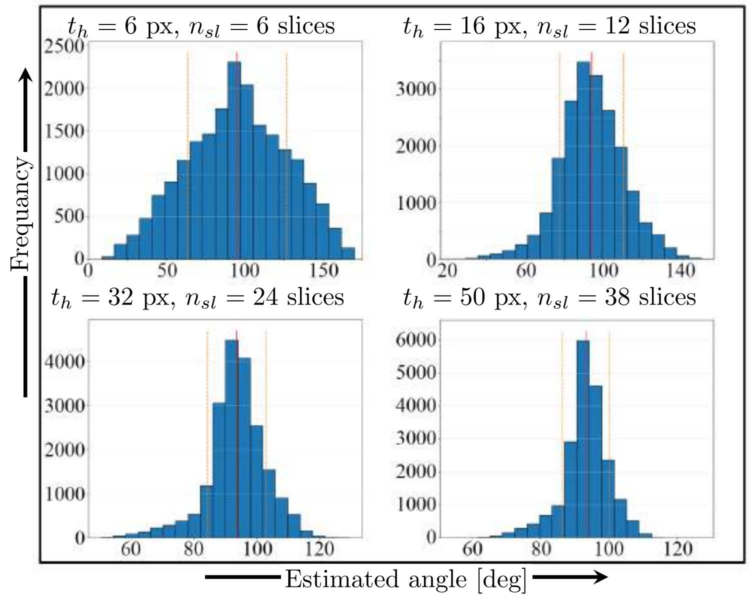

(a) Uncleaned images

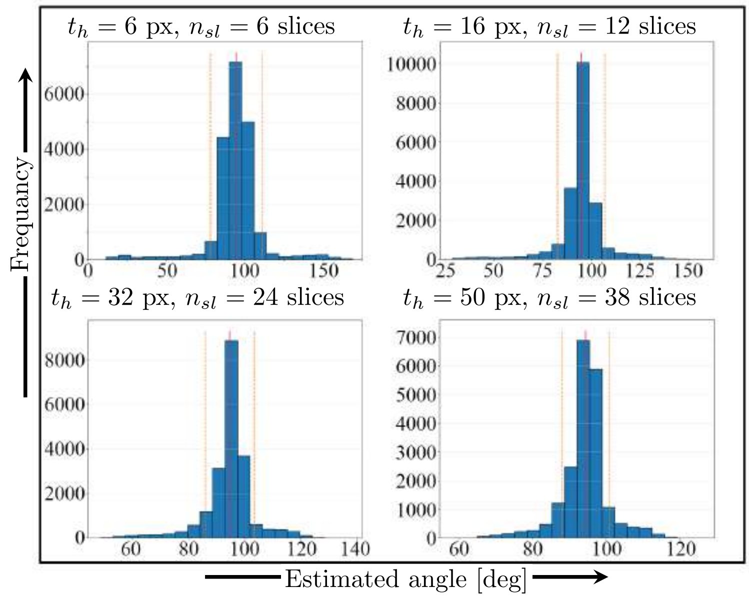

(b) Cleaned images

Figure 4.6: Histogram of all detected angles at sampling rate 15 kHz

The influence of sample size (n_{rs}) for angle estimation is shown in Figure 4.8. Accuracy notably decreased when n_{rs} fell below 30% of the total image set. This supported fundamental statistical

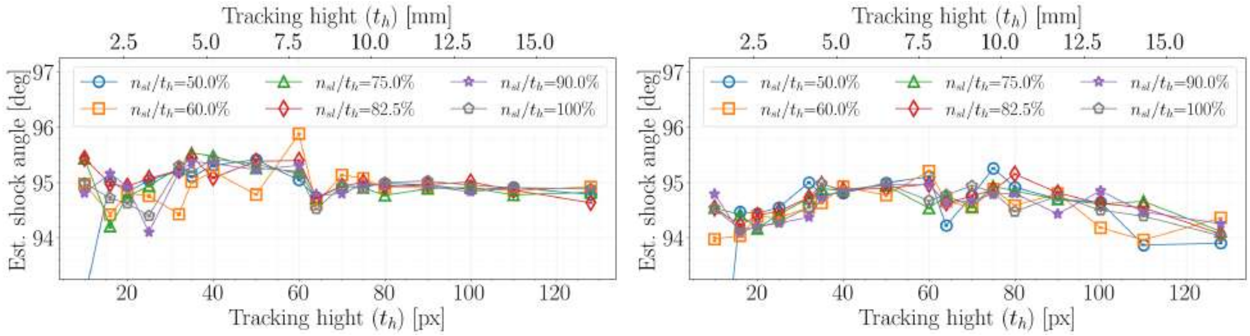

(a) Sampling rate of 2 kHz (b) Sampling rate of 3 kHz

Figure 4.7: The weighted average shock angle with varying number of slices (n_{sl}/t_h)

principles. The weighted average of the shock angle proved more robust than the arithmetic average. It is less sensitive to shock front curvature and varying t_h. Figure 4.9 shows that increasing the slice thickness (t_k) generally enhanced shock contrast. This contributed to lower tracking uncertainty and improved overall signal quality.

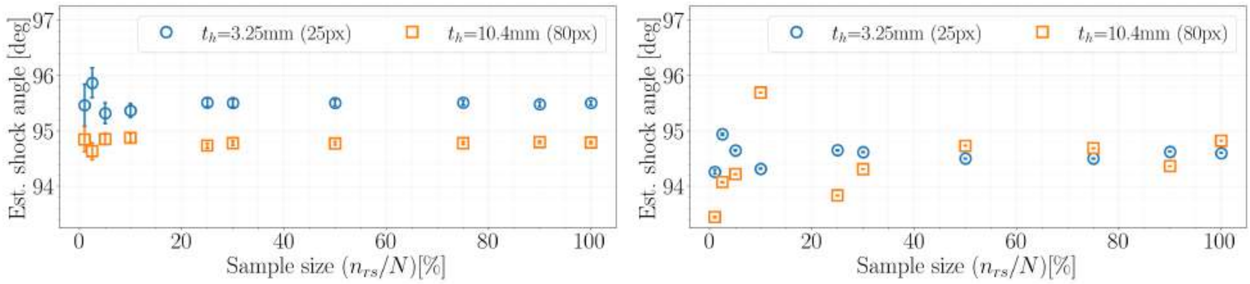

(a) Arithmetic Average (b) Weighted Average

Figure 4.8: The shock angle at sampling rate 10 kHz, with varying the sampled images (n_{rs}/N)

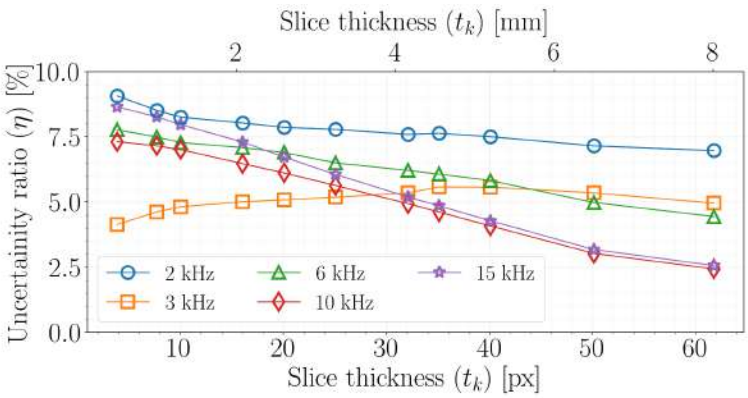

Figure 4.9: Slice thickness (t_k) effect on the tracking quality

4.2.3 Signal processing

After obtaining the shock displacement signal X_{shock}, the shock velocity signal is calculated (V_{shock}). A finite difference approach is employed to approximate the derivative [67]. The central difference scheme is used for interior points to maintain accuracy, while forward and backward difference schemes are used for the boundaries, The central difference formulation for the interior points is given by:

$$u_{shock,n} = \frac{X_{n+1} - X_{n-1}}{2\Delta\tau} \tag{4.13}$$

where X is the shock location (displacement) and $\Delta\tau$ is the time step. The time step $\Delta\tau$ is the inverse of the sampling frequency $f : \Delta\tau = 1/f$.

The Power Spectral Density (PSD) of both the shock displacement (X_{shock}) and velocity (V_{shock}) is then calculated. The PSD is estimated primarily using the periodogram method. This involves computing the squared magnitude of the Discrete Fourier Transform (DFT) of the entire signal and then normalising it. No windowing, overlap, or segmentation is applied in this process.

The DFT of the shock location signal, $X_{shock} = [X_1, ..., X_n, ..., X_N]$ where X_n is the shock location at snapshot n, is defined as:

$$f_k = \mathrm{DFT}(X)_k = \sum_{n=0}^{N-1} X_n e^{-i2\pi kn/N} \tag{4.14}$$

where N is the total number of snapshots, k is the frequency index.

The PSD of the displacement, $G(f_k)$, is calculated by normalising the squared magnitude of the DFT. The frequency range is typically limited to the Nyquist frequency ($f/2$). Using the given variables, the unnormalised PSD can be expressed as:

$$G(f_k) = \frac{2\mathcal{T}_\tau}{N^2}|f_k|^2 \tag{4.15}$$

where $\mathcal{T}_\tau = N/f$ is the total acquisition time, The frequencies f are defined as $f = k/\mathcal{T}_\tau$ and where $k \in \{0, 1, ..., N/2\}$ for the one-sided spectrum. The PSD analysis provides crucial insight into the frequency content and dominant energetic modes of the shock unsteadiness.

To reduce the variance from the periodogram, the Welch method may be applied [145]. This method provides a better, more reliable representation of the existing signals. It achieves this by dividing the signal into overlapping segments and averaging their periodograms. A Bartlett-Hann window of size 512 is used. This window is applied with a 256-point overlap between successive segments. This process offers crucial insight into the frequency content and dominant energetic modes of the shock unsteadiness.

A fundamental step in spectral analysis is the establishment of the relationship between the integrated PSD and the signal's total power. For a mean-subtracted shock oscillation signal, which is commonly assumed to be Wide Sense Stationary (WSS) and possess an average value of zero, the following equality holds true, as per Parseval's Theorem [146]:

$$\int_{-\infty}^{\infty} G(f)df = \sigma^2 \tag{4.16}$$

where σ^2 represents the signal's variance (i.e., the total unsteady energy). The normalisation of $G(f)$ by σ^2 is paramount as it converts the spectrum into a probability density function, enabling the direct comparison of the distribution of unsteady energy irrespective of the absolute magnitude of the total power, which may vary significantly between experiments due to disparate flow conditions.

To facilitate a more informative comparison of the unsteady energy contribution across the entire frequency range, particularly in contexts where lower frequencies may naturally dominate the raw PSD plot (a characteristic often seen in turbulent fluctuations), an enhanced spectral weighting technique is habitually applied. The spectral power is pre-multiplied by the frequency, yielding the term $f \cdot G(f)$. This manipulation is essential to ensure that the resultant spectrum, when plotted against the logarithm of frequency, directly reflects the contribution of each frequency band to the total variance, σ^2. The peak of the $f \cdot G(f)$ curve, therefore, precisely indicates the frequency at which the maximum unsteady energy content resides. Consequently, for shock unsteadiness analysis, the dimensionless quantity ($f \cdot G(f)/\sigma^2$) is commonly used to normalized PSD [138, 147–149].

The potential for multiple shock motions to be physically linked must be rigorously assessed. This is performed using the coherence function, $\mathrm{Coh}(f_x, f_y)$, a statistical measure defined in the frequency domain. The coherence function is calculated from simultaneously recorded two signals either distinct shock waves, or different location of the same shock wave if susbicted it is not oscilating as one unite but rather some parts are behaving differently, denoted x and y. It is defined as:

$$\text{Coh}(f_x, f_y) = \frac{|G(f_x, f_y)|^2}{G(f_x) \cdot G(f_y)} \tag{4.17}$$

Here, $G(f_x, f_y)$ represents the cross-spectral density. The terms $G(f_x)$ and $G(f_y)$ are the PSDs of the individual signals.The coherence is a real-valued function. It is bounded between zero and one, $0 \leq \text{Coh}(f_x, f_y) \leq 1$ [150]. The resultant value of $\text{Coh}(f_x, f_y)$ at any frequency f directly quantifies the degree of linear correlation between the two fluctuating signals f_x and f_y. If the coherence is close to one, it signifies a strong, coherent coupling between the two signals at that frequency. Conversely, a coherence value near zero indicates the motions are uncorrelated, suggesting they are driven by independent or highly non-linear mechanisms [58, 151].

Wavelet Morlet analysis

To analyse the temporal evolution of spectral signatures, the Continuous Wavelet Transform (CWT) is utilised. This transformative approach decomposes the fluctuating signal into highly localised wavelets. CWT enables detailed inspection in both the time and frequency domains, capturing transient features and varying spectral content. The method provides a powerful representation of time-frequency dynamics [152, 153].

The analysis employs complex Morlet wavelets, which are particularly well-suited for non-stationary signals. The Morlet wavelet is characterised by a complex sinusoidal function modulated by a Gaussian envelope (see Figure 4.10). This is implemented using an in-house wavelet tool [154], and is expressed as:

$$\psi(\sigma, f_w, \tau) = e^{2\pi i f_w \tau}.e^{(-\frac{\tau^2}{2\sigma})} \tag{4.18}$$

where f_w is the wavelet's centre frequency and t represents time. The standard deviation of the Gaussian envelope (σ) is determined by the non-dimensional number of cycles (n_c), as:

$$\sigma(f_w) = \frac{n_c}{2\pi f_w} \tag{4.19}$$

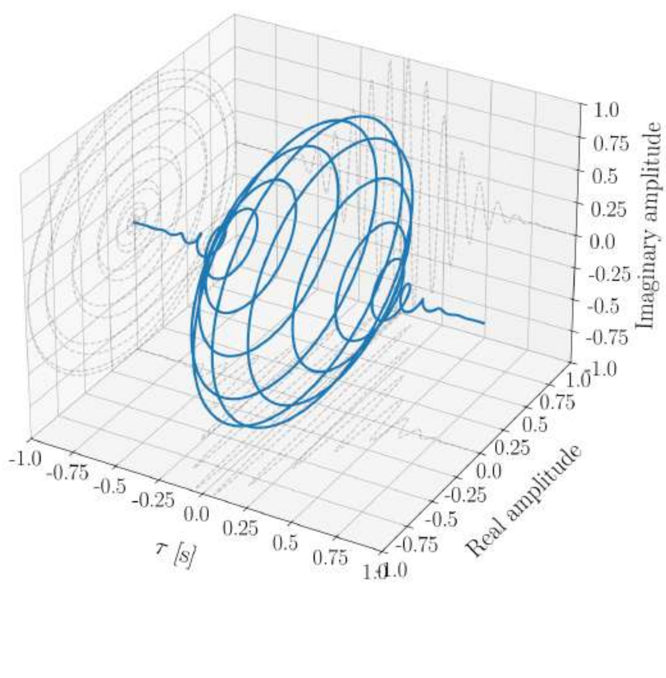

Figure 4.10: Morlet wavelet example

More insights about the wavelet analysis and implementation can be found in the Appendix C.

4.3 Reconstruction of profile surface from a single camera view

Surface flow visualization techniques are used to study the behavior of boundary layers in high-speed air flows close to the wall of a model or nozzle in a wind tunnel. Methods such temperature-sensitive paints (TSP), surface pressure using pressure-sensitive paint (PSP), or the streamlined pattern of the flow adjacent to the wall with an oil film provide valuable insights into the flow characteristics and can help optimize the design of aerodynamic systems for improved efficiency and safety [155]. Obtaining suitable optical access to the test section is crucial for achieving multi-dimensional flow behavior, for instance, when depicting shock structures and surface-flow responses to shock boundary/layer interactions. That requires specialized facility design and arrangement, which can be particularly challenging for test sections with complex geometries such as blade cascades and non-flat nozzle walls.

Side wind tunnel windows are a common and straightforward method for capturing surface flow; however, the camera perspective distorts the captured image. Image distortion can lead to unclear flow distribution (i.e., the lengths are scaled according to the distance from the camera and the lens focal lens) and inaccurate estimation of angles or areas of regions of interest. Although the recent development in computer vision made rectification of the distorted flat surface in images possible using perspective transformation algorithms [156], curved surface detection and reconstruction are still under development and mostly concerns rectification of curved document images [157, 158].

The current work proposes a method to flatten a prespactive image of a suction side of a constant chord airfoil using a single camera view while analyzing oil-flow visualization. To enhance the method's applicability, two different camera lenses were used, regardless of the camera location and distance from the window.

Setup and methodology

A diagram illustrating the camera setup is presented in Figure 4.11a. This system was employed to capture multiple images of oil flow across the surface of the lower profile, as detailed in Section 2.2, to investigate the effects of SBLI on surface flow topology. Two soft light boxes measuring 600×600 mm were used to enhance the lighting of the test section. The images were captured using the Canon EOS M50 camera with CANON lenses EF-M 15-45MM F/3.5-6.3 IS STM for highly distorted images as in Figure 4.11b and EF 100MM F/2.8 MACRO USM for images with lower distortion in Figure 4.11c.

The depicted perspective images are processed using Python and OpenCV library for image manipulation. The reconstruction process involves several steps as follows:

1- Preparing profile points Surface points are generated either from the CAD model depicted in Figure 4.12 or from profile coordinates, with the chord-line serving as the reference plane for the airfoil. The points are provided to the system, where the number of points represents the divisions of the curved surface. Theoretically, the more divisions, the cleaner and more accurate the reconstruction of the curved surface.

2- Camera calibration In this step, the user manually defines two vanishing points (V_z and V_y) by drawing them or specifying their coordinates. where V_z is defined by two lines passing by the leading and trailing edge along the profile span and represent the depth of the field. The accuracy of this step is crucial, as the focal length is estimated based on these given points, along with the third vanishing point. Using these vanishing points as a foundation, any point on the projection plane can be determined and mapped.

Figure 4.13 illustrates the pinhole model. This model employs two coordinate systems to describe the geometric relationship between the camera and the object in space. In the camera coordinate system, O_c is fixed at the camera's optical center or the center of projection. The image plane is perpendicular to the ray $\overrightarrow{O_cO_I}$, where O_I represents the projection of O_c onto the image

(a) Single camera setup

(b) lens EF-M 15-45MM F/3.5-6.3

(c) lens EF 100MM F/2.8

Figure 4.11: Acquiring image from single view camera

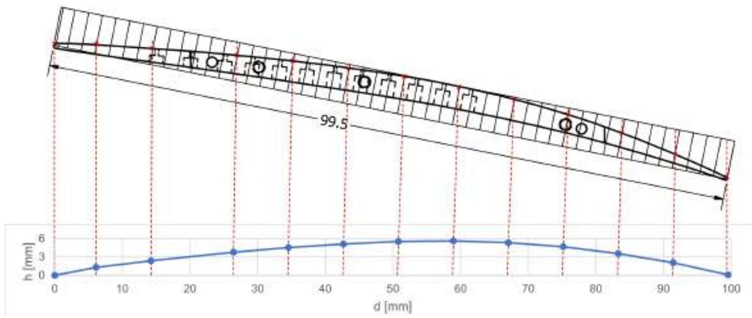

Figure 4.12: Preparing the profile coordinates

plane, and O_c is assumed to be the center of the image plane. The focal length (f_c) is defined as the distance between the center of projection and the projection plane ($||O_cO_I||$) and it is dependent on the camera focus which means it is not consent and changes from the image to image even with the same camera lens.

The focal length f_c is determined using the orthogonal triangle relation [156]:

$$f_c = ||O_cO_I|| = \sqrt{||XO_c||^2 - ||XO_I||^2} \tag{4.20}$$

This relationship, also noted in [159], is expressed as:

$$f_c = \sqrt{-(V_y - O_I) \cdot (V_z - O_I)} \tag{4.21}$$

While Equation 4.21 offers a simpler computation, it may introduce errors during implementation if the value beneath the square root is negative. By considering V'_x, V'_y and O'_I as the world coordinate of the vanishing points and the projection center:

$$V'_y = (v_{y_x}, v_{y_y}, f_c)$$

$$V'_z = (v_{z_x}, v_{z_y}, f_c)$$

$$O'_I = (o_{I_x}, o_{I_y}, 0)$$

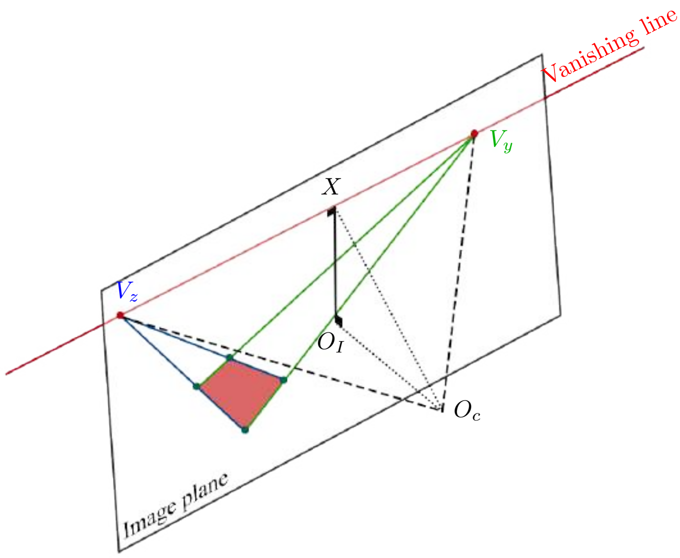

Figure 4.13: Focal length estimation from vanishing points

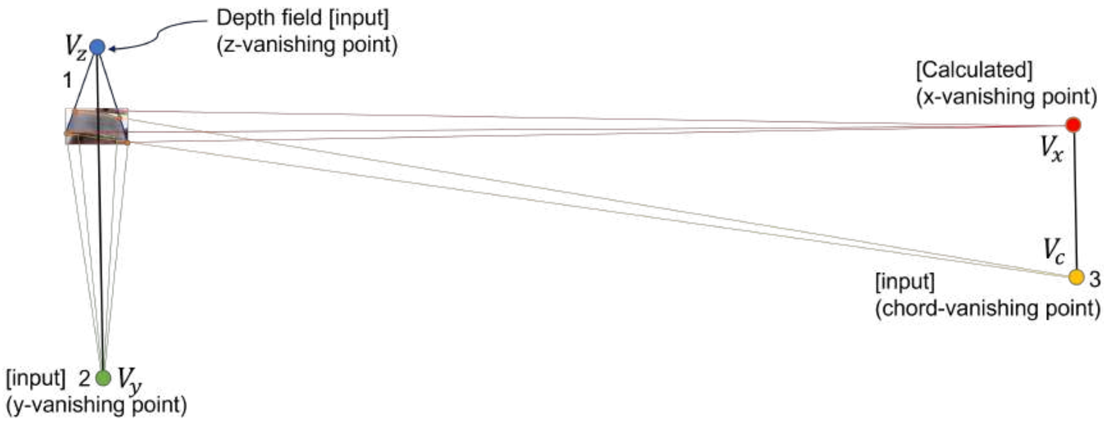

Figure 4.14: Finding 3 vanishing points

The world coordinate of the third vanishing point V_x can be:

$$V'_x = (V'_y - O'_I) \times (V'_z - O'_I) \tag{4.22}$$

And then:

$$V_x = \left(\frac{v'_{x_x}}{v'_{x_z}} f_c + o_{I_x}, \frac{v'_{x_y}}{v'_{x_z}} f_c + o_{I_y} \right) \tag{4.23}$$

The last manual input required is the profile chord line on both sides in the flow direction as shown in Figure 4.14. Typically, profiles are positioned with a certain angle of attack ($\alpha > 0$), indicating that the profile lies on a plane different from the main orthogonal planes with a vanishing point at V_c.

3- Mapping curve points from cartesian to homogeneous coordinates After acquiring the points in step 4.3 in metric domain, and the preparation of the homogeneous coordinates in step 4.3, mapping of these points into the domain take place. With the knowledge of the profile chord length l and the profile angle of attach θ the profile points can be mapped using cross-ratio method [160].

Figure 4.15 describes the implementation of the cross-ratio method to map the coordinates of profile points on the camera image. For any point on the profile B in homogeneous coordinates as illustrated in Figure 4.15a is projected on the chord line as B'. A and C are the leading and

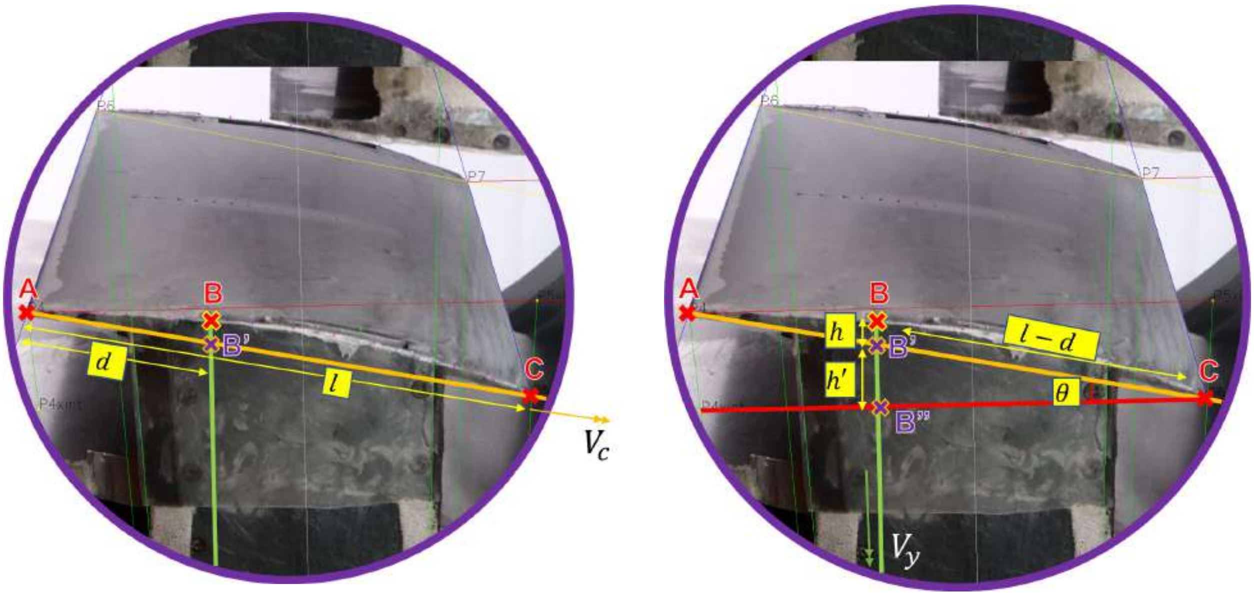

(a) (b)

Figure 4.15: Scaling real distances into image using cross-ratio theory

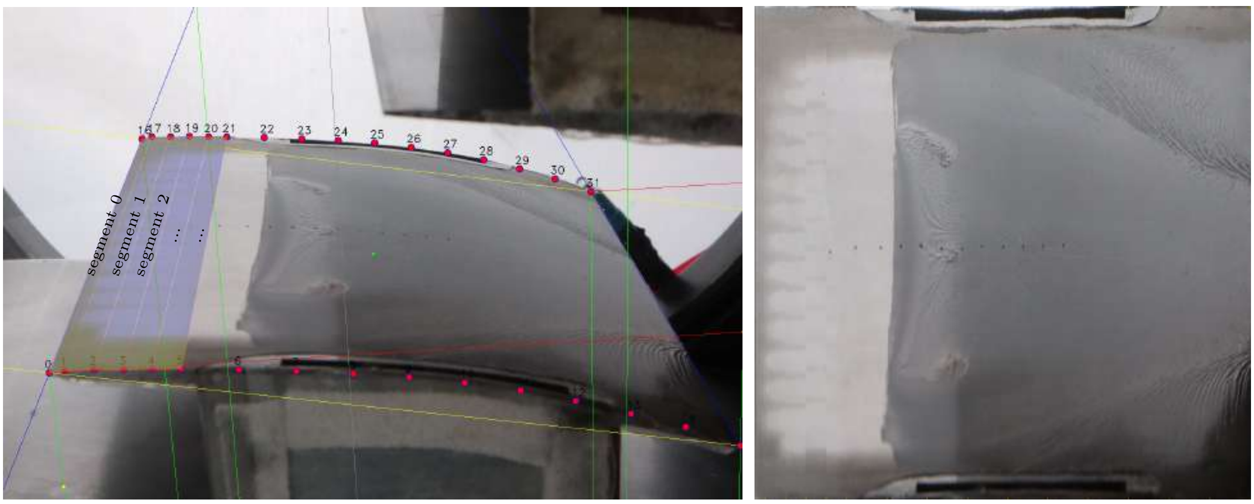

(a) Mapped profile points on camera image (b) Reconstructed image

Figure 4.16: Image reconstruction process

trailing edge points respectively, where $||AA'|| = ||CC'|| = 0$ and $||AC||$ is the chord length given as the intersection between V_c and V_z. The distance $||B'C||$ can be calculated as:

$$\frac{||AC||.(||B'C|| + ||CV_c||)}{||B'C||.||AV_C||} = \frac{l}{l-d} \tag{4.24}$$

and hence find B' coordinates on the image. B can be estimated from Figure 4.15b, where the metric distance $h' = (l-d)\sin\theta$ is the projection of the point B' on the chord line on the horizontal line at B" then the distance $||BB'||$ can be calculate as:

$$\frac{||B'V_y||.(||BB'|| + ||B'B"||)}{(||BB'|| + ||B'V_y||).||B'B"||} = \frac{h+h'}{h'} \tag{4.25}$$

This operation is repeated for each point of the metric coordinate on both sides of the profile as illustrated in Figure 4.16a.

4- Curved surface segmentation and transformation The process involves partitioning the mapped points within the image into groups, each comprising four points, as illustrated in

Figure 4.3. These groups serve as the basis for generating segmented planes along the V_z axis. For instance, points (0, 1, 17, 16) constitute segment 0, while points (1, 2, 18, 17) form the neighboring segment 1. Notably, both segments are linked along the line defined by points (1, 17). With n points delineating the profile, there exist $n-1$ segments in total.

Following segmentation, each plane undergoes flattening via the perspective transformation detailed in [161] before being scaled. The scaling of segment dimensions hinges on the pixel-to-mm ratio, derived from the minimum pixel distance between two opposing points, denoted as L_s, across the span l_s:

$$S_r = \frac{\min(L_s)}{l_s} \tag{4.26}$$

Subsequently, neighboring segments are stitched together as shown in Figure 4.16b. The core steps of the perspective correction method are formalised below in Algorithm 3.

4.4 Boundary layer features

The study of boundary layer (BL) characteristics is crucial for understanding SBLI, particularly when surface roughness is involved. Integral parameters and the Law of the Wall provide concise metrics. They allow for a comprehensive, yet simplified, analysis of the viscous flow impact on the overall flowfield. Most of the BL equations and constant values in this section are derived from [46].

Rigorous post-processing of the LDA data was required before the integral parameters could be determined. This process involved filtering, and the use of the Gaussian Mixture Model (GMM) then apply the weighted statistics menstioned in Section 2.3.4 to accurately characterise the mean flow, turbulence, and uncertainty.

4.4.1 Data filtering and pre-processing

A critical challenge in transonic LDA measurements involves particle fidelity. As the flow within the test section accelerates to supersonic speeds, or is rapidly deflected by the profiles, larger seeding particles may fail to follow the streamlines. Due to their higher inertia (high Stokes number), these particles lag behind the fluid velocity [162–164]. Consequently, they appear in the recorded LDA data as low-speed outliers, often forming secondary Gaussian peaks distinct from the true flow velocity. A filtering mechanism was applied to address these outliers. Two distinct cases were considered:

- Distinct Distributions: If the inertial particle lag resulted in a low-speed distribution that was completely distinct from the real high-speed Gaussian distribution, a simple threshold filter was employed. Data points falling outside a specified physical range $[u_{\text{lower}}, u_{\text{upper}}]$ were set to a null value. This effectively removed the outliers and shifted the remaining valid data points upwards.
- Overlapping Distributions: If the low-speed outlier distribution partially overlapped with the high-speed fluid distribution, simple thresholding was insufficient. In these cases, as well as in flow regions susceptible to separation and flow reversal where velocity distributions become multi-modal (non-Gaussian), a probabilistic approach was required. This was addressed using the Gaussian Mixture Model (GMM) described below.

Then the new data rate (f) for each velocity component was calculated from the total validated count (N) and the time difference between the first and last recorded arrival times (t_{min} and t_{max}):

$$f = \frac{N \times 1000}{t_{\text{max}} - t_{\text{min}}} \tag{4.27}$$

subsubsectionGaussian mixture model (GMM) To resolve overlapping particle distributions inertial lag or multi-modal flows separation, a Gaussian Mixture Model (GMM) was implemented. This methodology determines the responsibility (η_{wk}) of each velocity measurement (x_n) belonging to the k-th Gaussian component. The calculation is based on the component's mean (μ_k), variance (σ_k^2), and mixing weight (π_k):

$$\eta_{wk} = \frac{\pi_k \mathcal{N}(x_n \mid \mu_k, \sigma_k^2)}{\sum_{j=1}^{K} \pi_j \mathcal{N}(x_n \mid \mu_j, \sigma_j^2)} \tag{4.28}$$

The mixing weights were then iteratively updated (π_k^{new}) based on the calculated responsibilities:

$$\pi_k^{\text{new}} = \frac{1}{N} \sum_{i=1}^{N} \eta_{wk} \tag{4.29}$$

When GMM weights were available, the overall GMM-weighted mean velocity ($\overline{u}_{\text{GMM}}$) and RMS velocity ($\sigma_{u,\text{GMM}}$) were calculated using the component parameters. This allowed for the isolation of the true fluid velocity mode from the inertial particle lag mode [165, 166].

4.4.2 Integral parameters

Integral parameters offer a concise measure of the BL's overall influence on the external flow field. They are essential in integral solution techniques, such as the Kármán-Pohlhausen method [167, 168].

Displacement and momentum thickness (δ^*, δ^{**})

As disscused in Section 1.2.1, displacement thickness reflects the influence of the BL upon the hypothetical inviscid flow. But momentum thickness quantifies the loss of momentum flux within the BL.

Roughness modifies the velocity profile, changing δ^*, which in turn affects the effective body shape and the upstream influence of the shock [168]. While Roughness increases the wall shear stress, which is reflected as an increase in δ^{**}.

Shape factor (H)

Shape factor is a critical indicator of the velocity profile's shape. However, in compressible flow defining the integeral parameters is highly dependent on the pressure gradient and vertical density variation [169], researchers often use H_k (based only on velocity profiles) to isolate the physical shape of the boundary layer from density variations as it is a strong function of the Mach number, which makes it less practical as a universal parameter [55] .

$$H_k = \frac{\delta^*}{\delta^{**}} \tag{4.30}$$

where δ^* and δ^{**} are calculated using equations 1.6 and 1.7 respectively, neglecting changes in density.

Studying the change in these parameters across the interaction zone is the main objective of many SBLI prediction methods. Roughness increases friction and flow non-uniformity, which directly alters δ^*, δ^{**}, and consequently H.

The Shape factor (H_k) is perhaps the most significant global parameter for SBLI analysis. A change in H indicates a distortion of the velocity profile, which directly affects separation [44].

Increasing H corresponds to a progressive distortion and a general decrease in velocity levels near the wall. This evolution signifies a layer being subjected to an adverse pressure gradient, such as that imposed by a shock wave. The response of the BL to the shock is highly dependent on the incoming BL's shape parameter. The limit of validity for many approximate SBLI theories coincides with the point of incipient separation, making H a primary prediction objective. Roughness typically leads to a "fuller" turbulent profile compared to a laminar one. However, the presence of roughness in an adverse pressure gradient (like SBLI) can hasten the profile's movement towards higher H values, indicating an increased risk of separation [170].

A linear relationship between points and the no-slip condition at the wall is assumed and integral functions are numerically computes integral parameters using the trapezoidal rule, but it can lack precision, especially when only a few boundary layer points are captured. This is particularly true in the current case, where the upstream boundary layer is very thin, and limitations exist in probe volume and seeding. The best fit for the boundary layer points is achieved using optimization functions and employing the power law for the turbulent boundary layer:

$$\frac{u}{u_\infty} = \left(\frac{y}{\delta}\right)^{1/n} \tag{4.31}$$

where Python's SciPy library is used to minimise the error between the measured points and the theoretical profile by regulating the power n, ensuring a more accurate representation of the boundary layer characteristics.

Energy thickness (δ_E)

The energy-flow displacement thickness (δ_E), often denoted as δ_3, is computed to track the deficit in kinetic energy flow:

$$\delta_E = \int_0^\delta \frac{u}{u_\infty}\left(1 - \left(\frac{u}{u_\infty}\right)^2\right) dy \tag{4.32}$$

Recent investigations into Energy Thickness (δ_E) in turbulent boundary layer (TBL) flows reveal its strong relationship with energy transfer processes. By analyzing the energy-integral equation, a close relationship has been established between δ_E (which is derived solely from the mean streamwise velocity profile, u) and the Turbulent Kinetic Energy (TKE) production. This offers a practical method to estimate TKE production, which is challenging to measure directly in physical experiments.

The significance of δ_E becomes even more pronounced in TBLs under pressure gradient. Extensive analysis shows that the ratio between δ_E and the momentum thickness (δ^{**}) is a promising criterion for predicting flow separation [171].

4.4.3 Law of the wall: wall-layer interaction

The Law of the wall analysis is essential for characterising the turbulent flow's inner structure. This region, defined by non-dimensional wall coordinates u^+ and y^+, is where the surface roughness has its most direct impact.

The wall shear stress (τ_w) is the resistive force opposing the flow, and u_τ is derived from it:

$$u_\tau = \sqrt{\frac{\tau_w}{\rho}} \tag{4.33}$$

Roughness significantly alters τ_w. The Law of the Wall analysis, through the friction velocity, captures the increased surface friction due to the rough surface. For TBL τ_w can be estimated using empirical correlations of flat plat based on the Reynolds number (Re_x):

$$\tau_w = 0.0225\rho u_\infty^2 \left(\frac{\nu}{u_\infty \delta}\right)^{1/4} \tag{4.34}$$

The turbulent profile is plotted in coordinates $u^+ = u/u_\tau$ and $y^+ = yu_\tau/\nu$. For smooth walls, the profile follows the Log-Law:

$$u^+ = \frac{1}{\kappa}\ln(y^+) + B - \Delta u^+ \tag{4.35}$$

where $\kappa = 0.41$ and $B = 5$, Δu^+ represents the downward shift due to roughness defined in Equation 1.16.

A rough surface causes a downward shift in the profile on the u^+-y^+ plot. This shift, Δu^+, quantifies the effect of the roughness height on the velocity deficit. Thus, integral parameters quantify the global response, while the Law of the Wall provides insight into the local, near-wall mechanism by which roughness modifies the turbulent flow structure before and in the zone of SBLI.

Chapter 5

Sensitivity analysis of test section sittings

Achieving the desired design conditions while ensuring that the flow is influenced solely by profile roughness requires careful attention to the system's sensitivity to the test section control parameters, such as side wall suction, profiles relative location and angle to the nozzle. In complex experimental environments, particularly those designed to isolate specific aerodynamic or fluid dynamic phenomena, tiny changes in setup or control inputs can introduce significant parasitic effects that mask the intended results. A rigorous sensitivity analysis is therefore paramount to ensure the high fidelity, reliability, and repeatability of the experimental data.

This chapter details a comprehensive investigation into the test facility's sensitivity to various geometric and operational parameters. The primary goal of the investigation is the identification and quantification of the influence of these controls on the boundary layer characteristics and the overall flow quality. This process allows for the establishment of optimal, robust operating conditions. The desired design conditions, such as the pressure distribution on the profiles and the shock structure (such as in Figure 5.1), are thereby achieved. During these comparisons, the shock wave position was held constant. This was achieved by careful adjustment of the wind tunnel's back pressure.

The structure of this chapter is as follows:

- Section 5.1: The critical impact of the profiles' relative angle to the nozzle on flow symmetry and boundary layer growth initiation is assessed.
- Section 5.2: The influence of the test section upper channel size on mass flow distribution and shock structure is examined.
- Section 5.3: The sensitivity of the flow to the profiles' relative positioning to test section is studied.
- Section 5.4: A detailed analysis of the walls suction is conducted, covering both the effectiveness of the wall suction and the necessary optimization and control of suction for boundary layer manipulation.
- Section 5.5: Finally, the conclusions summarize the key findings, establishing the qualified operational parameters for subsequent roughness testing.

5.1 Inflow angle effect

Achieving the target isentropic inflow Mach number, as specified by the cascade design, necessitated a precise orientation of the profile relative to test section in order to achieve proper angle of attack (α). The flow characteristics at the leading edge, specifically the Mach number measured between $x/c \approx 0.15$ and $x/c \approx 0.2$, are exceptionally sensitive to any tiny variation in the profile inflow angle.

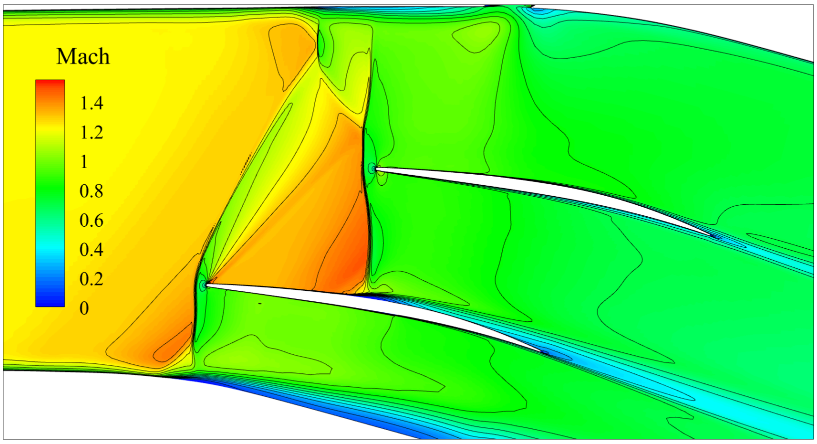

Figure 5.1: Reference CFD shock structure at design conditions [11]

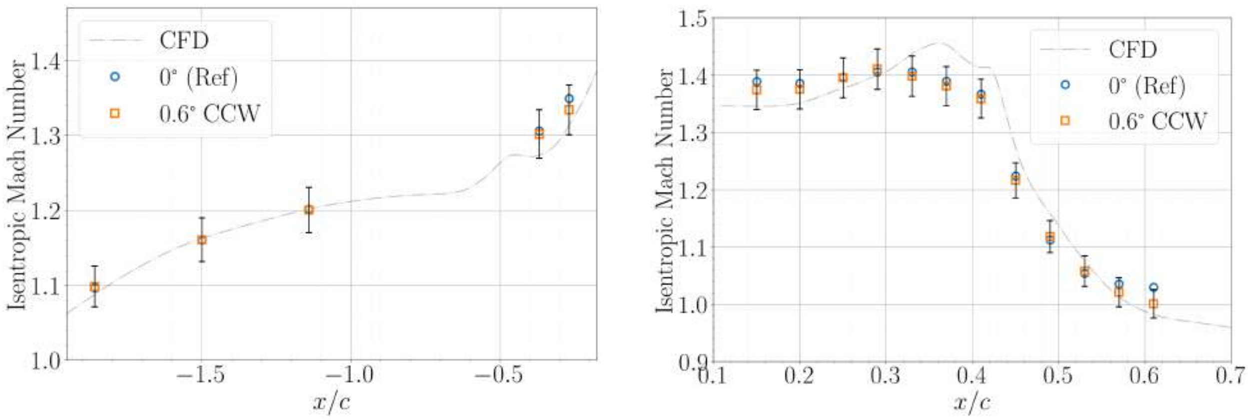

(a) In the nozzle upstream of the lower profile

(b) On lower profile (LP)

Figure 5.2: Isentropic Mach number, the error bars represents 2.5% error

For instance, Figure 5.2 demonstrates that a minimal counter-clockwise (CCW) adjustment of 0.6° is sufficient to alter the local inflow Mach number by a non-trivial ± 0.03. This angular shift does not merely affect the immediate inlet condition; it fundamentally reconfigures the entire transonic flow field, as evidenced by the schlieren visualisations shown in Figure 5.3. The rotation of the lower profile was performed according to the methodology described in Appendix A to achieve the target Mach number. Although this angular displacement is not perceptible to the naked eye, its profound impact was confirmed by returning the profile to its original position, which resulted in the restoration of the baseline flow state.

This geometric modification demonstrably reduces the effective throat area of the lower flow passage as evidant from the nozzle Mach number distribution in Figure 5.2a where it is reduced due to blockage. This geometrical constraint immediately imposes an adverse influence, leading to a local choke condition and a resultant decrease in the mass flow rate through that passage. This effective aerodynamic blockage in the lower passage forces the leading-edge shock system to translate upstream. As a direct consequence of this shift and the subsequent pressure field adjustment, the reflected shock wave is observed to re-attach to the passage shock beneath the upper profile. To counteract this induced asymmetry and restore the required mass flow balance between the adjacent passages, fine-tuning and strict regulation of the various parameters, including profile position to the test section, upper wall passage mass flow, and suction systems on the walls and controlled side walls suction, become essential operational procedures.

5.2 Upper channel wall

The geometry of the upper and lower channel walls was initially conceptualised based upon the streamlines of the cascade flow, as detailed in Section 2.2. However, due to practical constraints

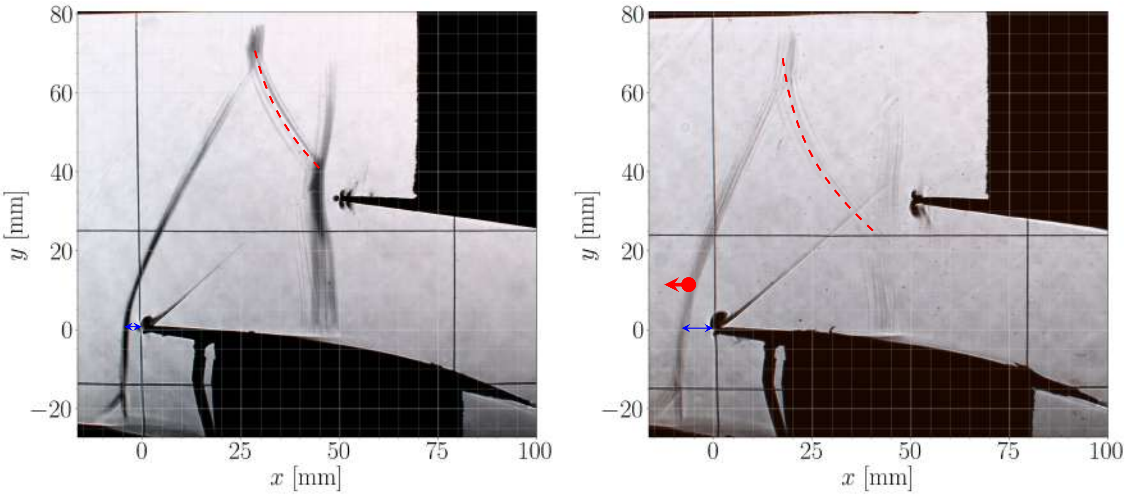

(a) Reference angle

(b) Rotated by 0.6° CCW

Figure 5.3: Average schlieren images, (- -) is the mean line of reflected shock

Table 5.1: Settings of the constant parameters during testing

Property	setting
Upper channel area ratio ($A_{i/o}$)	0.84
LP x-position from throat	225 mm
UP (x, y)-position from LP LE	(49, 34) mm
Upper wall suction	100%
Lower wall suction	100%
Side walls suction	100%

concerning the test section's physical size, passage size differentiation was necessitated. Specifically, the lower passage, the dimensions of which are intrinsically linked to the lower profile's angle and its position within the test section, was designed to be the smallest. Conversely, the upper passage was configured as the largest to facilitate the required mass flow balance and secure the target AVDR.

The upper passage inflow area ($l_i \times l_s$), where l_s denotes the constant wind tunnel span, is fixed by the upper profile setting (l_i=47 ±1 mm). The outflow area ($l_o \times l_s$) is controlled via a screw mechanism which adjusts the upper wall position, as illustrated in Figure 5.4a. The corresponding area ratio ($A_{i/o}$) is calculated as:

$$A_{i/o} = \frac{l_i}{l_o} \tag{5.1}$$

A series of upper wall configurations were tested to assess the system's sensitivity to variations in $A_{i/o}$, with the outlet dimension (l_o) always being maintained larger than the inlet (l_i), thus ensuring $A_{i/o} < 1$.

As shown in Figure 5.4b, which presents the isentropic Mach number distribution along the lower profile, the primary influence of the upper wall adjustment is observed in the flow field upstream of the shock wave. An increase in the area ratio ($A_{i/o}$), which corresponds to a reduction in the outlet height l_o, results in a measurable deceleration of the flow (indicated by a lower Mach number) in the pre-shock region. This deceleration is indicative of a change in the boundary layer behaviour and the resulting pressure gradient upstream of the shock wave.

Analysis of the distribution demonstrates that the $A_{i/o} = 0.92$ setting, representing the smallest outlet opening tested, yields the most significant upstream deceleration across the x/c range shown. Furthermore, in the downstream region ($x/c \approx 0.6$), the flow corresponding to $A_{i/o} = 0.92$ exhibits a relatively weaker overall pressure recovery compared to the more open settings. This suggests that the tighter passage configuration exerts a continuous influence on the local flow acceleration

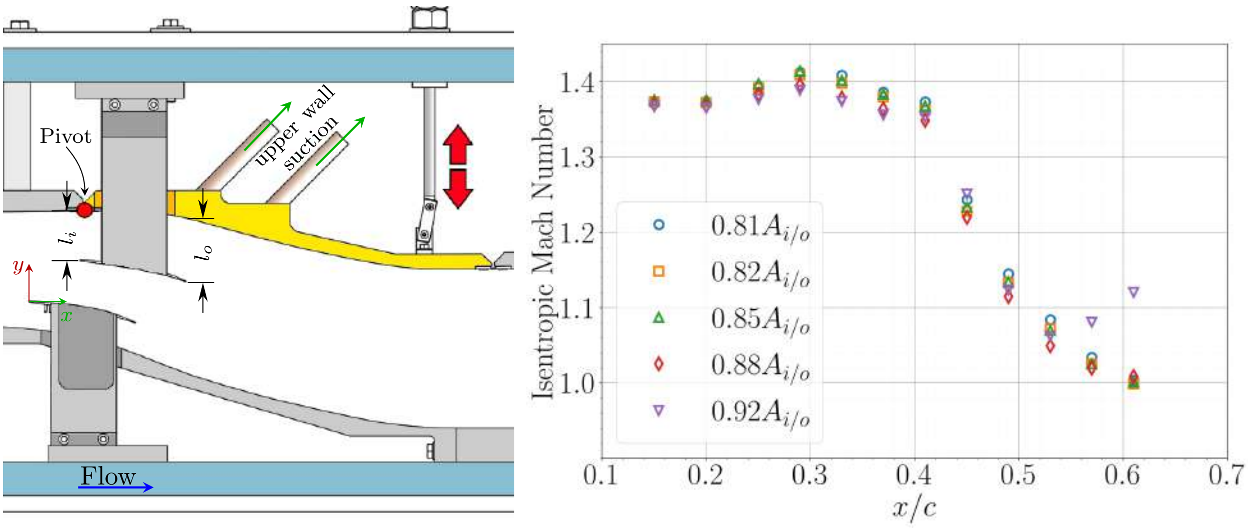

(a) Upper passage control and wall suction (b) Isentropic Mach number on LP for tested wall adjustment

Figure 5.4: Sensitivity of the system to profiles location to test section

Table 5.2: Settings of the constant parameters during testing

Property	setting
LP angle of attack (α)	11.2 -0.6°
LP x-position from throat	225 mm
UP (x, y)-position from LP LE	(49, 34) mm
Upper wall suction	100%
Lower wall suction	100%
Side walls suction	100%

and the subsequent shock-induced pressure rise.

The averaged schlieren images presented in Figure 5.5 show that no significant alteration to the overall shock structure is induced when the area ratio is maintained up to $A_{i/o} = 0.85$. This invariance is highly significant; it indicates that within this operational range, the upper wall suction system effectively controls the wall boundary layer growth and mitigates its influence on the upper passage flow. The suction thus preserves the intended flow characteristics up to this geometric limit.

Upon further increasing the area ratio to $A_{i/o} = 0.88$ and, more dramatically, to $A_{i/o} = 0.92$ (which corresponds to a minimum outlet height l_o), the aerodynamic flow field is perceptibly perturbed. At $A_{i/o} = 0.92$, a distinct compression wave is seen to grow downstream along the pressure side of the upper profile, suggesting increased local flow acceleration or a shift in the detachment point. Crucially, a highly unsteady third wave system (likely the passage shock) begins to emerge in the vicinity of $x/c \approx 0.6$ (a condition confirmed by the Mach number rise shown in Figure 5.4b). This is interpreted as evidence of an aerodynamic choke condition developing in the central (middle) passage. This choke is induced by the reduced outlet area of the upper passage, which forces an increase in mass flow through the middle passage.

5.3 Profiles positioning to test section

A systematic analysis was conducted to study the system's sensitivity to small variations in the profiles' position relative to the nozzle exit plane (Figure 5.6a). The positional changes tested comprised approximately ±1% of the chord in the horizontal (x) direction and approximately -2% of the chord in the vertical (y) direction, as summarised in Table 5.4. Here, xLP and xUP denote the horizontal displacement of the lower and upper profiles, respectively, from their nominal streamwise positions, while yUP denotes the vertical offset of the upper profile relative to the lower profile.

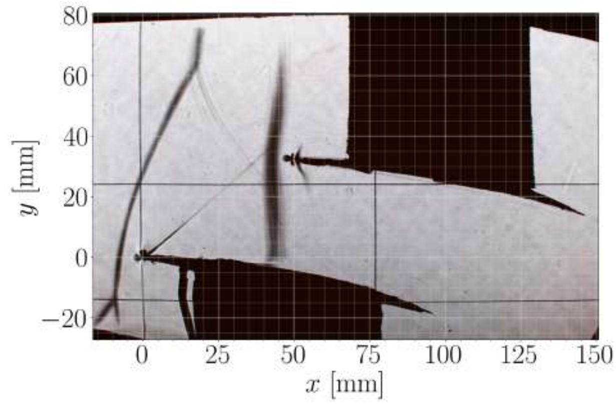

(a) $0.81A_{i/o}$

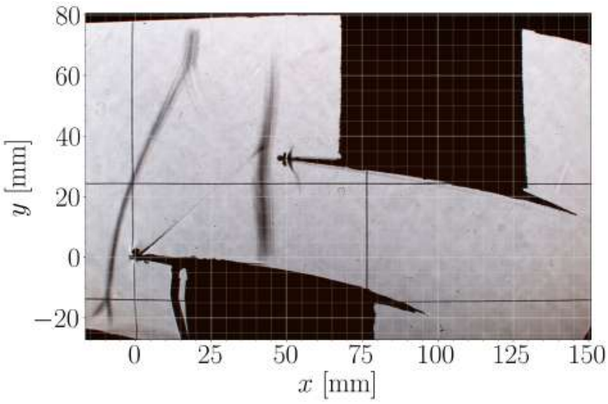

(b) $0.82A_{i/o}$

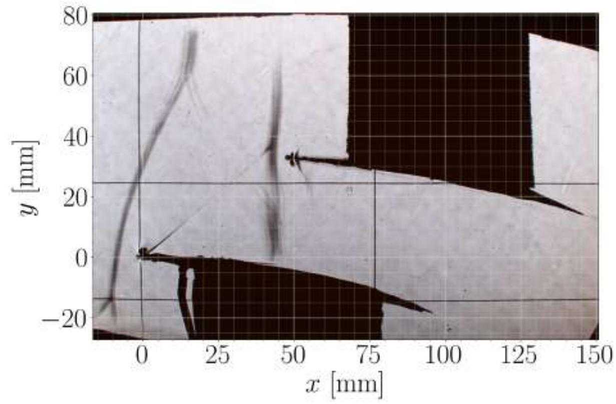

(c) $0.85A_{i/o}$

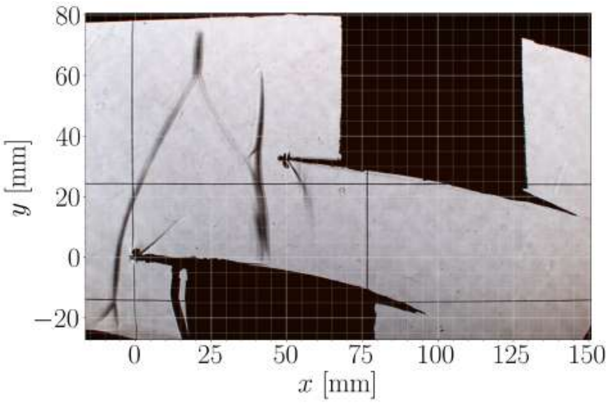

(d) $0.88A_{i/o}$

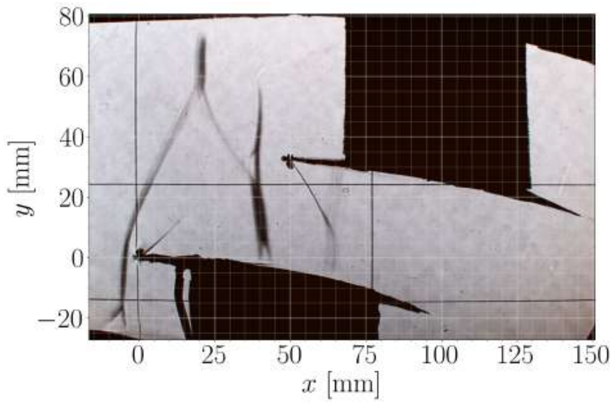

(e) $0.92A_{i/o}$

Figure 5.5: Average schlieren images for upper wall tested positions

The mechanical displacements do not solely modify the pitch (s); they concurrently induce significant variations in the stagger angle (χ), ranging from 43.40° to 47.18° (a change of approximately 3.8°). This dual geometrical change imposes two fundamental aerodynamic effects. First, pitch variation (passage width) directly control the geometric restriction of the flow. Wider passages (higher pitch) provide "geometric relief [172]" to the supersonic flow, reducing the peak Mach number ($M \approx 1.4$) feeding the passage shock. Since the irreversible shock loss is highly sensitive to the pre-shock Mach number, pitch directly controls the magnitude of the profile shock loss. Second, stagger variation which is the primary parameter governing the cascade's overall angular orientation, directly altering the aerodynamic incidence angle (i) for a constant inlet flow. This shift changes the distribution of aerodynamic loading across the blade. Furthermore, stagger variation fundamentally modifies the effective geometric throat area of the passage, which dictates the maximum mass flow rate (choke limit). The observed Mach number sensitivity is therefore a combined effect of both the local passage area (pitch) and the change in the effective loading/choke margin (stagger).

The results, presented in Figure 5.6b, indicate that the overall Mach number distribution along

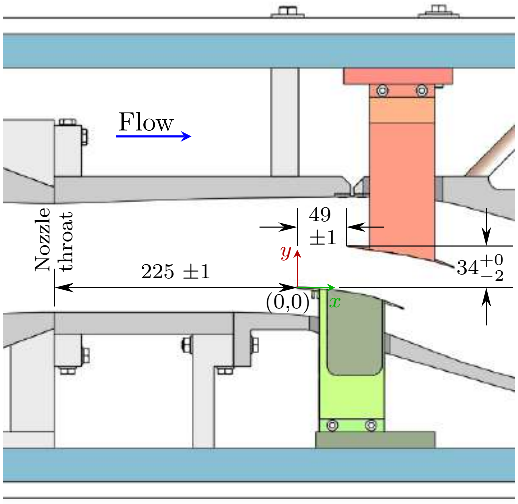

(a) Profile position to the test section

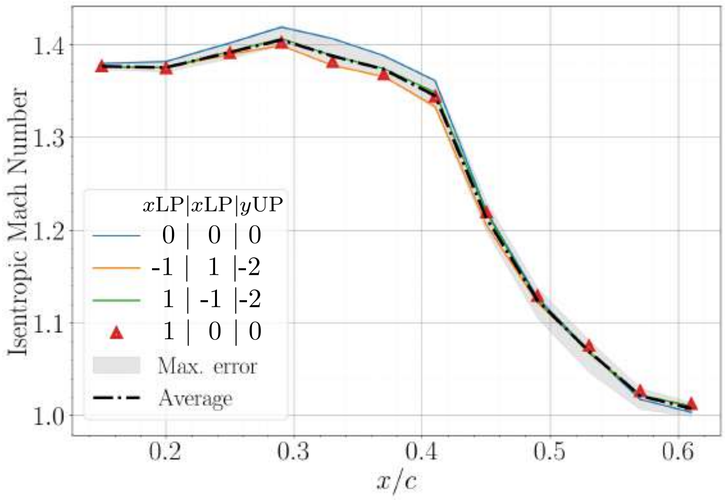

(b) Isentropic Mach number of LP for tested positions

Figure 5.6: Sensitivity of the system to profiles location to test section

Table 5.3: Settings of the constant parameters during testing

Property	setting
LP angle of attack (α)	11.2 -0.6°
Upper channel area ratio ($A_{i/o}$)	0.84
Upper wall suction	100%
Lower wall suction	100%
Side walls suction	100%

the lower profile is not significantly altered by these positional changes. However, a measurable effect is discernible in the local flow conditions just upstream of the passage shock, specifically within the range of 0.25-0.4 x/c. The baseline position (xLP=0, xUP=0, yUP=0) resulted in the highest local Mach number in this region. Conversely, the configuration where the profiles were furthest apart horizontally (xLP=-1, xUP=1, yUP=-2) yielded the lowest Mach number. This flow modulation is directly attributed to the influence of the mechanical displacement on the local aerodynamic pitch, which, in turn, dictates the mass flow distribution and the resulting flow acceleration in each of the three passages.

Furthermore, the flow structures observed in the averaged schlieren images (Figure 5.7) show a high degree of consistency, with no major changes to the overall shock topology. Only a minimal upstream shift of the leading-edge shock wave, quantified to be a few millimetres, was observed in some cases. More notably, in configurations where the profiles were closer together (e.g., 1 | -1 | -2 or 1 | 0 | 0), the passage shock wave was observed to develop a slight curvature or local deformation. This phenomenon is indicative of a subtle, yet measurable, change in the SBLI, likely caused by the tighter passage creating a locally intensified pressure gradient that influences the boundary layer's susceptibility to separation or changing the shock λ-foot size.

5.4 Secondary flow control

Experimental studies and investigations concerning transonic flows in the highly loaded compressor profile usually facing the streamwise corner flow effects which are impossible to eliminate entirely. Despite attempts to mitigate their effects by focusing measurements away from tunnel walls, achieving genuine two-dimensionality in flow remains elusive. Studies by Randall, Titchener and Bruce [173–175] underscore the significance of corner flows, highlighting that they persist even at the tunnel centerline. Furthermore, practical limitations often preclude measurements from being restricted to regions near the centerline, especially in smaller experimental setups, thus impeding their capacity to accurately simulate nominally two-dimensional flow fields.

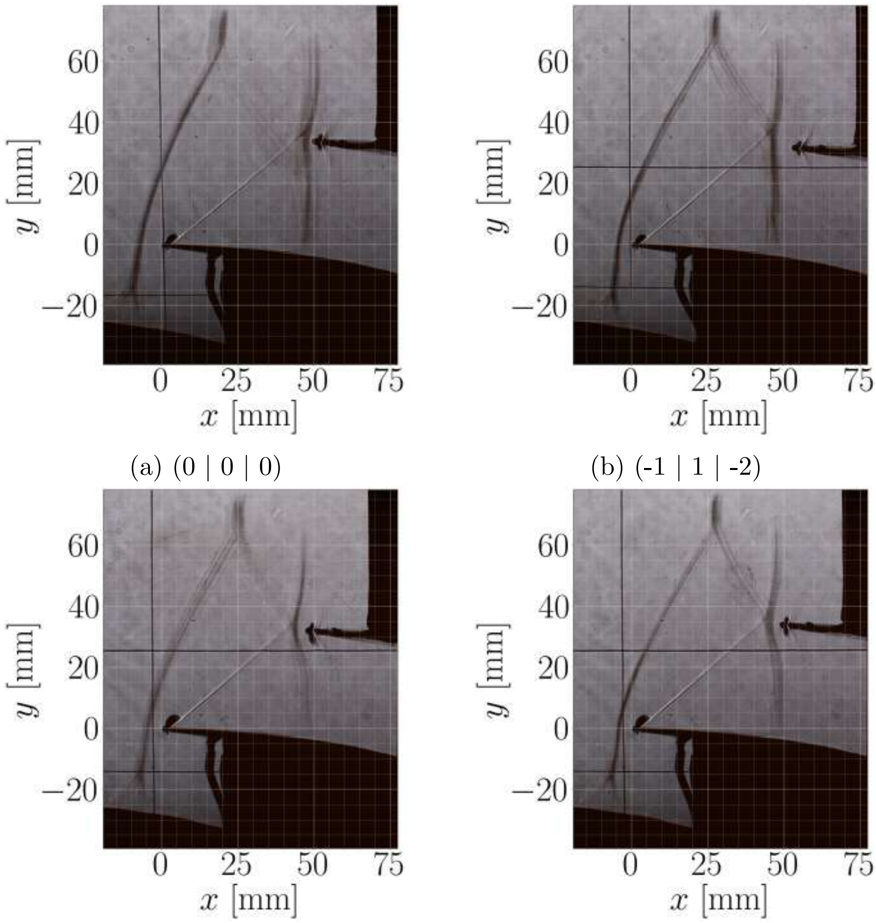

(a) (0 | 0 | 0)

(b) (-1 | 1 | -2)

(c) (1 | -1 | -2)

(d) (1 | 0 | 0)

Figure 5.7: Average schlieren images for selected tested positions (xLP | xUP | yUP)

Numerous flow control devices have been examined to diminish corner effects. In the former UFAST project, Paul Bruce et al. [176] investigated the manipulation of corner flows upstream of a $M = 1.4$ normal SBLI using corner suction. The application of suction demonstrated the potential to induce a separated region in a previously attached flow field, thereby reducing the magnitude of corner effects. However, the specific rationale behind the chosen suction flow rate remains unspecified.

Likewise, at the DLR transonic cascade facility referenced by Klinner et al. [72], and in the IMP-PAN test section cited in the work by Flaszynski et al. [36], suction slots were employed to mitigate corner flow effects in investigations of transonic compressor profiles. These studies demonstrated the high effectiveness of suction slots in manipulating the AVDR. However, they did not specify the amount of suction used nor provide details of the manipulation process.

5.4.1 Upper and lower walls suction

The upper and lower channel wall suction systems were incorporated into the test section design specifically to manage boundary layer growth along these surfaces and to facilitate mass flow balance across the three passages, as depicted in Figure 5.8.

The upper wall suction system (Figure 5.8a) operates by drawing air through a perforated plate using two suction tubes connected to vacuum tank pressure. Conversely, the lower wall suction system (Figure 5.8b) employs a suction slot positioned beneath the lower proile and connected to vacuum tank pressure through a channel below test section outlet. To quantify the influence of these systems on the flow stability, both were systematically investigated by partially or entirely blocking the suction vents. For the upper wall, the partially-blocked case involved closing one of the two tubes, whilst the fully-blocked scenario entailed closing both. For the lower wall, the suction slot was either half-covered or fully-covered using a thin mechanical insert. Following

Table 5.4: Profiles positions tested in the sensitivity analysis

Δ-position [mm]			s [mm]	χ [deg]
xLP	xUP	yUP		
0	0	0	60.00	44.53
0	+1	0	60.46	45.07
-1	+1	0	62.50	45.59
-1	0	0	61.18	45.07
-1	-1	0	60.00	44.53
1	-1	0	58.00	43.40
1	0	0	58.63	43.97
1	1	0	60.60	44.53
0	0	-1	59.07	45.33
0	1	-1	59.90	45.86
-1	-1	-1	59.07	45.33
-1	0	-1	60.92	45.86
-1	1	-1	62.00	46.38
1	0	-1	58.60	44.78
1	-1	-1	57.64	44.21
1	1	-1	59.07	45.33
0	1	-2	59.36	46.67
-1	1	-2	61.62	47.18
-1	0	-2	60.35	46.67
1	0	-2	58.10	45.59
1	-1	-2	56.90	45.04

Table 5.5: Settings of the constant parameters during testing

Property	setting
LP angle of attack (α)	11.2 -0.6°
Upper channel area ratio ($A_{i/o}$)	0.84
Side walls suction	100% for upper wall testing
	33.3% for lower wall testing

each configuration adjustment, the back pressure was carefully tuned to ensure the isentropic Mach number distribution on the lower profile maintained a consistent passage shock location for comparative analysis (Figure 5.9).

When testing the effect of the upper wall suction, the constant parameters were set as outlined in Table 5.5, with the upper channel area ratio fixed at $A_{i/o} = 0.84$. As illustrated in Figure 5.9a, the isentropic Mach number distribution along the lower profile remained nearly identical across all three suction settings (Fully-open, Partially-blocked, and Fully-blocked). This minimal sensitivity suggests that, with the upper wall geometry set at $A_{i/o} = 0.84$, the mass flow rate is adequately secured, and the natural growth of the upper wall boundary layer thickness has a negligible effect on the overall effective flow area in the channel. This conclusion is further corroborated by the schlieren visualisations presented in Figure 5.10, which show no significant change in the shock structure or behaviour was induced by varying the upper wall suction level.

In contrast, a more pronounced effect was exhibited upon adjustment of the lower wall suction system. As shown in Figure 5.9b, disabling the lower wall suction (Fully-blocked) led to a noticeable deviation in the Mach number distribution along the lower profile, particularly in the pre-shock acceleration region. Although the effect of partial blockage was minor, the absence of suction allowed for a substantial increase in boundary layer thickness along the lower wall, which consequently reduced the effective flow area and altered the local mass flow rate through the lower passage.

The corresponding schlieren images (Figure 5.11) further substantiate this finding, revealing dis-

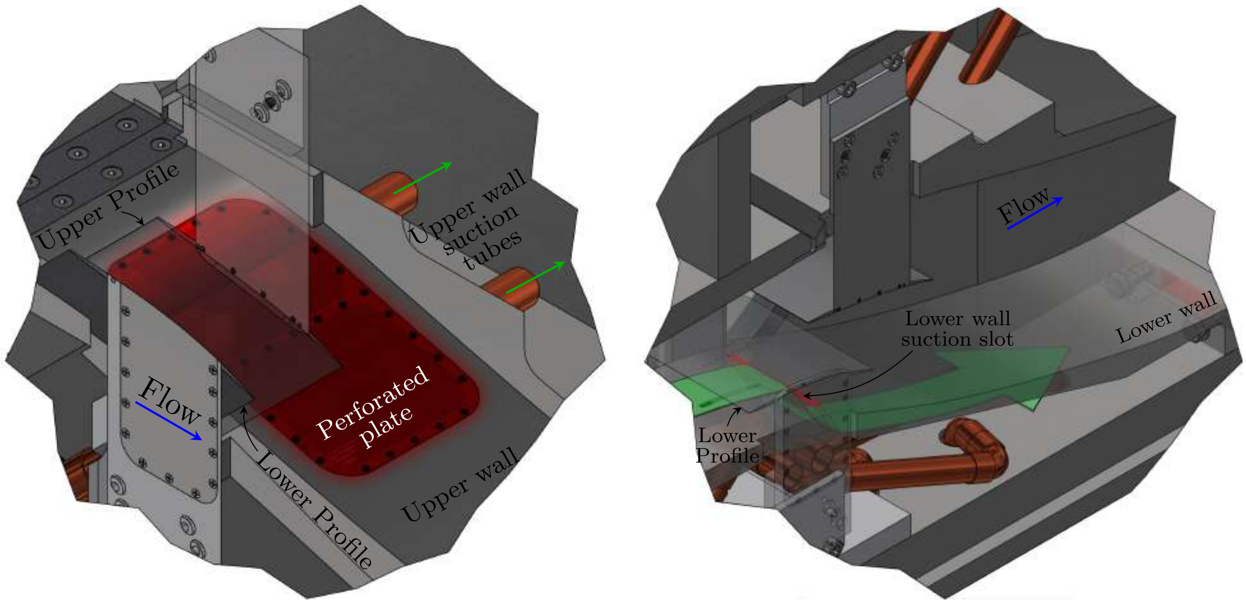

(a) Upper wall suction (b) Lower wall suction

Figure 5.8: Test section upper and lower wall suction systems

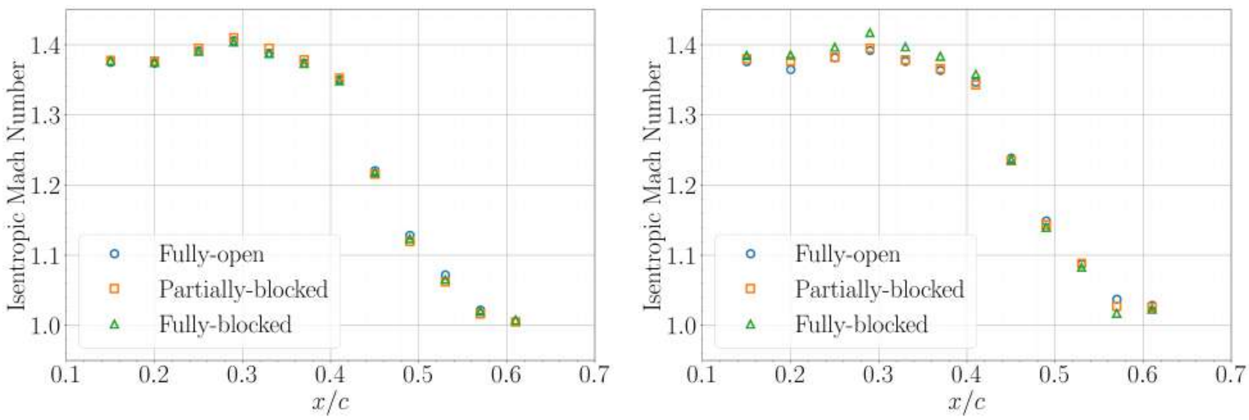

(a) Upper wall suction (b) Lower wall suction

Figure 5.9: Isentropic Mach number on LP for walls suction effect

cernible alterations in the shock structure when the lower wall suction was modified. Specifically, the increased blockage caused the leading-edge shock wave to translate upstream, which, in turn, resulted in the reflected shock wave interacting further upstream with wall and interact with the passage shock in the middle passage. It must be noted that during the lower wall suction investigation, the side wall suction level was maintained at 33.3% (Table 5.5), which has already modified the baseline shock structure compared to the upper wall suction test cases. The influence of the controlled side wall suction on the flow field is discussed in detail in the following Section 5.4.2.

5.4.2 Side walls suction slots

One of the key parameters in this study is the sidewall suction, illustrated in Figure 5.12 and the related system discribed in Section 2.2. This approach is commonly employed to manage the blockage resulting from the unavoidable growth of the boundary layer on the cascade sidewalls. The degree of this blockage is typically assessed using the AVDR parameter, which quantifies the effective flow area contraction between the inlet and outlet of the cascade.

The static pressure in the side wall suction tubes is highly dependent on the control valve setting, as demonstrated in Figure 5.13a (dashed line). As the suction valve is progressively closed, the static pressure (p_{suc}/p_{01}) is observed to rise significantly. This pressure increase directly indicates

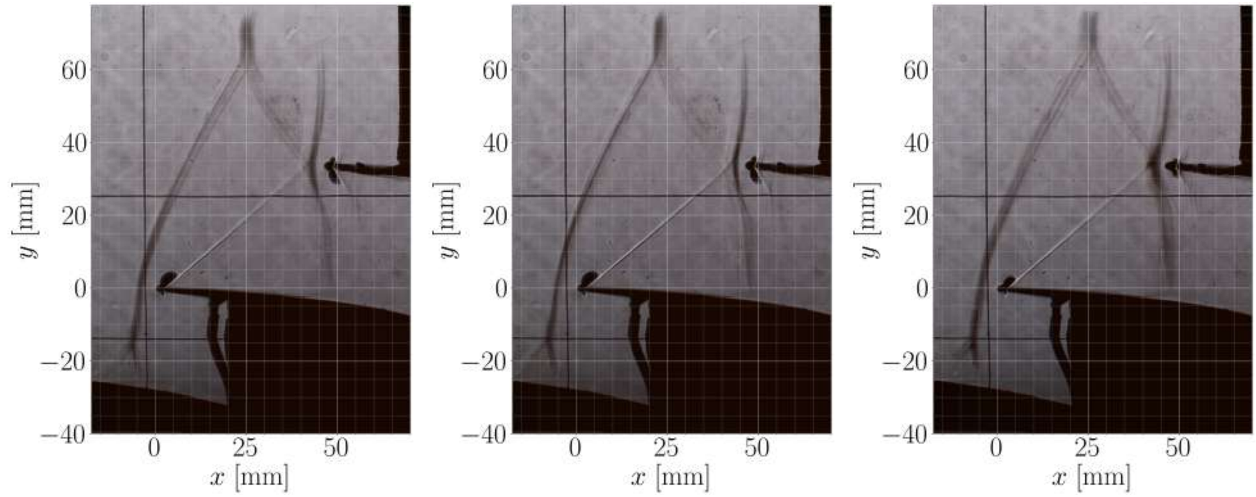

(a) Fully-blocked (b) Partially-blocked (c) Fully-Open

Figure 5.10: Average schlieren images for upper wall suction effect

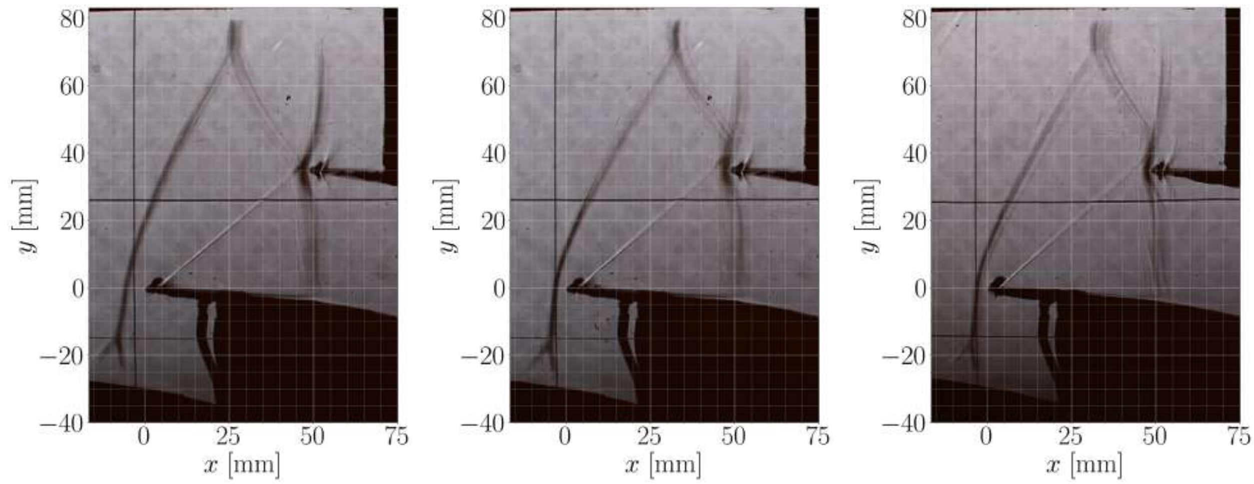

(a) Fully-blocked (b) Partially-blocked (c) Fully-Open

Figure 5.11: Average schlieren images for lower wall suction effect

a reduction in the mass flow rate extracted by the suction system. This diminished extraction rate inherently influences the thickness of the boundary layer along the walls' corner.

The total pressure ratio, p_{02}/p_{01}, measured far downstream, also exhibits sensitivity to the valve setting (Figure 5.13a, solid line). The highest total pressure recovery is seen between 50.0% and 66.7% valve opening. Generally, an increase in p_{02}/p_{01} as the valve opens suggests reduced overall aerodynamic losses within the passage. The vast difference between the ratios p_{suc}/p_{01} and p_{02}/p_{01} confirms the high level of flow losses inherent in the suction system itself. The system's non-linear operating characteristics are also readily apparent as the valve closure is adjusted.

The isentropic Mach number distribution along the lower profile mid-span is presented in Figure 5.13b. A distinct, albeit slight, effect of the side wall suction level on the mid-span Mach number is observed. As the suction is systematically reduced (valve closing from 100.0% to 16.7%), a decrease in the Mach number is evident in the pre-shock region ($x/c \approx 0.3 - 0.4$). This phenomenon implies that the reduction in suction permits the corner boundary layer to thicken considerably. This increased blockage (due to the decrease in free stream flow area) forces the flow to redistribute. Consequently, the low-momentum fluid associated with the corner flow separation spreads further inwards towards the mid-span measurement plane. The increased local blockage reduces the flow acceleration, leading to the observed drop in local Mach number. This boundary layer thickening is known to lead to a chord-wise elongation of the separated region by the shock [36]. The Mach number reduction is most significant when comparing the fully open and near-fully closed valve positions.

Table 5.6: Settings of the constant parameters during testing

Property	setting
LP angle of attack (α)	11.2 -0.6°
Upper channel area ratio ($A_{i/o}$)	0.84
Upper wall suction	100%
Lower wall suction	100%

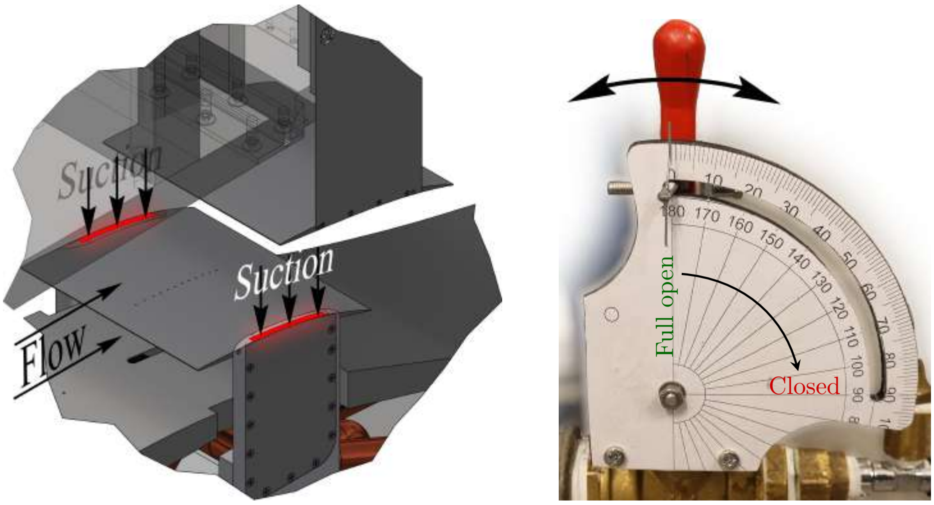

(a) Side suction slots (b) Suction valve

Figure 5.12: Sensitivity of the system to side wall suction

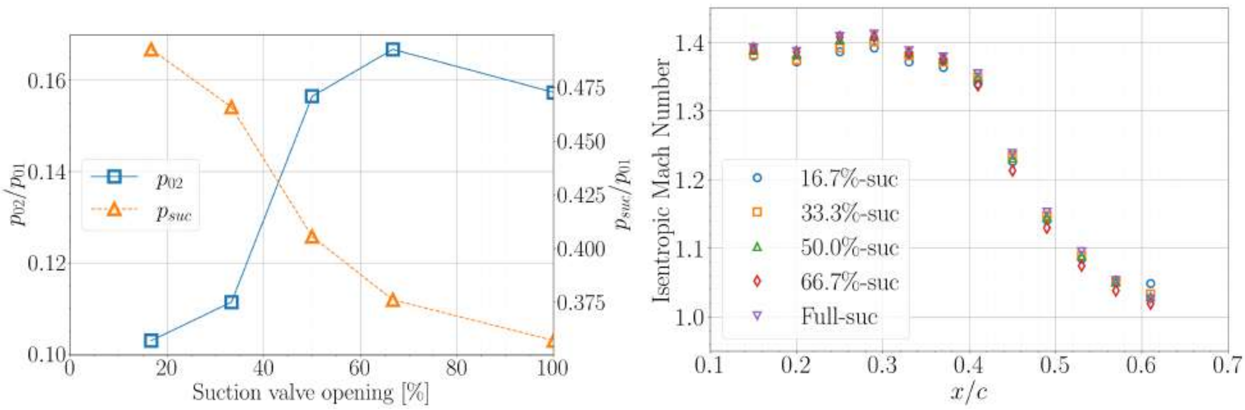

(a) Pressure in the tubes for tested suction (b) LP Isentropic Mach number for tested suction

Figure 5.13: Pressure evaluation for side wall suction effect

The impact of varying side wall suction on the flow field structure was documented through time-resolved schlieren photography. Average images, captured over a period of 4 s at a frame rate of 2 kHz, are presented in Figure 5.14. A clear trend in the Leading-edge shock wave position is visually demonstrated. As the suction level is reduced from 100.0% “Full-suc” to 16.7%, the shock wave is observed to translate progressively downstream. This translation is accompanied by a slight decrease in the shock’s inclination angle relative to the horizontal axis (Table 5.7). The average inclination angle of the leading-edge shock (relative to the horizontal) was evaluated within 10 to 45 mm above the leading-edge using the script mentioned in Section 4.2.The inclination angle is measured to decrease from 0.00° at full suction to -2.81° at 16.7% suction. This change signifies a more horizontal orientation of the shock wave as the blockage from the side wall boundary layer is increased.

Significant modifications are induced in the downstream shock structure. The reflected shock wave which is interacts with the upper wall before reflecting back into the flow field, is observed to

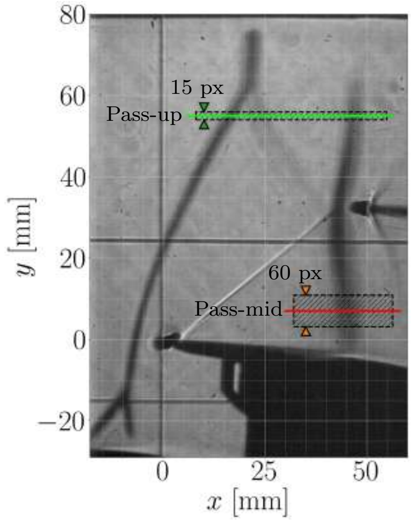

(a) Full-suc

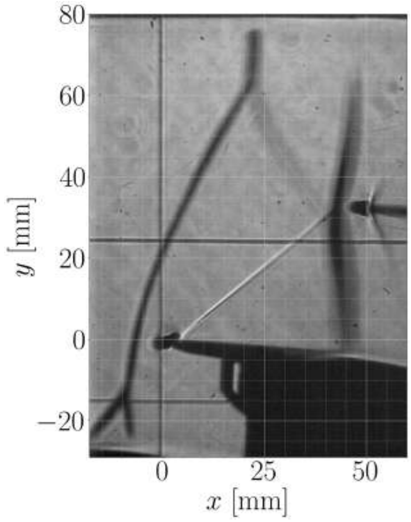

(b) 66.7%-suc

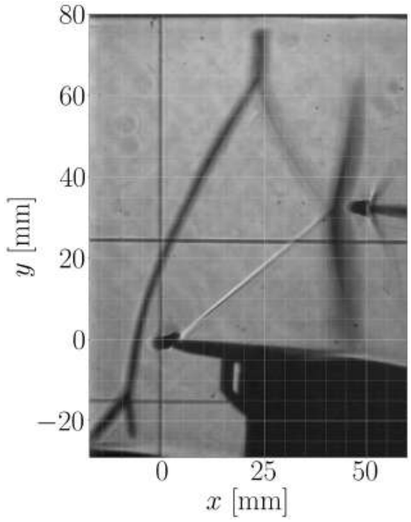

(c) 50.0%-suc

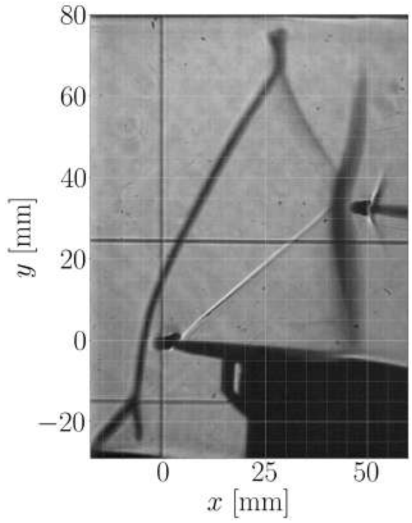

(d) 33.3%-suc

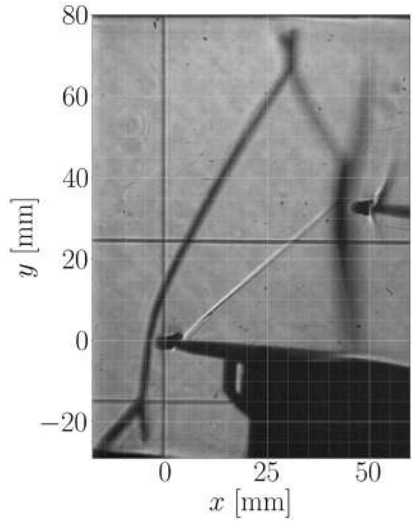

(e) 16.7%-suc

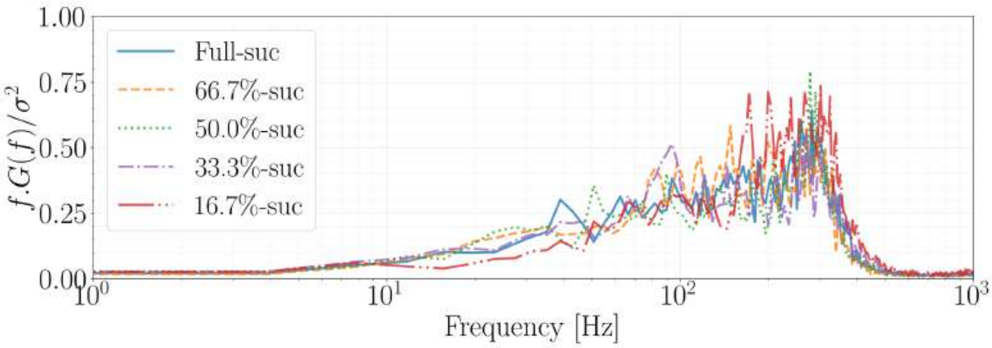

(f) Normalized-PSD at "Pass-mid"

Figure 5.14: Suction effect on shock structure

shift and strengthen then merge with the leading-edge shock.For the fully open case, the reflected shock is seen to merge with the passage shock in the middle passage. As the valve is closed to less than 50.0% suction, this merging point is shifted towards the upper passage. The flow structure achieved by the shock merging in the upper passage is representative of the desired flow configuration indicated during the design phase. as illustrated in Figure 5.1.

The unsteadiness of the Leading-edge shock is not significantly altered by the changes in side wall suction, as indicated by the small variation in the angle standard deviation (σ) across all settings (Table 5.7). The greatest impact of suction variation is on the downstream shock interactions.

The passage shock unsteadiness was investigated by tracking the shock position near the lower

Table 5.7: Leading-edge shock inclination to the horizontal

Case	Valve opening	Inclination difference ($\Delta\theta$) [deg]	Angle fluctuation ($\sigma(\theta)$) [deg]
Full-suc	0°	+0.00	0.55
66.7%-suc	30°	-0.14	0.53
50.0%-suc	45°	-0.53	0.59
33.3%-suc	60°	-1.92	0.59
16.7%-suc	75°	-2.81	0.57

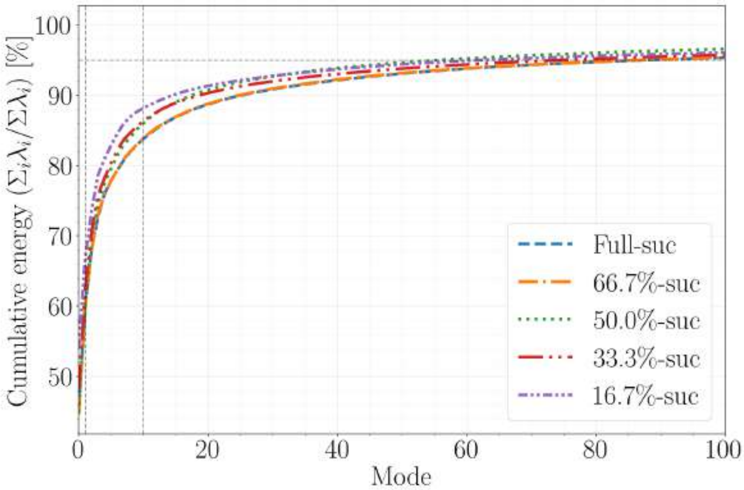

Figure 5.15: Cumulative energy of the first 100 POD modes

profile suction side ("Pass-mid" location, indecated in Figure 5.14a). The Normalised-PSD analysis reveals similar shock oscillation energy across all suction settings (Figure 5.14f). However, distinct frequency peaks are observed to appear for each setting: for example, a 40 Hz peak for full suction and a 120 Hz peak for 66.7% suction. These unique peaks are likely correlated with distinct shock oscillation modes, the characteristics of which are influenced by the specific flow field blockage.

Further analysis, specifically POD, was subsequently commissioned for further analysis. This was performed to establish the coherence of the shock waves. The technique was used to isolate the specific sources of flow unsteadiness. Through this process, assurance was gained that the observed spectral peaks were related solely to the passage shock interaction with the lower profile boundary layer. Interference from other sources, such as wall interactions or global passage blockage, was therefore discounted.

The cumulative energy of the first 100 POD modes is illustrated in Figure 5.15. The flow field energy is shown to be highly concentrated. The first ten modes contribute significantly, accounting for approximately 88% of the total system energy. The cumulative energy is observed to approach 95% of the total system energy with only 88 modes. This indicates that the flow unsteadiness is governed by a small number of dominant, coherent structures.

Typical spatial POD modes from the dominant first ten are presented in Table 5.8. Mode 1 accounts for approximately 16.2% of the total fluctuation energy on average. Its energy ratio is shown to range from 12.7% to 19.5%. The spatial structure of Mode 1 captures the leading-edge shock and the passage shock.

Notably, the oscillations of the leading-edge shock demonstrate a clear coherence with those of the passage shock. It is observed that as the side wall suction level is decreased, the energy contribution of the leading-edge shock oscillation within Mode 1 decreases. Conversely, the reflected shock component is seen to increase. This suggests that the dominant source of the passage shock oscillation energy is transformed from the leading-edge shock to the reflected shock as the side wall suction is reduced.

Mode 3 accounts for approximately 5.6% of the total fluctuation energy on average, with a range between 4.6% and 6.7%. The spatial characteristics of Mode 3 indicate that a portion of the passage shock oscillation energy is not transferred from the leading-edge or reflected shocks. This

Table 5.8: Special POD of the highest energy content modes

	Mode 1	Mode 3	Mode 5	Mode 9
Full-suc	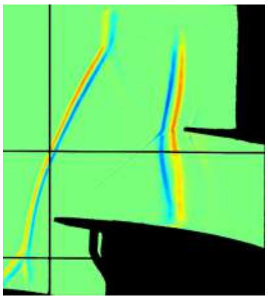 (a) (12.7%)	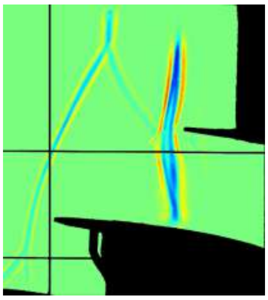 (b) (5.0%)	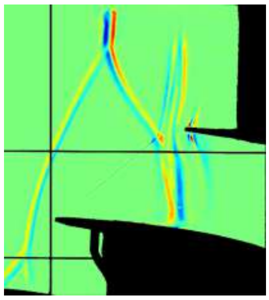 (c) (1.9%)	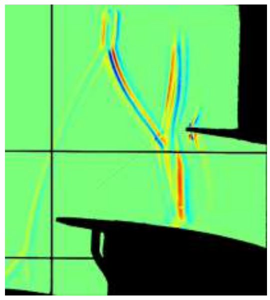 (d) (0.7%)
66.7%-suc	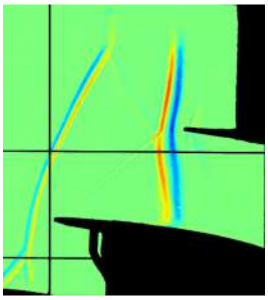 (e) (18.8%)	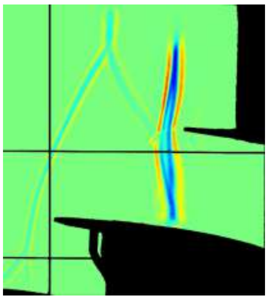 (f) (6.7%)	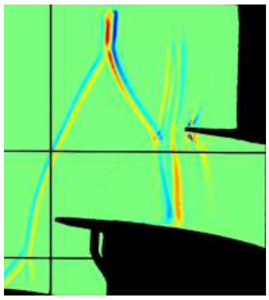 (g) (2.7%)	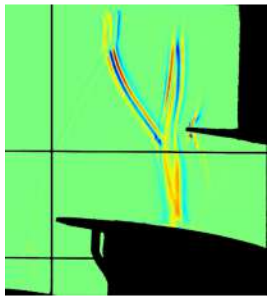 (h) (1.2%)
50.0%-suc	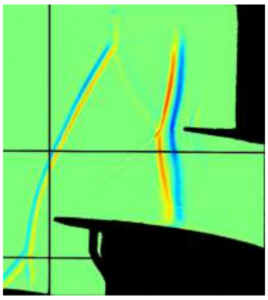 (i) (15.4%)	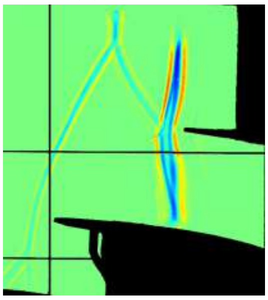 (j) (5.2%)	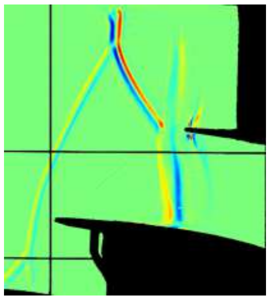 (k) (2.0%)	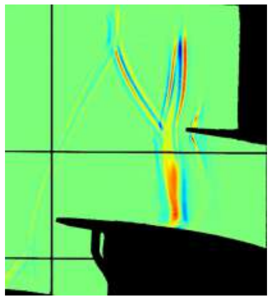 (l) (1.2%)
33.3%-suc	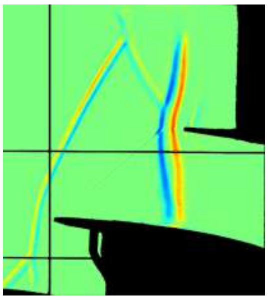 (m) (19.5%)	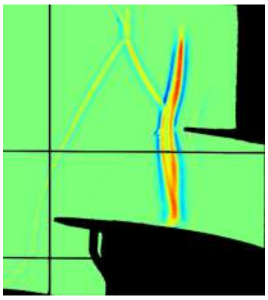 (n) (6.4%)	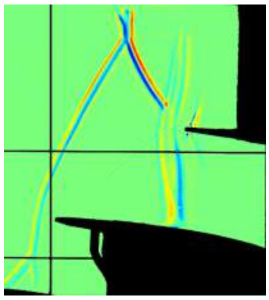 (o) (2.5%)	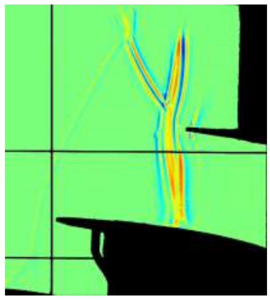 (p) (1.2%)
16.7%-suc	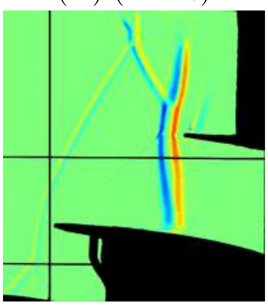 (q) (14.7%)	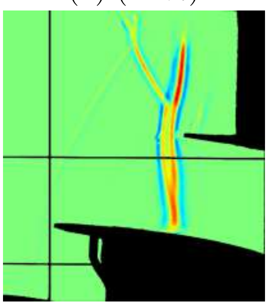 (r) (4.6%)	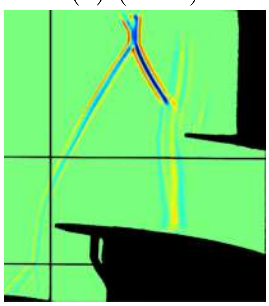 (s) (1.9%)	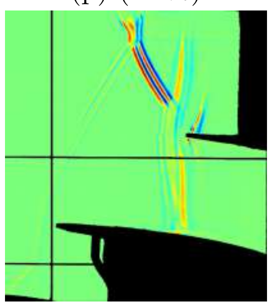 (t) (1.0%)

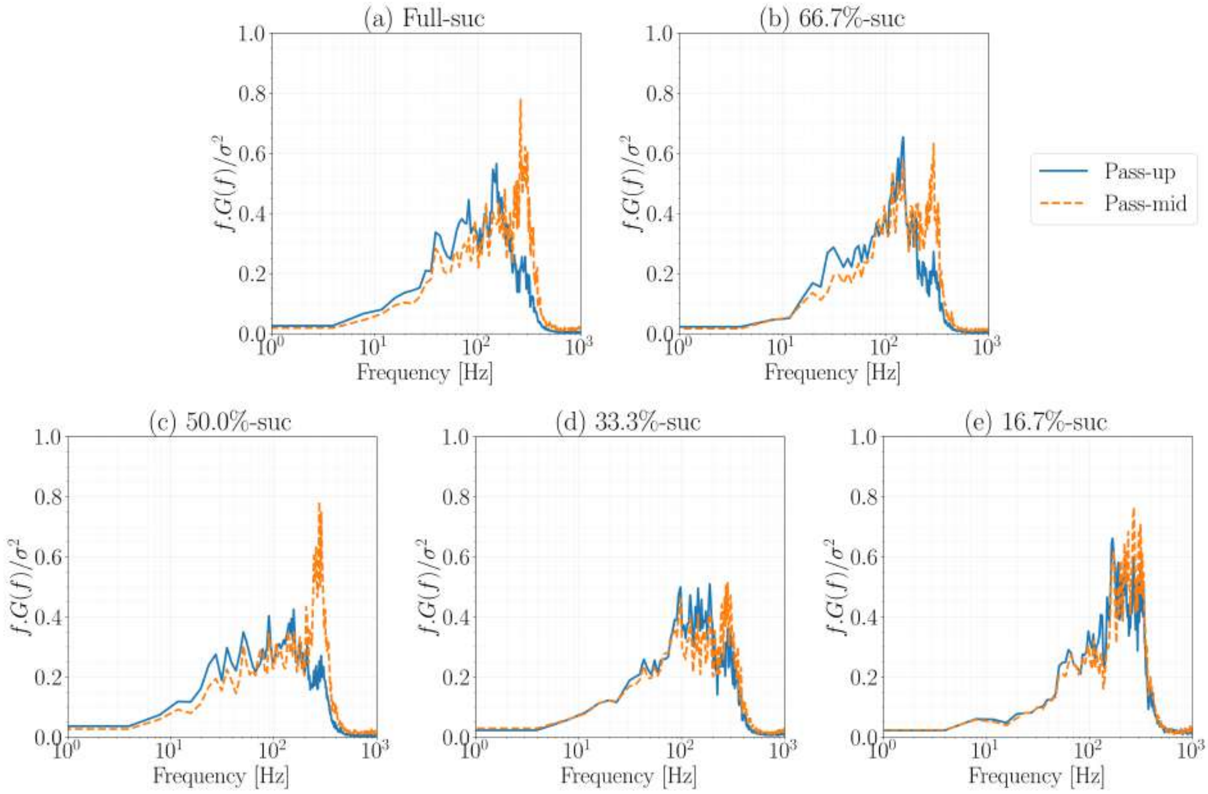

Figure 5.16: Normalized-PSD of the passage shock tracked at the upper and middle passage

strongly implies that a component of the passage shock unsteadiness is generated locally at the interaction point between the passage shock and the boundary layer on the lower profile suction side. This locally generated mode is characterised by larger oscillation amplitudes of the passage shock when compared to Mode 1.

Modes 5 and 9 are characterised by a comparatively lower energy content, each contributing less than 3% of the total fluctuation energy. These modes nonetheless provide valuable insights into the flow dynamics. A transformation of energy between the leading-edge, reflected, and passage shocks is visually demonstrated within these modes. The reflected shock is clearly the most energetic shock structure identified in Modes 5 and 9. Higher oscillation amplitudes of the reflected shock are also evident under conditions of decreased suction.Specifically, in Mode 5, the structure of the passage shock appears to be split into two distinct portions. These portions possess different dynamic characteristics. The upper portion of the passage shock exhibits a very weak energy content when compared to the portion located in the middle passage. This difference confirms that the unsteadiness is highly non-uniform across the spanwise extent of the passage shock.

Based on this analysis, the leading-edge, reflected, and passage shocks are confirmed as the primary oscillating structures in the flow field. The side wall suction significantly affects the oscillation dynamics of the leading-edge and reflected shocks. This effect is particularly evident in the passage between the upper profile and the test section walls. The change in the mass flow ratio between this passage and the main profile passage is understood to be the physical mechanism responsible for this sensitivity.

The dynamics of the passage shock oscillation were investigated by tracking the shock wave at two distinct spanwise locations. These locations were near the upper profile wall ("Pass-up") and near the lower profile wall ("Pass-mid"). This tracking was performed to further understand the different dynamic behaviour indicated by Mode 5 of the POD analysis.

The Normalised-PSD results are presented in Figure 5.16. The oscillation dynamics at the two locations are generally shown to be very similar across all suction settings. However, specific differences are observed within the 100 Hz to 400 Hz frequency band. A peak is present at approximately 270 Hz at the "Pass-mid" location, which is absent at the "Pass-up" location. This peak is most

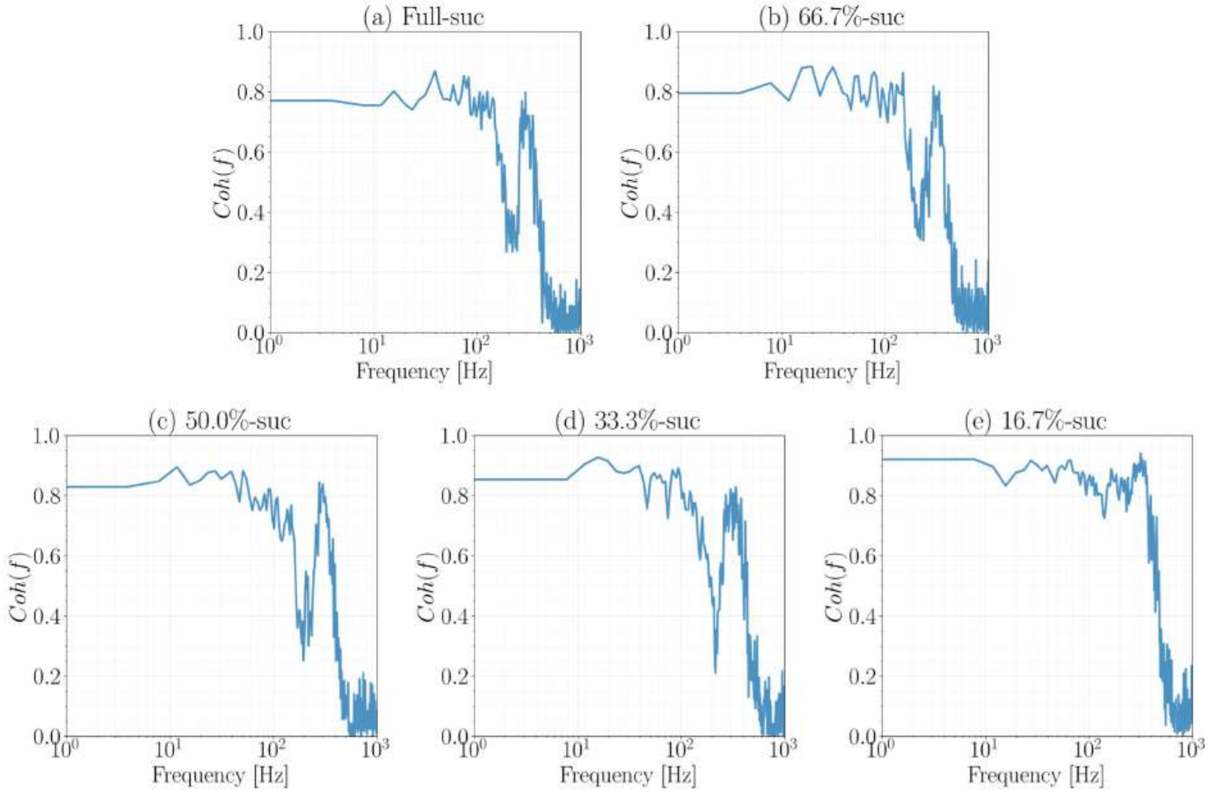

Figure 5.17: Coherance of the passage shock

pronounced under the Full-suc setting and is observed to diminish as the suction is decreased.

The difference in local dynamics was confirmed by a coherence analysis performed between the two shock tracking locations (Figure 5.17). A high coherence level (above 0.7) is maintained across a wide frequency range, specifically 0 Hz to 500 Hz, for all suction settings. This indicates that the passage shock generally oscillates as a single, coherent structure along its span.

However, a noticeable drop in coherence is observed within the 200 Hz to 400 Hz frequency band. This drop is particularly severe for the Full-suc case. This reduction in correlation suggests the presence of localised flow instabilities or interactions that affect the passage shock differently at the upper and middle passage locations. This localised effect is mitigated as the suction is decreased, leading to a more uniform oscillation behaviour of the passage shock across its span under lower suction conditions.

The coherence analysis was extended to include the leading-edge, reflected, and passage shocks at the "Pass-up" location to determine the origin of the passage shock oscillation (Figure 5.18). A generally low coherence level (below 0.6) is observed between the shocks.

Between the Leading-edge shock and the Passage shock, the coherence exceeds 0.6 within the 200 Hz to 400 Hz frequency band, particularly under the Full-suc setting. This suggests that the leading-edge shock oscillations exert a moderate influence on the passage shock behaviour at these specific frequencies. This influence is observed to decrease as the suction is reduced.

The coherence between the Reflected shock and the Passage shock is generally very low (below 0.4). However, under high suction settings (Full-suc, 66.7%-suc), it marginally reaches 0.6 at specific frequencies. A notable change occurs under lower suction settings: For the 33.3%-suc setting, the coherence escalates to above 0.6 within the 90 Hz to 200 Hz frequency band. For the 16.7%-suc setting, this high coherence band widens significantly (0 Hz to 500 Hz) and reaches above 0.8 between 90 Hz and 400 Hz. This increase in coherence confirms a high influence of the reflected shock on the passage shock at low suction conditions. This heightened correlation is directly related to the stronger interaction of the reflected shock with the upper wall and its merging with the passage shock. Further support for this mechanism is provided by the high coherence level (above 0.6) observed between the leading-edge shock and the reflected shock at 300 Hz.

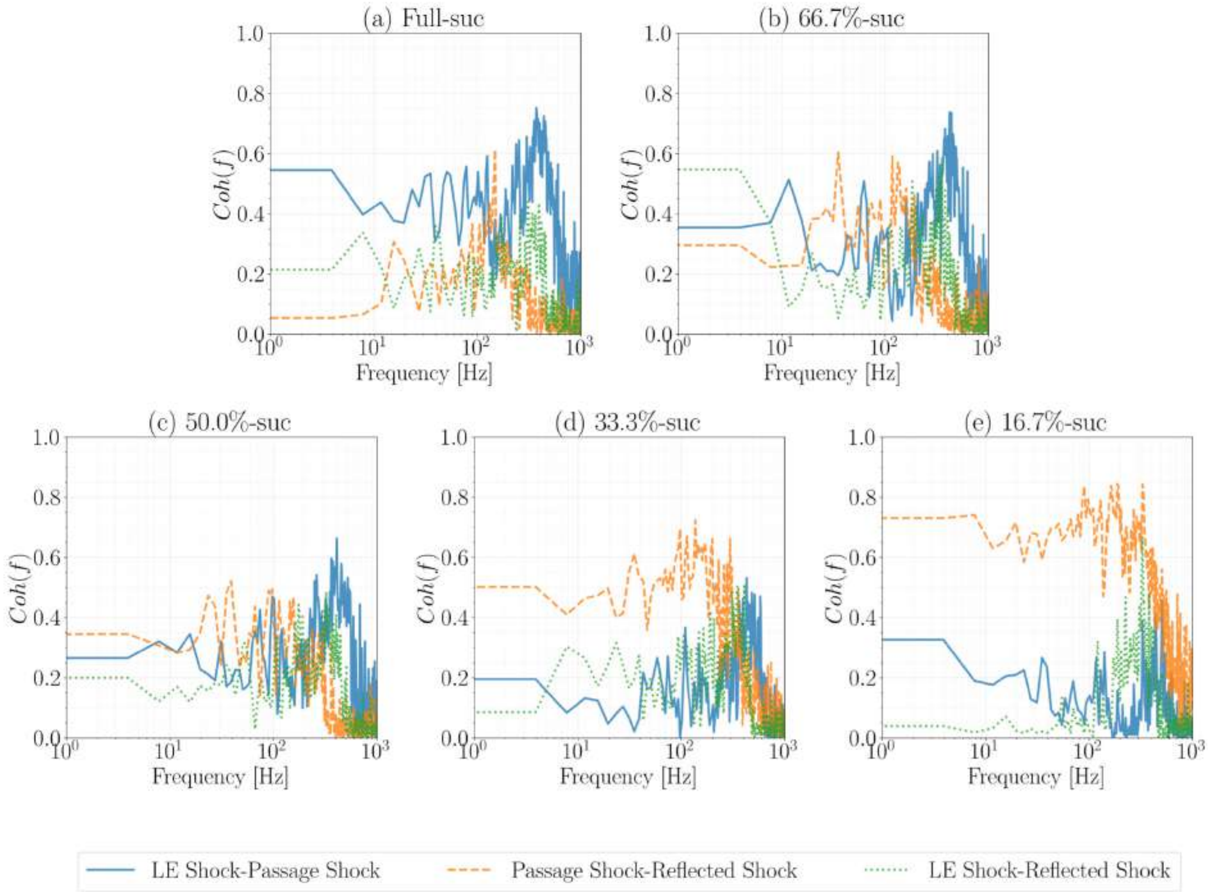

Figure 5.18: Coherance of the three shocks at the upper passage

The above Figures 5.16, 5.17, and 5.18, the oscillation of the passage shock is primarily coherent along its span. However, at certain frequency bands, localised flow instabilities or interactions induce differing dynamics across the shock's extent. The passage shock behaviour is influenced moderately by the leading-edge shock under high suction. Critically, the influence of the reflected shock becomes increasingly pronounced as the side wall suction is decreased. This is attributed to the reorganisation of the shock system (e.g., Leading-edge shock angle with the upper wall [177]) resulting from increased flow blockage, which enhances the reflected shock's interaction with the upper wall and leads to increased reflected shock instabilities and a stronger merging process with the passage shock.

5.5 Final operating configuration

Table 5.9: Final settings of the sensitivity analysis

Property	Final setting
LP angle of attack (α)	11.2 -0.6°
Upper channel area ratio ($A_{i/o}$)	0.83
LP x-position from throat	224 mm
UP (x, y)-position from LP LE	(49, 34) mm
Upper wall suction	100% suction
Lower wall suction	100% suction
Side walls suction	33% suction

The final settings, summarised in Table 5.9, were chosen to achieve the target flow structure and the design isentropic Mach number distribution of the cascade (Table 3.1).

It was demonstrated that a slight counter-clockwise rotation of the LP profile 0.6° improved the match between the experimental and design Mach number profiles, particularly in the throat region. This adjustment was necessary to achieve the correct initial leading-edge shock angle.

The upper channel profile setting (controlled by the area ratio $A_{i/o}$) dictates the flow in the upper passage between the upper profile and the test section wall. An area ratio of $A_{i/o} = 0.83$ was found to provide the desired flow acceleration in this passage and reduce the effect of boundary layer thickness on the upper wall even without the upperwall suction.

Full suction was applied to the upper and lower walls to minimise the boundary layer thickness in the flow direction and effectively reproduce a quasi-two-dimensional (2D) flow field in the core stream. Maximising this suction minimises wall blockage, which is essential for achieving the design static pressure recovery and ensuring the shock system is primarily driven by the profile geometry, as intended by the 2D cascade design.

The Side Walls suction was critically set to 33.3%. This setting was determined through the overall flow structure (presented in Figure 5.1) and pressure distribution (Mach number profile) were shown to be least sensitive to the side wall suction near the 33.3% setting.

The POD analysis provided critical insight into the shock interaction dynamics. A notable finding was the increased influence of the reflected shock upon the passage shock oscillation under conditions of low side wall suction.This influence was particularly dominant at the 16.7% suction setting. Such a dynamic was not considered during the initial aerodynamic design phase. This phenomenon is, however, critical for accurately understanding the shock dynamics within the cascade.Therefore, the 33.3% side wall suction setting was selected. This specific setting was chosen to balance the required flow structure with the need to minimise the reflected shock's dominating impact on the passage shock dynamics. This ensured that the primary source of measured unsteadiness remained the intended passage shock interaction with the boundary layer. Further investigation on Reynolds number and inflow turbulance intensity effects could be found in Appendix E

Chapter 6

Roughness effects on shock-boundary layer interaction

Surface roughness is known to significantly impact performance in turbomachinery. Blade surfaces rapidly accumulate roughness due to deposition, mechanical damage, and chemical effects. This surface condition introduces flow instabilities. The location of the laminar-turbulent transition is significantly altered. Consequently, both the aerodynamic performance and efficiency of the blade are impacted.

This chapter provides an overview of the influence of surface roughness on SBLI. Specific attention is given to the suction surface of a fan profile. The aerodynamic behaviour is the primary concern. The effects of roughness are specifically investigated concerning: The shock structure, The induced separation and The boundary layer characteristics and development.

The roughness study was carried out by replacing the lower profile with one of the profiles detailed in Chapter 3. Key operating conditions, including the profile location and inflow angle, were carefully verified to ensure consistency across all tests.

The detailed structure of the chapter is as follows:

- Section 6.1: The test section setup is evaluated to ensure that the geometric configuration of all mounted roughness profiles is consistent, thereby confirming that surface roughness is the sole variable influencing the flow structure and unsteadiness.
- Section 6.2: The effects of roughness on the overall shock wave position, structure, and induced separation are analysed.
- Section 6.3: The influence of roughness on the temporal characteristics and unsteadiness of the shock system is presented.
- Section 6.4: The resulting changes in the boundary layer properties (e.g., thickness, velocity profile) downstream of the SBLI are detailed.
- Section 6.5: The major conclusions regarding the SBLI-roughness interaction are summarised.

6.1 Test section setup evaluation

The extreme sensitivity of transonic shock structures to the geometric configuration of the test section was established in Chapter 5. Slight discrepancies in profile positioning, angular alignment, or passage mass flow distribution are known to precipitate significant alterations in flow stability and shock topology. The mounting of the various roughness profiles proved technically challenging, as minor geometric variations were introduced. These discrepancies were not immediately apparent during the experimental campaign and were only identified during the subsequent data analysis. Consequently, a comprehensive sensitivity analysis was performed to ensure a valid comparison across the five roughness configurations. The final measured positions are detailed in Table 6.1.

While the majority of the profiles fell within acceptable tolerance limits, specific variations were identified for Profiles P2-0.20Ra and P5-0.64Ra. Profile P2-0.20Ra exhibited the largest pitch value of 59.61 mm, which is approximately 1 mm greater than the average of the other test cases. This configuration was also characterised by a marginally higher angle of attack (10.80°) and stagger angle (44.88°). Similarly, Profile P5-0.64Ra displayed an increased angle of attack of 10.80°combined with a reduced stagger angle of 43.91°. These geometric deviations are significant in transonic regimes, as they directly modify the effective throat area and the local blockage.

Table 6.1: Profiles positions tested in the sensitivity analysis

Profile	LP-UP [mm] Δx	Δy	s [mm]	α [deg]	χ [deg]
P1-0.17Ra	48.11	33.3	58.51	10.57	44.74
P2-0.20Ra	49.23	33.6	59.61	10.80	44.88
P3-0.54Ra	48.00	34.0	58.82	10.69	44.12
P4-1.49Ra	47.27	33.2	57.76	10.66	44.26
P5-0.64Ra	47.45	33.6	58.13	10.80	43.91

The impact of these geometric disparities was further evidenced by the side-wall suction pressure requirements illustrated in Figure 6.1. Although the suction valve settings were held constant for Profiles P1, P2, P3, and P4, the recorded suction pressure for P2-0.20Ra was slightly elevated. Conversely, the suction pressure for P5-0.64Ra required adjustment to equalise the mass flow rate with the other profiles. These variations indicate that distinct local blockage effects were present, potentially masking the aerodynamic influence of the surface roughness itself. The presence of such confounding variables introduces uncertainty when comparing these two profiles to the wider dataset.

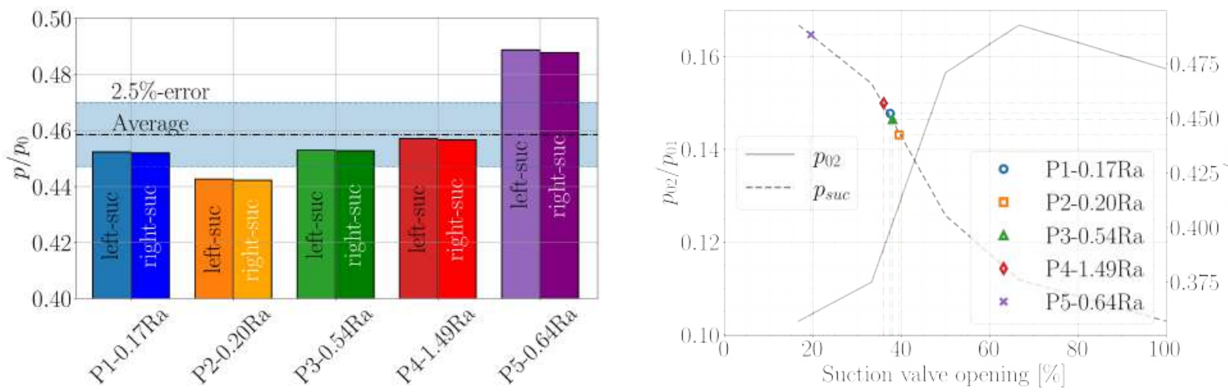

(a) Pressure on both profile sides

(b) Overall average pressure

Figure 6.1: Side wall suction pressure for different roughness profiles

To ensure the reliability of the core analysis, the results for Profiles P2-0.20Ra and P5-0.64Ra were analysed separately. The remaining three profiles (P1-0.17Ra, P3-0.54Ra, and P4-1.49Ra) possess distinct roughness scales while maintaining highly similar mounting positions and pneumatic requirements and will be the "baseline". This subset provides the most robust dataset for isolating the effects of surface roughness on shock structure and unsteadiness. Findings for P2 and P5 are presented as supplementary comparisons and are not utilised to formulate the primary conclusions regarding roughness-induced flow control.

6.2 Aerodynamic structure and shock topology

The time-averaged aerodynamic structure was first validated across the test profiles. Isentropic Mach number distributions were calculated from surface static pressure measurements and are presented in Figure 6.2 for profiles P1, P3, and P4. Uniformity of the inflow was confirmed by measurements taken upstream of the profile system (Figure 6.2a). The data curves were found to be coincident across all configurations, ensuring that the inlet conditions were held constant.

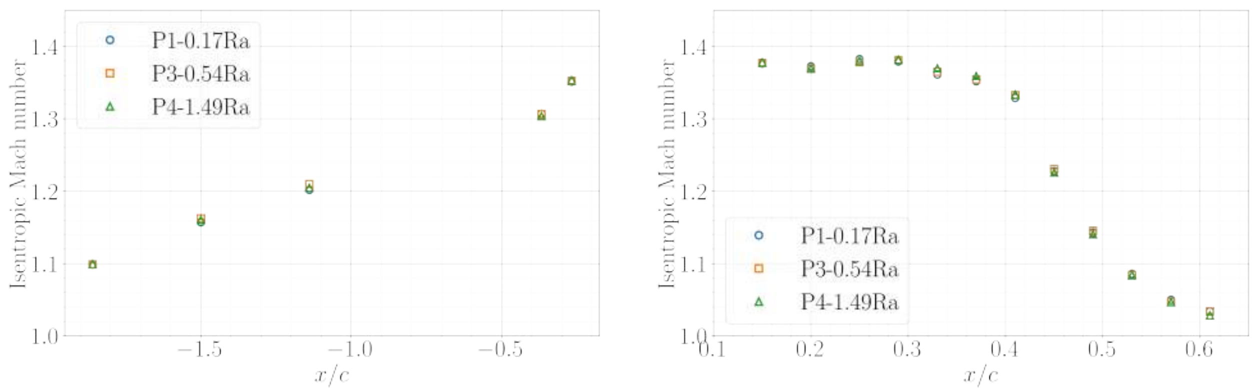

(a) Nozzle upstream of the lower profile

(b) On lower profile

Figure 6.2: Isentropic Mach number for different roughness profiles

On the suction side of the lower profile (Figure 6.2b), an extensive overlap of the pressure distributions is observed. This high degree of congruence indicates that the mean shock position and the global Mach number field are effectively identical for all tested profiles. The characteristic pressure smearing associated with the SBLI exhibits no measurable variation. Consequently, it is inferred that surface roughness exerts only a negligible influence on the time-averaged pressure field in the mid-span region.

Furthermore, no conclusive evidence of a premature laminar-to-turbulent transition was detected for the roughest profile (P4-1.49Ra). A marginal increase in the Mach number of approximately 0.01 was noted between 0.33 and 0.37 x/c for P4 relative to P1 and P3. However, this value is considered too small to be definitive and may be attributed to measurement uncertainty. This suggests that the roughness scale is insufficient to markedly alter the boundary layer development upstream of the shock foot under the investigated conditions.

The two profiles characterised by geometric discrepancies, P2-0.20Ra and P5-0.64Ra, exhibit distinct isentropic Mach number distributions compared to the established "baseline" (Figure 6.3). Despite these variations, consistent inflow conditions are confirmed by upstream nozzle measurements (Figure 6.3a) and the coincident data at 0.15 x/c. Furthermore, an identical average shock location is suggested by the Mach number agreement at 0.45 x/c. However, the suction side distribution reveals significant deviations from the baseline between 0.20 and 0.41 x/c. A significant aerodynamic effect is not expected for Profile P2, as its roughness scales are comparable to the baseline P1-0.17Ra. Similarly, the surface texture of Profile P5-0.64Ra is closely matched to Profile P3-0.54Ra. Consequently, the mounting discrepancies are identified as the primary factor responsible for the observed Mach number shifts in both P2 and P5.

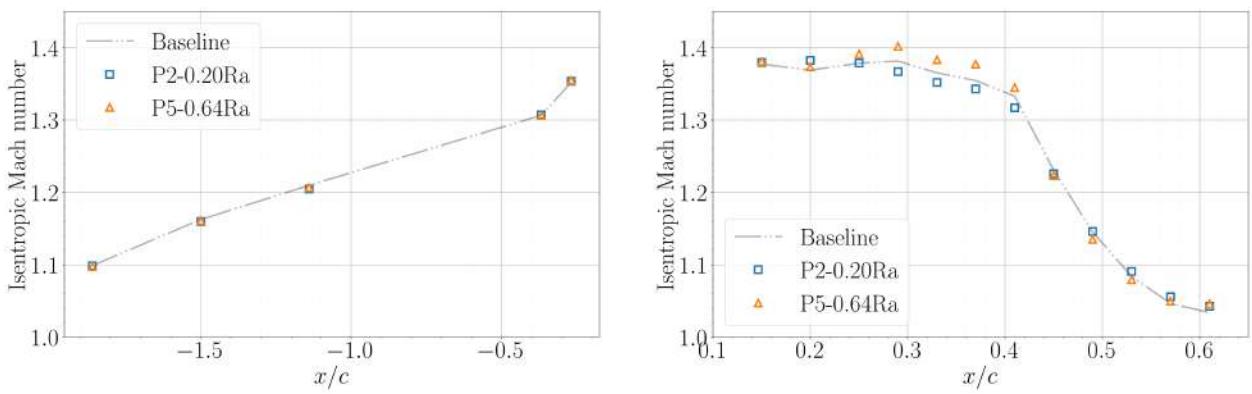

(a) Nozzle upstream of the lower profile

(b) On lower profile

Figure 6.3: Isentropic Mach number for (P2-0.20Ra) and (P5-0.64Ra)

A significant acceleration of the flow is observed for P5-0.64Ra between 0.25 and 0.41 x/c. The increase in Mach number reaches a peak of approximately 0.025 at 0.37 x/c, followed by a marginal decrease of less than 0.01 between 0.49 and 0.57 x/c. Although the reduction in suction pressure (and the resulting higher AVDR) was initially expected to influence the shock position, the observed Mach number increase is primarily attributed to geometric deviations. The combination of a higher angle of attack and a lower stagger angle appears to increase the passage mass flow rate, driving the local flow acceleration.

In contrast, a decrease in Mach number is recorded for P2-0.20Ra within the 0.20 to 0.41 x/c range, reaching a maximum deficit of 0.015 at 0.41 x/c. The larger pitch, combined with the relatively higher stagger and angle of attack, is found to restrict the effective throat area and reduce the passage mass flow rate. The higher suction pressure observed for P2 is thus a secondary effect of the increased geometric blockage rather than an independent operational change.

Instantaneous schlieren images, averaged over 50 random snapshots, are presented in Figure 6.4 for P1, P3 and P4. A strong similarity in the time-averaged shock structure is confirmed across all three cases: the leading-edge shock is consistently located approximately 5 mm upstream of the Lower Profile leading edge (LP-LE); the passage shock is positioned within 40 mm to 50 mm downstream of the LP-LE; and the reflected shock is observed to be almost merged with the passage shock 45 mm to 50 mm above the LP-LE.

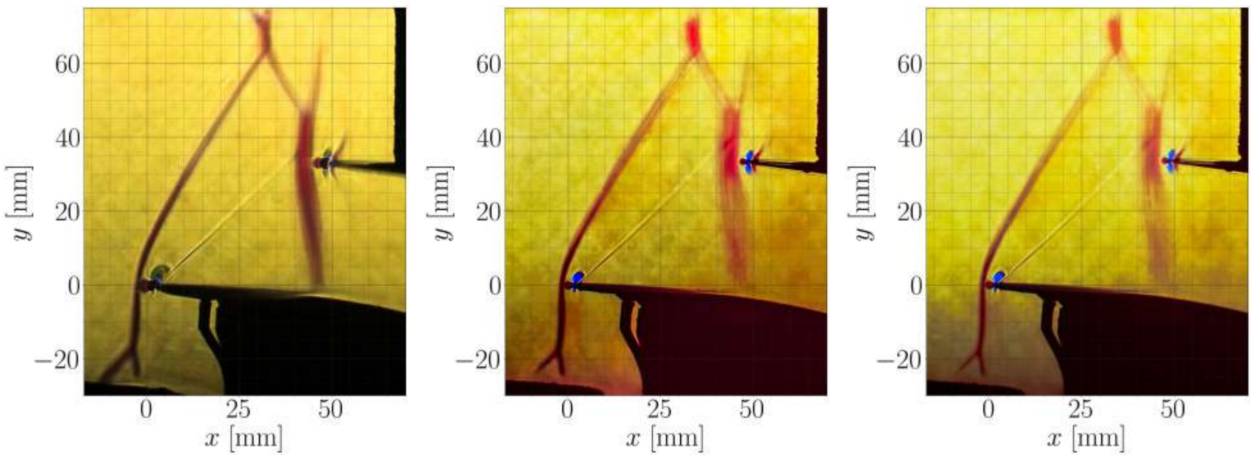

(a) P1-0.17Ra (b) P3-0.54Ra (c) P4-1.49Ra

Figure 6.4: Schlieren images for the baseline cases

While the mean positions are fixed, critical differences are observed in the shock contrast. The passage shock in the smoothest case (P1-0.17Ra) exhibits the highest contrast in the average image. This implies a high degree of spatial coherence and low oscillation amplitude. Conversely, the shock appears more blurry in P3-0.54Ra and is almost disappeared (fully smeared out) in the roughest case (P4-1.49Ra). This significant reduction in mean image contrast is a direct, qualitative indicator of higher time-averaged shock oscillation amplitude and substantially increased unsteadiness for the rougher profiles. This visual evidence suggests a significant influence of roughness on the aerodynamic damping mechanism of the shock system, which will be quantitatively analysed in the next section.

A noticeable change in the shock structure is observed for Profiles P2-0.20Ra and P5-0.64Ra when compared to the baseline configuration, as illustrated in the averaged Schlieren visualisations (Figure 6.5). For Profile P2-0.20Ra, the passage shock interacts with the lower profile between 40 mm and 50 mm downstream of the leading edge, which is consistent with the baseline. However, the leading-edge shock is observed to translate downstream to the exact location of the leading edge (0 mm), whereas it is positioned approximately 4 to 5 mm upstream in the baseline case.

Furthermore, the reflected shock for P2 is observed to merge with the passage shock at a higher vertical coordinate, approximately 50 to 55 mm above the profile surface. Significant smearing of the reflected shock is also evident, which is interpreted as a manifestation of increased shock unsteadiness.

Similarly, distinct deviations in shock topology are identified for Profile P5-0.64Ra. While the passage shock remains at a similar chordwise position (40 to 50 mm), the leading-edge shock is

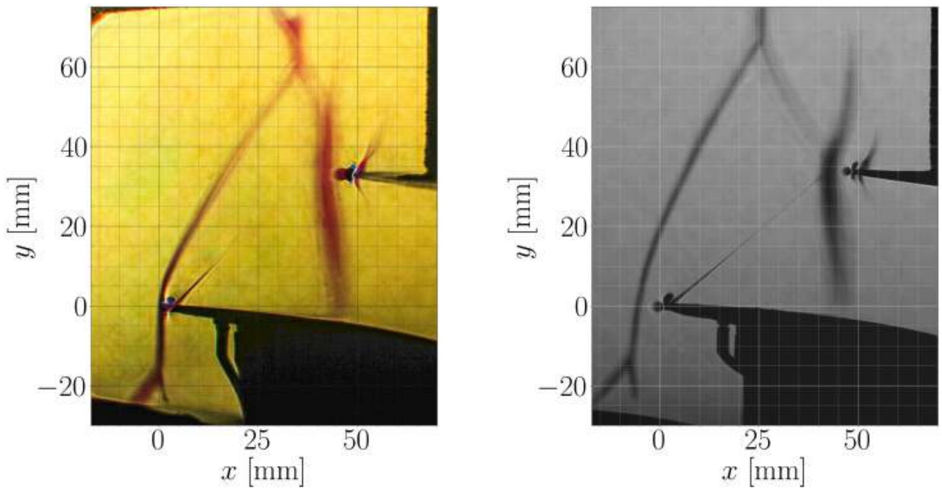

(a) P2-0.20Ra (b) P3-0.64Ra

Figure 6.5: Average schlieren images for (P2-0.20Ra and P5-0.64Ra)

forced approximately 6 to 7 mm upstream of the leading edge. The lower portion of this shock exhibits a more normal orientation relative to the profile surface compared to the baseline. Additionally, the reflected shock merges with the passage shock at a lower vertical position of approximately 40 mm.

These topological shifts confirm that the shock structure is dominated by the altered mass flow distribution and local blockage effects rather than surface roughness. The detachment distance and shock merging points are clearly dictated by passage-scale blockage. Consequently, these effects are independent of the micro-scale roughness influences investigated in the primary study.

The time-averaged separation topology is illustrated by the oil-flow visualisation presented in Figure 6.6. The existence of a separation bubble induced by the SBLI is confirmed in all cases. The stagnation zone onset (representing the time-averaged separation line) is located consistently around 0.37 x/c at the midspan for all three profiles. Similarly, the separation zone terminates at a similar location, approximately 0.52 x/c, aligning with the observed pressure plateau stability (Figure 6.2b).

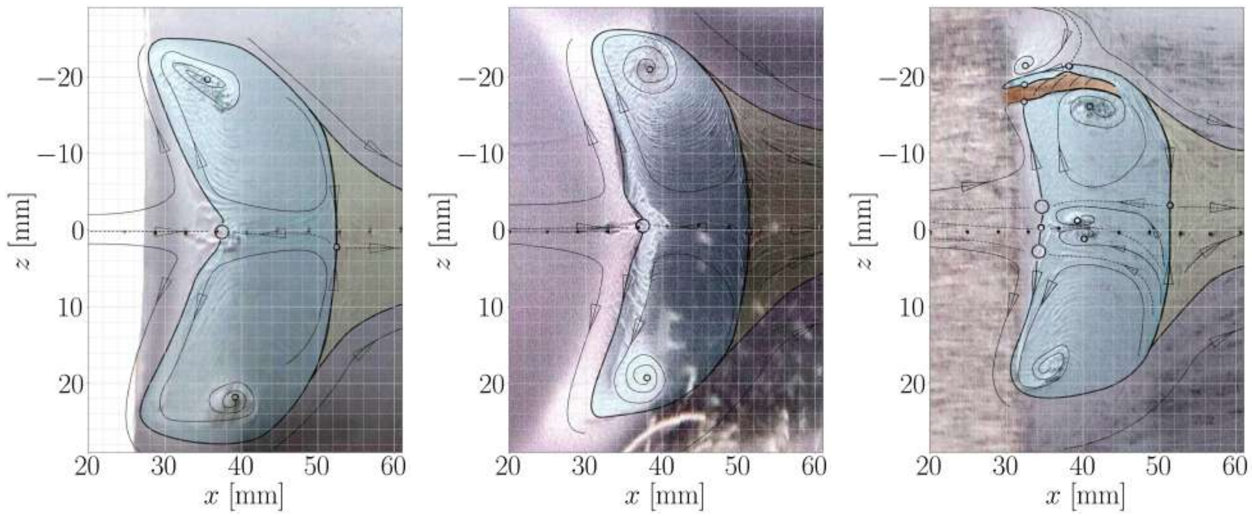

(a) P1-0.17Ra (b) P3-0.54Ra (c) P4-1.49Ra

Figure 6.6: Oil-flow visualisation for separation area on lower profile surface of baseline cases

However, the spanwise flow topology is markedly altered by the increasing roughness. The separation line reveals a noticeable V-shape in cases P1-0.17Ra and P3-0.54Ra, where the separation is slightly retarded towards the mid-span due to the influence of passage secondary flows. Conversely, in P4-1.49Ra, the separation line is remarkably straighter and more orthogonal to the flow direction across the measured span. This observation suggests that the substantial roughness-induced three-dimensional effects in P4-1.49Ra have become the dominant mechanism, effectively overriding the spanwise influence of the end-wall secondary flows observed in the smoother profiles.

Cases P1-0.17Ra and P3-0.54Ra show a relatively sorted and two-dimensional separation zone, spanning approximately 24 mm from the centreline. In contrast, case P4-1.49Ra exhibits a highly chaotic structure with multiple scattered nodes and saddle points. This indicates severe three-dimensional separation in the region of the SBLI. A large, vortex-like flow structure is evident, which acts to disrupt the integrity of the separation bubble. This specific local flow feature could be attributed to the non-uniformity of the measured macro-roughness in that region, where high peak-to-valley heights (Sz) were documented to be asymmetric across the profile span, as discussed in detail in Section 3.5. The three-dimensional mixing could be enhancing the transportation of high-momentum fluid toward the wall a phenomenon report by Dussauge and Piponniau [178]. This mechanism effectively re-energises the boundary layer, leading to a local flow structure that is more resistant to separation caused by the adverse pressure gradient.

Table 6.2: Separation size of baseline cases

	P1-0.17Ra	P3-0.54Ra	P4-1.49Ra
As/Ap [%]	8.8	8.7	8.1

The resulting separation zone size, quantified as a percentage of the total suction area (A_s/A_p), is summarised in Table 6.2. The separation area is smallest for the roughest profile (P4-1.49Ra) at 8.1%, compared to 8.8% for P1-0.17Ra and 8.7% for P3-0.54Ra. This shrunken separation zone for the roughest case is consistent with the concept that the roughness-induced three-dimensional effects generate stronger secondary flows which act to contain the separation bubble more effectively, leading to a smaller overall time-averaged separation area.

The separation topologies of Profiles P2-0.20Ra and P5-0.64Ra oil-flow visualisation is depected in Figure 6.7. For Profile P2-0.20Ra, the separation line is observed to be more V-shaped and is skewed relative to the mid-span. A delay in the separation onset is recorded at the mid-span (0.40 x/c). Although the suction pressures on both side-walls are nearly identical, the separation nodes are found to be asymmetrically shifted towards the walls, and the saddle points are non-centrally aligned. The chordwise extent of the separation at the mid-span is restricted to 0.52 x/c. The resulting separation area ratio is approximately 7%, which is significantly smaller than the baseline value. This reduced separation size is attributed to a weakened SBLI stemming from the lower local Mach number previously identified for this configuration.

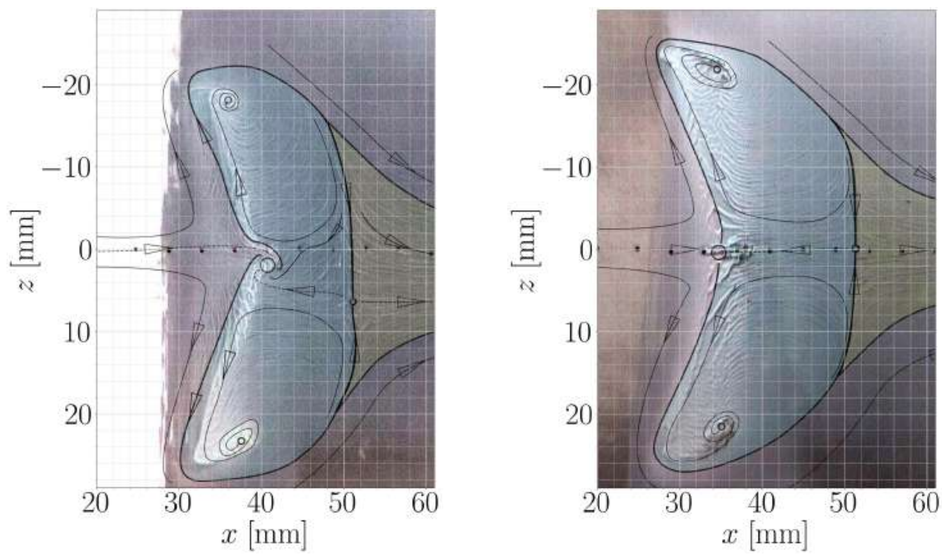

(a) P2-0.20Ra (b) P5-0.64Ra

Figure 6.7: Oil-flow visualisation for separation area for (P2-0.20Ra and P5-0.64Ra)

In contrast, the separation line for Profile P5-0.64Ra is observed to be straighter and exhibits less spanwise skewness. The onset of separation is identified much earlier than in the baseline case, occurring at approximately 0.33-0.34 x/c. The separation zone is found to be more symmetric and organized, possessing a structure comparable to Profile P1-0.17Ra. The separation area ratio is measured at 8.7%, which is consistent with the values recorded for Profiles P1 and P3. This topology is attributed to a stronger interaction, facilitated by the flow acceleration and higher pre-shock Mach number associated with the geometric mounting of this profile.

6.3 Impact on unsteady shock dynamics

The temporal behaviour of the passage shock was investigated using time-resolved schlieren imaging captured at high frame rates (P1 at 15 kHz, P3 at 5 kHz, and P4 at 10 kHz). The shock wave was tracked at a consistent height of 5 mm above the Lower Profile leading edge (LP-LE). The resulting tracking statistics are summarised in Table 6.3.

Table 6.3: Passage shock tracking parameters for baseline cases

Profile	Accuracy [mm/px]	shock angle [deg]		shock displacement [mm]		
		$\overline{\theta}$	$\sigma(\theta)$	$\max\lvert x_{shock}\rvert$	$\overline{\max\lvert x_{shock}\rvert}$	$\sigma(x_{shock})$
P1-0.17Ra	0.12	93.83	4.34	12.37	7.22	2.39
P3-0.54Ra	0.13	94.59	3.04	11.84	6.34	2.70
P4-1.49Ra	0.13	92.18	4.53	15.95	10.15	5.25

Consistency in the mean flow conditions is confirmed by the shock angle measurements. Across all cases, the mean shock angle ($\overline{\theta}$) remains approximately 94°, with minor fluctuations ($\sigma \approx 4$). This stability indicates that the upstream Mach number and the overall shock strength are effectively constant over the measurement period, regardless of the surface roughness.

Significant differences arise in the oscillation amplitude. The roughest profile (P4-1.49Ra) exhibits the highest instability, characterised by a global maximum displacement ($\max|x_{shock}|$) of 15.95 mm. This represents an increase of 3.6 mm compared to the smoothest profile (P1-0.17Ra). To provide a robust metric less sensitive to individual outliers, the average maximum displacement ($\overline{\max|x_{shock}|}$) was calculated. This metric is derived by segmenting the signal into N windows of length k:

$$\overline{\max|x_{shock}|} = \frac{1}{N}\sum_{j=1}^{N}[\max|x_{shock}|_{n:n+k}]_j \tag{6.1}$$

Based on this reliable metric, P4-1.49Ra again shows the highest amplitude (10.15 mm), confirming the destabilising effect of large-scale roughness. This high amplitude is also reflected in the standard deviation (σ) of the shock position.

Interestingly, the smoothest profile (P1-0.17Ra) exhibits the second-highest oscillation amplitude (7.22 mm), exceeding that of the intermediate roughness case (P3-0.54Ra, 6.34 mm). However, P1 has the lowest standard deviation ($\sigma = 2.39$ mm). This statistical combination suggests that while the shock in P1 is generally stable, it is subject to occasional, high-amplitude excursions. This intermittent behaviour is often characteristic of laminar or transitional SBLIs, where the separation bubble can undergo low-frequency "breathing" cycles. The intermediate case (P3) shows moderate values comparable to P1, suggesting that at this roughness level (Ra=0.54 µm), the profile behaves largely as hydraulically smooth.

The frequency content of the shock motion is analysed in Figure 6.8. The displacement PSD (Figure 6.8a) reveals that the high amplitude observed in the rough case (P4) is dominated by low-frequency contributions, specifically a peak near 10 Hz. In contrast, P1 and P3 show comparable low-frequency behaviour, although P3 exhibits slightly more energetic peaks at specific frequencies (e.g., 8, 15, 27, 73 Hz).

The normalised PSD (Figure 6.8b) identifies a common characteristic frequency band for all profiles, ranging between 270 Hz and 380 Hz. The smoothest profile (P1) appears most strongly influenced by this characteristic frequency. This sensitivity in the smooth case may be linked to

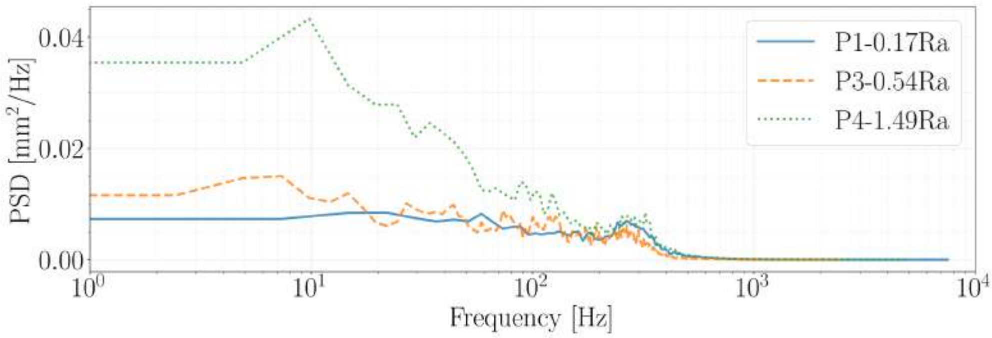

(a) Shock displacement PSD

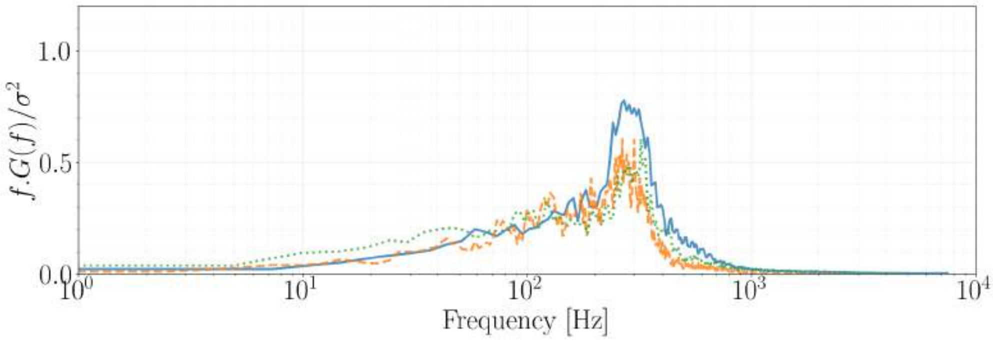

(b) Shock normalized-PSD

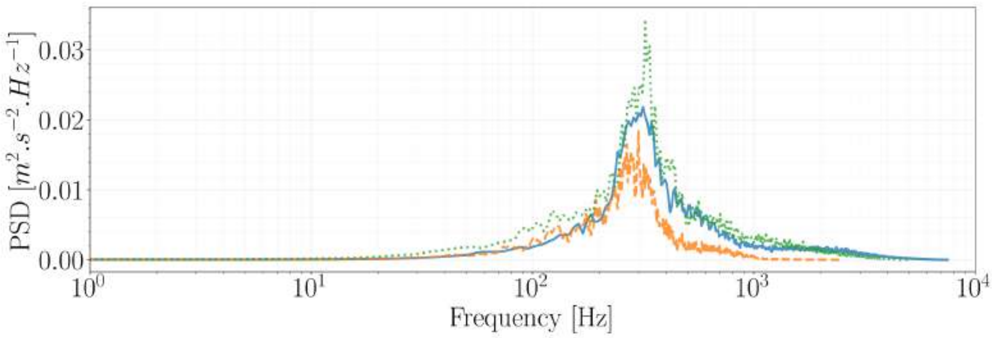

(c) Shock velocity PSD

Figure 6.8: Shock PSD analysis for different roughness profiles

an acoustic feedback mechanism, which is known to drive oscillations in laminar SBLIs. In the rougher cases, the boundary layer disturbances likely disrupt this feedback loop, introducing new, broadband signals generated by the roughness-induced turbulence.

The shock velocity PSD (Figure 6.8c) further emphasises this characteristic band. The high velocity amplitude for P4 at these frequencies indicates that while the displacement is dominated by low frequencies, the shock experiences rapid acceleration events driven by the characteristic instability.

The shock tracking parameters for Profiles P2-0.20Ra and P5-0.64Ra are summarised in Table 6.4. The mean passage shock angle ($\overline{\theta}$) is found to be consistent with the baseline range, although the standard deviation for P5-0.64Ra indicates slightly higher angular fluctuations. Both profiles exhibit higher maximum and average maximum displacements compared to the baseline cases. Specifically, a average maximum displacement of 8.36 mm is recorded for P2-0.20Ra, while 8.39 mm is measured for P5-0.64Ra. These values represent an increase of approximately 1-2 mm over the profiles with comparable roughness scales.

The spectral characteristics of these oscillations are illustrated in the PSD analysis in Figure 6.9 with P1-0.17Ra graph as a reference scale. In Figure 6.9a, the displacement PSD reveals that Profile P2-0.20Ra possesses relatively higher energy levels at low frequencies, specifically below 100 Hz, compared to Profiles P1-0.17Ra and P5-0.64Ra. These energy levels are found to be comparable to those recorded for the rougher Profile P3-0.54Ra. While the frequency ranges of the low-frequency

Table 6.4: Passage shock tracking parameters for (P2-0.20Ra and P5-0.64Ra)

Profile	Accuracy [mm/px]	shock angle [deg]		shock displacement [mm]		
		$\overline{\theta}$	$\sigma(\theta)$	max $\lvert x_{shock}\rvert$	$\overline{\max \lvert x_{shock}\rvert}$	$\sigma(x_{shock})$
P2-0.20Ra	0.12	94.55	3.67	14.63	8.36	3.21
P5-0.64Ra	0.14	92.68	4.91	13.76	8.39	3.09

peaks are consistent with the baseline cases, the correlation between these peaks and the reflected shock is more pronounced for Profile P2-0.20Ra.

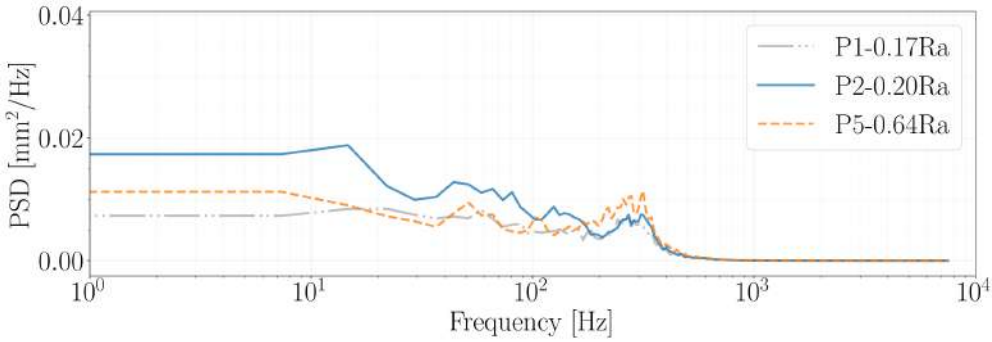

(a) Shock displacement PSD

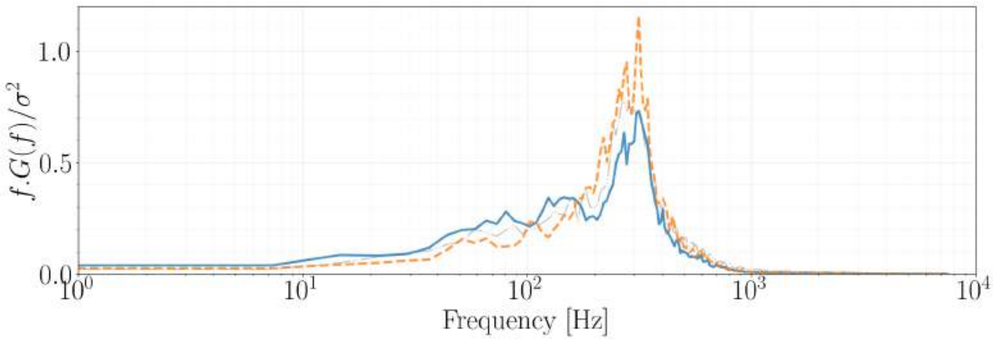

(b) Shock normalized-PSD

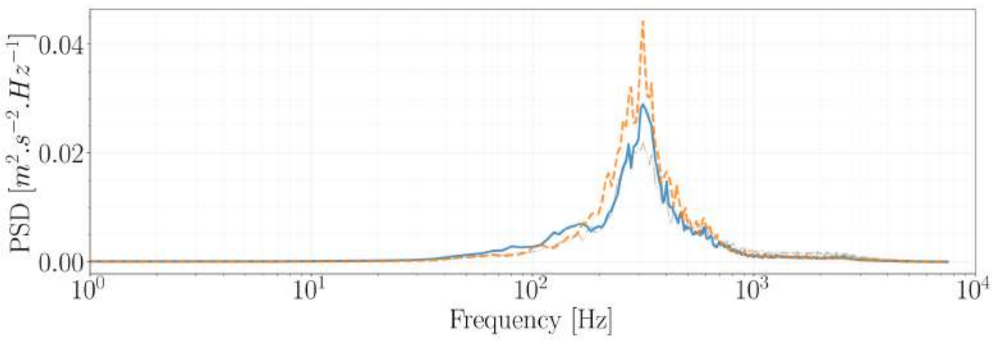

(c) Shock velocity PSD

Figure 6.9: Shock PSD analysis for (P2-0.20Ra and P5-0.64Ra)

A distinct λ-foot is observed at the upper wall reflection point for Profile P2-0.20Ra in the schlieren visualisations (see Figure 6.5a). This structure is accompanied by high signs of unsteadiness, which are absent in the more stable baseline configurations. Consequently, the low-frequency energy is likely driven by the dynamics of the reflected shock. This behaviour is attributed to the geometric blockage and the resulting mass flow instabilities previously identified in the upstream measurements and discussed in Section 5.4.2.

Despite variations in low-frequency energy between Profiles P2 and P5, a nearly identical dominant frequency peak is exhibited by both configurations. While the low-frequency content in Profile P5-0.64Ra is found to be less energetic than in Profile P2, the characteristic frequency of the interaction is more prominently defined. This dominant mode is further elucidated in the weighted PSD and shock velocity PSD analysis in (Figures 6.9b and 6.9c). A distinct peak is observed between 300 Hz and 350 Hz for both configurations similar to the baseline profiles. The amplitudes of this peak are observed to exceed those of the baseline profiles P3 and P4. This is particularly significant for Profile P5, as its roughness scale is comparable to Profile P3.

This frequency range is physically attributed to the dynamic response of the separation bubble and the instability of the shear layer within the interaction region. These dynamics may be influenced by the behaviour of the reflected shock, which is observed to merge in a lower point to passage shock. As discussed in Section 5.4.2, this lower merging point results in a more stable reflected shock with a diminished impact on the passage shock unsteadiness. A noticeable increase in the dominant frequency peak is subsequently facilitated by this increased stability. Consequently, the heightened spectral amplitudes in P5 are most likely to be as a consequence of the modified passage aerodynamics rather than an effect of the micro-scale surface roughness.

To investigate the intermittency of these oscillations, a CWT analysis was performed, as illustrated in Figure 6.10. For the smoothest profile (P1-0.17Ra), the spectra are characterised by steady, low-energy peaks centred around 300 Hz, interspersed with occasional, random, short-duration events in the lower frequency bands between 70 Hz and 300 Hz. In the intermediate case (P3-0.54Ra), the characteristic frequency band (200-300 Hz) exhibits high amplitude peaks, yet these occur less frequently, indicating a higher degree of intermittency compared to P1. This is accompanied by a higher density of low-amplitude events extending across the lower frequency range.

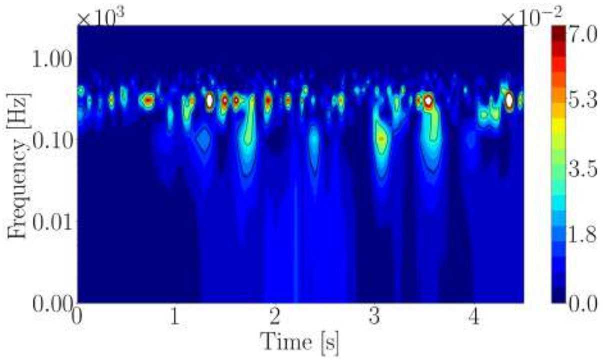

(a) P1-0.17Ra

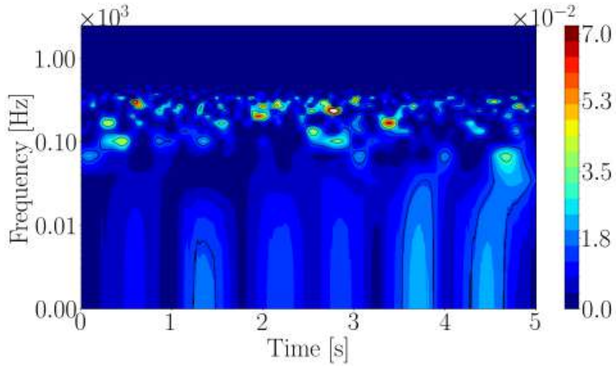

(b) P3-0.55Ra

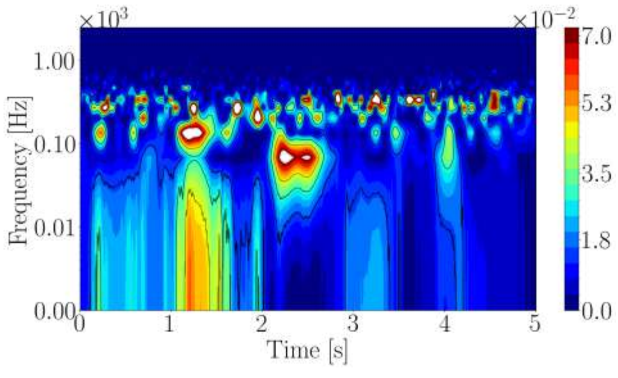

(c) P4-1.48Ra

Figure 6.10: Temporal analysis for shock unsteadiness for baseline profiles

Conversely, the roughest profile (P4-1.49Ra) displays the most aggressive dynamic behaviour. High-energy peaks at the characteristic frequency are observed to be both frequent and intense. Furthermore, strong local peaks are evident across a broad range from 70 Hz up to 300 Hz. This broadband spectral content indicates a significant increase in the number of unsteadiness contributors associated with the rough surface. This complexity suggests that the shock dynamics for rough surfaces are inherently less predictable and potentially more difficult to control than those observed over smooth surfaces.

The temporal evolution of the shock unsteadiness of profiles (P2-0.20Ra) and (P5-0.64Ra) is presented in Figure 6.11. For Profile P2-0.20Ra, energy is primarily concentrated in an intermittent band centred around 300 Hz. This frequency mode is punctuated by periodic, high-amplitude bursts at lower frequencies, specifically near 100 Hz. These low-frequency events are most prominent between $\tau = 1.8$ s and $\tau = 2.2$ s.

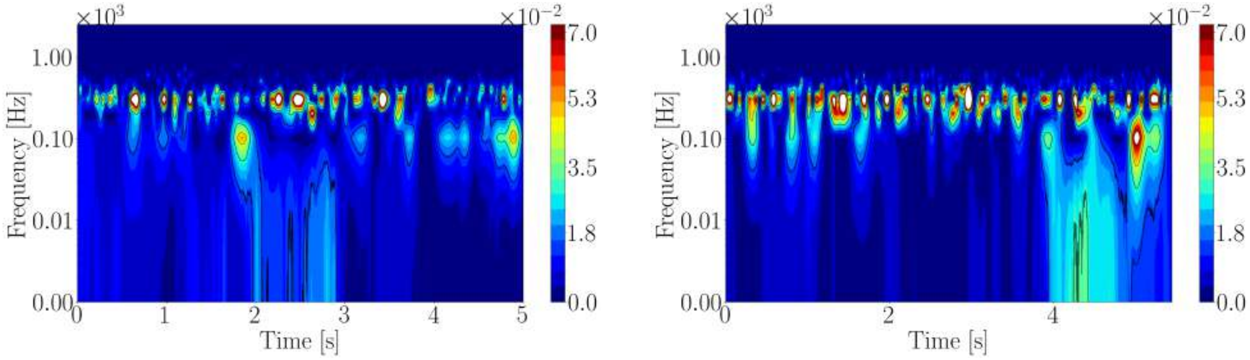

(a) P2-0.20Ra

(b) P5-0.64Ra

Figure 6.11: Temporal analysis for shock unsteadiness for (P2-0.20Ra and P5-0.64Ra)

In contrast, Profile P5-0.64Ra exhibits a more sustained and energetic distribution of power around the dominant frequency of 300-350 Hz. The spectral peaks within this band are observed to be more temporally dense than those recorded for Profile P2. A significant transient event is recorded for Profile P5-0.64Ra toward the end of the sampled duration. Between $\tau = 4.2$ s and $\tau = 4.8$ s, a high-amplitude energetic peak is observed, which extends down to 100 Hz. This duration-specific unsteadiness suggests a temporary increase in the separation bubble volume or a transient mass flow fluctuation within the passage. Despite this event, the overall CWT signature confirms that the unsteadiness in P5 is more regular and governed by the dominant-frequency response of the interaction region.

6.4 Boundary layer characteristics

The development of the boundary layer was investigated to quantify the influence of surface roughness on the viscous flow evolution. Velocity profiles were acquired using LDA at three distinct streamwise locations: 0.25 x/c, 0.60 x/c, and 0.75 x/c. These locations were selected to capture the flow state upstream of the shock, within the reattachment zone, and in the fully developed wake region, respectively as described in Section 2.3.4. The resulting velocity profiles, normalised by the free-stream velocity (u_∞), are presented in Figure 6.12. The full boundary layer data set can be found in Appendix D.

The boundary layer at 0.25 x/c was expected to be laminar and extremely thin. Consequently, significant challenges were encountered during the data acquisition as detailed in Section 2.3.4. However, reliable data points were successfully captured through the application of filtering very low speed particles and Gaussian Mixture Model filtering technique, as detailed in Section 4.4.1.

The profile shapes for the smooth profile, P1-0.17Ra, and the intermediate roughness, P3-0.54Ra, exhibit a gradual velocity gradient consistent with a classic laminar boundary layer development. In contrast, the profile for the roughest case, P4-1.49Ra, displays a noticeably steeper gradient . This modification suggests a local alteration of the near-wall flow field.

Table 6.5: Boundary layer parameters at 0.25 x/c

Profile	δ [mm]	τ_w	Δu^+	Re_k
P1-0.17Ra	0.24	243.552	0.553	16
P3-0.54Ra	0.29	230.664	1.391	48
P4-1.46Ra	0.23	243.040	2.878	138

Estimated boundary layer parameters are summarised in Table 6.5. While the calculated δ values appear similar, the derived parameters, such as the roughness Reynolds number (Re_k), must

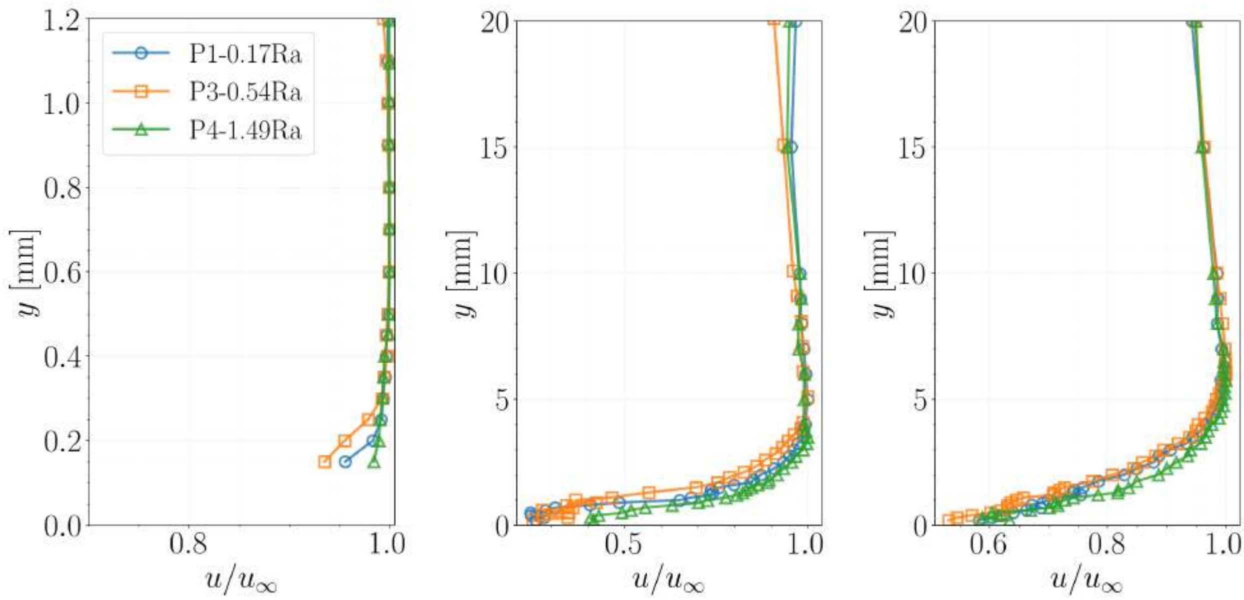

(a) 0.25 x/c (b) 0.60 x/c (c) 0.75 x/c

Figure 6.12: Boundary layer velocity profiles at different locations of the shock

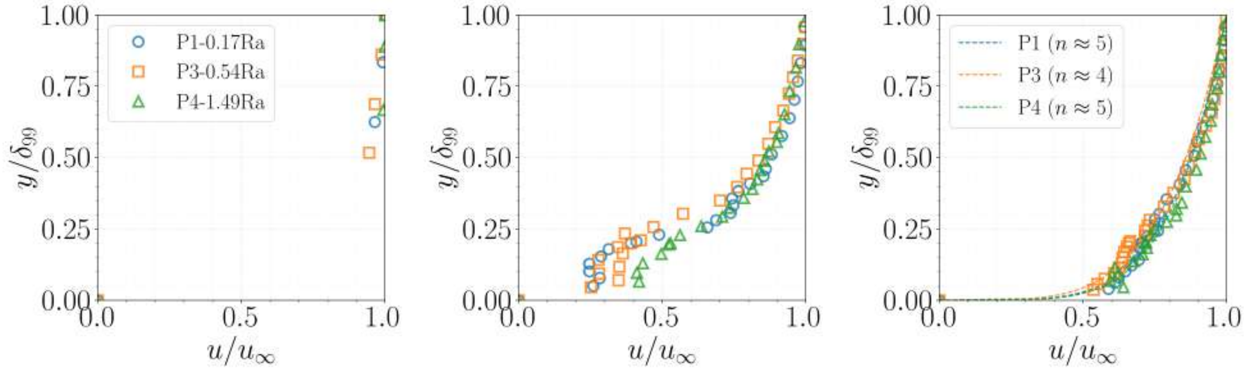

(a) 0.25 x/c (b) 0.60 x/c (c) 0.75 x/c

Figure 6.13: Normalised boundary layer velocity profiles

be treated with caution, which simplifies the complex three-dimensional nature of the roughness elements and ignores their specific shape or lay direction. Furthermore, the Re_k values are derived from a limited dataset; therefore, Re_k should be considered an indicative estimation of the roughness regime rather than a precise measure of the immediate flow state. The high value of $Re_k \approx 138$ for P4-1.49Ra merely indicates that the flow operates in a regime where roughness is expected to induce turbulence.

Despite the ambiguity arising from the sparse velocity data and the estimated parameters, the global nature of the flow interaction is governed by the time-averaged pressure field. The existence of a mean pressure plateau observed in the isentropic Mach number distribution (Figure 6.2b) confirms that the flow separation remains characteristic of a laminar separation bubble for all cases. Therefore, regardless of the local profile modification detected in the limited P4-1.49Ra data at 0.25 x/c, the overall SBLI is classified as a laminar-type interaction, driven by the specific pressure field imposed by the shock wave. The boundary layer, whether laminar or highly disturbed-transitional upstream, all separates due to the adverse pressure gradient.

The profiles at 0.60 x/c corresponds to the flow reattachment zone, immediately downstream of the separation bubble. The velocity profiles are presented in Figure 6.12b and the normalised versions in Figure 6.13b.

All profiles exhibit a velocity deficit near the wall. This inflection is a characteristic signature of the recent flow separation. The flow is in a state of recovery. However, a marked difference is

Table 6.6: Boundary layer parameters at 0.60 x/c

Profile	δ [mm]	δ^{*} [mm]	δ^{**} [mm]	H_k	δ_E[mm]
P1-0.17Ra	3.91	0.988	0.420	2.35	0.674
P3-0.54Ra	4.28	1.202	0.540	2.23	0.859
P4-1.49Ra	3.01	0.705	0.371	1.90	0.619

Table 6.7: Boundary layer parameters at 0.75 x/c

Profile	δ [mm]	δ^{*} [mm]	δ^{**} [mm]	$H_{k,opt}$	δ_E [mm]	Re_k	k_s^+
P1-0.17Ra	4.94	0.823	0.540	1.40	0.951	15.24	0.560
P3-0.54Ra	5.31	0.928	0.591	1.45	1.026	44.53	1.655
P4-1.49Ra	4.37	0.676	0.435	1.38	0.772	126.95	4.812

observed in the recovery rate between the profiles. The roughest profile (P4-1.49Ra) displays a significantly steeper velocity gradient compared to the smoother cases. The near-wall velocity for P4 recovers to the free-stream value over a shorter vertical distance. This provides quantitative evidence of a faster flow reattachment process.

The integral parameters calculated at this location are presented in Table 6.6. The physical thickness of the boundary layer (δ) varies significantly. P1 and P3 exhibit thicknesses of 3.91 mm and 4.28 mm, respectively. In contrast, the boundary layer for P4 is notably thinner at 3.01 mm. This reduction in thickness is attributed to the reduction of the separation bubble size, as discussed in the oil flow analysis. A smaller separation bubble results in a smaller vertical displacement of the shear layer, leading to a thinner reattached boundary layer.

The Shape Factor (H_k) at this location, P1 and P3 possess high shape factors of 2.35 and 2.23, respectively. These values are typical of a boundary layer that is barely attached or on the verge of separation. Conversely, P4 exhibits a shape factor of 1.90. A value below 2 in this region indicates a "fuller", more robust profile. This confirms that the enhanced turbulent mixing generated by the large roughness elements has effectively re-energised the boundary layer, accelerating its recovery to a stable state.

At 0.75 x/c, near the trailing edge, the boundary layers have evolved into fully developed turbulent profiles, as shown in Figure 6.12c. The normalised profiles in Figure 6.13c demonstrate a high degree of similarity in shape across all roughness levels. This similarity is consistent with the self-preserving nature of equilibrium turbulent flows.

Despite the similarity in shape, the integral parameters in Table 6.7 reveal persistent differences in the boundary layer scale. The boundary layer thickness (δ) for P4 remains the lowest 4.37 mm, compared to 4.94 mm for P1 and 5.31 mm for P3. The momentum thickness (δ^{**}), which represents the total momentum deficit, is also lowest for the roughest profile (P4). This result initially appears counter-intuitive, as surface roughness typically increases skin friction and, consequently, momentum loss. However, in this specific flow topology, the momentum deficit is dominated by the history of the separation bubble. Since P4 generated a significantly smaller separation zone (Table 6.2), the integrated momentum loss associated with the separation was much lower. This reduction in separation loss outweighed the increased local skin friction loss caused by the roughness elements.

The shape factors were re-evaluated using an optimisation function based on the turbulent power law ($H_{k,opt}$) using Equation 4.31. The resulting values are all close to 1.4, which is the canonical value for a zero-pressure-gradient turbulent boundary layer. The slightly higher value for P3 (1.45) suggests a slightly slower recovery compared to P4 (1.38), which exhibits the most advanced recovery state. The roughness Reynolds number (Re_k) and the equivalent sand grain roughness in wall units (k_s^+) were also calculated at this location. The Re_k value of 126.95 for P4 and the k_s^+ value of 4.812 confirming the predicted values from CFD results in Sections 3.3 and 3.4.

The boundary layer structure was further analysed using the Law of the Wall scaling. The velocity profiles at 0.75 x/c are plotted in inner-scaled wall coordinates (y^+ vs u^+) in Figure 6.14. Due to the limitations of the measurement technique near the wall, the data captures the region starting from approximately $y^+ \approx 100$. This corresponds to the outer portion of the logarithmic layer and the wake region. The viscous sublayer and the buffer layer were not resolved.

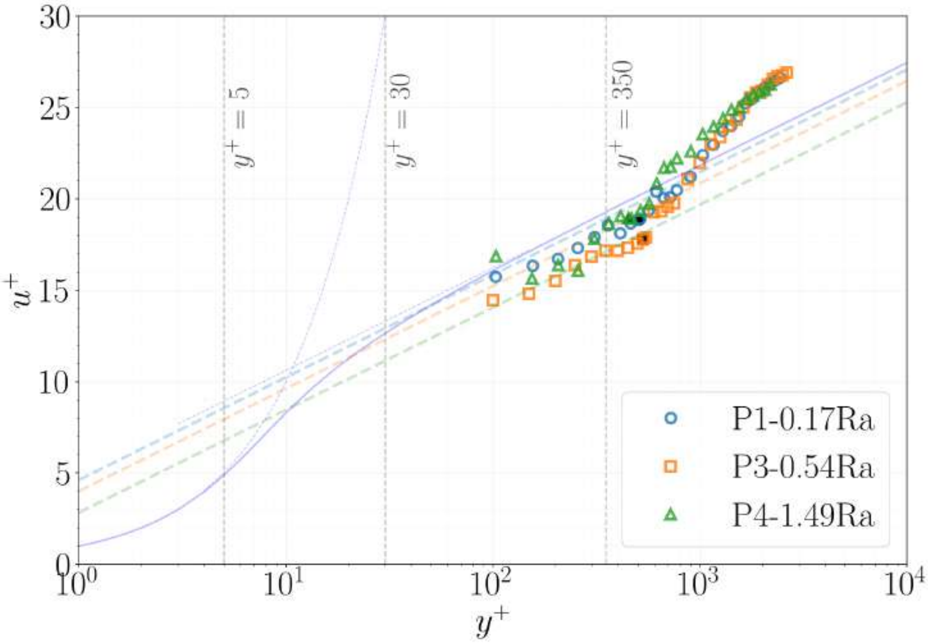

Figure 6.14: Boundary layer estimation of wall law variables

The profile for the smoothest case (P1-0.17Ra) aligns closely with the standard logarithmic law for smooth walls (solid blue line, where the constant $B \approx 5$). This indicates a canonical turbulent boundary layer structure. The intermediate roughness (P3-0.54Ra) shows a highly uniform profile shape but exhibits a parallel downward shift (Δu^+). This shift is the classic signature of roughness effects in the log-law region, representing the increased momentum deficit caused by form drag on the roughness elements.

The roughest profile (P4-1.49Ra) displays a more complex behaviour. The data points exhibit significant scatter, referred to as "chaotic behaviour" in the plot. This scatter is likely attributable to the high levels of turbulence intensity and unsteadiness persisting in the wake of the large roughness elements. Despite the scatter, the overall trend confirms the roughness-induced momentum deficit. The profile generally sits below the smooth wall line, consistent with the higher skin friction coefficient expected for this roughness regime.

Boundary layer measurements were performed for Profile P2-0.20Ra at chordwise locations of 0.25, 0.60, and 0.75 x/c. In contrast, Profile P5-0.64Ra was characterised only at the 0.75 x/c station. The calculated boundary layer parameters are summarised in Tables 6.8, 6.9, and 6.10.

Table 6.8: Boundary layer parameters at 0.25 x/c for P2-0.20Ra

Profile	δ [mm]	τ_w	Δu^+	Re_k
P2-0.20Ra	0.17	264.426	0.661	18

At the 0.25 x/c station, the boundary layer thickness for Profile P2-0.20Ra is recorded as 0.17 mm, which represents a significant departure from the baseline range and numerical predictions. Since the free-stream velocity is approximately 399 m/s, matching the baseline average, the local Reynolds number does not provide a physical basis for such substantial thinning. This is also evident from Mach number values at this location (see Figure 6.3), where it is overlap the baseline value. Instead, this discrepancy is identified as an artifact of limited spatial resolution during the experimental traverse.

As illustrated in Figure 6.15a, the capture of only a single data point within the boundary layer necessitates the use of linear interpolation between the wall and the first measurement height. This discrete sampling is found to be insufficient for an accurate calculation of the integral parameters at this chordwise position. Consequently, the reported thickness of 0.17 mm and the resulting high shear stress in Table 6.8 are interpreted as an underestimation caused by probe resolution limits rather than a fundamental modification of the near-wall flow field. The boundary layer is therefore assumed to follow the baseline development trend at this location, despite the anomalous calculated value.

Table 6.9: Boundary layer parameters at 0.60 x/c for P2-0.20Ra

Profile	δ [mm]	δ^* [mm]	δ^{**} [mm]	H_k	δ_E[mm]
P2-0.20Ra	3.24	0.701	0.373	1.88	0.624

Faster boundary layer recovery is observed for Profile P2-0.20Ra at the 0.60 x/c station. The shape factor (H_k) is recorded as 1.88, which is notably lower than the 2.35 recorded for the baseline Profile P1. This indicates a "healthier" boundary layer development following the interaction. The physical state of the BL is further evidenced in Figure 6.15b, where the profile shape suggests a transition toward a zero-pressure-gradient state with minimal energy loss (δ_E = 0.624 mm). This rapid recovery is attributed to the smaller separation bubble identified in the surface flow visualisations for this profile.

Table 6.10: Boundary layer parameters at 0.75 x/c for P2-0.20Ra and P5-0.64Ra

Profile	δ [mm]	δ^* [mm]	δ^{**} [mm]	$H_{k,opt}$	δ_E [mm]	Re_k	k_s^+
P2-0.20Ra	4.60	0.662	0.443	1.34	0.796	17.25	0.650
P5-0.64Ra	4.17	0.732	0.456	1.44	0.797	53.87	2.056

At the 0.75 x/c location, Profile P5-0.64Ra is observed to possess a thinner turbulent boundary layer ($\delta \approx 4.17$ mm) than Profile P2-0.20Ra ($\delta \approx 4.60$ mm), as summarised in Table 6.10. This thinning is attributed primarily to the accelerated free-stream flow, which reaches 312 m/s due to passage blockage and a lower local AVDR compared to the 302 m/s baseline average. The increased inertial momentum effectively suppresses the vertical growth of the boundary layer. Since both profiles remain within the hydraulically smooth regime ($k_s^+ \approx 0.65$ for P2 and 2.06 for P5), the observed δ are governed almost entirely by these macro-scale passage aerodynamics rather than micro-scale surface texture. Additionally, the combination of high free-stream velocity and the specific surface topography of P5 leads to an increase in the non-dimensional roughness height (k_s^+) and the roughness Reynolds number (Re_k).

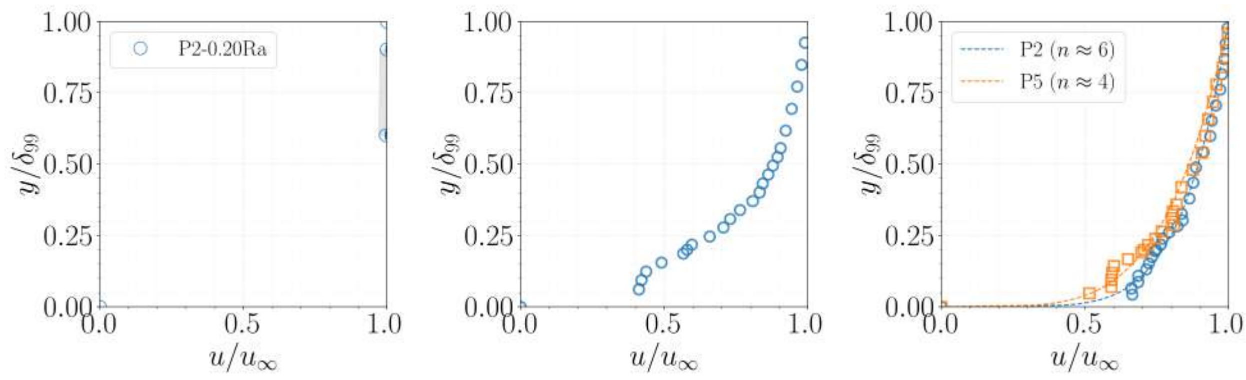

(a) 0.25 x/c

(b) 0.60 x/c

(c) 0.75 x/c

Figure 6.15: Normalised boundary layer velocity profiles

The structural differences between the two profiles are elucidated by the power-law fits in Figure 6.15c. Profile P2 follows an $n \approx 6$ distribution, while P5 exhibits a slightly modified $n \approx 4$ profile. Despite the differences in the exponent n, the integral parameters in Table 6.10 remain comparable; for instance, the energy loss thickness (δ_E) is nearly identical at approximately 0.8 mm for both cases.

6.5 Summary and key findings

This chapter has investigated the influence of surface roughness on the SBLI by examining the mean flow topology, shock unsteadiness, and boundary layer development across three distinct roughness regimes: smooth (P1-0.17Ra, P2-0.20Ra), intermediate (P3-0.54Ra, P5-0.64Ra), and rough (P4-1.49Ra).

The aerodynamic analysis of Profiles P2-0.20Ra and P5-0.64Ra concludes that passage-scale geometric discrepancies and mounting errors exert a dominant influence on the transonic flow field, surpassing the impact of surface topography when compared to the baseline configurations. For P2-0.20Ra, increased geometric blockage reduces the pre-shock Mach number, which results in a weakened SBLI and a significantly reduced separation area of approximately 7%. While this reduced interaction leads to a healthier boundary layer recovery, it is accompanied by high-amplitude, low-frequency oscillations of the shock front, physically driven by the instability of the reflected shock affected by λ-foot at the upper wall. In contrast, Profile P5-0.64Ra undergoes local flow acceleration that shifts the leading-edge shock upstream and triggers an earlier separation onset. That led to a higher inertial momentum of the free stream suppresses the final boundary layer thickness to 4.17 mm close to the trailing edge. These findings demonstrate that the shock detachment distance, the chordwise extent of the separation zone, and the spectral unsteadiness are primarily governed by the effective contraction ratio and local blockage of those two profiles. Consequently, the sensitivity of the transonic flow to these macro-scale passage dynamics outweighs the influence of surface finish, as the observed aerodynamic shifts are dictated by geometric fidelity rather than micro-scale roughness effects.

Nevertheless, for the other three profiles representing the baseline configuration: P1-0.17Ra, P3-0.54Ra, and P4-1.49Ra the mean pressure distribution and time-averaged schlieren visualisations confirmed that the global shock position and strength remained identical for all profiles. This crucial finding isolated the boundary layer characteristics as the primary variable, ensuring that any observed changes in separation dynamics were solely attributable to the surface finish. However, qualitative analysis revealed that the average shock contrast decreased significantly with increasing roughness, indicating a marked increase in temporal unsteadiness for the roughest case (P4).

Analysis of the time-averaged oil flow visualisation provided key insights into the separation topology. While the smoothest profiles (P1 and P3) exhibited a relatively two-dimensional separation bubble with the characteristic V-shaped upstream extension influenced by secondary flows, the roughest profile (P4) displayed a highly chaotic and three-dimensional separation zone. The separation line for P4 was notably straighter, suggesting that the intense roughness-induced turbulent mixing became the dominant mechanism, effectively overriding the subtle spanwise effects of the end-wall secondary flows. Critically, the overall separation area for P4 was measured to be the smallest, a direct consequence of this enhanced three-dimensional mixing which re-energises the boundary layer and allows the flow to reattach faster. Additionally, the difference in roughness between the two sides of P4 in particular at location 'a' where peak to valley height Sz is significantly different, which lead trigger additional streamwise vortices. while such vortices are not experienced in the other side of the profile suggesting when $Sz/\delta > 0.086$ may lead to such vortices formation.

The investigation of the unsteady shock dynamics revealed that the highest oscillation amplitude was observed for the roughest profile, P4. This increased amplitude was primarily driven by low-frequency energy contributions (≈10 Hz). This spectral characteristic suggests a significant large-scale, low-frequency "breathing" motion of the separation bubble, likely amplified by the modified boundary layer structure. This observation aligns with prior investigations which reported that laminar interactions tend to be more stable, as noted by Giepman et al. [74]. However, conflicting evidence exists: Klinner et al. [68] demonstrated that a specific roughness implementation could decrease shock unsteadiness by significantly reducing the separation size. Given that only a single, optimised patch was tested in that work, this finding may be circumstantial rather than representative of a universal roughness effect. Furthermore, in studies by Szwaba et al. [71], most tested roughness implementations resulted in higher shock unsteadiness compared to the smooth reference, though rare instances of unsteadiness reduction were noted, a condition Further confirmed by Godse et al. [179]. For the current study, wavelet analysis confirmed that P4 exhibited a highly broadband and temporally high-amplitude oscillation signature across the entire characteristic frequency range (70 Hz to 380 Hz). This confirms the existence of multiple, active unsteadiness contributors inherent to the rough-wall turbulent SBLI, which renders the rough surface shock dynamics significantly less predictable.

The final element of the study involved the boundary layer profile measurements, which confirmed the physical mechanism behind the observed flow changes. At the reattachment zone 0.60 x/c, the roughest profile (P4) exhibited a significantly thinner boundary layer and the lowest shape factor ($H = 1.90$). This is conclusive evidence of a faster flow recovery compared to the smoother cases ($H \approx 2.2 - 2.3$). While roughness is typically known to increase the momentum deficit, as indicated by Giepman et al. [73], the turbulent mixing in P4 induced a smaller macroscopic separation bubble. Aligning with Leipold et al. [113], this reduction in separation area led to a lower overall momentum loss integrated across the interaction zone, successfully counteracting the effects of higher local skin friction.

These findings demonstrate that surface roughness fundamentally alters the SBLI from a primarily two-dimensional laminar-type interaction to a highly three-dimensional, turbulence-dominated interaction, resulting in a smaller separation zone and significantly higher shock unsteadiness.

Chapter 7

Conclusions

The effects of controlled surface roughness on the complex flow phenomenon of the Shock Wave Boundary Layer Interaction (SBLI) in a transonic compressor cascade have been investigated. The primary objective of the study was to quantify the aerodynamic consequences of transitioning a nominally smooth aerofoil surface into a high-rough regime, with specific focus placed on understanding the physical mechanisms governing boundary layer stability, separation dynamics, and shock unsteadiness.

The experimental investigation was conducted in a single passage transonic fan profile in a blowdown wind tunnel, as detailed in Chapter 2. The setup was designed to impose a steady, high adverse pressure gradient on the suction surface, replicating conditions typical of a turbomachinery operating point where SBLI-induced separation is prone to occur. Isentropic surface Mach numbers just ahead of the shock were maintained at approximately $M_i \approx 1.22$ which replicated conditions typical of real designed working conditions. Several measurement techniques were employed to capture the complex flow features, including Laser Doppler Anemometry (LDA) for boundary layer profiling and time-resolved schlieren photography.

Manufactured profiles and evaluation were discussed in Chapter 3, focusing on the design and meticulous evaluation of the test articles. Five profiles were manufactured using wire electrical discharge machining (WEDM) technology to ensure high quality surface finish and geometric accuracy. Dimensional fidelity was ensured by verifying the manufactured profile shapes against the nominal CAD model, with all profiles conforming closely to the design specifications. Three of these profiles were selected for additional machining to introduce controlled surface roughness levels: P1 (Ra = 0.17 µm) and P2 (Ra = 0.20 µm) represented the smooth baseline; P3 (Ra = 0.54 µm) and P5 (Ra = 0.63 µm), represented the intermediate roughness; and P4 (Ra = 1.49 µm), represented the high-rough regime. Subsequent detailed three-dimensional optical analyses revealed significant discrepancies from 2D measurements and indicated similar average roughness for all profiles except P4. P4 exhibited a critical non-uniformity in roughness: the near leading edge on one side had a significantly higher peak-to-valley height (Sz $\approx$ 31.01 µm) compared to the opposing side (Sz $\approx$ 17.75 µm). When normalised by the local boundary layer thickness near the leading edge, the maximum roughness ratio of $\mathrm{Sz}/\delta \approx 0.124$ on P4 was deemed highly significant. This indicated the potential for the elements to act as a trip wire, thereby forcing a transition and influencing the subsequent interaction with the shock.

Advanced measurement methods developed to analyse the flowfield were presented in Chapter 4, with a focus on overcoming the challenges associated with precise data processing in the complex SBLI environment. The dominant unsteady structures governing the energy transfer were identified; this was achieved via Proper Orthogonal Decomposition (POD) analysis of the time-resolved schlieren images. Advanced flow visualisation techniques were subsequently enhanced, which permitted shockwave tracking to be performed using computer vision algorithms applied to high-speed schlieren imagery. To ensure optimal optical access and clarity for whole-field oil visualisation measurements, the camera view was modified. Finally, for quantitative analysis, a comprehensive post-processing methodology was developed for the LDA data. The fidelity of this data was secured through the implementation of a Gaussian Mixture Model (GMM) for the systematic removal of inertial particle outliers. Accurate boundary layer integral parameters were subsequently determined using weighted statistics and rigorous uncertainty quantification.

System sensitivity analysis was conducted in Chapter 5 to quantify the uncertainties inherent to various geometric and operational parameter variations. This analysis ensured a quasi-two-dimensional flow and the target shock structure were achieved. This was accomplished by requiring a 0.6°counter-clockwise rotation of the lower profile to match the design Mach number distribution. Full suction was applied to the upper and lower walls to minimise boundary layer blockage, while the side wall suction was critically set to 33.3% to suppress the influence of the reflected shock on the passage shock dynamics. Analysis revealed that two profiles (P2 and P5) exhibited minor geometric mismatches and different local suction pressures, leading to their exclusion from the core analysis to maintain data integrity. Consequently, the conclusive comparison of surface roughness effects was restricted to the three most reliably mounted profiles: P1-0.17Ra, P3-0.54Ra, and P4-1.49Ra.

7.1 Key findings and aerodynamic impact

The findings presented in Chapter 6 demonstrate a profound influence of surface macro-roughness across three distinct roughness regimes: smooth (P1-0.17Ra), intermediate (P3-0.54Ra), and rough (P4-1.49Ra) on the aerodynamic characteristics of the SBLI.

A critical finding was that the time-averaged aerodynamic structure remained remarkably consistent regardless of surface roughness. Pressure measurements confirmed that the mean shock position, global Mach number distribution, and the extent of the SBLI pressure plateau were identical across all profiles. This consistency suggested that roughness did not induce a measurable earlier laminar-turbulent transition based on mean pressure data, classifying the overall SBLI as a laminar-type interaction for all tested cases.

Qualitative schlieren imaging initially revealed a pronounced effect on the shock structure as surface roughness was increased. The passage shock was observed to be progressively smeared out in the rougher cases, which served as a direct visual indicator of substantially increased time-averaged oscillation amplitude and reduced spatial coherence. This unsteadiness was confirmed quantitatively through shock tracking analysis. The roughest profile, P4-1.49Ra, was found to exhibit the highest instability in its dynamic behaviour. The average maximum displacement for P4 was measured at 10.15 mm, representing an increase in oscillation amplitude, of approximately 40.58% relative to the smoothest case, P1 (7.22 mm).

The underlying physical mechanism for this dynamic degradation was elucidated through frequency analysis of the shock motion. The high oscillation amplitude noted for P4 was overwhelmingly dominated by low-frequency energy contributions, with a prominent peak near 10 Hz. This spectral signature was indicative of a significant, large-scale, low-frequency "breathing" motion originating from the modified separation bubble. Conversely, the smoothest profile (P1) was found to be strongly influenced by a common characteristic frequency band (270 Hz to 380 Hz). This higher-frequency activity suggests the dominance of an acoustic feedback mechanism that was progressively disrupted by the roughness-induced boundary layer turbulence in the rougher profiles, resulting in a formation of a less predictable, broadband dynamic response.

Analysis of the oil flow visualisation provided key insights into the separation topology and a significant aerodynamic advantage. While the smoother profiles (P1 and P3) exhibited a V-shaped, relatively two-dimensional separation bubble influenced by secondary flows, the roughest profile (P4) showed a three-dimensional separation zone. The crucial consequence of the enhanced turbulent mixing and induced streamwise vortices was that the overall separation area for P4 was measured to be the smallest. The separation area for P4 was 8.1% of the total suction area, which represented an advantage of approximately 7.95% compared to the smoothest profile P1 (8.8%).

The superior flow recovery was confirmed by the boundary layer measurements taken at the reattachment zone (0.60 x/c) and near the trailing edge (at 0.75 x/c). The roughest profile (P4) exhibited a lower shape factor ($H = 1.90$), confirming a faster flow recovery. Near the trailing edge, the momentum thickness (δ^{**}), which quantifies the total momentum deficit, was lowest for P4 at 0.435 mm versus 0.540 mm for the smoothest profile P1. This represents a crucial aerodynamic reduction in momentum deficit of approximately 19.4% at the trailing edge, relative to the smoothest profile P1.

7.2 Final summary and recommendations

The thesis concludes that the introduction of surface high-roughness fundamentally redefined the internal flow mechanics within the SBLI region of the transonic compressor aerofoil. The most significant scientific contribution is the clear establishment of a quantifiable trade-off between aerodynamic performance and shock unsteadiness. This was achieved by demonstrating the physical mechanisms that forced a highly three-dimensional, locally turbulent flow structure within the interaction and separation zones. This occurred despite the time-averaged pressure distribution remaining consistent with a laminar-type SBLI classification.

The resultant flow state within the interaction zone yielded a profound, dual-natured consequence that anchors the observed trade-off. On the one hand, the enhanced turbulent mixing successfully re-energised the boundary layer, leading to superior flow recovery confirmed by a 19.4% reduction in momentum deficit at the trailing edge. This macroscopic performance gain was achieved despite the microscopic increase in skin friction. Conversely, the cost was borne by the dynamic system: the induced turbulence led to a spectral broadening of the shock unsteadiness, marked by a low-frequency "breathing" motion. This effect dramatically degraded the dynamic stability, quantified by a 40.58% increase in shock oscillation amplitude relative to the smoothest profile.

This investigation provides an enriched dataset and effectively delineates the operational limits where roughness transitions from being a passive feature to an active aerodynamic element. While the complexity of roughness parameters and the limited sample size restrict generalisation, the study isolates the mechanisms governing this critical trade-off. Future work is strongly recommended to focus on selective roughness application strategies. The objective must be to leverage the proven aerodynamic benefits (mixing and flow recovery) without simultaneously triggering the destructive broadband, low-frequency shock oscillations, potentially through targeted application in only the most critical spanwise locations.

Appendix A

Full test section model

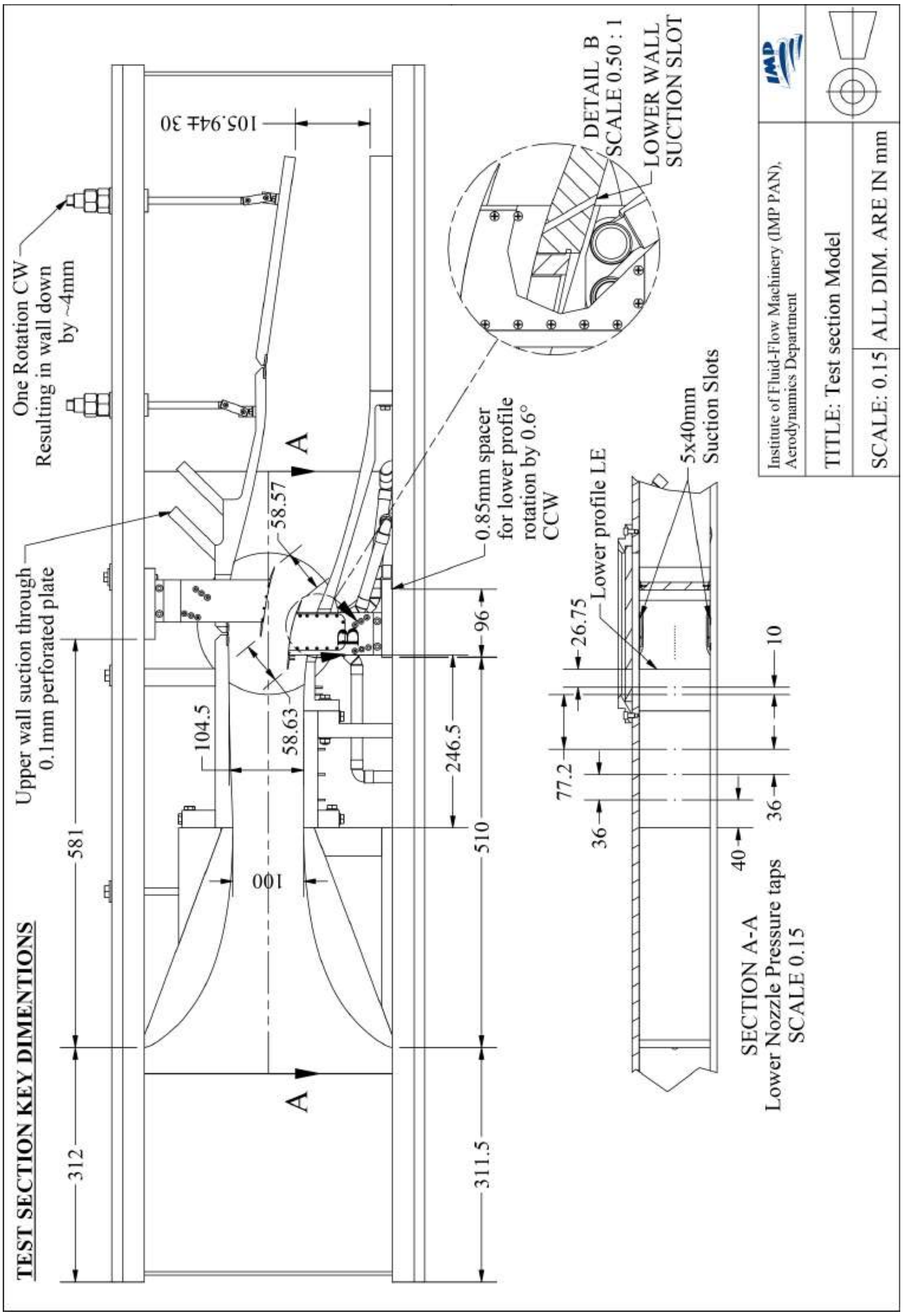

Figure A.1: Test section with dimensions as implemented in the wind tunnel research area

Appendix B

Roughness full data set

B.1 2D Roughness measurement

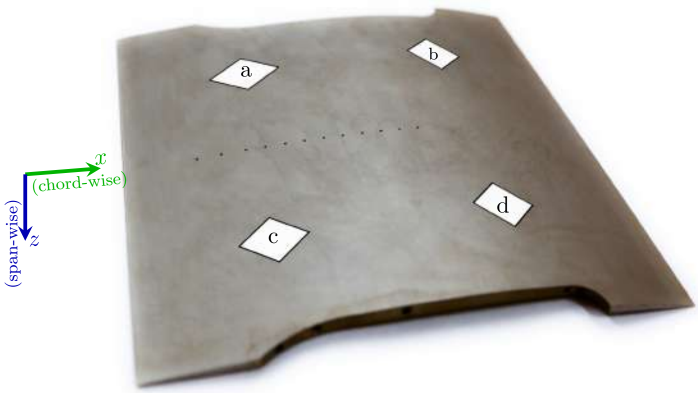

Figure B.1: Roughness evaluation location

B.1.1 Manufactured profiles surface roughness evaluation

Table B.1: Profile 1 main roughness features in [µm]

Dirction	Loc	Ra	Rq	Rsk	Rp	Rz	Rk	Rpk	Rvk
Chord-wise	a	0.604	0.775	0.317	2.745	4.981	1.878	0.905	0.821
	b	0.628	0.819	0.528	2.902	5.306	1.843	1.049	0.792
	c	0.552	0.707	0.554	2.459	4.250	1.671	0.891	0.565
	d	0.611	0.778	0.467	2.557	4.751	1.937	0.893	0.769
Span-wise	a	0.579	0.732	0.520	2.310	4.002	1.813	1.079	0.532
	b	0.564	0.707	0.185	2.047	3.917	1.779	0.731	0.591
	c	0.601	0.777	0.650	2.856	4.666	1.899	1.138	0.507
	d	0.537	0.680	0.402	2.142	3.754	1.663	0.886	0.544

Table B.2: Profile 2 main roughness features in [µm]

Dirction	Loc	Ra	Rq	Rsk	Rp	Rz	Rk	Rpk	Rvk
Chord-wise	a	0.646	0.841	0.720	2.698	4.709	1.846	1.223	0.602
	b	0.619	0.783	0.710	2.480	4.299	1.887	1.001	0.556
	c	0.637	0.801	0.505	2.654	4.607	2.050	1.023	0.536
	d	0.601	0.783	0.918	2.636	4.334	1.763	1.261	0.549
Span-wise	a	0.622	0.767	0.395	2.258	3.946	1.997	0.865	0.444
	b	0.648	0.831	0.540	2.836	4.839	2.052	1.167	0.555
	c	0.649	0.814	0.197	2.471	4.659	2.079	0.900	0.722
	d	0.632	0.813	0.363	2.563	4.576	1.840	1.094	0.717

Table B.3: Profile 3 main roughness features in [µm]

Dirction	Loc	Ra	Rq	Rsk	Rp	Rz	Rk	Rpk	Rvk
Chord-wise	a	0.526	0.673	0.400	2.138	3.936	1.590	0.859	0.573
	b	0.528	0.660	0.626	2.257	3.794	1.772	0.772	0.474
	c	0.536	0.670	0.272	2.005	3.857	1.731	0.734	0.542
	d	0.524	0.682	0.779	2.625	4.225	1.540	0.958	0.556
Span-wise	a	0.548	0.679	0.339	2.036	3.593	1.714	0.770	0.479
	b	0.572	0.716	0.305	2.069	4.001	1.776	0.829	0.598
	c	0.548	0.692	0.220	2.586	3.852	1.668	0.813	0.576
	d	0.548	0.698	0.420	2.407	4.143	1.698	0.898	0.531

Table B.4: Profile 4 main roughness features in [µm]

Dirction	Loc	Ra	Rq	Rsk	Rp	Rz	Rk	Rpk	Rvk
Chord-wise	a	0.574	0.719	0.339	2.202	4.122	1.856	0.768	0.587
	b	0.531	0.673	0.755	2.457	4.083	1.744	0.884	0.430
	c	0.601	0.764	0.434	2.500	4.563	1.864	0.914	0.641
	d	0.549	0.693	0.721	2.437	3.865	1.769	0.912	0.370
Span-wise	a	0.623	0.790	0.557	2.795	4.678	1.931	1.039	0.483
	b	0.582	0.624	0.402	2.333	4.157	1.721	0.937	0.622
	c	0.619	0.775	0.521	2.536	4.335	1.881	1.065	0.474
	d	0.585	0.729	0.470	2.236	3.869	1.844	0.914	0.440

Table B.5: Profile 5 main roughness features in [µm]

Dirction	Loc	Ra	Rq	Rsk	Rp	Rz	Rk	Rpk	Rvk
Chord-wise	a	0.673	0.864	0.670	2.894	5.024	2.102	1.129	0.650
	b	0.581	0.730	0.589	2.183	3.895	1.781	0.860	0.463
	c	0.622	0.796	0.606	2.694	4.659	1.920	0.999	0.601
	d	0.610	0.762	0.611	2.418	4.066	1.949	0.894	0.470
Span-wise	a	0.601	0.775	0.558	2.774	4.658	1.734	1.086	0.574
	b	0.649	0.873	0.837	3.528	5.570	1.873	1.397	0.591
	c	0.650	0.814	0.489	2.602	4.421	2.068	0.993	0.469
	d	0.694	0.901	0.661	3.026	4.994	1.926	1.521	0.593

B.1.2 Textured profiles evaluation

Table B.6: Profile 1 (Robot-polishing) main roughness features in [µm]

Dirction	Loc	Ra	Rq	Rsk	Rp	Rz	Rk	Rpk	Rvk
Chord-wise	a	0.262	0.340	-0.274	0.948	2.378	0.762	0.262	0.469
	b	0.299	0.379	-0.161	0.938	2.386	0.849	0.259	0.550
	c	0.219	0.278	-0.385	0.658	1.818	0.647	0.176	0.413
	d	0.231	0.295	-0.190	0.735	1.971	0.627	0.197	0.463
Span-wise	a	0.074	0.095	-0.494	0.244	0.505	0.226	0.089	0.119
	b	0.106	0.134	-0.131	0.409	0.771	0.309	0.118	0.198
	c	0.060	0.077	0.331	0.230	0.429	0.181	0.096	0.085
	d	0.089	0.110	-0.048	0.297	0.555	0.257	0.113	0.139

Table B.7: Profile 2 (Robot-polishing) main roughness features in [µm]

Dirction	Loc	Ra	Rq	Rsk	Rp	Rz	Rk	Rpk	Rvk
Chord-wise	a	0.310	0.399	-0.566	0.953	2.595	0.904	0.259	0.605
	b	0.297	0.374	-0.224	0.900	2.473	0.832	0.224	0.547
	c	0.302	0.381	-0.338	0.885	2.392	0.934	0.248	0.504
	d	0.300	0.375	-0.031	0.900	2.374	0.865	0.222	0.519
Span-wise	a	0.082	0.104	-0.373	0.267	0.541	0.250	0.125	0.116
	b	0.123	0.156	0.150	0.500	0.847	0.384	0.219	0.135
	c	0.109	0.134	-0.107	0.313	0.649	0.338	0.133	0.148
	d	0.103	0.127	0.341	0.323	0.588	0.317	0.111	0.130

Table B.8: Profile 4 (Manual-hand drill) main roughness features in [µm]

Dirction	Loc	Ra	Rq	Rsk	Rp	Rz	Rk	Rpk	Rvk
Chord-wise	a	0.945	1.197	0.147	2.653	5.020	2.261	1.786	1.567
	b	0.526	0.697	0.481	2.124	4.039	1.368	1.047	1.148
	c	0.410	0.513	-0.260	1.374	2.873	1.147	0.641	0.726
	d	0.828	1.020	0.382	2.282	4.550	2.297	0.955	1.922
Span-wise	a	2.908	3.720	-0.591	8.372	20.365	8.436	2.483	5.677
	b	2.068	2.826	-0.667	7.717	17.755	4.665	3.400	4.759
	c	1.771	2.311	-0.830	5.438	13.454	4.863	2.132	3.915
	d	2.457	3.127	-0.408	7.713	17.369	7.217	2.714	4.299

Appendix C

Algorithms summary

C.1 High-speed schlieren shock wave detection and tracking algorithms

Algorithm 1 Generating slice list

Require: I_{flow}: Set of high-speed schlieren images (snapshots)
Require: $I_{\text{no-flow}}$: Optional background image
Require: t_{crit}: RANSAC inlier tolerance (e.g., 1 px)

procedure PRE-PROCESSING AND ALIGNMENT($I_{\text{flow}}, I_{\text{no-flow}}$)
  if $I_{\text{no-flow}}$ is available **then**
    $I_{\text{clean}} \leftarrow I_{\text{flow}} - I_{\text{no-flow}}$ (Background Subtraction)
  else
    $I_{\text{avg}} \leftarrow \text{Average}(I_{\text{flow}})$
    $I_{\text{inpaint}} \leftarrow \text{Inpaint}(I_{\text{avg}}, \text{Shock Mask})$ (Mitigate blending)
    $I_{\text{clean}} \leftarrow I_{\text{flow}} - I_{\text{inpaint}}$
  end if
  $I_{\text{final}} \leftarrow \text{Median Filter}(I_{\text{clean}})$ (Remove salt-and-pepper noise)
  $n_{rs} \leftarrow$ Sample size
  for $n = 1$ to n_{rs} **do**
    $X_{\text{raw}} \leftarrow \text{TrackShock}(\text{Slice}(I_{\text{final},i}))$ (Using integral method, temporary)
    $m_n \leftarrow \text{RANSAC-LineFit}(X_{\text{raw}}, t_{\text{crit}})$
  end for
  $\overline{m_w} \leftarrow \text{WeightedAverage}(m_n)$
  $I_{\text{rotated}} \leftarrow \text{Rotate}(I_{\text{final}}, \overline{m_w})$ (Align shock perpendicular to slice)
  $L_{\text{slice}} \leftarrow \text{CropAndAverage}(I_{\text{rotated}})$ (Generate 1D slice list)
end procedure

Algorithm 2 The integral method for shock unsteadiness quantification

Require: L_{slice}: Snapshot slice list
Require: ϵ: Valley area acceptance threshold (e.g., 0.3)
Ensure: X_{shock}: Shock position signal
Ensure: $Uncr$: Uncertainty list

procedure IntegralShockTracking(L_{slice})
  for each slice S_n in L_{slice} **do**
    $Uncr_n = \text{False}$
    $\overline{I} \leftarrow \text{Average}(S_n)$
    $[K] \leftarrow \{K_j \mid I_x < \overline{I} \text{ in } S_n\}$ (Identify local minima/valleys)
    $[A] \leftarrow \{A_j \mid A_j = \lvert \int K_j dx \rvert\}$ (Calculate valley areas)
    $A_{\max} = \max \left\{ A_j \;\middle|\; \frac{\overline{I} - I_{j_{\min}}}{\overline{I} - I_{\min}} > \varepsilon \right\}$ (Identify largest deep valley)
    $K_{\text{shock}} \leftarrow$ Valley corresponding to $A_{\max}$
    $[k] \leftarrow$ Sub-valleys within K_{shock}
    if $\lvert [k] \rvert = 1$ **then**
      Condition 1: Fully merged/detached
      $K_{\text{rms}} \leftarrow \text{ShiftDown}(\text{Average}(K_{\text{shock}}), \text{RMS})$
      $X_i \leftarrow \text{Midpoint}(K_{\text{rms}})$
      if $A_{\max -1} > 0.6 A_{\max}$ **then**
        $Uncr_n = \text{True}$
      end if
    else
      Condition 2: Transitional/multi-sub-valley
      $[a] \leftarrow \{a_\kappa \mid a_\kappa = \lvert \int k_\kappa dx \rvert\}$ (Calculate sub-valley areas)
      if $n > 1$ **then**
        $k_{\text{shock}} \leftarrow$ Sub-valley closest to X_{n-1}
      else
        $Uncr_n = \text{True}$
        $k_{\text{shock}} \leftarrow$ Valley corresponding to $a_{\max}$
      end if
      if $a_{\text{shock}} \mathrel{!}= a_{\max}$ **then**
        $Uncr_n = \text{True}$
      end if
      $k_{\text{rms}} \leftarrow \text{ShiftDown}(\text{Average}(k_{\text{shock}}), \text{RMS})$
      $X_n \leftarrow \text{Midpoint}(k_{\text{rms}})$
    end if
    $X_{\text{shock}} \leftarrow X_{\text{shock}} \cup \{X_n\}$
    $Uncr \leftarrow Uncr \cup \{Uncr_n\}$
  end for
  $N \leftarrow$ Total snapshots
  $N_{\text{uncr}} \leftarrow$ Total True $Uncr$
  $\eta \leftarrow (N_{\text{uncr}}/N) \times 100\%$ (Estimate uncertainty ratio)
end procedure

C.2 CWT implementation and normalisation

The CWT is computationally implemented using a frequency-domain convolution framework. This approach maintains computational efficiency while preserving signal fidelity. The convolution of the signal and the wavelet is performed via the Fourier Transform ($\mathcal{F}$):

$$\text{conv}(f) = \mathcal{F}(s).\mathcal{F}(\psi) \tag{C.1}$$

where $\mathcal{F}(s)$ is the Fourier transform of the input signal (s) and $\mathcal{F}(\psi)$ is the Fourier transform of the Morlet wavelet.

To preserve the amplitude integrity of the decomposition, the wavelet's Fourier transform is normalised prior to convolution:

$$\mathcal{F}(\psi) \leftarrow \frac{\mathcal{F}(\psi)}{\max \mathcal{F}(\psi)} \tag{C.2}$$

The filtered or decomposed signal (s_f) is then reconstructed by applying the inverse Fourier transform ($\mathcal{F}^{-1}$) to the resulting convolution:

$$s_f = \mathcal{F}^{-1}(\text{conv}(f)) \tag{C.3}$$

This robust framework allows for the simultaneous analysis of time and frequency components, accommodating both single-frequency and multi-frequency flow analyses.

C.3 Reconstruction of profile surface from a single camera view algorithm

Algorithm 3 Image perspective correction

Require: Input Image (I_{raw}), Image Shape (S_{img}), Profile Data (P_{surf}), Physical Dimensions (CordLen)
Ensure: Orthographic Image (I_{ortho})

```
function DetermineVanishingPoints(I_raw)
    Manually define two pairs of parallel lines (Z-rays and Y-rays)
    Calculate V_z and V_y as intersection points
    Calculate Principal Point P0 (image centre)
    Compute Focal Length f = −(V_z − P0).(V_y − P0)
    Compute V_x using 3D world coordinates and cross product
    return V_z, V_y, V_x, f
end function
function MapProfilePoints(V_z, V_y, V_x, P_surf)
    Manually define near and far profile chord lines
    Calculate Chord Vanishing Point P_Chint
    Calculate intersection points (P_near, P_far) for profile points on the image plane using V_y and
P_Chint
    return (P_near, P_far)
end function
function RebuildPerspective(I_raw, P_near, P_far)
    Determine segment width W_i and full width W_total based on chord length and physical scale
    Determine span height H from known dimensions
    Initialise I_ortho
    for each profile segment i do
        Define input points P_in (quadrilateral on I_raw)
        Define output points P_out (rectangle on I_ortho)
        Compute Perspective Transform M_i = cv2.getPerspectiveTransform(P_in, P_out)
        Apply transform: I_seg = cv2.warpPerspective(I_raw, M_i)
        Concatenate I_seg to I_ortho
    end for
    return I_ortho
end function
V_z, V_y, V_x, f ← DetermineVanishingPoints(I_raw)
P_near, P_far ← MapProfilePoints(V_z, V_y, V_x, P_surf)
I_ortho ← RebuildPerspective(I_raw, P_near, P_far)
```

Appendix D

Boundary layer measurements full data set

Profile 1 (P1-0.17Ra) boundary layer data

Table D.1: Profile 1: Velocity profile at 0.25 x/c

y	u	u_{rms}	$\zeta_{\overline{u}}$
0.15	390.407	12.808	0.792
0.20	401.819	9.075	0.490
0.25	405.138	8.083	0.260
0.30	405.868	8.032	0.279
0.35	406.689	9.039	0.301
0.40	407.099	11.856	0.290
0.45	407.400	11.373	0.433
0.50	408.263	9.808	0.239
0.60	408.495	9.329	0.073
0.70	408.355	9.623	0.084
0.80	408.353	9.627	0.096
0.90	407.925	10.457	0.086
1.00	407.892	10.518	0.103
1.10	407.911	10.484	0.103
1.20	407.837	10.619	0.073
1.30	407.869	10.560	0.102
1.40	407.853	10.590	0.100
1.50	407.893	10.517	0.100
1.75	408.017	10.287	0.106
2.00	407.433	11.319	0.102
3.00	407.244	11.627	0.213
4.00	408.083	10.161	0.234
5.00	408.551	9.210	0.575
6.00	407.931	10.447	0.257
7.00	407.263	11.596	0.124
8.00	407.495	11.215	0.124
9.00	407.493	11.219	0.125
10.00	407.416	11.347	0.132
12.50	407.401	11.372	0.142
15.00	407.542	11.135	0.145

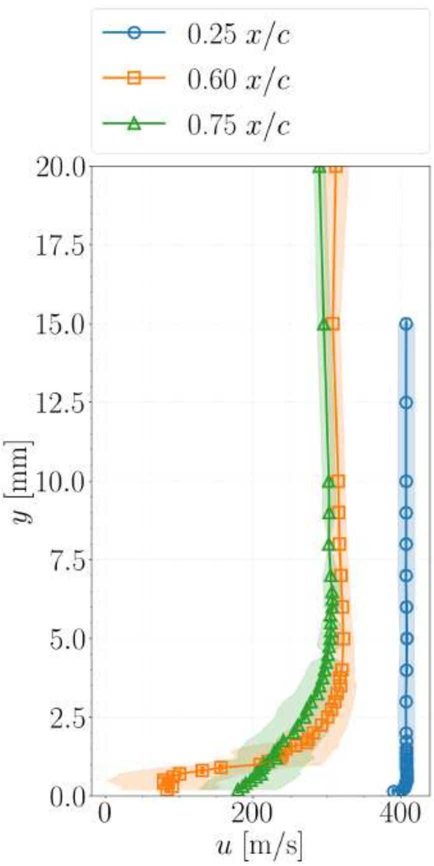

BL velocity profiles at different chordwise locations (The shaded area behind the graphs indicates the RMS of the velocity fluctuations)

Table D.2: Profile 1: velocity profile at 0.60 x/c

y	$\overline{u}$	u_{rms}	$\zeta_{\overline{u}}$
0.20	83.099	64.339	2.448
0.30	90.354	64.708	2.217
0.39	78.711	67.749	2.209
0.50	78.545	76.532	1.125
0.60	91.503	78.199	1.420
0.70	100.169	82.077	1.622
0.80	131.028	87.390	1.298
0.90	156.401	82.017	1.574
1.00	209.818	81.680	1.284
1.10	219.827	75.625	1.039
1.20	236.238	62.479	1.205
1.30	239.120	65.072	1.111
1.40	237.569	68.760	1.201
1.50	244.506	66.758	1.097
1.60	257.729	59.173	0.699
1.70	272.532	42.965	0.829
1.80	274.705	42.735	0.929
2.00	281.297	40.955	0.762
2.25	293.003	34.830	0.561
2.50	301.275	29.297	0.308
2.75	306.444	27.225	0.377
3.00	310.651	25.672	0.356
3.25	313.714	24.011	0.333
3.50	318.745	21.245	0.294
3.75	317.559	19.041	0.187
4.00	320.351	17.086	0.237
5.00	322.591	12.706	0.176
6.00	320.880	11.042	0.153
7.00	319.172	10.154	0.141
8.00	317.167	9.857	0.093
9.00	316.198	9.306	0.123
10.00	315.562	9.390	0.128
15.00	308.208	8.830	0.135
20.00	312.166	17.570	0.221

Table D.3: Profile 1: velocity profile at 0.75 x/c

y	$\overline{u}$	u_{rms}	$\zeta_{\overline{u}}$
0.20	179.048	53.386	0.874
0.30	185.905	54.038	0.849
0.40	190.157	56.135	0.633
0.50	196.867	56.502	0.792
0.60	203.743	55.743	0.704
0.70	211.199	53.078	0.393
0.80	206.240	54.773	0.473
0.90	212.183	55.209	0.436
1.00	214.912	55.717	0.468
1.10	220.168	54.364	0.469
1.20	231.863	51.051	0.338
1.30	227.921	49.490	0.567
1.40	228.651	50.208	0.576
1.50	233.019	50.365	0.575
1.75	241.120	49.344	0.550
2.01	254.740	45.885	0.384
2.25	261.092	42.443	0.588
2.50	269.781	40.014	0.555
2.75	272.736	39.476	0.547
3.00	278.629	37.502	0.520
3.25	286.969	31.219	0.288
3.50	290.055	28.094	0.356
3.75	294.512	25.930	0.306
4.00	296.931	24.059	0.312
4.25	299.752	21.074	0.269
4.50	301.328	0.155	0.110
4.75	303.173	16.594	0.216
5.00	304.751	15.864	0.210
5.25	305.358	14.635	0.212
5.50	305.274	13.058	0.170
5.75	304.900	0.122	0.086
6.00	307.419	12.055	0.168
6.25	307.466	11.548	0.160
6.50	307.016	11.726	0.180
7.00	305.329	10.827	0.166
8.00	302.838	0.095	0.067
9.00	303.099	9.191	0.128
10.00	302.825	8.917	0.124
15.00	295.786	9.018	0.127
20.00	289.823	7.740	0.107

Profile 2 (P2-0.20Ra) boundary layer data

Table D.4: Profile 2: Velocity profile at 0.25 x/c

y	u	u_{rms}	$\zeta_{\overline{u}}$
0.15	399.208	8.750	0.423
0.20	400.920	7.555	0.196
0.25	402.167	6.837	0.068
0.30	402.466	7.071	0.070
0.35	402.117	7.415	0.073
0.40	402.169	7.374	0.059
0.45	402.322	7.848	0.109
0.50	402.877	7.517	0.104
0.60	402.247	7.281	0.071
0.70	402.738	7.564	0.105
0.80	402.729	7.602	0.105
0.90	402.832	7.480	0.081
1.00	403.393	7.670	0.135
1.10	402.852	7.631	0.149
1.20	401.953	8.951	0.128
1.30	403.156	7.471	0.157
1.40	403.430	7.660	0.163
1.50	402.968	7.584	0.164
1.75	401.492	7.459	0.182
2.00	399.803	11.254	0.175
3.00	403.558	7.525	0.173
4.00	403.614	8.374	0.276
5.00	403.807	6.444	0.248
6.00	402.257	7.864	0.197
7.00	402.646	7.496	0.118
8.00	400.955	7.829	0.181
9.00	402.494	7.882	0.182
10.00	403.428	7.324	0.160
12.50	402.320	7.432	0.146
15.00	401.547	8.265	0.161

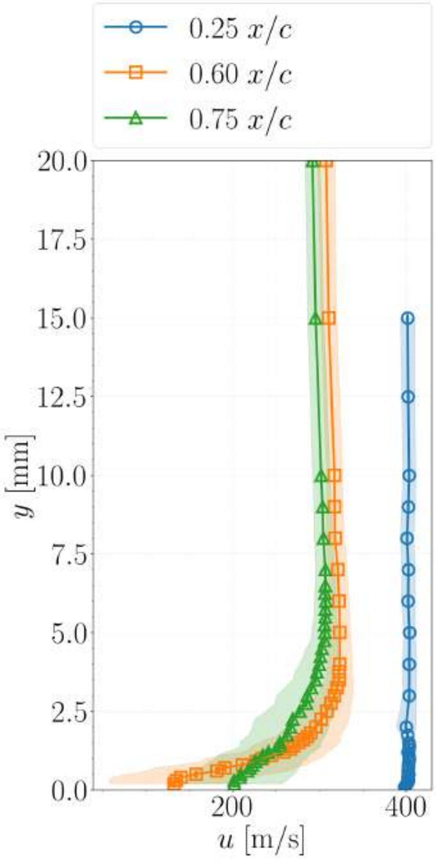

BL velocity profiles at different chordwise locations (The shaded area behind the graphs indicates the RMS of the velocity fluctuations).

Table D.5: Profile 2: velocity profile at 0.60 x/c

y	$\overline{u}$	u_{rms}	$\zeta_{\overline{u}}$
0.20	132.093	74.867	1.376
0.30	134.983	78.150	1.291
0.40	139.999	79.892	1.352
0.50	157.562	81.473	0.784
0.60	181.468	80.979	0.729
0.70	190.727	80.775	0.737
0.80	210.955	73.826	0.488
0.90	226.449	64.290	0.478
1.00	233.993	65.174	0.539
1.10	244.730	60.413	0.427
1.20	258.876	48.804	0.661
1.30	266.507	48.049	0.596
1.40	269.819	48.429	0.610
1.50	276.246	46.332	0.539
1.60	281.215	42.554	0.353
1.70	286.348	36.743	0.509
1.80	289.780	36.122	0.501
2.00	295.659	34.386	0.477
2.25	302.102	31.429	0.436
2.50	308.399	26.754	0.262
2.75	313.437	23.092	0.320
3.00	317.305	21.294	0.295
3.25	320.441	18.640	0.258
3.50	322.782	16.504	0.229
3.75	322.537	14.490	0.142
4.00	323.542	14.435	0.200
5.00	323.574	11.872	0.165
6.00	322.672	10.955	0.152
7.00	321.139	10.632	0.147
8.00	317.966	10.396	0.102
9.00	317.337	9.260	0.135
10.00	317.251	9.147	0.136
15.00	310.522	9.064	0.129
20.00	307.692	9.886	0.135

Table D.6: Profile 2: velocity profile at 0.75 x/c

y	$\overline{u}$	u_{rms}	$\zeta_{\overline{u}}$
0.20	201.936	54.987	0.411
0.30	201.360	59.889	0.640
0.40	208.201	57.619	0.415
0.50	208.518	61.247	0.501
0.60	216.861	57.130	0.391
0.70	219.811	55.348	0.352
0.80	222.801	55.256	0.360
0.90	225.937	53.639	0.391
1.00	232.503	53.139	0.338
1.10	234.393	52.209	0.422
1.20	241.187	50.756	0.307
1.30	249.784	47.142	0.589
1.40	255.254	46.488	0.585
1.50	254.142	46.716	0.570
1.75	262.501	44.442	0.537
2.00	266.382	43.785	0.414
2.25	269.086	43.757	0.606
2.50	277.464	39.574	0.548
2.75	284.846	36.348	0.504
3.00	285.920	35.680	0.495
3.25	290.656	30.482	0.291
3.50	295.268	26.484	0.358
3.75	296.996	25.810	0.338
4.00	299.859	22.758	0.284
4.25	301.240	20.390	0.230
4.50	302.775	18.286	0.163
4.75	305.850	16.135	0.239
5.00	306.105	15.026	0.217
5.25	306.079	14.463	0.225
5.50	306.783	12.854	0.199
5.75	306.549	12.798	0.134
6.00	307.126	12.701	0.176
6.25	306.211	12.174	0.169
6.50	306.785	11.698	0.162
7.00	306.660	11.120	0.154
8.00	304.417	10.396	0.102
9.00	303.527	10.029	0.139
10.00	301.867	10.007	0.139
15.00	295.573	9.297	0.129
20.00	291.895	8.660	0.120

Profile 3 (P3-0.54Ra) boundary layer data

Table D.7: Profile 3: Velocity profile at 0.25 x/c

y	u	u_{rms}	$\zeta_{\overline{u}}$
0.15	380.0424	10.29872	3.206988
0.2	388.2202	11.82463	1.640476
0.25	397.7469	10.83764	0.980683
0.3	403.4344	12.78851	0.66543
0.35	404.0452	9.277618	0.840922
0.4	405.5277	7.957415	0.566638
0.45	404.9482	8.870203	0.443655
0.5	405.8293	9.285037	0.608106
0.6	406.1273	8.2521	0.46543
0.7	406.4274	6.147283	0.078641
0.8	406.2507	10.03293	0.137308
0.9	405.9395	10.65249	0.107703
1	405.7369	11.03263	0.07921
1.1	405.0923	10.50643	0.1083
1.2	403.9047	10.1198	0.109131
1.3	402.5211	10.22151	0.111909

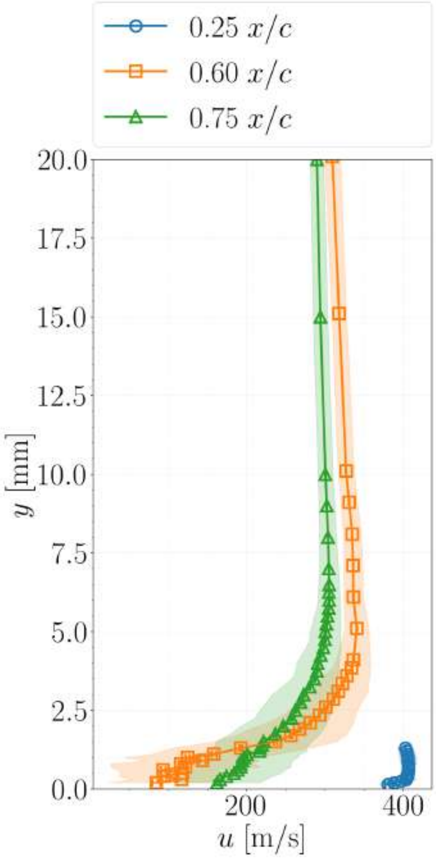

BL velocity profiles at different chordwise locations (The shaded area behind the graphs indicates the RMS of the velocity fluctuations).

Table D.8: Profile 3: velocity profile at 0.60 x/c

y	$\overline{u}$	u_{rms}	$\zeta_{\overline{u}}$
0.20	84.999	60.671	5.232
0.30	117.434	63.321	5.590
0.40	94.371	57.404	3.491
0.50	118.339	79.373	5.200
0.60	93.753	57.672	2.987
0.70	122.213	94.894	2.866
0.80	116.112	89.107	2.595
0.90	143.609	73.013	3.875
1.00	124.836	80.588	2.362
1.10	158.498	79.553	3.289
1.30	192.724	87.329	1.537
1.50	236.773	77.388	2.072
1.70	256.649	70.247	1.490
1.90	267.831	64.015	1.211
2.10	281.314	55.110	0.954
2.35	293.175	45.900	0.707
2.60	301.034	42.205	2.343
2.85	310.802	38.331	1.354
3.10	317.141	37.813	1.388
3.35	322.240	33.351	1.012
3.60	327.877	29.352	0.656
3.85	333.957	23.980	0.831
4.10	336.405	21.627	0.686
5.10	340.577	15.293	0.434
6.10	336.162	12.409	0.338
7.10	336.004	11.967	0.227
8.10	334.692	11.319	0.340
9.10	330.814	10.653	0.295
10.10	326.979	10.283	0.282
15.10	318.097	9.260	0.236
20.10	309.363	10.067	0.269

Table D.9: Profile 3: velocity profile at 0.75 x/c

y	$\overline{u}$	u_{rms}	$\zeta_{\overline{u}}$
0.20	162.245	54.902	3.244
0.30	166.267	58.265	3.257
0.40	174.038	58.853	3.630
0.50	183.866	60.314	3.339
0.60	188.865	59.278	3.095
0.70	192.566	63.865	2.355
0.80	192.626	63.870	4.797
0.90	194.413	63.979	4.177
1.00	197.118	67.622	3.989
1.10	200.762	67.104	3.775
1.20	216.197	60.810	1.697
1.30	216.706	58.454	1.760
1.40	219.635	59.889	1.933
1.50	221.799	60.862	2.040
1.75	236.506	57.135	1.611
2.00	246.686	53.622	0.995
2.25	257.671	47.202	1.295
2.50	262.348	45.781	1.269
2.75	269.245	44.009	1.105
3.00	273.089	40.501	0.910
3.25	280.603	35.146	0.607
3.50	286.523	28.970	0.671
3.75	289.822	27.502	0.632
4.00	291.011	26.873	0.533
4.25	294.432	24.879	0.488
4.50	298.230	22.061	0.374
4.75	299.852	19.623	0.628
5.00	300.426	19.746	0.564
5.25	302.098	17.942	0.525
5.50	303.232	16.687	0.483
5.75	304.929	15.211	0.257
6.00	305.433	14.248	0.308
6.25	304.932	13.600	0.294
6.50	305.173	13.240	0.280
7.00	305.033	12.020	0.276
8.00	303.788	10.842	0.169
9.00	302.327	10.072	0.218
10.00	300.606	9.433	0.189
15.00	294.171	9.252	0.196
20.00	289.622	8.465	0.184

Profile 4 (P4-1.49Ra) boundary layer data

Table D.10: Profile 4: Velocity profile at 0.25 x/c

y	u	u_{rms}	$\zeta_{\overline{u}}$
0.15	392.873	11.762	1.312
0.20	394.846	9.977	1.126
0.25	395.523	11.077	0.994
0.30	396.316	10.083	0.540
0.35	396.727	8.223	0.741
0.40	397.067	7.543	0.610
0.45	398.636	6.475	0.163
0.50	398.734	5.698	0.105
0.60	399.177	11.419	0.066
0.70	399.135	11.484	0.058
0.80	399.160	11.445	0.101
0.90	399.139	11.478	0.103
1.00	399.070	11.586	0.075
1.10	399.022	11.660	0.109
1.20	399.023	11.658	0.107
1.30	397.397	12.870	0.072
1.40	397.395	12.873	0.101
1.60	397.397	12.871	0.102
1.80	397.409	12.855	0.103
2.00	397.357	12.925	0.105
2.50	396.581	10.314	0.076
3.00	396.291	10.863	0.112
3.50	396.196	11.036	0.078
4.50	396.396	10.668	0.106
5.00	396.470	10.528	0.077
5.50	396.454	10.559	0.104
6.00	396.396	10.668	0.104
6.50	396.349	10.757	0.105
7.00	396.281	10.881	0.106
7.51	396.344	10.766	0.061
8.00	396.227	10.979	0.076
9.00	396.256	10.927	0.075
10.00	396.172	11.079	0.077
12.50	396.218	10.997	0.076
15.00	395.983	11.411	0.080

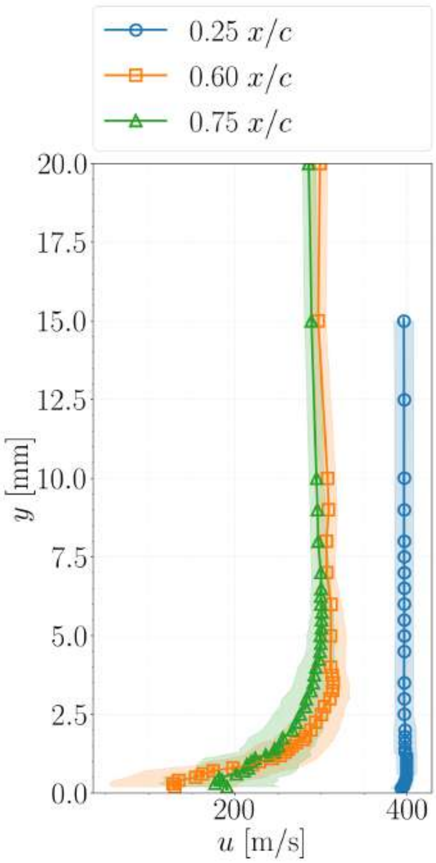

BL velocity profiles at different chordwise locations (The shaded area behind the graphs indicates the RMS of the velocity fluctuations).

Table D.11: Profile 4: velocity profile at 0.60 x/c

y	$\overline{u}$	u_{rms}	$\zeta_{\overline{u}}$
0.20	130.510	72.614	1.284
0.30	128.102	74.303	1.163
0.40	134.964	76.426	1.292
0.50	154.705	79.785	0.931
0.60	162.588	78.205	1.272
0.70	174.816	79.916	1.230
0.80	197.819	74.038	0.829
0.90	220.661	59.593	0.749
1.00	228.301	59.322	0.810
1.10	243.915	51.141	0.455
1.20	253.196	44.038	0.610
1.30	258.479	43.692	0.606
1.40	261.673	43.000	0.596
1.50	266.065	42.881	0.594
1.60	271.117	39.831	0.461
1.70	279.771	35.125	0.748
1.80	281.596	33.882	0.711
2.00	288.075	32.109	0.559
2.25	293.596	29.117	0.448
2.50	300.475	25.335	0.248
2.75	303.965	23.847	0.331
3.00	310.404	22.350	0.310
3.25	313.346	19.106	0.265
3.50	314.339	17.580	0.244
3.75	312.839	16.550	0.195
4.00	311.067	16.335	0.275
5.00	311.301	17.741	0.406
6.00	311.473	12.115	0.192
7.00	306.551	9.569	0.156
8.00	306.354	11.006	0.128
9.00	308.637	10.204	0.164
10.00	307.455	9.427	0.174
15.00	296.715	8.429	0.085
20.00	298.755	8.708	0.100

Table D.12: Profile 4: velocity profile at 0.75 x/c

y	$\overline{u}$	u_{rms}	$\zeta_{\overline{u}}$
0.20	190.892	59.819	0.601
0.30	176.926	65.283	0.709
0.40	185.176	64.757	0.542
0.50	181.921	66.266	0.683
0.60	201.628	62.829	0.542
0.70	211.032	59.327	0.390
0.80	215.494	57.833	0.466
0.90	214.052	58.520	0.452
1.00	218.867	58.856	0.444
1.10	223.377	59.551	0.487
1.20	235.824	52.153	0.323
1.30	245.740	40.445	0.561
1.40	246.112	40.967	0.568
1.50	251.437	40.659	0.564
1.75	255.637	39.832	0.552
2.00	266.569	35.271	0.346
2.25	270.920	31.989	0.443
2.50	275.780	31.424	0.436
2.75	281.486	29.458	0.408
3.00	282.893	28.389	0.393
3.25	288.276	24.623	0.253
3.50	290.660	22.583	0.324
3.75	292.014	21.428	0.320
4.00	293.868	20.424	0.294
4.25	297.445	18.198	0.254
4.50	298.621	16.155	0.165
4.75	299.844	16.044	0.249
5.00	299.177	16.012	0.253
5.25	300.524	14.618	0.233
5.50	300.409	14.318	0.207
5.75	301.027	12.607	0.143
6.00	299.831	12.404	0.185
6.25	299.675	11.834	0.177
6.50	299.923	11.645	0.176
7.00	299.834	10.593	0.173
8.00	296.558	9.279	0.102
9.00	295.732	8.924	0.145
10.00	294.643	8.652	0.136
15.00	288.801	8.042	0.124
20.00	285.758	7.605	0.109

Appendix E

Low Reynolds number investigation

This study addresses the critical challenge of SBLI in transonic compressors, particularly under conditions simulating high-altitude flight. At altitude, reduced air density results in lower Reynolds numbers, which typically exacerbates laminar boundary layer separation and increases aerodynamic losses [53, 180–182]. The research aimed to experimentally quantify how SBLI is affected by changes in the Reynolds number on a representative fan profile in a linear cascade. The experimental approach utilized an inlet valve system to manipulate the total pressure and, consequently, the Reynolds number [183].

E.1 Inlet valve setup

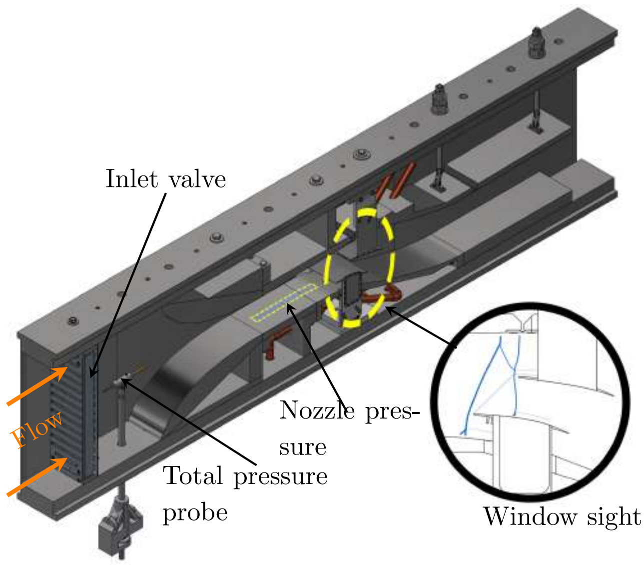

Figure E.1: Test section with the inlet valve

The Reynolds number control was achieved via a novel inlet valve installed in the upstream section of the IMP-PAN transonic wind tunnel as shown in Figure E.1. The valve system, located 240 mm upstream of the test section, employed sliding slotted plates and a perforated screen to modulate the total pressure (p_{01}). The study compared a High-Re case ($Re_c \approx 1.11 \times 10^6$) and a Low-Re case ($Re_c \approx 0.79 \times 10^6$), both at a constant isentropic Mach number ($M_i \approx 1.22$). The operation of this valve system, while controlling Re_c, simultaneously acted as a turbulence generator. The inflow turbulence intensity (t_I) increased from the baseline 2.66% (valve open/removed) to approximately 4-5% in the tested conditions confirmed by the normalized upstream velocity traverses (Figures E.2a and E.2b).

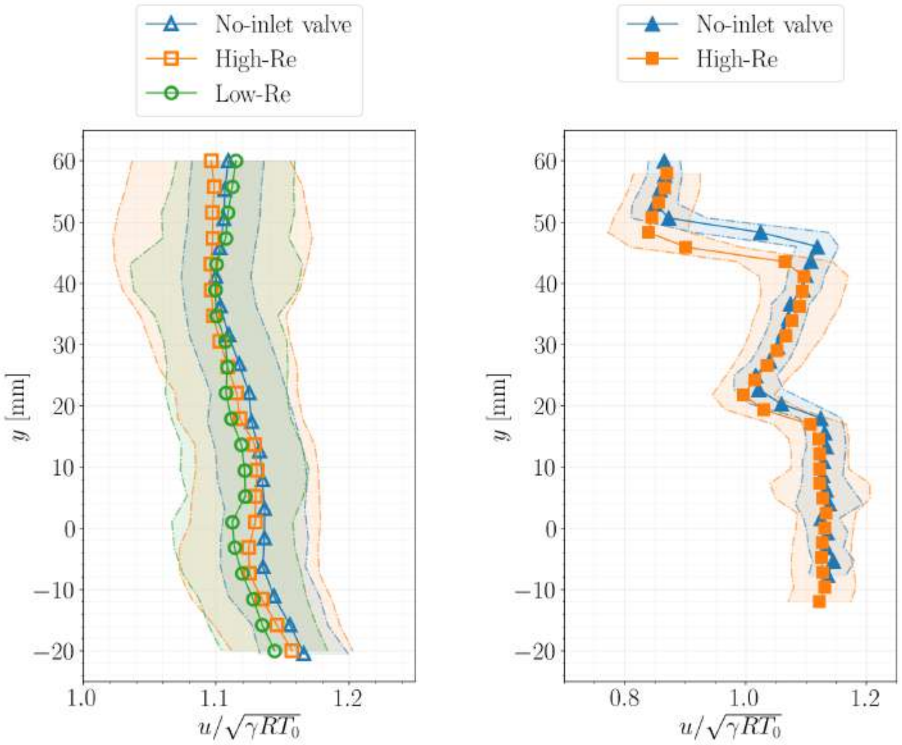

(a) Normalized traverse-a (b) Normalized traverse-b

Figure E.2: Inflow LDA traverse at postions indicated in Figure 2.8

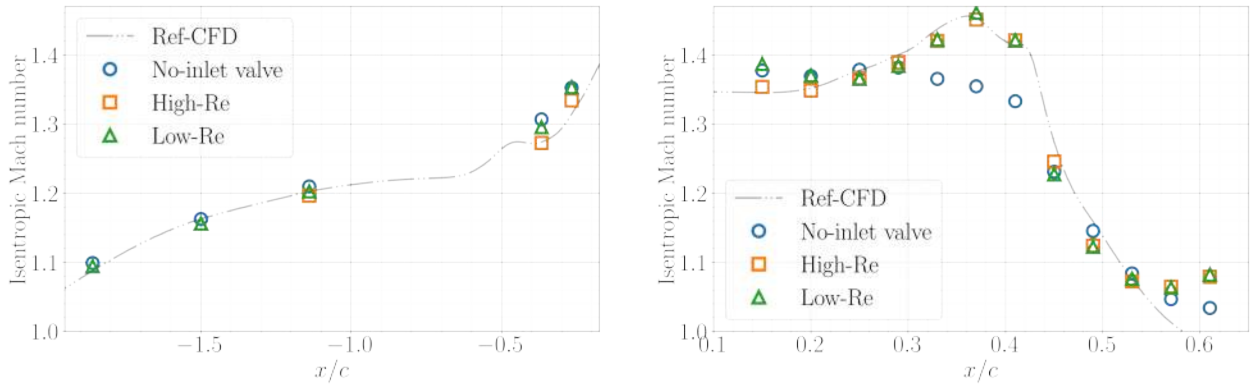

(a) Nozzle upstream of the lower profile (b) On lower profile

Figure E.3: Isentropic Mach number for different Reynolds number configurations

E.2 Flow structure

Surface pressure measurements revealed a consistent time-averaged shock position across all configurations, located at approximately 0.48 x/c. However, the flow physics upstream of the shock was distinctly modified by the high inflow turbulence. Both valved cases exhibited an isentropic Mach number peak immediately preceding the shock, as illustrated in Figure E.3 , a signature absent in the smooth baseline. This peak is attributed to the high inflow turbulence inducing a laminar-to-turbulent transition upstream of the SBLI. The resulting turbulent boundary layer is thicker and more energetic, locally accelerating the free stream before the shock compression. Oil flow visualisation, comparing the baseline (Figure E.4a)and the High-Re case (Figure E.4b) , further showed that the turbulent SBLI led to a smaller separation bubble compared to the baseline, which featured a laminar-type separation.

provided quantitative details on the boundary layer structure. The velocity profiles measured upstream of the shock (0.25 x/c) for the valved cases were already fuller and possessed steeper near-wall gradients, supporting the transition to a turbulent-like state before the interaction. This turbulent boundary layer proved to be more robust and resistant to separation when encountering

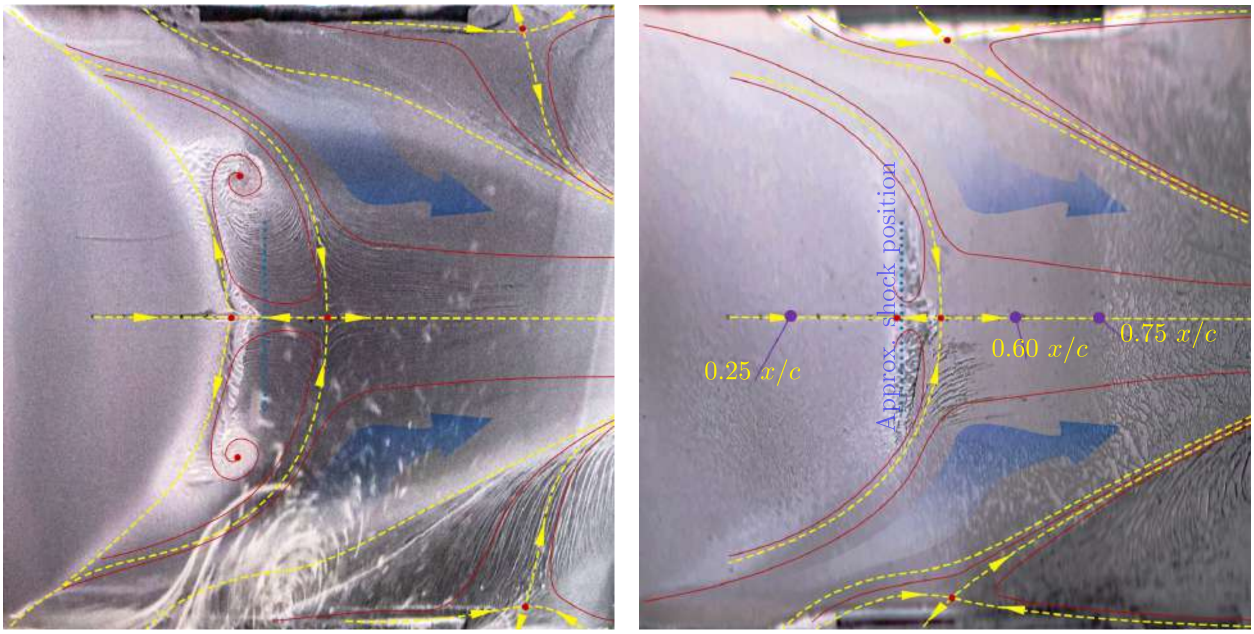

(a) No-inlet valve (b) High-Re

Figure E.4: Surface flow topology comparison

the shock-induced adverse pressure gradient. This robustness was evidenced by a smaller increase in boundary layer thickness across the SBLI region in the High-Re case compared to the baseline, validating the visual confirmation of a smaller physical separation zone.

E.3 Unsteady shock behaviour

The transition to a turbulent SBLI, while beneficial for boundary layer stability, resulted in a significant degradation of the flow's stability. High-speed Schlieren tracking showed a notable increase in the shock displacement amplitude, with the High-Re case exhibiting nearly 2 mm greater displacement than the baseline. PSD analysis further indicated a pronounced shift in energy content towards higher frequencies in the valved cases. Finally, Wavelet analysis highlighted the highly intermittent, dynamic nature of the shock movement when interacting with the turbulent boundary layer, evidenced by multiple, abrupt high-amplitude peaks across the time domain.

E.4 Conclusions

The study concluded that the introduction of high inflow turbulence via the inlet valve system fundamentally altered the SBLI from a laminar-type to a fully turbulent interaction. This turbulent SBLI yielded a key aerodynamic benefit—a smaller, more controlled separation bubble and greater resistance to separation—at the significant cost of an aeroacoustic deterioration, marked by highly increased shock unsteadiness, larger displacements, and elevated high-frequency energy content. The research provides valuable experimental data quantifying the complex trade-off between boundary layer stability and shock wave unsteadiness in a highly turbulent flow environment.

Bibliography

[1] European Union Aviation Safety Agency. *European aviation environmental report 2025.* LU: Publications Office, 2025. DOI: 10.2822/1537033 (cit. on p. 1).

[2] Oleksandr Zaporozhets, Volodymyr Isaienko, and Kateryna Synylo. "PARE preliminary analysis of ACARE FlightPath 2050 environmental impact goals". In: *CEAS Aeronautical Journal* 12.3 (July 2021), pp. 653–667. ISSN: 1869-5590. DOI: 10.1007/s13272-021-00525-7 (cit. on p. 1).

[3] European Commission. Directorate General for Research et al. *Flightpath 2050 :Europe's vision for aviation : maintaining global leadership and serving society's needs.* LU: Publications Office, 2011. DOI: 10.2777/50266 (cit. on p. 1).

[4] Ali Shahsavari and Mahdi Nili-Ahmadabadi. "A novel approach for the design of axial flow fan by increasing by-pass ratio in a constant-diameter turbofan". In: *Propulsion and Power Research* 9.2 (June 2020), pp. 142–158. ISSN: 2212-540X. DOI: 10.1016/j.jppr.2020.04.005 (cit. on p. 1).

[5] Lars Müller et al. "Experimental and numerical evaluation of a high turning transonic compressor stator cascade at flight idle conditions". In: *9th European Conference on Turbomachinery Fluid Dynamics and Thermodynamics.* ETC9. European Turbomachinery Society, 2011. DOI: 10.29008/etc2011-311 (cit. on p. 1).

[6] Jannik Eckel et al. "3D Numerical and Experimental Investigation of High Turning Compressor Tandem Cascade". In: *Deutscher Luft- und Raumfahrtkongress 2016.* DLRK 2016 (Braunschweig, Germany, Sept. 2016). Sept. 2016. URL: https://www.researchgate.net/publication/308992333_3D_Numerical_and_Experimental_Investigation_of_High_Turning_Compressor_Tandem_Cascade (cit. on p. 1).

[7] Mohamed Mohsen, Farouk M. Owis, and Ali A. Hashim. "The impact of tandem rotor blades on the performance of transonic axial compressors". In: *Aerospace Science and Technology* 67 (Aug. 2017), pp. 237–248. ISSN: 1270-9638. DOI: 10.1016/j.ast.2017.04.019 (cit. on p. 1).

[8] Jack L. Kerrebrock. "Flow in Transonic Compressors". In: *AIAA Journal* 19.1 (Jan. 1981), pp. 4–19. ISSN: 1533-385X. DOI: 10.2514/3.50919 (cit. on p. 2).

[9] Seymour Lieblein and Irving A. Johnsen. "Résumé of Transonic-Compressor Research at NACA Lewis Laboratory". In: *Journal of Engineering for Power* 83.3 (July 1961), pp. 219–232. ISSN: 0022-0825. DOI: 10.1115/1.3673177 (cit. on pp. 2, 3, 6).

[10] Donald R. Seyler and Jr. Leroy H. Smith. *Single Stage Experimental Evaluation of High Mach Number Compressor Rotor Blading. Part I – Design of Rotor Blading.* Tech. rep. NASA-CR-54581. Washington, DC: National Aeronautics and Space Administration, Apr. 1967. URL: https://ntrs.nasa.gov/citations/19670015749 (cit. on p. 2).

[11] Michał Piotrowicz. *Oddziaływanie fali uderzeniowej z warstwą przyścienną na profilu sprężarki lotniczej.* Gdańsk, Poland: Instytut Maszyn Przepływowych, Polskiej Akademii Nauk, 2025. ISBN: 978-83-66928-17-6. URL: www.researchgate.net/publication/395953373 (cit. on pp. 2, 64).

[12] Roberto Biollo. "Systematic Investigation on Swept and Leaned Transonic Compressor Rotor Blades". Doctoral Thesis. Padua, Italy: University of Padua, 2008. URL: http://hdl.handle.net/11577/3425959 (cit. on p. 2).

[13] Erik Dick. “Basic Components”. In: *Fundamentals of Turbomachines*. Springer International Publishing, 2022, pp. 53–98. ISBN: 9783030935788. DOI: 10.1007/978-3-030-93578-8_2 (cit. on pp. 3, 5).

[14] Royce N. Brown. “Compressors: Selection and Sizing”. In: 3rd ed. Gulf Professional Publishing, 2005. Chap. 6: Axial Compressors, pp. 262–294 (cit. on pp. 3, 4).

[15] S.L. Dixon and C.A. Hall. “Axial-Flow Compressors and Ducted Fans”. In: *Fluid Mechanics and Thermodynamics of Turbomachinery*. 7th ed. Elsevier, 2014, pp. 169–214. ISBN: 9780124159549. DOI: 10.1016/b978-0-12-415954-9.00005-x (cit. on p. 3).

[16] J. D. Denton and L. Xu. “The Effects of Lean and Sweep on Transonic Fan Performance”. In: *Volume 5: Turbo Expo 2002, Parts A and B*. GT2002. ASMEDC, Jan. 2002. DOI: 10.1115/gt2002-30327 (cit. on p. 4).

[17] I. J. Day and C. Freeman. “The Unstable Behavior of Low and High Speed Compressors”. In: *Volume 1: Aircraft Engine; Marine; Turbomachinery; Microturbines and Small Turbomachinery*. GT1993. American Society of Mechanical Engineers, May 1993. DOI: 10.1115/93-gt-026 (cit. on p. 4).

[18] Scott C. Morris and Thomas C. Corke. *Aero-Mechanical Coupling in a High-Speed Compressor*. Final Technical Report UND-SM10-0338. AFOSR Contract No. FA9550-07-1-0166. University of Notre Dame, 2010 (cit. on p. 4).

[19] Xiaofeng SUN, Xu DONG, and Dakun SUN. “Recent development of casing treatments for aero-engine compressors”. In: *Chinese Journal of Aeronautics* 32.1 (Jan. 2019), pp. 1–36. ISSN: 1000-9361. DOI: 10.1016/j.cja.2018.11.005 (cit. on p. 4).

[20] Nicholas A. Cumpsty. *Compressor Aerodynamics*. Harlow, Essex, England: Longman Scientific & Technical, 1989 (cit. on pp. 4, 5, 7, 8, 11, 13).

[21] S. Can Gülen. In: *Gas Turbines for Electric Power Generation*. Cambridge University Press, Feb. 2019. Chap. 11: Compressor Aero*, pp. 265–307. DOI: 10.1017/9781108241625.012 (cit. on p. 4).

[22] Ronald H. Aungier. In: *Axial-Flow Compressors*. ASME Press, 2003, pp. 117–152. ISBN: 0791801926. DOI: 10.1115/1.801926.ch6 (cit. on pp. 5, 6).

[23] W. A. Benser. “Transonic Compressor Technology Advancements”. In: *Fluid Mechanics, Acoustics, and Design of Turbomachinery, Part 2*. Conference paper; NASA Accession No. 75N11199. NASA Lewis Research Center. Pennsylvania State University, USA, 1974. URL: https://ntrs.nasa.gov/citations/19750003127 (cit. on p. 6).

[24] Alistair John, Shahrokh Shahpar, and Ning Qin. “Alleviation of Shock-Wave Effects on a Highly Loaded Axial Compressor Through Novel Blade Shaping”. In: *Volume 2A: Turbomachinery*. GT2016. American Society of Mechanical Engineers, June 2016. DOI: 10.1115/gt2016-57550 (cit. on p. 6).

[25] C. C. Koch. “Stalling Pressure Rise Capability of Axial Flow Compressor Stages”. In: *Journal of Engineering for Power* 103.4 (Oct. 1981), pp. 645–656. ISSN: 0022-0825. DOI: 10.1115/1.3230787 (cit. on p. 6).

[26] Seymour Lieblein, Francis C. Schwenk, and Robert L. Broderick. *Diffusion Factor for Estimating Losses and Limiting Blade Loadings in Axial-Flow-Compressor Blade Elements*. Tech. rep. NACA-RM-E53D01. Also distributed as AD-11178 by the Armed Services Technical Information Agency (ASTIA). Cleveland, Ohio: National Advisory Committee for Aeronautics, 1953 (cit. on p. 6).

[27] Jiabin LI and Lucheng JI. “An improved prediction model for corner stall in axial compressors with dihedral effect”. In: *Chinese Journal of Aeronautics* 33.5 (May 2020), pp. 1433–1443. ISSN: 1000-9361. DOI: 10.1016/j.cja.2019.12.031 (cit. on p. 6).

[28] Baojie Liu, Du Fu, and Xianjun Yu. “Maximum Loading Capacity of Tandem Blades in Axial Compressors”. In: *Volume 2C: Turbomachinery*. GT2018. American Society of Mechanical Engineers, June 2018. DOI: 10.1115/gt2018-76770 (cit. on p. 6).

[29] Edwin J. Munoz Lopez et al. "The New Chapter of Transonic Compressor Cascade Design at the DLR". In: *Journal of Turbomachinery* 145.8 (Apr. 2023). ISSN: 1528-8900. DOI: 10.1115/1.4056982 (cit. on p. 6).

[30] Pierre de Haller. "Das verhalten von tragflügelgittern in axialverdichtern und im windkanal". In: *Brennstoff-Wärme-Kraft (BWK)* 5.333 (1953), p. 24 (cit. on p. 6).

[31] Dengke Xu et al. "Effect of rotor blade loading distribution on flow stability of transonic compressor". In: *Aerospace Science and Technology* 127 (Aug. 2022), p. 107729. ISSN: 1270-9638. DOI: 10.1016/j.ast.2022.107729 (cit. on p. 6).

[32] Jian Li et al. "An improved stall prediction model for axial compressor stage based on diffuser analogy". In: *Aerospace Science and Technology* 127 (Aug. 2022), p. 107692. ISSN: 1270-9638. DOI: 10.1016/j.ast.2022.107692 (cit. on p. 6).

[33] Hans A. Schreiber and Hans Starken. "An Investigation of a Strong Shock Wave Turbulent Boundary Layer Interaction in a Supersonic Compressor Cascade". In: *Journal of Turbomachinery* 114.3 (July 1992), pp. 494–503. ISSN: 1528-8900. DOI: 10.1115/1.2929170 (cit. on pp. 7, 13).

[34] Edwin Joseph Munoz Lopez et al. "The Current Gap between Design Optimization and Experiments for Transonic Compressor Blades". In: *International Journal of Turbomachinery, Propulsion and Power* 8.4 (Nov. 2023), p. 47. ISSN: 2504-186X. DOI: 10.3390/ijtpp8040047 (cit. on p. 7).

[35] Joachim Klinner, Alexander Hergt, and Christian Willert. "Experimental investigation of the transonic flow around the leading edge of an eroded fan airfoil". In: *Experiments in Fluids* 55.9 (Aug. 2014). ISSN: 1432-1114. DOI: 10.1007/s00348-014-1800-y (cit. on p. 7).

[36] Pawel Flaszynski et al. "Shock wave boundary layer interaction on suction side of compressor profile in single passage test section". In: *Journal of Thermal Science* 24.6 (Nov. 2015), pp. 510–515. ISSN: 1993-033X. DOI: 10.1007/s11630-015-0816-9 (cit. on pp. 7, 69, 72).

[37] C. C. Koch and L. H. Smith. "Loss Sources and Magnitudes in Axial-Flow Compressors". In: *Journal of Engineering for Power* 98.3 (July 1976), pp. 411–424. ISSN: 0022-0825. DOI: 10.1115/1.3446202 (cit. on pp. 7, 19, 20, 22).

[38] Roberto Biollo and Ernesto Benini. "Recent advances in transonic axial compressor aerodynamics". In: *Progress in Aerospace Sciences* 56 (Jan. 2013), pp. 1–18. ISSN: 0376-0421. DOI: 10.1016/j.paerosci.2012.05.002 (cit. on p. 8).

[39] B. Becker, M. Reyer, and M. Swoboda. "Steady and unsteady numerical investigation of transitional shock-boundary-layer-interactions on a fan blade". In: *Aerospace Science and Technology* 11.7-8 (Nov. 2007), pp. 507–517. ISSN: 1270-9638. DOI: 10.1016/j.ast.2007.05.002 (cit. on p. 8).

[40] Piotr Doerffer et al., eds. *Transition Location Effect on Shock Wave Boundary Layer Interaction: Experimental and Numerical Findings from the TFAST Project.* Springer Cham, 2020. ISBN: 978-3-030-47461-4. DOI: 10.1007/978-3-030-47461-4 (cit. on pp. 8, 14, 26).

[41] Bernhard Kusters and Hans A. Schreiber. "Compressor Cascade Flow with Strong Shock-Wave/Boundary-Layer Interaction". In: *AIAA Journal* 36.11 (Nov. 1998), pp. 2072–2078. ISSN: 1533-385X. DOI: 10.2514/2.308 (cit. on p. 8).

[42] Hermann Schlichting and Klaus Gersten. *Boundary-Layer Theory.* Springer Berlin Heidelberg, 2017. ISBN: 9783662529195. DOI: 10.1007/978-3-662-52919-5 (cit. on pp. 8, 9).

[43] R. G. Jacobs and P. A. Durbin. "Simulations of bypass transition". In: *Journal of Fluid Mechanics* 428 (Feb. 2001), pp. 185–212. ISSN: 1469-7645. DOI: 10.1017/s0022112000002469 (cit. on p. 9).

[44] Jean Delery, Joe G. Marvin, and Eli Reshotko. *Shock-wave boundary layer interactions.* Tech. rep. AGARD-AG-280. AGARD Advisory Report, AD-A171302. Neuilly-sur-Seine, France: Advisory Group for Aerospace Research and Development (AGARD), Feb. 1986. URL: https://ntrs.nasa.gov/citations/19860019701 (cit. on pp. 9, 61).

[45] Jean Délery. "Physical Introduction". In: *Shock Wave-Boundary-Layer Interactions*. Ed. by Holger Babinsky and John K.Editors Harvey. Cambridge Aerospace Series. Cambridge University Press, 2011, pp. 5–86. DOI: 10.1017/cbo9780511842757.002 (cit. on pp. 9, 11).

[46] Frank M White and Joseph Majdalani. *Viscous fluid flow*. 3rd ed. McGraw-Hill New York, 2006, pp. 216–223 (cit. on pp. 9, 19, 60).

[47] Ronald D. Joslin. "AIRCRAFT LAMINAR FLOW CONTROL". In: *Annual Review of Fluid Mechanics* 30.1 (Jan. 1998), pp. 1–29. ISSN: 1545-4479. DOI: 10.1146/annurev.fluid.30.1.1 (cit. on p. 10).

[48] Antonio Ferri. *Experimental Results with Airfoils Tested in the High-Speed Tunnel at Guidonia*. Tech. rep. NACA-TM-946. Washington, D.C.: National Advisory Committee for Aeronautics, July 1940. URL: https://ntrs.nasa.gov/citations/19930094471 (cit. on p. 11).

[49] Kshitij Sabnis and Holger Babinsky. "A review of three-dimensional shock wave–boundary-layer interactions". In: *Progress in Aerospace Sciences* 143 (Nov. 2023), p. 100953. ISSN: 0376-0421. DOI: 10.1016/j.paerosci.2023.100953 (cit. on p. 12).

[50] Gang He, Jin Zhou, and Yu-xin Zhao. "Application of free interaction theory in swept shock wave/turbulent boundary layer interactions". In: *Journal of Visualization* 21.2 (Nov. 2017), pp. 203–214. ISSN: 1875-8975. DOI: 10.1007/s12650-017-0454-2 (cit. on p. 11).

[51] Dean R. Chapman, Donald M. Kuehn, and Howard K. Larson. *Investigation of Separated Flows in Supersonic and Subsonic Streams with Emphasis on the Effect of Transition*. Technical Report NACA-TR-1356. National Advisory Committee for Aeronautics, 1958. URL: https://ntrs.nasa.gov/citations/19930092343 (cit. on p. 11).

[52] H. W. Liepman, A. Roshko, and S. Dhawan. *On Reflection of Shock Waves from Boundary Layers*. Technical Report NACA-TR-1100. California, US: National Advisory Committee for Aeronautics, 1952. URL: https://ntrs.nasa.gov/citations/19930090967 (cit. on p. 12).

[53] Todd S. Davidson and Holger Babinsky. "Influence of transition on the flow downstream of normal shock wave–boundary layer interactions". In: *54th AIAA Aerospace Sciences Meeting*. American Institute of Aeronautics and Astronautics, Jan. 2016. DOI: 10.2514/6.2016-0044 (cit. on pp. 12, 116).

[54] Erik Dick. "Axial Compressors". In: *Fundamentals of Turbomachines*. Springer International Publishing, 2022, pp. 489–538. ISBN: 9783030935788. DOI: 10.1007/978-3-030-93578-8_13 (cit. on p. 13).

[55] Holger Babinsky and Jean Délery. "Transonic Shock Wave\Boundary-Layer Interactions". In: *Shock Wave-Boundary-Layer Interactions*. Cambridge University Press, Sept. 2011, pp. 87–136. ISBN: 9781107646537. DOI: 10.1017/cbo9780511842757.003 (cit. on pp. 13, 14, 61).

[56] P. Doerffer and J. Zierep. "An experimental investigation of the Reynolds number effect on a normal shock wave-turbulent boundary layer interaction on a curved wall". In: *Acta Mechanica* 73.1-4 (Aug. 1988), pp. 77–93. ISSN: 1619-6937. DOI: 10.1007/bf01177032 (cit. on p. 13).

[57] Marius Swoboda and Wolfgang Nitsche. "Shock boundary-layer interaction on transonic airfoils for laminar and turbulent flow". In: *Journal of Aircraft* 33.1 (Jan. 1996), pp. 100–108. ISSN: 1533-3868. DOI: 10.2514/3.46909 (cit. on pp. 13, 47).

[58] Jean-Paul Dussauge, Pierre Dupont, and Jean-François Debiéve. "Unsteadiness in shock wave boundary layer interactions with separation". In: *Aerospace Science and Technology* 10.2 (Mar. 2006), pp. 85–91. ISSN: 1270-9638. DOI: 10.1016/j.ast.2005.09.006 (cit. on pp. 13, 55).

[59] L. Agostini, L. Larchevêque, and P. Dupont. "Mechanism of shock unsteadiness in separated shock/boundary-layer interactions". In: *Physics of Fluids* 27.12 (Dec. 2015). ISSN: 1089-7666. DOI: 10.1063/1.4937350 (cit. on p. 13).

[60] Paul J. Bruce and Holger Babinsky. "Unsteady shock wave dynamics". In: *Journal of Fluid Mechanics* 603 (Apr. 2008), pp. 463–473. ISSN: 1469-7645. DOI: 10.1017/s0022112008001195 (cit. on p. 13).

[61] Piotr Doerffer et al. *Unsteady Effects of Shock Wave induced Separation*. en. Ed. by Piotr Doerffer et al. Vol. 114. Notes on Numerical Fluid Mechanics and Multidisciplinary Design. Berlin, Germany: Springer Science & Business Media, Dec. 2010. DOI: 10.1007/978-3-642-03004-8 (cit. on p. 13).

[62] Alexander Hergt et al. "The Present Challenge of Transonic Compressor Blade Design". In: *Journal of Turbomachinery* 141.9 (May 2019). ISSN: 1528-8900. DOI: 10.1115/1.4043329 (cit. on pp. 13, 47).

[63] Patrick Grothe et al. "WP-3 Internal Flows—Compressors". In: *Transition Location Effect on Shock Wave Boundary Layer Interaction*. Springer International Publishing, July 2020, pp. 229–296. ISBN: 978-3-030-47461-4. DOI: 10.1007/978-3-030-47461-4_4 (cit. on pp. 14, 33).

[64] Pawel Flaszynski, Holger Babinsky, and Piotr Doerffer, eds. *Towards Effective Flow Control and Mitigation of Shock Effects in Aeronautical Applications*. Cham: Springer Nature Switzerland, 2025. ISBN: 978-3-031-86605-0. DOI: 10.1007/978-3-031-86605-0 (cit. on p. 14).

[65] Philipp L. Nel et al. "Research configuration to study shock oscillation mechanisms in highly loaded transonic fans". In: *Aerospace Science and Technology* 166 (Nov. 2025), p. 110636. ISSN: 1270-9638. DOI: 10.1016/j.ast.2025.110636 (cit. on p. 14).

[66] Philipp L. Nel et al. "Effect of Transition on Self-Sustained Shock Oscillations in Highly Loaded Transonic Rotors". In: *AIAA Journal* 62.6 (June 2024), pp. 2063–2075. ISSN: 1533-385X. DOI: 10.2514/1.j063378 (cit. on p. 14).

[67] Joachim Klinner et al. "High-Speed PIV of shock boundary layer interactions in the transonic buffet flow of a compressor cascade". In: *Experiments in Fluids* 62.3 (Mar. 2021). ISSN: 1432-1114. DOI: 10.1007/s00348-021-03145-3 (cit. on pp. 14, 53).

[68] Joachim Klinner et al. "Investigation of shock-induced flow separation over a transonic compressor blade by conditionally averaged PIV and high-speed shadowgraphs". In: *17th International Symposium on Applications of Laser Techniques to Fluid Mechanics*. 19th International Symposium on Applications of Laser Techniques to Fluid Mechanics (Lisbon, Portugal, July 16–19, 2016). July 16, 2018. ISBN: 978-989-98777-9-5. URL: https://elib.dlr.de/120895/ (cit. on pp. 14, 96).

[69] A. Joseph et al. "Boundary layer tripping on a transonic compressor profile". en. In: *Archives of Mechanics* (2024). DOI: 10.24423/AOM.4514 (cit. on pp. 14, 39).

[70] Pawel Flaszynski et al. "Laminar-turbulent transition tripped by step on transonic compressor profile". In: *Journal of Thermal Science* 27.1 (Jan. 2018), pp. 1–7. ISSN: 1993-033X. DOI: 10.1007/s11630-018-0977-4 (cit. on p. 14).

[71] Ryszard Szwaba, Piotr Kaczynski, and Piotr Doerffer. "Roughness effect on shock wave boundary layer interaction area in compressor fan blades passage". In: *Aerospace Science and Technology* 85 (Feb. 2019), pp. 171–179. ISSN: 1270-9638. DOI: 10.1016/j.ast.2018.12.006 (cit. on pp. 14, 21, 96).

[72] Joachim Klinner et al. "Experimental investigation of shock-induced separation and flow control in a transonic compressor cascade". In: *Experiments in Fluids* 60.6 (May 2019). ISSN: 1432-1114. DOI: 10.1007/s00348-019-2736-z (cit. on pp. 14, 21, 69).

[73] Rogier Giepman et al. "Experimental investigation of boundary layer tripping devices for shock wave - boundary layer control". In: *45th AIAA Fluid Dynamics Conference*. American Institute of Aeronautics and Astronautics, June 2015. DOI: 10.2514/6.2015-2780 (cit. on pp. 14, 21, 97).

[74] R. H. M. Giepman, F. F. J. Schrijer, and B. W. van Oudheusden. “High-resolution PIV measurements of a transitional shock wave–boundary layer interaction”. In: *Experiments in Fluids* 56.6 (May 2015). ISSN: 1432-1114. DOI: 10.1007/s00348-015-1977-8 (cit. on pp. 14, 96).

[75] Argyris G. Panaras and Frank K. Lu. “Micro-vortex generators for shock wave/boundary layer interactions”. In: *Progress in Aerospace Sciences* 74 (Apr. 2015), pp. 16–47. ISSN: 0376-0421. DOI: 10.1016/j.paerosci.2014.12.006 (cit. on p. 14).

[76] G. Humrutha, Mrinal Kaushik, and K. P. Sinhamahapatra. “Micro-vortex Generator Controlled Shock-Boundary Layer Interactions in Supersonic Intake”. In: *31st International Symposium on Shock Waves 1*. Springer International Publishing, 2019, pp. 1025–1031. ISBN: 9783319910208. DOI: 10.1007/978-3-319-91020-8_123 (cit. on p. 14).

[77] Charles Pitt Ford and Holger Babinsky. “Micro-Ramp Control for Oblique Shock Wave / Boundary Layer Interactions”. In: *37th AIAA Fluid Dynamics Conference and Exhibit*. American Institute of Aeronautics and Astronautics, June 2007. DOI: 10.2514/6.2007-4115 (cit. on p. 14).

[78] Yongzhen LIU et al. “Passage shock wave/boundary layer interaction control for transonic compressors using bumps”. In: *Chinese Journal of Aeronautics* 35.2 (Feb. 2022), pp. 82–97. ISSN: 1000-9361. DOI: 10.1016/j.cja.2021.05.014 (cit. on pp. 14, 15).

[79] Bartosz Ziegler. “Boundary layer control in transonic compressor flows”. In: *Journal of mechanical and transport engineering* 67.3 (2015). DOI: 10.21008/J.2449-920X.2015.67.3.06 (cit. on p. 15).

[80] Bharat Bhushan. “Surface Roughness Analysis and Measurement Techniques”. In: *Modern Tribology Handbook, Two Volume Set*. CRC Press, Dec. 2000. ISBN: 9780849377877. DOI: 10.1201/9780849377877.ch2 (cit. on p. 17).

[81] Luiz Alberto Franco and Amilton Sinatora. “3D surface parameters (ISO 25178-2): Actual meaning of Spk and its relationship to Vmp”. In: *Precision Engineering* 40 (Apr. 2015), pp. 106–111. ISSN: 0141-6359. DOI: 10.1016/j.precisioneng.2014.10.011 (cit. on p. 18).

[82] *Geometrical Product Specifications (GPS) — Surface Texture: Areal — Part 2: Terms, Definitions and Surface Texture Parameters*. International Standard ISO 25178-2. Dec. 2021 (cit. on p. 18).

[83] Mohammadreza Kadivar, David Tormey, and Gerard McGranaghan. “A review on turbulent flow over rough surfaces: Fundamentals and theories”. In: *International Journal of Thermofluids* 10 (May 2021), p. 100077. ISSN: 2666-2027. DOI: 10.1016/j.ijft.2021.100077 (cit. on pp. 18, 20).

[84] John A. Redford, Neil D. Sandham, and Graham T. Roberts. “Compressibility Effects on Boundary-Layer Transition Induced by an Isolated Roughness Element”. In: *AIAA Journal* 48.12 (Dec. 2010), pp. 2818–2830. ISSN: 1533-385X. DOI: 10.2514/1.j050186 (cit. on pp. 18–20).

[85] Promode R. Bandyopadhyay. “Rough-wall turbulent boundary layers in the transition regime”. In: *Journal of Fluid Mechanics* 180 (July 1987), pp. 231–266. ISSN: 1469-7645. DOI: 10.1017/s0022112087001794 (cit. on p. 18).

[86] J. Bons. “A Critical Assessment of Reynolds Analogy for Turbine Flows”. In: *Journal of Heat Transfer* 127.5 (May 2005), pp. 472–485. ISSN: 1528-8943. DOI: 10.1115/1.1861919 (cit. on pp. 18, 20).

[87] S. K. Roberts and M. I. Yaras. “Boundary-Layer Transition Affected by Surface Roughness and Free-Stream Turbulence”. In: *Journal of Fluids Engineering* 127.3 (Feb. 2005), pp. 449–457. ISSN: 1528-901X. DOI: 10.1115/1.1906266 (cit. on p. 18).

[88] Nisat Nowroz Anika, Lyazid Djenidi, and Sedat Tardu. “Bypass transition mechanism in a rough wall channel flow”. In: *Physical Review Fluids* 3.8 (Aug. 2018). ISSN: 2469-990X. DOI: 10.1103/physrevfluids.3.084604 (cit. on pp. 18, 19).

[89] Donald P. Rizzetta and Miguel R. Visbal. "Direct Numerical Simulations of Flow Past an Array of Distributed Roughness Elements". In: *AIAA Journal* 45.8 (Aug. 2007), pp. 1967–1976. ISSN: 1533-385X. DOI: 10.2514/1.25916 (cit. on p. 18).

[90] Nagabhushana Rao Vadlamani, Paul G. Tucker, and Paul Durbin. "Distributed Roughness Effects on Transitional and Turbulent Boundary Layers". In: *Flow, Turbulence and Combustion* 100.3 (Oct. 2017), pp. 627–649. ISSN: 1573-1987. DOI: 10.1007/s10494-017-9864-4 (cit. on pp. 18, 19).

[91] Jr. Harper W. R. and R. M. Hicks. *A Comparison of Spherical and Triangular Boundary-Layer Trips on a Flat Plate at Supersonic Speeds*. Technical Memorandum NASA-TM-X-2146. Also issued as Report No. A-3722. Moffett Field, CA, United States: NASA Ames Research Center, Dec. 1970. URL: https://ntrs.nasa.gov/citations/19710004288 (cit. on p. 19).

[92] Karen A. Flack and Michael P. Schultz. "Review of Hydraulic Roughness Scales in the Fully Rough Regime". In: *Journal of Fluids Engineering* 132.4 (Apr. 2010). ISSN: 1528-901X. DOI: 10.1115/1.4001492 (cit. on p. 19).

[93] J. P. Bons. "A Review of Surface Roughness Effects in Gas Turbines". In: *Journal of Turbomachinery* 132.2 (Jan. 2010). ISSN: 1528-8900. DOI: 10.1115/1.3066315 (cit. on pp. 19, 20).

[94] Martin N. Goodhand. "Admissible Roughness in Gas Turbines". In: *Volume 5C: Heat Transfer*. GT2015. American Society of Mechanical Engineers, June 2015. DOI: 10.1115/gt2015-43326 (cit. on pp. 19, 20).

[95] Matteo Bernardini, Sergio Pirozzoli, and Paolo Orlandi. "Compressibility effects on roughness induced boundary layer transition". In: *International Journal of Heat and Fluid Flow* 35 (June 2012), pp. 45–51. ISSN: 0142-727X. DOI: 10.1016/j.ijheatfluidflow.2012.02.007 (cit. on p. 19).

[96] Takashi Watanabe and Ryoji Kobayashi. "Effect of a single roughness element on boundary layer transition over a wedge". In: *Experimental Thermal and Fluid Science* 4.5 (Sept. 1991), pp. 558–566. ISSN: 0894-1777. DOI: 10.1016/0894-1777(91)90034-o (cit. on p. 19).

[97] Russell Quadros and Matteo Bernardini. "Numerical Investigation of Transitional Shock-Wave/Boundary-Layer Interaction in Supersonic Regime". In: *AIAA Journal* 56.7 (July 2018), pp. 2712–2724. ISSN: 1533-385X. DOI: 10.2514/1.j056650 (cit. on pp. 19, 20).

[98] Javier Jiménez. "Turbulent flows over rough walls". In: *Annual Review of Fluid Mechanics* 36.1 (Jan. 2004), pp. 173–196. ISSN: 1545-4479. DOI: 10.1146/annurev.fluid.36.050802.122103 (cit. on p. 20).

[99] Jasem Alqallaf and Joao A. Teixeira. "Blade Roughness Effects on Compressor and Engine Performance—A CFD and Thermodynamic Study". In: *Aerospace* 8.11 (Nov. 2021), p. 330. ISSN: 2226-4310. DOI: 10.3390/aerospace8110330 (cit. on p. 20).

[100] Mingyang WANG et al. "Effects of surface roughness on the aerodynamic performance of a high subsonic compressor airfoil at low Reynolds number". In: *Chinese Journal of Aeronautics* 34.3 (Mar. 2021), pp. 71–81. ISSN: 1000-9361. DOI: 10.1016/j.cja.2020.08.020 (cit. on p. 20).

[101] Sukhyeon Lim et al. "Impact of Additive Manufacturing Surface Roughness on the Aerodynamic Performance of Axial Compressor Blades". In: *International Journal of Aeronautical and Space Sciences* 26.1 (July 2024), pp. 42–49. ISSN: 2093-2480. DOI: 10.1007/s42405-024-00769-7 (cit. on p. 20).

[102] V. T. Forster. "Performance Loss of Modern Steam-Turbine Plant Due to Surface Roughness". In: *Proceedings of the Institution of Mechanical Engineers* 181.1 (June 1966), pp. 391–422. ISSN: 2058-1203. DOI: 10.1243/pime_proc_1966_181_038_02 (cit. on p. 20).

[103] A. Scha¨ffler. “Experimental and Analytical Investigation of the Effects of Reynolds Number and Blade Surface Roughness on Multistage Axial Flow Compressors”. In: *Journal of Engineering for Power* 102.1 (Jan. 1980), pp. 5–12. ISSN: 0022-0825. DOI: 10.1115/1.3230232 (cit. on p. 20).

[104] Frank Hummel et al. “Surface Roughness Effects on Turbine Blade Aerodynamics”. In: *Journal of Turbomachinery* 127.3 (2005), p. 453. ISSN: 0889-504X. DOI: 10.1115/1.1860377 (cit. on p. 20).

[105] Philipp Gilge et al. “Surface roughness of real operationally used compressor blade and blisk”. In: *Proceedings of the Institution of Mechanical Engineers, Part G: Journal of Aerospace Engineering* 233.14 (May 2019), pp. 5321–5330. ISSN: 2041-3025. DOI: 10.1177/0954410019843438 (cit. on p. 20).

[106] K.A. Flack et al. “Skin-friction behavior in the transitionally-rough regime”. In: *International Journal of Heat and Fluid Flow* 61 (Oct. 2016), pp. 21–30. ISSN: 0142-727X. DOI: 10.1016/j.ijheatfluidflow.2016.05.008 (cit. on p. 20).

[107] Mostafa Aghaei Jouybari et al. “Data-driven prediction of the equivalent sand-grain height in rough-wall turbulent flows”. In: *Journal of Fluid Mechanics* 912 (Feb. 2021). ISSN: 1469-7645. DOI: 10.1017/jfm.2020.1085 (cit. on p. 20).

[108] Haoran Ma et al. “Data-driven prediction of the equivalent sand-grain roughness”. In: *Scientific Reports* 13.1 (Nov. 2023). ISSN: 2045-2322. DOI: 10.1038/s41598-023-46564-4 (cit. on p. 20).

[109] A. Ramani et al. “An assessment of effective slope as a parameter for turbulent drag prediction over multi-scaled roughness”. In: *Experiments in Fluids* 65.6 (May 2024). ISSN: 1432-1114. DOI: 10.1007/s00348-024-03813-0 (cit. on p. 20).

[110] H. Babinsky and G. R. Inger. “Effect of Surface Roughness on Unseparated Shock-Wave/Turbulent Boundary-Layer Interactions”. In: *AIAA Journal* 40.8 (Aug. 2002), pp. 1567–1573. ISSN: 1533-385X. DOI: 10.2514/2.1825 (cit. on p. 20).

[111] Matthias Boese and Leonhard Fottner. “Effects of Riblets on the Loss Behavior of a Highly Loaded Compressor Cascade”. In: *Volume 5: Turbo Expo 2002, Parts A and B*. GT2002. ASMEDC, Jan. 2002, pp. 743–750. DOI: 10.1115/gt2002-30438 (cit. on p. 21).

[112] Christoph Lietmeyer, Karsten Oehlert, and Joerg R. Seume. “Optimal Application of Riblets on Compressor Blades and Their Contamination Behavior”. In: *Journal of Turbomachinery* 135.1 (Oct. 2012). ISSN: 1528-8900. DOI: 10.1115/1.4006518 (cit. on p. 21).

[113] Robert Leipold, Matthias Boese, and Leonhard Fottner. “The Influence of Technical Surface Roughness Caused by Precision Forging on the Flow Around a Highly Loaded Compressor Cascade”. In: *Journal of Turbomachinery* 122.3 (Feb. 1999), pp. 416–424. ISSN: 1528-8900. DOI: 10.1115/1.1302286 (cit. on pp. 21, 97).

[114] Janusz Telega. “Eksperymentalne badania wpływu wirów wzdłużnych na niestacjonarne oderwanie wywołane falą uderzeniową”. Polish. Ph.D. Dissertation. Gdańsk, Poland: Instytut Maszyn Przepływowych im. Roberta Szewalskiego, Polska Akademia Nauk, June 2018 (cit. on p. 24).

[115] *9000 Series Intelligent Pressure Scanners User's Manual*. 4th Edition. Models 9010, 9015, 9016, 9020, 9021. Pressure Systems, Inc. Hampton, Virginia, Mar. 1998. URL: https://engineering.purdue.edu/~aae520/9000manual.pdf (cit. on p. 28).

[116] Ahmed Hanfy et al. *CoGenerator Liberary*. 2024. DOI: 10.5281/ZENODO.12538002 (cit. on p. 32).

[117] M Piotrowicz and P Flaszyński. “Numerical investigations of shock wave interaction with laminar boundary layer on compressor profile”. In: *Journal of Physics: Conference Series* 760 (Oct. 2016), p. 012023. ISSN: 1742-6596. DOI: 10.1088/1742-6596/760/1/012023 (cit. on pp. 33, 39).

[118] *BSA Flow Software User's Guide*. Version 5.11. Build no.: 5.11.00.11. Dantec Dynamics A/S. Tonsbakken 16-18, P.O. Box 121, DK-2740 Skovlunde, Denmark, 2013 (cit. on p. 33).

[119] D. K. McLaughlin and W. G. Tiederman. "Biasing correction for individual realization of laser anemometer measurements in turbulent flows". In: *The Physics of Fluids* 16.12 (Dec. 1973), pp. 2082–2088. ISSN: 0031-9171. DOI: 10.1063/1.1694269 (cit. on p. 34).

[120] W. K. Jr. George. "Limitations to measuring accuracy inherent in the laser-Doppler signal". In: *The Accuracy of Flow Measurements by Laser Doppler Methods, Proceedings of the LDA Symposium 1975*. Washington, D.C.: Hemisphere, 1977, pp. 20–63 (cit. on p. 34).

[121] Lance H. Benedict and Richard D. Gould. "Towards better uncertainty estimates for turbulence statistics". In: *Experiments in Fluids* 22.2 (Dec. 1996), pp. 129–136. ISSN: 1432-1114. DOI: 10.1007/s003480050030 (cit. on p. 35).

[122] Dorota Oniszczuk-Świercz and Rafał Świercz. "Effects of Wire Electrical Discharge Finishing Cuts on the Surface Integrity of Additively Manufactured Ti6Al4V Alloy". In: *Materials* 16.15 (Aug. 2023), p. 5476. ISSN: 1996-1944. DOI: 10.3390/ma16155476 (cit. on p. 38).

[123] Laurenţiu Slătineanu et al. "Wire Electrical Discharge Machining—A Review". In: *Machines* 8.4 (Oct. 2020), p. 69. ISSN: 2075-1702. DOI: 10.3390/machines8040069 (cit. on p. 38).

[124] A. Pramanik et al. "Methods and variables in Electrical discharge machining of titanium alloy - A review". In: *Heliyon* 6.12 (Dec. 2020), e05554. ISSN: 2405-8440. DOI: 10.1016/j.heliyon.2020.e05554 (cit. on p. 38).

[125] K. L. Suder et al. "The Effect of Adding Roughness and Thickness to a Transonic Axial Compressor Rotor". In: *Journal of Turbomachinery* 117.4 (Oct. 1995), pp. 491–505. ISSN: 1528-8900. DOI: 10.1115/1.2836561 (cit. on p. 40).

[126] Alexander Hergt et al. "Effect of Leading-Edge Erosion on the Performance of Transonic Compressor Blades". In: *International Journal of Turbomachinery, Propulsion and Power* 9.1 (Jan. 2024), p. 1. ISSN: 2504-186X. DOI: 10.3390/ijtpp9010001 (cit. on p. 40).

[127] John E. Lamar. *Flow-visualization techniques used at high speed by configuration aerodynamics wind-tunnel-test team*. NASA Technical Memorandum TM-2001-210848. Hampton, VA: National Aeronautics and Space Administration, Langley Research Center, 2001 (cit. on p. 45).

[128] John Leask Lumley. "The Structure of Inhomogeneous Turbulent Flows". In: *Atmospheric Turbulence and Radio Wave Propagation*. Ed. by A. M. Yaglom and V. I. Tatarsky. Moscow: Nauka, 1967, pp. 166–177 (cit. on p. 46).

[129] Matthew G. Berry., Andrew S. Magstadt, and Mark N. Glauser. "Application of POD on time-resolved schlieren in supersonic multi-stream rectangular jets". In: *Physics of Fluids* 29.2 (Feb. 2017). ISSN: 1089-7666. DOI: 10.1063/1.4974518 (cit. on p. 46).

[130] Shanguang GUO, Yun WU, and Hua LIANG. "Strong interactions of incident shock wave with boundary layer along compression corner". In: *Chinese Journal of Aeronautics* 33.12 (Dec. 2020), pp. 3149–3157. ISSN: 1000-9361. DOI: 10.1016/j.cja.2020.09.045 (cit. on p. 46).

[131] Daniel Caruana et al. "Buffet and buffeting control in transonic flow". In: *Aerospace Science and Technology* 9.7 (Oct. 2005), pp. 605–616. ISSN: 1270-9638. DOI: 10.1016/j.ast.2004.12.005 (cit. on p. 47).

[132] Jayaprakash N. Murugan and Raghuraman N. Govardhan. "Shock wave-boundary layer interaction in supersonic flow over a forward-facing step". In: *Journal of Fluid Mechanics* 807 (Oct. 2016), pp. 258–302. ISSN: 1469-7645. DOI: 10.1017/jfm.2016.574 (cit. on p. 47).

[133] Cosimo Corsi et al. "Wall-pressure measurements in a Mach 2 Turbulent SBLI by Means of a PVDF Piezo-Film Sensor Array." In: *AIAA AVIATION 2023 Forum*. American Institute of Aeronautics and Astronautics, June 2023. DOI: 10.2514/6.2023-3574 (cit. on p. 47).

[134] Paul J. K. Bruce and Holger Babinsky. "An experimental study of transonic shock/boundary layer interactions subject to downstream pressure perturbations". In: *Aerospace Science and Technology* 14.2 (2010), pp. 134–142. ISSN: 1270-9638. DOI: 10.1016/j.ast.2009.11.006 (cit. on p. 47).

[135] Zhengzhong Sun, Xin Miao, and Chetan Jagadeesh. "Experimental investigation of the transonic shock-wave/boundary-layer interaction over a shock-generation bump". In: *Physics of Fluids* 32.10 (Oct. 2020), p. 106102. DOI: 10.1063/5.0018763 (cit. on p. 47).

[136] Shanguang Guo, Yun Wu, and Hua Liang. "Strong interactions of incident shock wave with boundary layer along compression corner". In: *Chinese Journal of Aeronautics* 33.12 (2020), pp. 3149–3157. DOI: 10.1016/j.cja.2020.09.045 (cit. on p. 47).

[137] Piotr Doerffer and Janusz Telega. "Flow control effect on unsteadiness of shock wave induced separation". In: *Journal of Thermal Science* 22 (2013), pp. 511–516. DOI: 10.1007/s11630-013-0656-4 (cit. on p. 47).

[138] Christopher S. Combs et al. "Image-based analysis of shock-wave/boundary-layer interaction unsteadiness". In: *AIAA Journal* 56.3 (2018), pp. 1288–1293. DOI: 10.2514/1.J056390 (cit. on pp. 47, 54).

[139] Ahmed H. Hanfy et al. "Enhanced line-scanning method for shock wave tracking in high-speed schlieren imaging". In: *Aerospace Science and Technology* 168 (Jan. 2026), p. 111022. ISSN: 1270-9638. DOI: 10.1016/j.ast.2025.111022 (cit. on p. 47).

[140] Ahmed Hanfy et al. *Shock Oscillation Analysis Library.* [software] (Version 2.15.10). July 2025. URL: https://github.com/EngAhmedHady/ShockTrackingLibrary (cit. on p. 48).

[141] Marcelo Bertalmio, Andrea L. Bertozzi, and Guillermo Sapiro. "Navier-stokes, fluid dynamics, and image and video inpainting". In: *Proceedings of the 2001 IEEE Computer Society Conference on Computer Vision and Pattern Recognition. CVPR 2001.* Vol. 1. CVPR-01. IEEE Comput. Soc, 2001, pp. I–355–I-362. DOI: 10.1109/cvpr.2001.990497 (cit. on p. 48).

[142] Martin A. Fischler and Robert C. Bolles. "Random sample consensus: a paradigm for model fitting with applications to image analysis and automated cartography". In: *Communications of the ACM* 24.6 (June 1981), pp. 381–395. ISSN: 1557-7317. DOI: 10.1145/358669.358692 (cit. on p. 49).

[143] W. A. Wallis. "Tolerance intervals for linear regression". In: *Proceedings of the Second Berkeley Symposium on Mathematical Statistics and Probability.* Vol. 2. University of California Press, 1951, pp. 43–52. URL: https://digicoll.lib.berkeley.edu/record/112745 (cit. on p. 49).

[144] Iain Pardoe. "Simple Linear Regression". In: *Applied Regression Modeling.* Wiley, Dec. 2020, pp. 39–93. ISBN: 9781119615941. DOI: 10.1002/9781119615941.ch2 (cit. on p. 49).

[145] Peter Welch. "The use of fast Fourier transform for the estimation of power spectra: A method based on time averaging over short, modified periodograms". In: *IEEE Transactions on Audio and Electroacoustics* 15.2 (June 1967), pp. 70–73. ISSN: 0018-9278. DOI: 10.1109/tau.1967.1161901 (cit. on p. 54).

[146] Steven L. Brunton and J. Nathan Kutz. "Fourier and Wavelet Transforms". In: *Data-Driven Science and Engineering: Machine Learning, Dynamical Systems, and Control.* Cambridge University Press, 2019, pp. 47–83. DOI: 10.1017/9781108380690.003 (cit. on p. 54).

[147] Morgan L. Funderburk and Venkateswaran Narayanaswamy. "Spectral signal quality of fast pressure sensitive paint measurements in turbulent shock-wave/boundary layer interactions". In: *Experiments in Fluids* 60.10 (Sept. 2019). ISSN: 1432-1114. DOI: 10.1007/s00348-019-2799-x (cit. on p. 54).

[148] Noel T. Clemens and Venkateswaran Narayanaswamy. "Low-Frequency Unsteadiness of Shock Wave/Turbulent Boundary Layer Interactions". In: *Annual Review of Fluid Mechanics* 46.1 (Jan. 2014), pp. 469–492. ISSN: 1545-4479. DOI: 10.1146/annurev-fluid-010313-141346 (cit. on p. 54).

[149] Mehmet E. Erengil and David S. Dolling. "Unsteady wave structure near separation in a Mach 5 compression rampinteraction". In: *AIAA Journal* 29.5 (May 1991), pp. 728–735. ISSN: 1533-385X. DOI: 10.2514/3.10647 (cit. on p. 54).

[150] Pauli Virtanen et al. "SciPy 1.0: fundamental algorithms for scientific computing in Python". In: *Nature Methods* 17.3 (Feb. 2020), pp. 261–272. ISSN: 1548-7105. DOI: 10.1038/s41592-019-0686-2 (cit. on p. 55).

[151] W. Manneschmidt et al. "Normal shock wave coherence relative to other flow events with high and low levels of inlet Mach wave unsteadiness". In: *Shock Waves* 34.6 (Nov. 2024), pp. 497–513. ISSN: 1432-2153. DOI: 10.1007/s00193-024-01202-4 (cit. on p. 55).

[152] Jérémy Basley, Laurent Perret, and Romain Mathis. "Spatial modulations of kinetic energy in the roughness sublayer". In: *Journal of Fluid Mechanics* 850 (July 2018), pp. 584–610. ISSN: 1469-7645. DOI: 10.1017/jfm.2018.458 (cit. on p. 55).

[153] Brian Russell and Jiajun Han. "Jean Morlet and the continuous wavelet transform". In: *CREWES Research Report* 28 (2016), p. 115. URL: https://www.crewes.org/Documents/ResearchReports/abstract.php?docid=CRR201668 (cit. on p. 55).

[154] Ahmed Hanfy et al. *Morlet Continuous Wavelet Transform (CWT) Analysis*. 2024. DOI: 10.5281/ZENODO.14230808 (cit. on p. 55).

[155] Slavica Ristic. "Flow Visualisation Techniques in Wind Tunnels Part I - Non optical Methods". In: *Scientific Technical Review LVII N.* 57.1 (Jan. 2007), pp. 39–50. ISSN: 1820-0206. URL: http://www.vti.mod.gov.rs/ntp/rad2007/1-07/rist/rist.pdf (cit. on p. 56).

[156] Erwan Guillou et al. "Using vanishing points for camera calibration and coarse 3D reconstruction from a single image". In: *The Visual Computer* 16 (Nov. 2000), pp. 396–410. ISSN: 1432-2315. DOI: 10.1007/PL00013394 (cit. on pp. 56, 57).

[157] Yuandong Tian and Srinivasa G. Narasimhan. "Rectification and 3D reconstruction of curved document images". In: *CVPR 2011*. IEEE, June 2011, pp. 377–384. DOI: 10.1109/cvpr.2011.5995540 (cit. on p. 56).

[158] Shaodi You et al. *Multiview Rectification of Folded Documents*. 2016. arXiv: 1606.00166 [cs.CV] (cit. on p. 56).

[159] Jakub Sochor. "Traffic analysis from video". PhD thesis. Example City, CA: Diplomová práce, Brno University of Technology, Faculty of Information Technology, May 2014. URL: https://www.itspy.cz/wp-content/uploads/2014/11/acmspy2014_submission_25.pdf (cit. on p. 57).

[160] Richard Courant and Herbert Robbins. "What is Mathematics?: an elementary approach to ideas and methods". In: NY, USA: Oxford University Press, 1996. Chap. 4, pp. 172–179 (cit. on p. 58).

[161] David Liebowitz and Andrew Zisserman. "Metric rectification for perspective images of planes". In: *Proceedings. 1998 IEEE Computer Society Conference on Computer Vision and Pattern Recognition (Cat. No. 98CB36231)*. IEEE. 1998, pp. 482–488. DOI: 10.1109/CVPR.1998.698649 (cit. on p. 60).

[162] Maximilian L. Eggersdorfer et al. "Rapid Production of Submicron Drug Substance Particles by Supersonic Spray Drying". In: *Crystal Growth & Design* 17.4 (Mar. 2017), pp. 2046–2053. ISSN: 1528-7505. DOI: 10.1021/acs.cgd.7b00033 (cit. on p. 60).

[163] Siegfried Grundmann. *Einsteins Akte: Wissenschaft und Politik - Einsteins Berliner Zeit*. Springer Berlin Heidelberg, 2004. ISBN: 9783642185953. DOI: 10.1007/978-3-642-18595-3 (cit. on p. 60).

[164] G. Tedeschi, M. Elena, and H. Gouin. "Particle motion through an oblique shock wave". In: *Fifth International Conference on Laser Anemometry: Advances and Applications*. Ed. by J. M. Bessem et al. Vol. 2052. SPIE, Aug. 1993, pp. 273–278. DOI: 10.1117/12.150514 (cit. on p. 60).

[165] Douglas Reynolds. “Gaussian Mixture Models”. In: *Encyclopedia of Biometrics*. Springer US, 2009, pp. 659–663. ISBN: 9780387730035. DOI: 10.1007/978-0-387-73003-5_196 (cit. on p. 61).

[166] Ahmed Hanfy et al. *BSA Data AnalysisTool for LDA measurements*. Version 2.0.0. 2025 (cit. on p. 61).

[167] K. Pohlhausen. “Zur näherungsweisen Integration der Differentialgleichung der Iaminaren Grenzschicht”. In: *ZAMM - Journal of Applied Mathematics and Mechanics / Zeitschrift für Angewandte Mathematik und Mechanik* 1.4 (Jan. 1921), pp. 252–290. ISSN: 1521-4001. DOI: 10.1002/zamm.19210010402 (cit. on p. 61).

[168] Ernst Heinrich Hirschel, Jean Cousteix, and Wilhelm Kordulla. “Boundary-Layer Integral Parameters”. In: *Three-Dimensional Attached Viscous Flow*. Springer Berlin Heidelberg, 2014, pp. 99–105. ISBN: 9783642413780. DOI: 10.1007/978-3-642-41378-0_5 (cit. on p. 61).

[169] Oskar Szulc. “Pasywna kontrola oddziaływania fali uderzeniowej z warstwą przyścienną”. Polish. Rozprawa doktorska. Gdańsk, Poland: Instytut Maszyn Przepływowych im. Roberta Szewalskiego, Polska Akademia Nauk, May 2019, pp. 17–27. DOI: 10.13140/RG.2.2.29478.06721 (cit. on p. 61).

[170] Giel S. Cohen. “Control of shock-induced boundary layer separation at supersonic speeds”. PhD thesis. Queen Mary University of London, 2007. URL: http://qmro.qmul.ac.uk/xmlui/handle/123456789/1724 (cit. on p. 61).

[171] Tie Wei, Tobias Knopp, and Zhaorui Li. “Energy thickness in turbulent boundary layer flows”. In: *Journal of Fluid Mechanics* 1003 (Jan. 2025). ISSN: 1469-7645. DOI: 10.1017/jfm.2024.1195 (cit. on p. 62).

[172] Demetrios Lefas and Robert J. Miller. “Transonic Relief in Fans and Compressors”. In: *Journal of Turbomachinery* 144.5 (Nov. 2021). ISSN: 1528-8900. DOI: 10.1115/1.4052755 (cit. on p. 67).

[173] Randall M. Chriss et al. “An LDA investigation of three-dimensional normal shock wave boundary-layer interactions”. In: *Proceedings of Transonic Symposium: Theory, Application and Experiment*. Vol. 1. 2. 1989, pp. 741–764. DOI: 10.2514/6.1987-1369 (cit. on p. 68).

[174] Neil Titchener and Holger Babinsky. “Microvortex Generators Applied to a Flowfield Containing a Normal Shock Wave and Diffuser”. In: *AIAA Journal* 49.5 (2011), pp. 1046–1056. DOI: 10.2514/1.J050760 (cit. on p. 68).

[175] Paul J. K. Bruce et al. “Corner Effect and Asymmetry in Transonic Channel Flows”. In: *AIAA Journal* 49.11 (2011), pp. 2382–2392. DOI: 10.2514/1.J050497 (cit. on p. 68).

[176] Paul J. K. Bruce et al. “Corner effect and separation in transonic channel flows”. In: *Journal of Fluid Mechanics* 679 (May 2011), pp. 247–262. ISSN: 1469-7645. DOI: 10.1017/jfm.2011.135 (cit. on p. 69).

[177] Jan Matheis and Stefan Hickel. “On the transition between regular and irregular shock patterns of shock-wave/boundary-layer interactions”. In: *Journal of Fluid Mechanics* 776 (July 2015), pp. 200–234. ISSN: 1469-7645. DOI: 10.1017/jfm.2015.319 (cit. on p. 79).

[178] Jean-Paul. Dussauge and S. Piponniau. “Shock/boundary-layer interactions: Possible sources of unsteadiness”. In: *Journal of Fluids and Structures* 24.8 (Nov. 2008), pp. 1166–1175. ISSN: 0889-9746. DOI: 10.1016/j.jfluidstructs.2008.06.003 (cit. on p. 86).

[179] Prashant B. Godse, Harshal D. Akolekar, and A. M. Pradeep. “Surface roughness effects in a transonic axial flow compressor operating at near-stall conditions”. In: *Physics of Fluids* 36.10 (Oct. 2024). ISSN: 1089-7666. DOI: 10.1063/5.0230815 (cit. on p. 96).

[180] Yaozhi Lu et al. “Effect of Geometry Variability on Transonic Fan Blade Untwist”. In: *International Journal of Turbomachinery, Propulsion and Power* 4.3 (Aug. 2019), p. 24. ISSN: 2504-186X. DOI: 10.3390/ijtpp4030024 (cit. on p. 116).

[181] Richard P Geye and James G Lucas. *Investigation of Effects of Reynolds Number on Over-All Performance of an Eight-Stage Axial-Flow Research Compressor With Two Transonic Inlet Stages*. Tech. rep. 19930089630. Washington: NASA National Advisory Committee for Aeronautics, 1957 (cit. on p. 116).

[182] Arun Joseph et al. "Low Reynolds Number Effect on Highly Loaded Compressor Stator Cascade". In: *15th European Conference on Turbomachinery Fluid Dynamics and Thermodynamics*. ETC15. European Turbomachinery Society, 2023. DOI: `10.29008/etc2023-239` (cit. on p. 116).

[183] MG Silva, JBPF Falcao, and OAF Mello. "Control of High Speed Wind Tunnel Stagnation Pressure". In: *Proceedings of the 11th Brazilian Congress of Thermal Sciences and Engineering*. Curitiba, Brazil, 2006, pp. 05–08 (cit. on p. 116).